Fundamental data and conceptual framework for the
exploration of geothermal resources in the Himalaya-Karakoram
Orogenic belt, northern Pakistan

Dissertation

for the award of the degree

"Doctor rerum naturalium" (Dr.rer.nat.)

of the Georg-August-Universität Göttingen

within the doctoral program Geoscience

of the Georg-August University School of Science (GAUSS)

submitted by

Muhammad Anees

from

Haripur, Pakistan

Göttingen, 2023

Thesis Committee

Prof. Dr. Jonas Kley
(Department of Structural Geology and Geodynamics, Geoscience Centre, Georg August University Göttingen).

Dr. Bernd Leiss
(Department of Structural Geology and Geodynamics, Geoscience Centre, Georg August University Göttingen).

Prof. Dr. Mumtaz Muhammad Shah
(Department of Earth Science, Quaid-i-Azam University Islamabad, Pakistan).

Members of the Examination Board

Reviewer: Prof. Dr. Jonas Kley
(Department of Structural Geology and Geodynamics, Geoscience Centre, Georg August University Göttingen).

Second Reviewer: Prof. Dr. Mumtaz Muhammad Shah
(Department of Earth Science, Quaid-i-Azam University Islamabad, Pakistan).

Further members of the Examination Board:

Prof. Dr. Inga Moeck
(Department of Applied Geology, Geoscience Centre, Georg August University Göttingen).

Dr. Klaus Wemmer
(Department of Geochemistry and Isotope Geology, Geoscience Centre, Georg August University Göttingen).

Dr. Bernd Leiss
(Department of Structural Geology and Geodynamics, Geoscience Centre, Georg August University Göttingen).

Dr. Graciela Miriam Sosa
(Department of Applied Geology, Geoscience Centre, Georg August University Göttingen).

Dr. Alfons Van den Kerkhof
(Department of Applied Geology, Geoscience Centre, Georg August University Göttingen).

Dr. David Hindle
(Department of Structural Geology and Geodynamics, Geoscience Centre, Georg August University Göttingen).

Date of the oral examination: 19.01.2024

Abstract

Northern Pakistan lies within the collision zone of the Indian and Asian plates comprising Himalaya, Kohistan, and Karakoram, with numerous hot springs associated with the Himalayan Geothermal Belt, extending 3000 km along the Himalayas. The magnitude of terrestrial heat flow and the characteristics of potential heat sources for the present geothermal systems in this belt are of great importance and interest in geoscientific disciplines. The geothermal exploration in this remote region is limited to a two-decade-old geochemical analysis of hot springs. At the same time, the rugged topography, limited road infrastructure, and harsh climate hinder any prospect of large-scale exploration. Despite the indication of high surface heat flow in neighboring Indian Kashmir, the absence of reliable geophysical data and petrophysical parameters prevents the establishment of the thermal state of the lithosphere, which is a prerequisite for geothermal modeling and evaluation. Moreover, high radiogenic heat production (RHP) and fast exhumation of the basement crystalline complexes and granitoid batholiths are assumed to contribute significantly to the upper crust's heat flow.

The focus of the thesis was to understand and assess the geothermal resources of the Himalaya-Karakoram region of Pakistan on a reconnaissance scale and provide the baseline information and zones of interest as potential targets for future detailed exploration. To this end, it concentrated on the following objectives: 1) Identifying the areas with high lineament density, thermal anomalies, and hydrothermal alteration associated with active and paleo-geothermal zones. 2) Estimating the magnitude and variation of radiogenic heat production in different lithological units and understanding its role and contribution to overall heat flow and local geothermal systems. 3) Petrological, geochemical, and petrophysical characterization of outcrop analogs of subsurface reservoirs. 4) Creation of conceptual geological and geothermal models for understanding the geothermal play-types in the area and propose potential development scenarios. A multi-method and multi-scale approach is followed, which started from a regional level large-scale study through remote sensing, geological mapping, and literature review to analyze and understand the tectonic mechanism and structural features, surface temperature patterns, and hydrothermal alterations. A portable gamma spectrometer was used to measure radioelement concentration on the ground. Lab analysis (XRD, optical and cathodoluminescence microscopy, XRF, ICP-MS) of altered and unaltered samples were carried out to determine the mineralogical, petrological, geochemical, and petrophysical properties.

The remote sensing results confirmed the presence of high lineament density, thermal anomalies, and hydrothermal alteration in the regions close to hot springs and suture zones. The hydrothermal alteration results from remote sensing, later confirmed by XRD analysis, provided base information for subsequent field investigation. The radiogenic heat production in the Nanga Parbat Massif – NPM (with > 4 µWm^{-3}) is classified as high heat-producing, the

Karakoram batholith – KB (with 2 – 4 µWm^{-3}) as moderately heat-producing, and the Kohistan-Ladakh batholith – KLB (with < 2 µWm^{-3}) as low heat producing. Geochemical results indicate that the gneisses and granites of the NPM are mostly peraluminous alkaline S-type, enriched in REEs and radioactive elements, indicating partial melting and high fractionation. The granitoids of the KB are syenitic to granitic in composition, with the presence of REE-rich allanites in syenite. The KLB granitoids are calc-alkaline I-type and show depletion of REEs and radiogenic elements. Low matrix porosities (0.6 – 3.5%) and higher fault zone alteration indicate hydrothermal fluids' feedback effect on the host rocks via alteration-induced permeability. The crustal-scale thermal models revealed that the surface radiogenic heat production cannot be extrapolated to mid-crustal depth in the case of a subducting or under-thrusting layer. This layer's magnitude of heat production and thickness mainly control surface heat flow. Exhumation transports hot rocks to the surface, resulting in higher surface heat flow, even in an upper crust with low RHP. However, the lateral influence of exhumation is limited compared to the RHP. The shape of the near-surface isotherms is greatly influenced by topography, which gets expanded under mountains and compressed in valleys.

A conceptual model explaining the genetic mechanism for current hot springs considers increased concentrations of radiogenic elements and high exhumation for increasing the geothermal gradient, which is accessed by meteoric waters via deep faults. Finally, combining multi-scale and multi-method studies, the Nanga Parbat region, central Karakoram, and eastern Karakoram are potential geothermal targets identified for detailed and site-specific investigations. This thesis suggests the presence of hydrothermal and hot-dry rock geothermal play types in these identified areas. The findings presented in this work provide new key data for understanding of the region's geothermal regime on a larger scale and are fundamental for future geothermal exploration.

Zusammenfassung

Nordpakistan liegt in der Kollisionszone zwischen der indischen und der asiatischen Platte, die den Himalaya, Kohistan und Karakorum umfasst. Der geothermische Gürtel des Himalaya erstreckt sich über 3000 km und weist zahlreiche heiße Quellen auf. Die Höhe des terrestrischen Wärmeflusses und die Charakteristik der potenziellen Wärmequellen in diesem Gürtel sind von großer Bedeutung und Interesse für das Verständnis und die Quantifizierung der geothermischen Systeme in der Region. Die geothermische Erkundung in dieser abgelegenen Region beschränkt sich bislang auf eine zwei Jahrzehnte alte geochemische Analyse heißer Quellen. Gleichzeitig erschweren die starke Topographie, die begrenzte Straßeninfrastruktur und das raue Klima eine groß angelegte Exploration. Obwohl es Hinweise auf einen starken Oberflächenwärmefluss im benachbarten indischen Kaschmir gibt, ist es aufgrund des Fehlens zuverlässiger geophysikalischer Daten und petrophysikalischer Parameter nicht möglich, die thermische Charakterisitk der Lithosphäre zu bestimmen, was aber Voraussetzung für eine geothermische Modellierung und Nutzungsbewertung ist. Dabei wird davon ausgegangen, dass die hohe radiogene Wärmeproduktion (RHP) und die schnelle Exhumierung der kristallinen Grundgebirgskomplexe und granitoiden Batholithe wesentlich zum Wärmefluss in der oberen Kruste beitragen.

Das Ziel dieser Arbeit war es, die geothermischen Ressourcen in der Himalaya-Karakorum-Region Pakistans auf einer Erkundungsebene zu verstehen und zu bewerten, sowie grundlegende Daten bereitzustellen und Areale zu identifizieren, die als potenzielle Ziele für künftige detaillierte Explorationen dienen sollen. Zu diesem Zweck konzentrierte sich das Projekt auf folgenden Ziele: (1) Identifizierung der Gebiete mit hoher Lineamentdichte, thermischen Anomalien und hydrothermaler Alteration in Verbindung mit aktiven und fossilen geothermischen Zonen, (2) Schätzung der Höhe und der Schwankungen der radiogenen Wärmeproduktion in verschiedenen lithologischen Einheiten sowie das Verständnis ihrer Rolle und ihres Beitrags zum gesamten Wärmefluss und zu lokalen geothermischen Systemen, (3) Petrologische, geochemische und petrophysikalische Charakterisierung von Aufschlüssen, die als Analogien zu krustalen Wärmereservoiren darstellen (4) Erstellung konzeptioneller geologischer und geothermischer Modelle zum Verständnis der geothermischen Vorkommen in dem Gebiet und Vorschläge zu potenziellen Entwicklungsszenarien. Es wurde eine multimethodische und multiskalige Strategie angewandt, die mit einer Studie auf regionaler Ebene durch Fernerkundung, geologische Kartierung und Literaturrecherche begann, um die tektonischen Mechanismen und strukturellen Merkmale, Oberflächentemperaturmuster und hydrothermale Veränderungen zu analysieren und zu verstehen. Ein tragbares Gammaspektrometer wurde zur Messung der Radioelementkonzentration an der Gesteinsoberfläche im Feld eingesetzt. Laboranalysen (XRD, optische und

Kathodolumineszenz-Mikroskopie, XRF, ICP-MS) von alterierten und nicht alterierten Proben wurden durchgeführt, um die jeweilige Mineralogie zu bestimmen.

Die Fernerkundungsergebnisse zeigen eine hohe Lineamentdichte, thermische Anomalien und hydrothermale Alteration in den Regionen in der Nähe von heißen Quellen und Suturzonen. Die Ergebnisse der Fernerkundung zur hydrothermalen Umwandlung wurden durch XRD-Analysen bestätigt, die eine Informationsgrundlage für die weitere Felduntersuchung vor Ort bildeten. Die radiogene Wärmeproduktion im Nanga-Parbat-Massiv (NPM) (mit > 4 μWm^{-3}) wird als stark wärmeproduzierend eingestuft, der Karakoram-Batholith (KB) (mit 2 - 4 μWm^{-3}) als mäßig wärmeproduzierend und der Kohistan-Ladakh-Batholith (KLB) (mit < 2 μWm^{-3}) als gering wärmeproduzierend. Geochemische Ergebnisse deuten darauf hin, dass die Gneise und Granite des NPM überwiegend peraluminöser, alkalischer S-Typ sind, der mit REEs und radioaktiven Elementen angereichert ist, was auf partielles Schmelzen und hohe Fraktionierung hindeutet. Die Granitoide der KB haben eine syenitische bis granitische Zusammensetzung, wobei im Syenit REE-reiche Allanite vorkommen. Die KLB-Granitoide sind vom kalkalkhaltigen I-Typ und weisen eine Verarmung an REEs und radiogenen Elementen auf. Niedrige Matrixporositäten (0,6 - 3,5 %) und eine stärkere Alteration von Störungszonen deuten auf einen Rückkopplungseffekt der hydrothermalen Fluide mit dem Wirtsgestein hin, was einealterationsbedingte Permeabilität zur Folge hat. Die thermischen Modelle auf der Krustenskala zeigen, dass die radiogene Wärmeproduktion an der Oberfläche im Falle einer subduzierenden oder unterschiebenden Kruste nicht auf die mittlere Krustentiefe extrapoliert werden kann. Die Höhe der Wärmeproduktion einer solchen Kruste und ihre Dicke bestimmen hauptsächlich den Wärmefluss an der Oberfläche. Durch die Exhumierung wird heißes Gestein an die Oberfläche transportiert, was zu einem höheren Wärmefluss an der Oberfläche führt, selbst in einer oberen Kruste mit niedrigem RHP. Der seitliche Einfluss der Exhumierung ist jedoch im Vergleich zur RHP begrenzt. Der Abstand der oberflächennahen Isothermen wird stark von der Topografie beeinflusst; er nimmt unter Bergen zu und ist in Tälern komprimiert .

Ein konzeptionelles Modell, das den genetischen Mechanismus der heutigen heißen Quellen erklärt, geht von hohen Konzentrationen radiogener Elemente und einer starken Exhumierung aus, was zu einem erhöhten den geothermischen Gradienten führt. Meteorisches Wasser gelangt über tiefreichende Störungen in diese Zonen erhöhter Temperatur. Durch die Kombination von Multiskalen- und Multimethodenstudien wurden die Nanga Parbat-Region, der zentrale Karakorum und der östliche Karakorum als potenzielle geothermische Ziele für detaillierte und standortspezifische Untersuchungen identifiziert. Die Arbeit weist auf das Vorhandensein hydrothermaler und "Hot-Dry-Rock" geothermischen Systeme in diesen Gebieten hin. Die in dieser Arbeit vorgestellten Ergebnisse liefern neue Schlüsseldaten für das Verständnis des geothermischen Regimes der Region in einem größeren Maßstab und sind grundlegend für die zukünftige geothermische Exploration.

Acknowledgements

"And, when you want something, all the universe conspires in helping you to achieve it." — Paulo Coelho, The Alchemist

Table of contents

List of figures

List of tables

Chapter 1: Introduction

1.1 Background

In a world with ever-increasing energy demand and ensuing climate change challenges, developing renewable energy sources has become vital. Geothermal energy, the earth's heat, is one of the oldest renewable energy resources humans use for their domestic use (Stober & Bucher, 2012). In the early 20th century, the world's first geothermal power plant was built in Larderello, Italy (Bertini et al., 2006). With the dawn of the 21st century, the state of the art in geothermal energy (like other renewable resources) has achieved significant milestones. Once limited to conventional hot spots (volcanically active regions) (Huenges, 2010), modern technology has enabled the exploration and exploitation of unconventional geothermal resources that can be explored theoretically everywhere on Earth (Huenges, 2010; Aghahosseini & Breyer, 2020). Hot-dry rock is one of such unconventional geothermal resources, in which the rocks (primarily crystalline) contain internal heat and are now considered the most significant potential for geothermal energy, with an estimate of 1.3×10^{27} J predicated in the top 10 km of earth's crust (Huenges, 2010; Lu, 2018).

Geothermal activity in the form of hot springs can be commonly observed in mountainous orogenic belts even without active volcanism, which is attributed to fault-assisted deep circulation of meteoric water under hydraulic gradients induced by extreme topographic reliefs (Taillefer et al., 2017; Toth, 2009; Wanner et al., 2019). These systems are now termed "Orogenic geothermal systems," where the basement rocks, metamorphic strain, and the uplift of the orogen control background geothermal heat flow. Additionally, the orogenic belts contain crystalline metamorphic cores and granitic intrusions enriched in radioelements, which can significantly increase geothermal gradients (Jaupart et al., 2016). This background geothermal heat based on low permeable but conductive rocks acts as hot-dry rock (HDR) or petrothermal reservoirs, accessed at depths up to 10 km by percolating meteoric water (Diamond et al., 2018). Thus, the orogenic belts with hot-dry rocks offer optimal settings for geothermal energy exploration.
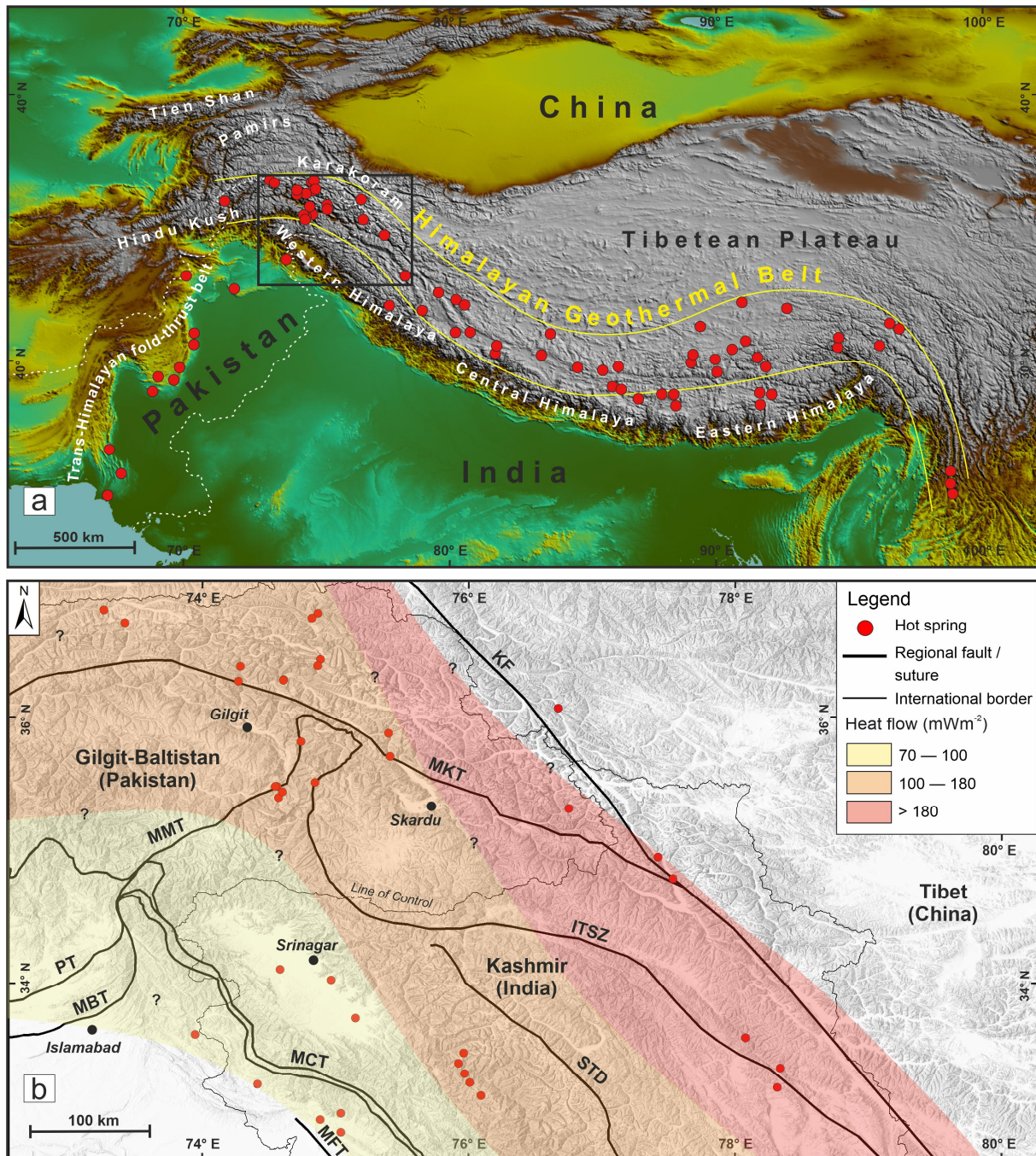
Figure 1.1 (a) Topographic map of south Asia showing the distribution of hot springs of the Himalaya Geothermal Belt-HGB (after Hochstein & Zhongke, 1995) within the hinterland of India-Asia collision zone. Other hot springs (outside HGB) in Pakistan are in the foreland region of the Trans-Himalayan fold-thrust belt. The black rectangle shows the location of Fig 1.1b. (b) Distribution of geothermal manifestations (as hot springs) in the hinterland of western Himalaya and Karakoram and associated interpolated heat flow map (modified after Craig et al., 2013; Shanker, 1988; Thussu, 2002). Heat flow is calculated from geothermal fields in Indian Kashmir and has been projected towards northwest Pakistan (marked by "?") by previous authors and may not represent background heat flow. Abbreviations: KF-Karakoram Fault; ISTZ-Indus Tsangpo Suture Zone; MBT-Main Boundary Thrust; MCT-Main Central Thrust; MFT-Main Frontal Thrust; MKT-Main Karakoram Thrust; MMT-Main Mantle Thrust; STD-South Tibet Detachment.

Northern Pakistan lies within the collision zone of Indian and Asian plates comprising Himalaya, Karakoram, and Tibet. More than 500 hot springs have been reported in this collision zone, collectively named the Himalayan Geothermal Belt (Tong & Zang, 1981). It is a 3000 km long EW trending belt stretching from the western Himalayas in north Pakistan to the eastern Himalayas in northwest India and includes parts of Pamir and Tibet (Fig 1.1a). The magnitude of terrestrial heat flow and the characteristic of potential heat sources for the present geothermal systems in this belt are of great importance and interest in geoscientific disciplines. Despite numerous Cenozoic intrusions, the lack of active volcanism and ^{3}He suggest the crustal origin of this anomalous heat (Hochstein & Zhongke, 1995). Most of the geothermal activity is concentrated along the belt's regional crustal faults and suture zones, with hot springs discharging in deeply incised valleys (Hochstein & Regenauer-Lieb, 1998). The near-surface interaction of meteoric water with the rapidly exhuming hot rocks during the ongoing continent-continent collision explains the hydrothermal activity (Chamberlain et al., 2002).

1.2   Research Problem

The exploration of geothermal resources requires surface and subsurface information, which is used for modeling, resource estimation, and risk assessment. Surface information, including identification of active and fossil systems, geochemical analysis of thermal fluids (in case of surface activity), fracture analysis, hydrothermal alteration, and outcrops analog studies, provide the initial estimates based on which zones of interest are identified from which subsurface information is extracted. This subsurface information includes geophysical surveys and borehole logs, which provide information about critical physical parameters (geothermal gradient, thermal conductivity, hydraulic conductivity, permeability, porosity, pressure, and reservoir volume) for reservoir characterization. This multi-parameter information is incorporated in a geological model for numerical modeling to simulate the temperature distribution at subsurface, heat, and fluid flow, which are used for geothermal resource estimation.

The rugged topography, limited road infrastructure, and harsh climate restrict large-scale exploration in the Himalaya-Karakoram region of Pakistan. Some studies have conducted geochemical analysis of hot springs and predicted their reservoir temperatures based on solute geothermometers (Ahmed et al., 2001; 2002). However, the physiochemical properties of hot springs are transient and vary with time (Chen et al., 2014; Gao et al., 2019), which reduces the usability of this two-decade-old data. There is a lack of comprehensive evaluation of the geothermal potential of the region by considering the genetic mechanisms of the geothermal systems. The thermal state of the lithosphere in the region has never been modeled, due to

which subsurface thermal structure is still unconstrained. Subsurface data such as heat flow, borehole, seismic, gravity, and magnetic are either lacking or limited, which hinders the imaging of spatial variation of lithospheric and crustal architecture in the study area. Additionally, no information is available on the radioelement concentrations, hydrothermal alteration, and petrophysical properties (density, porosity, thermal conductivity, specific heat capacity) of the crystalline rocks required for a geothermal model.

High heat flow values of >100 mWm^{-2} have been estimated from the geothermal fields adjacent to the east of this region in Indian Kashmir with similar geological settings (Fig 1.1b; Craig et al., 2013; Shanker, 1988). However, as these high estimates are based only on geothermally active areas, these heat flow values could not represent background heat flow. The background heat flow in the amagmatic orogenic belts is mainly controlled by the radiogenic heat production in the upper crust, amount of uplift, and tectonic strain (frictional heating) (Craw et al., 1997; Hochstein & Regenauer-Lieb, 1998; Jaupart et al., 2016). While the exhumational and frictional heating are primarily concentrated in the spatially constrained active zones (Ai et al., 2021; Furlong et al., 2021; Thigpen et al., 2021), rocks enriched in heat-producing elements occur widely and probably have been responsible for partial crustal melting in the Himalayas (Molnar et al., 1983). Enriched crustal rocks may significantly impact surface heat flux (Jaupart et al., 2016). Several authors have proposed high heat production in basement crystalline and granitoids to explain the metamorphic conditions (Faccenda et al., 2008; Pinet & Jaupart, 1987; Treloar, 1997), but no study has ever systematically measured the heat production in this region.

Near-surface high heat-producing rocks are now considered potential HDR resources because they can generate enough heat (when present in large volume) to significantly raise the geothermal gradients (McCay & Younger, 2017). Generally, hydrothermal systems exploit deep permeable pathways provided by faults to reach the subsurface reservoirs and when they travel back to the surface. This means that such systems are only restricted to the fault zones and cannot represent the actual geothermal capacity of a region. Contrary to the hot springs, the heat-producing rocks have a wider distribution and larger volumes. If proven that they are significant contributors to the local geothermal gradient, they could be exploited through direct drilling as potential enhanced geothermal targets.

1.3   Objectives

The focus of the thesis is to understand and assess the geothermal resources of the Himalaya-Karakoram region of Pakistan on a reconnaissance scale and provide the baseline information

and zones of interest as potential targets for future detailed exploration. In this regard, this work aims to;

- identify the areas with high lineament density, thermal anomalies, and hydrothermal alteration associated with active and fossil geothermal zones
- estimate the magnitude and variation of radiogenic heat production in different lithological units and understand its role and contribution to overall heat flow and local geothermal systems
- characterize the relevant lithological units as outcrop analogs of subsurface reservoirs based on their petrological, geochemical, and petrophysical properties
- to create conceptual geological and geothermal models, understand the geothermal plays-types in the area, and propose potential development scenarios

1.4   Research methods

A multi-method and multi-scale methodology is followed in this work to overcome challenges posed by limited literature, inaccessible terrain, and the size of the area (Fig 1.2). Initially, regional level large-scale study through remote sensing, geological mapping, and literature review to analyze and understand the tectonic mechanism and structural features, surface temperature patterns, and hydrothermal alterations. Based on satellite remote sensing, thermal anomalies are identified from nighttime land surface temperature, deformation zones are identified from lineament density, and hydrothermal alteration zones are identified from multispectral satellite imagery.

Based on remote sensing results and literature, ground surveys were carried out using gamma spectrometry, in which concertation of radioelements was measured using a portable gamma spectrometer. Altered and unaltered samples were collected for lab analysis. Lab investigations (XRD, optical and cathodoluminescence microscopy, XRF, ICP-MS) were carried out to determine the mineralogical, petrological, geochemical, and petrophysical properties.

Based on lab results and field survey, a conceptual geological model was proposed based on which thermal modeling was carried out based on parameters from this work. The remote sensing results were reanalyzed based on all the data to identify the potential zones of interest.

Figure 1.2 An overview of the methodology and its workflow followed in the thesis.

1.5   Significance of the research

The study area lies within the administrative boundaries of Gilgit Baltistan, which has crucial strategic and economic importance due to its border with China and the headwaters of the main rivers. However, this region (except for a few cities) is disconnected from the national power grid due to remoteness and limited road infrastructure. It relies on a few localized micro-hydropower plants only limited to specific perennial streams. Additionally, this region experiences prolonged winters with snowfall, and wood is the only available (but rapidly diminishing) heating source for the local population. While there are few hot springs that locals use for domestic purposes, i.e., spa, laundry, and cooking, there is a huge demand for sustainable energy sources for electric power and heating.

The large volume and wide distribution of heat-producing rocks in the region signifies that the surface manifestations may only represent a small portion of available heat in the subsurface. This suggests a possible hot dry rock potential for which the results of this thesis are crucial for the development of conceptual geological and geothermal base models. Additionally, this work significantly contributes to identifying potential geothermal zones for further detailed exploration and feasibility studies. The methodology of this work has proven cost and time-effective in geothermal exploration at a reconnaissance scale. In addition to its scientific and economic value, this work aims to promote research and awareness of the possibilities of geothermal exploration and development in Pakistan among government and private sectors.

1.6 Thesis outline

Chapter 2 focuses on northern Pakistan's regional tectonic settings in relation to the collision of Indian and Asian plates. A brief history of tectonic evolution is provided to understand the processes this region underwent before and after the formation of the Himalayan-Karakoram orogenic belt. This chapter also briefly explains the lithological units which were the focus of this thesis. The summary of the location of active hot springs, characteristics, and geological settings compiled from the literature is provided at the end of this chapter.

Chapter 3 focuses on applying satellite remote sensing to identify areas of interest that formed the base maps for later ground-based investigations. Results related to lineament density, thermal anomalies, and hydrothermal alteration are discussed. This chapter also discusses the problems related to identifying and mapping anomalous thermal zones. The results of hydrothermal alteration are compared with XRD analysis of samples collected from alteration zones, which show agreement and confidence in remote sensing results.

Chapter 4, published in Geothermal Energy, focuses on estimating the radiogenic heat production in prevailing crystalline lithologies using the concentration of radioelements (U, Th, and K) measured with a field gamma spectrometer. Furthermore, the intrinsic variations in radiogenic heat production associated with different rock types are examined to understand the factors controlling these variations, and their possible geothermal implications are discussed. These results provide better constraints for thermal modeling studies to explore the geothermal potential of the study area.

Chapter 5, submitted to Geothermics, focuses on an outcrop analog study in combination with a multi-parameter characterization to understand better the thermophysical, geochemical, and petrographic properties of crystalline (mostly granitoids and gneisses) rocks of the western Himalaya orogenic belt. The results of this chapter provide a preliminary but extensive dataset

of outcrop analogs for granitoid reservoirs in the study area. Compiling such data is necessary for numerical modeling and selecting suitable sites for further detailed and costly investigations.

Chapter 6 focuses on thermal modeling based on the parameters complied in Chapters 4 and 5. To establish a basal geothermal, 1D steady-state conductive thermal modeling is carried out with different scenarios of the heat-producing layer. 1D transient advective-conductive thermal model is used to test the effect exhumation. Then, a 2D near-surface (up to 10 km below sea level) model is used to model lateral temperature variations. The results provide an insight into the vital role of heat production and its potential influence on crustal geotherms.

Chapter 7 synthesizes the key findings of the four previous chapters. It discusses the potential geothermal targets in the area and possible modes of exploitation scenarios for them. It also proposes the strategies for future geothermal exploration and exploitation.

Chapter 2: Geological settings and geothermal activity in northern Pakistan

2.1 Tectonic framework of northern Pakistan

The western part of Himalayan-Karakoram orogen forms most of northern Pakistan and is tectonically subdivided from the north to the south into the Karakoram block (Asian plate), Kohistan (-Ladakh) arc, and the Indian plate (Nanga Parbat Massif) (Fig 2.1; Kazmi & Jan, 1997; Gaetani et al., 1996). The Kohistan arc (largely intra-oceanic) got sandwiched between Asian and Indian plates due to the closing of Neotethys along two suture zones and their subsequent collision in the Cenozoic era (Tahirkheli, 1979). These tectonic contacts are namely the Main Karakoram Thrust (MKT), which marks the boundary between the Karakoram and Kohistan, and the Main Mantle Thrust (MMT), which marks the suture between the Kohistan arc and Himalayas (Gansser, 1980; Kazmi et al., 1984).

The study area forms part of three tectonic domains, i.e., the Nanga Parbat Massif of the Himalaya, Kohistan (and Ladakh) batholith of the Kohistan (-Ladakh) arc, and Karakoram batholith of the Karakoram block (Fig 2.1). The following sections include further details about important tectonic features and geological units related to the study area.

2.1.1 Indian plate

The Nanga Parbat Massif (NPM) is the northernmost part of the Himalayas in Pakistan, where the Proterozoic Indian basement crust is exposed up to the elevation of ~8 km (Fig 2.1). The region exhibited a remarkably high uplift of up to 30 km during Himalayan orogeny (15 km in the last 3 Ma), forming an N-S striking syntaxis thrusting onto the Kohistan arc (Butler et al., 1989; Zeitler et al., 1993). It comprises Archean to mid-Proterozoic migmatitic quartzofeldspathic gneissic core, flanked by late Proterozoic calcareous and pelitic gneisses and amphibolites, with late Cenozoic pegmatitic and leucogranitic intrusions (Butler and Prior 1988; Zeitler et al., 1989). The metamorphic grade increases from amphibolite along the margins to granulite toward the massif's core (Fig 2.2).

The rock units of the massif, collectively termed the Nanga Parbat Group, are subdivided into Iskere Gneiss, Shengus Gneiss, and Haramosh Schist (Madin et al., 1989; Tahirkheli, 1983). The Iskere Gneiss, with zircons ranging in age up to 1.85 Ga, comprises coarse-grained biotite orthogneisses with minor biotite schist, amphibolite, and calc-silicates (Zeitler et al., 1989). The Shengus Gneiss incorporates laminated fine-grained amphibolite-grade paragneisses of pelitic and psammitic origin, interlayered with calc-silicates and amphibolites (Madin, 1986). The

Haramosh Schist comprises biotite schist and gneiss of amphibolite grade with subordinate marble and calc-silicates.
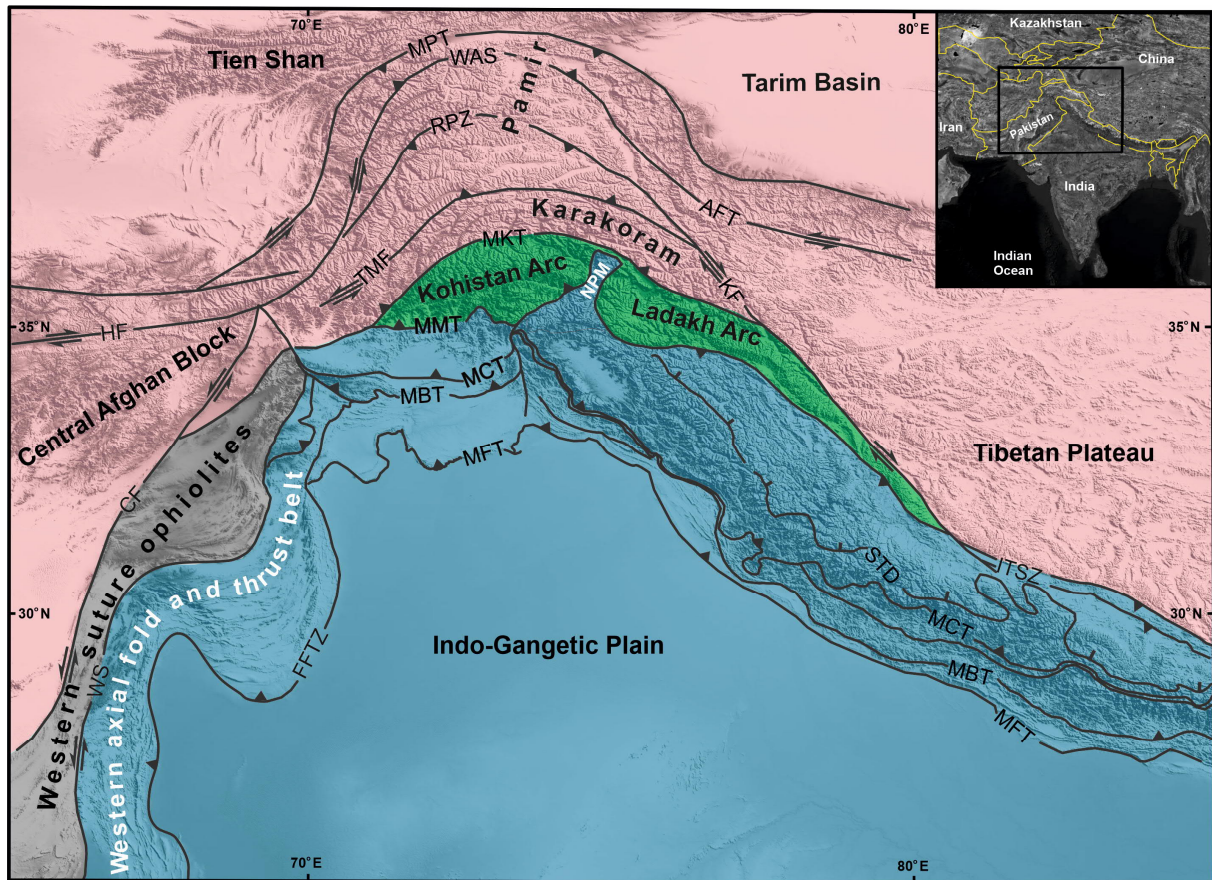
Figure 2.1 Regional tectonic map of Himalaya and surrounding regions (modified after Beck et al. (1996); Badshah et al. (2000); Dipietro and Pogue (2004); Faisal et al. (2018)). The Kohistan and Ladakh arcs (in green) are sandwiched between the colliding Indian (in blue) and Asian (in pink) plates. The study area comprises the Karakoram, Kohistan-Ladakh arc, and Nanga Parbat Massif. The inset map shows the geographic location. Abbreviations: AFT-Altyn Tagh Fault; CF-Chaman Fault; FFTZ-Frontal Fold Thrust Zone; HF-Herat Fault; KF-Karakoram Fault; ISTZ-Indus Tsangpo Suture Zone; MBT-Main Boundary Thrust; MCT-Main Central Thrust; MFT-Main Frontal Thrust; MKT-Main Karakoram Thrust; MMT-Main Mantle Thrust; NPM-Nanga Parbat Massif; RPZ-Rushan-Pshart Zone; STD-South Tibet Detachment; TMF-Tirich Mir Fault; WAS-Wanch-Ak Baital Suture.

The Miocene age intrusions resulted from late Cenozoic uplift and partial melting, distributed in the older rocks in the form of migmatites, small granitic plutons (~ 1 km^2), leucogranite, pegmatite dikes, and cordierite-bearing veins (Zeitler et al., 1993). The dikes and veins range from 1 cm to 50 m thick and consist of quartz, feldspar, muscovite, biotite, tourmaline, and garnets.

2.1.2   Kohistan-Ladakh arc

The Kohistan-Ladakh arc is ca. 700 km long, mainly E-W trending island-arc terrane, and is sandwiched between Karakoram (of Asian plate) to the north along Shyok suture zone and the Himalaya (Indian plate) to the south along MMT. This Cretaceous intra-oceanic island arc complex has been deformed and partly metamorphosed due to its obduction onto the Indian plate to the south along MMT. The NPM's exhumation has eroded Kohistan's overlaying mass and split it into the Kohistan arc in the west and the Ladakh arc to the east (Fig 2.1; Tahirkheli, 1979; Petterson, 2010). The Kohistan arc comprises a complete crustal section of the mantle to the uppermost crustal rocks. In contrast, the Ladakh arc predominantly comprises upper crustal volcanic and plutonic rocks (Treloar et al., 1990).

The Kohistan Island arc consists of ca. 30 km thick igneous and sedimentary rock sequences of the Cretaceous age subdivided into five following parts (Petterson, 2010);

(1) The Jijal complex, towards the north of the MMT, is composed of ultramafic to mafic rocks (including harzburgites, upper granulite facies garnet granulites, websterites, and pyroxenites) and forms the lower and southernmost part. (2) The Kamilia Amphibolites are exposed towards the north of the Jijal complex and consist of metavolcanics (basalts and basaltic andesites) and metaplutonics (basalts and basaltic andesites). (3) The Chilas complex comprises basic–ultrabasic plutonic gabbro-norite rocks. (4) The Jaglot group, a volcanic-metasedimentary group, has lithologies such as metasandstones, carbonates, siltstones, mudstones, and turbidites with local metabasalt, andesite, and rhyolite volcanic rocks. (5) The Kohistan batholith is exposed north of the Jaglot group, intrusive into the Chalt volcanic group, and overlain by Yasin volcaniclastics towards the north until the MKT (Petterson & Treloar, 2004).

The Kohistan batholith is formed due to magmatism (lasting ca. 86 Ma) due to the subducting Neo-Tethyan oceanic crust leading to the India-Eurasia collision (Petterson, 2010). It is a composite of gabbro-diorites, trondhjemites (Matum Das pluton), granites, and leucogranite sills and dikes (Hanzel, Jutal and Confluence granite) (Petterson et al., 1993; Treloar et al., 1996). Three distinct growth phases have been identified, i.e., deformed plutons (ca. 102 Ma), which are intruded by undeformed gabbros, granites, and diorites, cut by late granite sheets (50-26 Ma) (Petterson & Windley, 1985). The Ladakh batholith (the eastern equivalent of the Kohistan batholith) is predominantly composed of biotite-hornblende granites, tonalites, diorites, gabbros, and norites. It also includes volcanic units primarily exposed in its eastern parts (Singh, 1993).

2.1.3   Karakoram

The Karakoram terrane represents the southern margin of the Asian plate. It is subdivided (from north to south) into the Northern Karakoram sedimentary belt, Karakoram Batholith, and Karakoram Metamorphic Complex (Searle & Khan, 1996). The northern Karakoram represents a back-arc sedimentary basin with Paleozoic carbonates and clastic sedimentary rock deposits that extend northward toward the southern Pamir (Palin et al., 2012).

The Karakoram Batholith is an E-W trending, 600 km long, and up to 30 km wide axial batholith that separates the northern sedimentary sequence from the southern metamorphic complex (Crawford & Searle, 1992; Searle et al., 1989). The batholith comprises plutonic units of different ages, chemical and mineralogical composition, and tectonometamorphic history (Debon et al., 1987). It predominantly comprises Cretaceous I-type granodiorites and diorites intruded by Cenozoic leucogranites (Searle & Tirrul, 1991). The lithological units exposed in the western and central parts comprise sub-alkaline and calc-alkaline subduction-related Andean-type pre-Himalayan granitioids (Hunza plutonic unit) of mid-Cretaceous age (Crawford & Searle, 1992). The eastern part consists Jurassic diorite gneiss (Hushe gneiss) intruded by exhumation-related post-collisional leucogranites and monzogranites (Baltoro plutonic unit, Kande plutonic complex) to syenite of Miocene age (Fig 2.2; Searle et al., 2010; Villa et al., 1996). Searle et al., 1989 have described the Kande plutonic complex (KPC) as a composite of older mafic granitoids intruded by younger (~ 24 Ma) leucocratic intrusions. The composition of the complex varies from oldest diorite, latter tonalite to granodiorite, and youngest K-feldspar porphyritic, with all units containing biotite and hornblende.

The Karakoram Metamorphic Complex contains kyanite to sillimanite grade schists, paragneisses, amphibolites, and interlayered marbles and pegmatites (Bertrand et al., 1988; Searle et al., 1989). The high-grade gneisses of the Karakoram metamorphic complex are in thrust contact with low-grade metavolcanics of the Kohistan along the MKT (Searle et al., 1989). The Dassu gneiss exposed in the Shigar valley, comprising biotite-K-feldspar-plagioclase-quartz-sillimanite-garnet ± muscovite gneisses, forms a lower crustal dome composed of felsic orthogneiss containing zircons of Precambrian inheritance and intruded by numerous aplite-pegmatite dikes formed by partially melting in Pliocene time (Fig 2.2; Searle et al., 1989).

2.2   Tectonic Evolution during pre and post India-Asia collision

The Himalaya-Karakoram-Tibet orogen as a whole is built from the amalgamation of Indian lithosphere, intra-oceanic island arcs, and different Gondwanian terranes that accreted to

Eurasia following the breakup of Pangea between the Triassic and Early Cretaceous (Kapp & DeCelles, 2019). Late Permian to Early Triassic rifting of the Cimmerian microcontinent (as Karakoram block in northern Pakistan) led to the opening of Neotethys and closing of Paleotethys till suturing with the Asian plate (Gaetani, 1997). The Late Jurassic accretion of the Karakoram block to Asia was followed by multiple subduction-related magmatic episodes lasting until the Cretaceous (Crawford & Searle, 1992). The closure of Neotethys started with the northward drift of the Indian plate from Gondwana at ~140 Ma ago (Kumar et al., 2007), which resulted in intra-oceanic subduction and formation of Kandahar, Nuristan, and Kohistan-Ladakh arcs (Treloar & Izzat, 1993; Searle et al., 1999). The Kohistan-Ladakh represents Cretaceous to Paleocene subduction-related magmatism spanning over 40 million years (Petterson & Windley, 1985). Later, the intrusion of large-scale granodioritic batholith marked its evolution into an Andean-type magmatic arc (Petterson & Windley, 1991). The collision of the Indian continent with the Kohistan-Ladakh arc along the Indus suture zone is estimated to have occurred 54 to 50 Ma (Garzanti et al., 1987; Najman et al., 2017). The collision of Kohistan with the Karakoram is still under debate, with some authors suggesting it happened between 100-90 Ma (Borneman et al., 2015; Gaetani et al., 1990; Gaetani et al., 1993; Petterson & Windley, 1985), while others suggesting it to be as young as 40 Ma (Bouilhol et al., 2013; Brookfield & Reynolds, 1981; Martin et al., 2020).

The Himalayan orogeny was initiated subsequently after the closure of Neotethys and India-Asia collision at ~50 Ma when the northern margin of the Indian plate started subducting under Kohistan and Ladakh. This collision led to crustal shortening and thickening of the Indian plate which underwent barrovian metamorphism spanning for at least 41-11 Ma (Carosi et al., 2015; Green et al., 2008). The Proterozoic to Paleozoic rocks (of the Indian upper crust) experienced up to migmatitic conditions, which peaked at ~ 10 Ma after the collision and caused the formation of Himalayan leucogranite (with crystallization ranging between 21-18 Ma) (Searle, 2015). With the continued northward collision of India, the deformation in the Indian plate started propagating southwards to the plate interior. Major thrusts such as MCT (Early Miocene), MBT (~10 Ma), and MFT (4-5 Ma) were formed, which accommodated the crustal shortening (Burbank & Beck, 1989; Meigs et al., 1995; Robinson et al., 2003). These thrusts brought the basement to cover sequence to the surface, causing the uplift of the Himalayas.

Throughout the India-Asia collision (~50 to 13 Ma), crustal thickening, regional metamorphism, and migmatization occurred in the southern Karakoram and north margin of India (Searle & Hacker, 2019). The stacking of the Indian lower crust (Archean granulites) beneath the southern Karakoram margin caused the crustal thickening, which, upon imbrication and thermal relaxation, led to dehydration melting (Searle et al., 1989). The subsequent large-scale

melting in the lower crust and the extension along the old Karakoram batholith units and the northern sedimentary cover is believed to be responsible for the intrusion of the Baltoro batholith in the Miocene (Searle et al., 2010). The recent uplift in Karakoram is accommodated along MKT, a late Tertiary breakback thrust (Searle et al., 1989).

2.3 Geothermal activity in northern Pakistan

Hot springs commonly occur in the Himalayan collision zone comprising Himalaya, Karakoram, and Tibet, collectively named the Himalayan Geothermal Belt (Tong & Zang, 1981). It is a 3000 km long E–W trending belt stretching from the western Himalayas in north Pakistan to the eastern Himalayas in northeast India and includes parts of Pamir and Tibet. The geothermal activity is mainly concentrated along the belt's regional crustal faults and suture zones, and hot springs manifested in incised valleys (Hochstein & Regenauer-Lieb, 1998). The near-surface interaction of meteoric water with the rapidly exhuming hot rocks during the ongoing continent-continent collision explains the hydrothermal activity (Chamberlain et al., 2002).

In northern Pakistan, the geothermal activity is mainly manifested as hot springs located near suture zones and active faults indicating deep fluid circulation (Fig. 2.2; Yousafzai et al., 2010). The hot springs in the Karakoram block mostly emerge along the MKT and associated faults. In the upper Hunza valley, the hot springs reported at Shachktar, Belli, and Hussaini emerge in the sedimentary units of northern Karakoram with surface temperatures of 51, 48, and 50 ºC, respectively (Muhammad & Haq, 2022). Whereas towards the south, in the lower Hunza valley, a cluster of ca 6000 m^2 of several hot springs (35 - 94ºC) along with fumarole deposits are reported at Murtazabad and Hakuchar. They are located on the opposite banks of the Hunza River (Ahmed et al., 2002). These hot springs are associated with medium to high-grade metapelites from the Karakoram metamorphic complex. However, the radiogenic heat from the Karakoram batholith (located ca. 10-15 km north of the hot spring site) has been suggested as a probable heat source (Zaigham et al., 2009).

Further southwest, another hot spring site with surface temperatures of 46 ºC is located at Budelas, where dioritic plutons intrude the metamorphic complex. Towards the east, along the MKT, hot springs emerge along the Basha River north of Shigar valley at Chutran and Bisil with surface temperatures of 44 ºC and 60 ºC, respectively. Proximal lithologies in this region are orthogneiss of the Karakoram metamorphic complex with scattered marbles intruded by a syenitic pluton and pegmatitic dikes. In the Kondus Valley, located northeast of Saltoro Valley, hot springs with a surface temperature of ~65 ºC emerge from fractured granite. Towards the west, along the MKT, hot springs associated with the Karakoram batholith are reported near

Darkot Pass (north of Yasin Valley) and Pechus glacier (about 105 km northeast of Mastuj) (Shuja, 1986).

Along the MMT, several hot springs are present along the margins of the Nanga Parbat massif. On the eastern margin, at Mushkin, a hot spring with 57 ºC has been reported (Ahmad et al., 2002). The western margin of the massif shows higher geothermal activity with numerous hot springs at Tattapani (near Raikot bridge) and Sassi (northeast of Jaglot), with surface temperatures in the range of 42 – 81 ºC (Ahmad et al., 2002). This high concentration of hot springs along the western margin has been attributed to the seismically active Raikot fault, which provides an escape channel for deeply infiltrated meteoric waters (Butler, 2019). Towards the core of the massif along Raikot Valley, at Tato village, a hot steaming geyser and numerous hot springs with near-boiling water (~92 ºC) are present. Besides these hot springs, alteration zones are common, indicating the interaction of meteoric water with hot rocks during exhumation and erosion (Chamberlain et al., 1995).
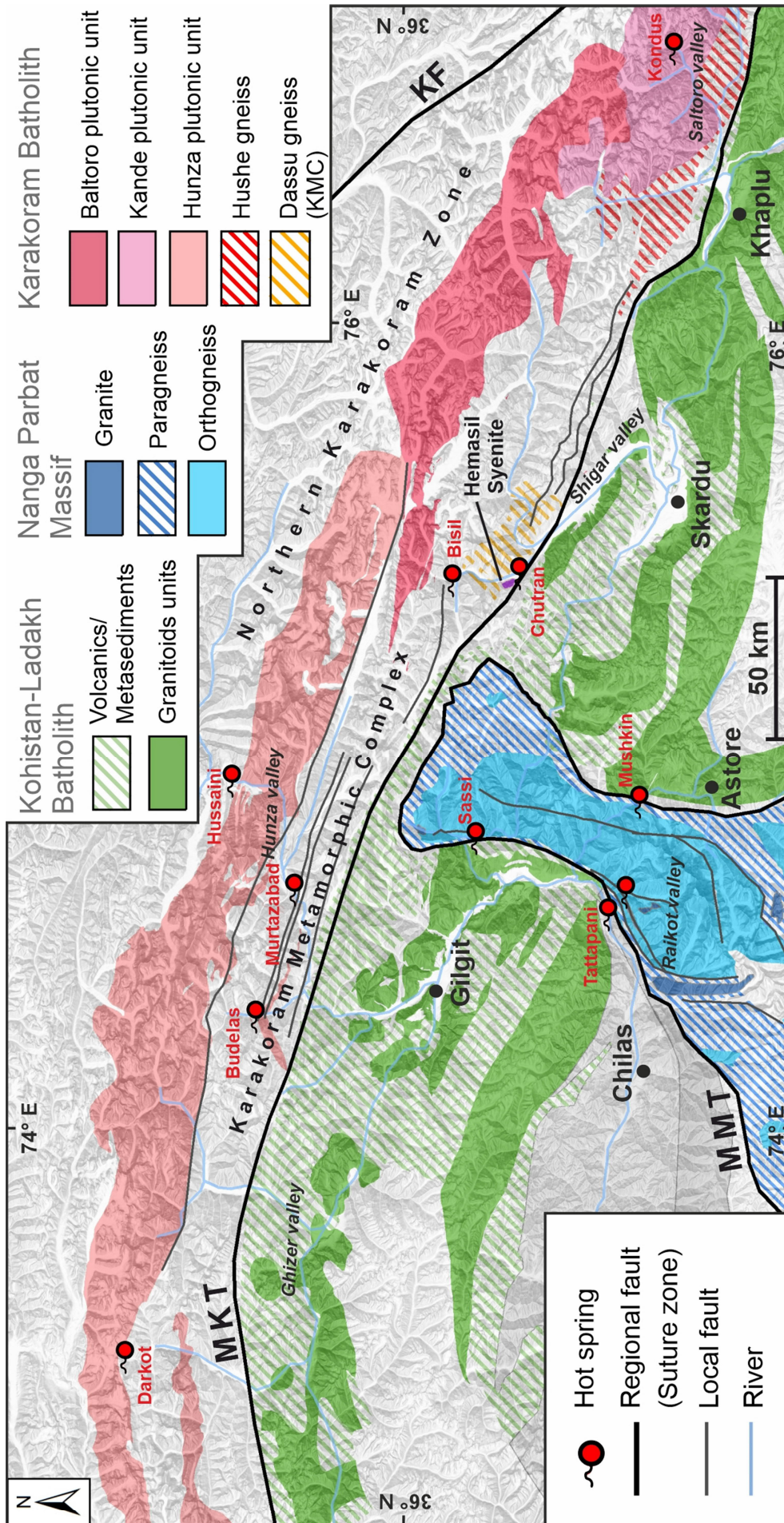
Figure 2.2 Map of the study area showing the locations of hot springs and geological units (redrawn after Madin et al., 1989; Schneider et al., 1999; Searle & Khan, 1996).

Chapter 3: Identification of potential geothermal zones using remote sensing

This chapter is based on an article titled "Exploration of Potential Geothermal Resources in the Himalaya-Karakoram Orogenic Belt, Northern Pakistan" accepted for proceedings of the Stanford Geothermal Workshop, California, USA, 12 – 14 February 2024. The abstract is not included here and the alphanumeric order of figures and tables may differ from the original article. Likewise, the formatting was adjusted to fit the layout of this work.

3.1 Introduction

The hot springs in northern Pakistan form the Himalayan Geothermal Belt's western part, extending along the Himalayas (Tong & Zang, 1981). The Himalayan Orogen, due to the active collision between the Indian and Eurasian plates, has a high heat flow due to thick radiogenic crust, fast exhuming mountains, and young intrusions (Butler et al., 1997; Craw et al., 1997; Hochstein & Regenauer-Lieb, 1998; Chamberlain et al., 2002; Zaigham et al., 2009). The concentration of hydrothermal activity along tectonic sutures and intraplate thrust faults suggests that the percolating meteoric water can access this high background heat flow deep enough to reach boiling temperatures. Additionally, numerous alteration zones on the surface indicate high spatial and temporal variability of geothermal activity due to the rapidly evolving landscape in this mountainous area. These geothermal indications provide a promising potential for geothermal energy.

Geothermal resources are traditionally explored by surveying vast areas at a reconnaissance scale to identify geothermal reservoirs and then applying data from geophysical and geochemical surveys for modeling and resource estimation (Arnórsson et al., 2006; Barbier, 2002; Kana et al., 2015). The Gilgit-Baltistan region (of north Pakistan) is characterized as the terrain with one of the world's highest topographic reliefs, with high snow-covered mountains with glaciers and deep and narrow valleys. This mountainous terrain with limited accessibility makes traditional geological and geophysical exploration challenging. Additionally, the high cost and associated logistical problems limit the exploration over a large area. Due to these reasons, no detailed exploration or mapping has been conducted so far despite the enormous geothermal potential. Only a few studies have performed geothermal investigations, of which most analyzed the chemical composition of hot springs and calculated their reservoir temperatures using chemical geothermometers (Ahmad et al., 2001; 2002). With technological advancement, there is a need to apply novel methodologies to explore the geothermal resources in this region.

In recent decades, remote sensing technology has developed to a level commonly used for geoscience exploration, specifically geothermal exploration (van der Meer et al., 2012; 2014). Remote sensing data can be used to provide information on mineralogy, temperature, and deformation on a surface over a large and inaccessible area, which can help in better understanding the geothermal potential (Haselwimmer et al., 2013; van der Meer et al., 2014). Lineament density extracted from remote sensing data can help identify areas with faults and fractures associated with tectonic deformation (Wajid et al., 2021). Thermal infrared (TIR) can provide synoptic coverage of surface indicators of geothermal systems. It can be helpful in mapping and quantification of surface thermal anomalies related to geothermal features like geysers, fumaroles, and hot springs (Coolbaugh et al., 2007). Moreover, near-short wave infrared remote sensing data is helpful in the identification and mapping of alteration minerals that are associated with hydrothermal processes in geothermal fields (Yang et al., 2001).

This study aims to employ remote sensing data to identify areas of interest that formed the base maps for later ground-based investigations. The identification and mapping of thermal anomalous zones has been carried out using satellite imagery. Surface lineaments and density maps have been extracted to indicate areas with high deformation. The multispectral satellite imagery was used for alteration mineral mapping to identify the areas affected by circulating hydrothermal fluids. Finally, the remote sensing results are compared with XRD analysis of samples collected from alteration zones.

3.2   Data and methods

3.2.1   Lineament extraction

Lineaments are usually regarded as linear (or curvilinear) features on the earth surface which can be the expressions of geology (faults, shear zones, dykes, etc), geomorphology (valleys, rivers, ridges, etc) or other manmade (roads, canals, etc) features (O'leary at al., 1976; Sabins, 1996). Satellite based topographic data has been commonly used to extract the orientations of surface landforms and interpret them as linear features (from here on termed as lineaments). In the Himalaya-Karakoram region the surface geomorphology and topography are greatly influenced by the tectonic activity and therefore, the lineaments based on geomorphological features should be in close resemblance with the surface geological features.

A semi-automated approach was to extract the lineaments using the SRTM digital elevation model (30m resolution) by shaded relief mapping through directional filtering in the ArcGIS 10.6, which sharpened the boundaries or discontinuities between the adjacent areas and helped identify lineament features such as straight valleys, straight streams segments, and rock boundaries, edges, cliffs, fault traces (Suzen & Toprak, 1998). The shaded relief map

extracts lineaments based on four different azimuth angles (0°, 45°, 90°, 135°). The LINE module in PCI Geomatica was used to extract lineaments from shaded relief images obtained after directional filtering (Table 3.1; Thannoun, 2013). The finalized lineaments from four azimuth angles were merged in ArcGIS to generate a single vector shapefile. Postprocessing removed duplicates and redundant lineaments to obtain the final lineament data set, which was used to generate lineament density maps using ArcGIS.

Table 3.1 Values assigned for input parameters for extraction of lineaments in LINE module of PCI-Geomatica

Parameter	Range	Opted value
RADI/Filter radius (pixels)	0–8192	5
GTHR/Edge gradient threshold	0–255	50
LTHR/Curve length threshold (pixels)	0–8192	10
FTHR/Line fitting error threshold (pixels)	0–8192	3
ATHR/Angular difference threshold (degrees)	0–90	15
DTHR/Linking distance threshold (pixels)	0–8192	20

3.2.2   Thermal data

ASTER Level-1T thermal infrared imagery of night-time (with 90m resolution) was radiometrically and atmospherically corrected by applying respective corrections in ENVI 5.3 software. An emissivity normalization algorithm was applied to normalize emissivity values and to calculate land surface temperature (LST). Ulusoy et al. (2012) used a topographic correction to minimize the topographic effects. This correction uses statistical regression to remove the effects of elevation, aspect, and slope. Topographic correction was applied in three steps:

1. A temperature versus elevation scatter plot was used to calculate the lapse rate, which was then subtracted from the original LST image to remove the effect of elevation.
2. The elevation-corrected data was plotted against aspect data to calculate the aspect gradient, which was used to remove aspect-related errors.
3. Slope data was used to calculate and remove the slope gradient from the corrected image to obtain a final elevation, aspect, and slope corrected image.

The resultant corrected images produced thermal anomaly images in the form of positive and negative with variable magnitude from the mean.

3.2.3 Multispectral data

ASTER Level-1T (at sensor-radiance) multispectral imagery with three near and six shortwave infrared bands was resampled to 30 meters. The data was converted from radiance to surface reflectance using the FLAASH algorithm, which also removes the atmospheric effects from the data (Kruse, 2004). Areas with vegetation and snow were masked to exclude from the analysis. Principal component analysis (PCA) was performed to reduce the correlation among similar bands. PCA is a multivariate statistical technique that decorrelates the high-variance variables into low-variance linear principal components (Singh & Harrison, 1985). Crosta technique was applied after Crosta et al., 2003, in which PCA was applied on four bands with reflectance and absorption specific to the target minerals, e.g., alunite, chlorite, epidote, illite, kaolinite, and sericite (or white mica). These minerals are selected as indicators of argillic (alunite and kaolinite), phyllic (illite and sericite), and prophylitic (chlorite, epidote and calcite) alterations. The resultant eigenvector matrix between the principal components (PC) indicated whether the resultant PC band corresponding to the target mineral's highest reflectance is positive or negative (Yalcin et al., 2020). If the eigenvector was positive, the target mineral was displayed in bright pixels, and if it was negative, then the dark pixels represented the target mineral (Crosta et al., 2003).

3.2.4 X-ray Diffraction

X-ray diffraction (XRD) analysis was carried out to determine semi-quantitative mineralogical analysis of the rock samples collected from the alteration zones. The bulk sample was crushed to powder (<60 μm) using an agate ball mill. The analysis was conducted using XRD-Eigenmann's Orion Komet P2 diffractometer, equipped with a Cu anode applying 40 KV and 40 mA for measurements. The 2θ scan range was 4 to 70⁰ and the 2θ step size 0.02⁰, with each step of 2 seconds. The data analysis was carried out using HighScore Plus software by Malvern Panalytical.

3.3 Results

3.3.1 Lineament analysis

A total of 12,221 lineaments covering an area of approximately 50,000 km^2 have been extracted, which were then classified into four classes according to their azimuths, i.e., N-S, NE-SW, E-W, and NW-SE (Fig 3.1a). Table 3.2 shows the details of the distribution of classified lineaments. Of these four classes, 40 % or 4,896 are classified as E-W, followed by NE-SW lineaments amounting to 2,993 (24.5 %). Lineaments with NW-SE and N-S orientation have lower totals of 2,576 (21 %) and 1,756 (14.5 %), respectively. Similarly, out of the estimated total length of lineaments of 36,635 km, 13,935 belong to the E-W class, 9,039

belong to the NE-SW class, 7,772 belong to the NW-SE class, and 5889 belong to the N-S class. The rose diagram in Figure 3.1a indicates a predominant N-S orientation of lineaments along with a minor NE-SW component.

Figure 3.1b shows the lineament density map in the study area, which varies from 0 to 5.68 km/km^2 and is classified into five classes, i.e., very low (<1 km/km^2), low (1 to 2 km/km^2), moderate (2 to 3 km/km^2), high (3 to 4 km/km^2) and very high (>4 km/km^2). Glacial regions of Karakoram towards the east of the study area show low to moderate lineament density. In contrast, high lineament density is present in Kohistan and Nanga Parbat and near faults.

Class-wise lineament density distribution show high lineament density of N-S lineaments most prominent along MMT in the southwestern part of NPM (Fig 3.2a), with other small spots scattered mostly around faults. High-density regions for NE-SW lineaments lie parallel to MKT and Kohistan (Fig 3.2b). E-W oriented lineaments have a moderate density coverage all over the study area with prominent hot spots north of MKT, in the Karakoram, along the faults (Fig 3.2c). The NW-SE lineaments are dense in Kohistan and northern Karakoram (Fig 3.2d).

Figure 3.3 represents various rose diagrams showing the orientation of lineaments in high-density areas. High density in the southern Kohistan batholith has NE-SW orientation, which changes to NW-SE in the central part and eventually orientates to N-S in the northern part along MKT. The Karakoram batholith has WNW-ESE-oriented high-density zones. Towards the east, high-density zones in the Ladakh batholith show ENE-WSW orientations. In NPM, the southern part shows WNW-ESE orientation, while the central and north parts have ENE-WSW high-density lineament zones with a minor N-S component.

Table 3.2 Azimuth-based classification of lineaments showing the number, proportion, and total length of lineaments for each respective class

Lineaments Class	Azimuths	No. of lineaments	% of lineaments	Total length of lineaments (km)
N-S	337.5 – 022.5 157.5 – 202.5	1756	14.5	5889
NE-SW	022.5 – 067.5 202.5 – 247.5	2993	24.5	9039
E-W	067.5 – 112.5 247.5 – 292.5	4896	40	13935
NW-SE	112.5 – 157.5 292.5 – 337.5	2576	21	7772
Total		12221	100	36635
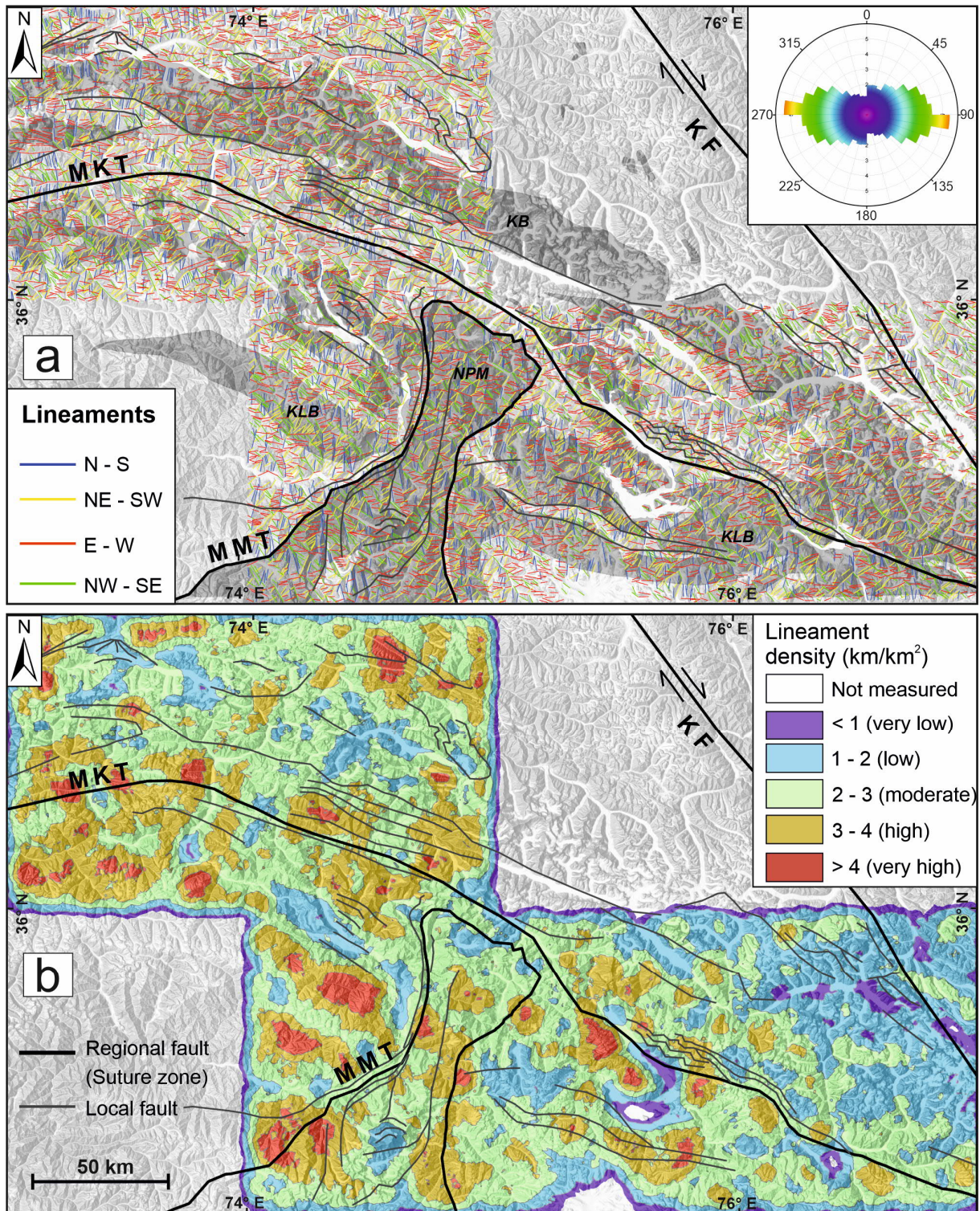
Figure 3.1 (a) Spatial distribution and classification of all lineaments extracted in this study overlaid on a multi-direction shaded-relief map. The rose diagram on the top right shows the E-W orientation of most lineaments. (b) Lineament density map with classification into five classes (very low to very high) shows the distribution of different classes with respect to the structures in the study area. Abbreviations: NPM-Nanga Parbat Massif; KLB-Kohistan-Ladakh batholith; KB-Karakoram batholith; MMT-Main Mantle Thrust; MKT-Main Karakoram Thrust; KF-Karakoram Fault. The extent of figures is same as in Fig 2.2.
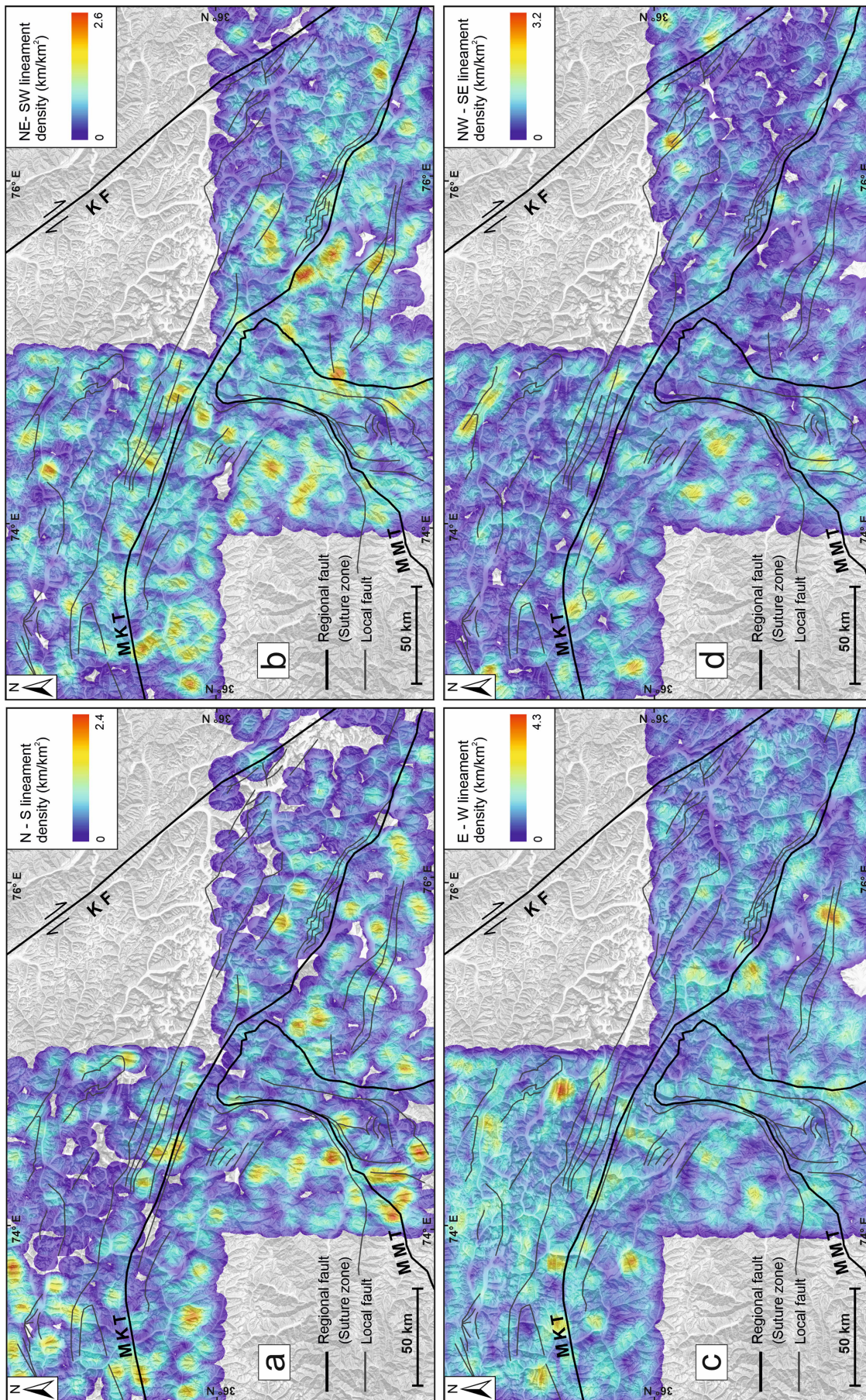
Figure 3.2 Spatial distribution lineament densities of four azimuth-based classes overlaid on a multi-direction hillshade. (a) N-S. (b) NE-SW. (c) E-W. (d) NW-SE.
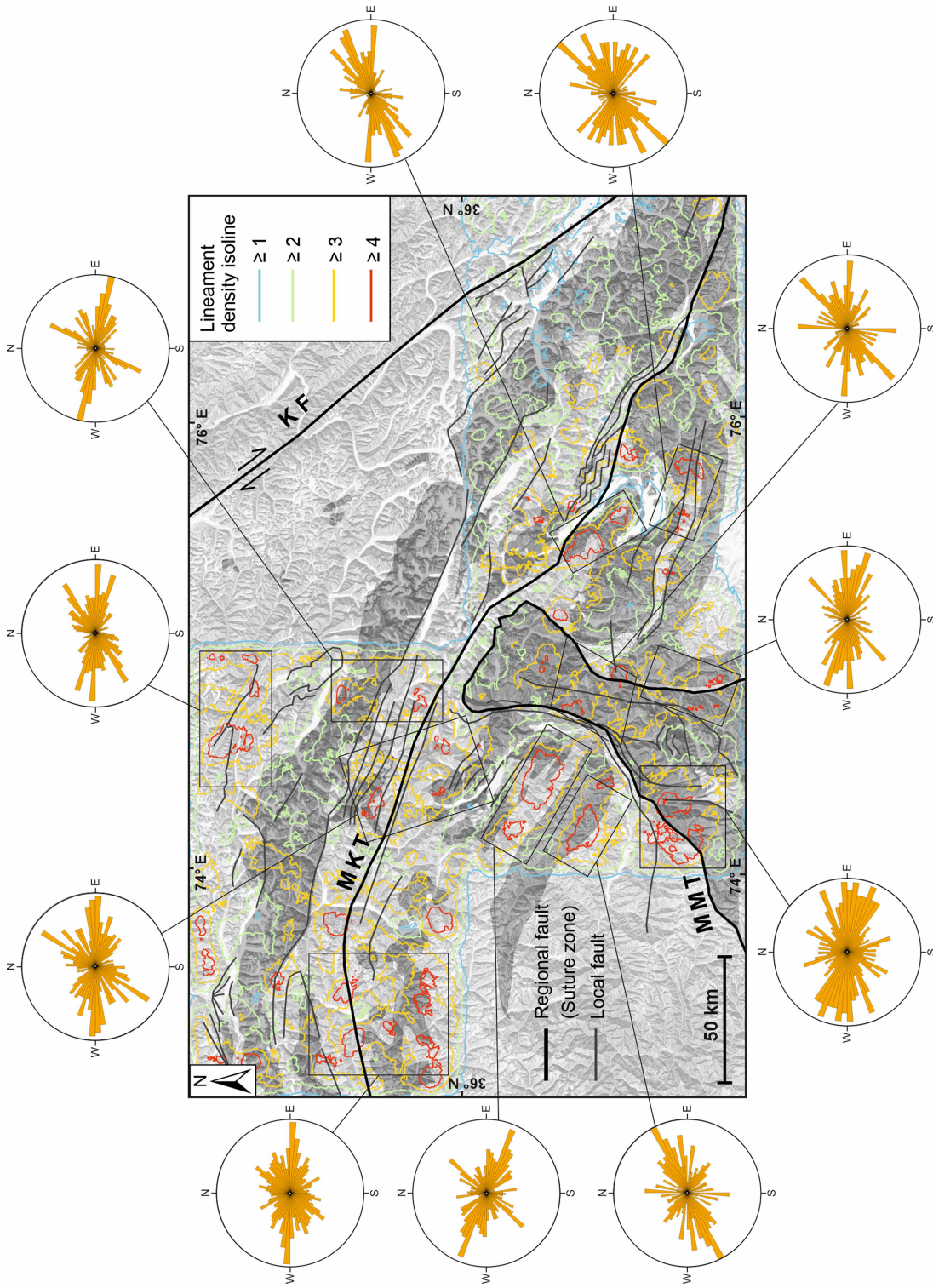
Figure 3.3 Rose diagrams show the orientation of lineaments in various high-lineament density zones within the study area. The filled grey polygons in the background indicate the lithological units of interest, i.e., granitoids and gneisses.
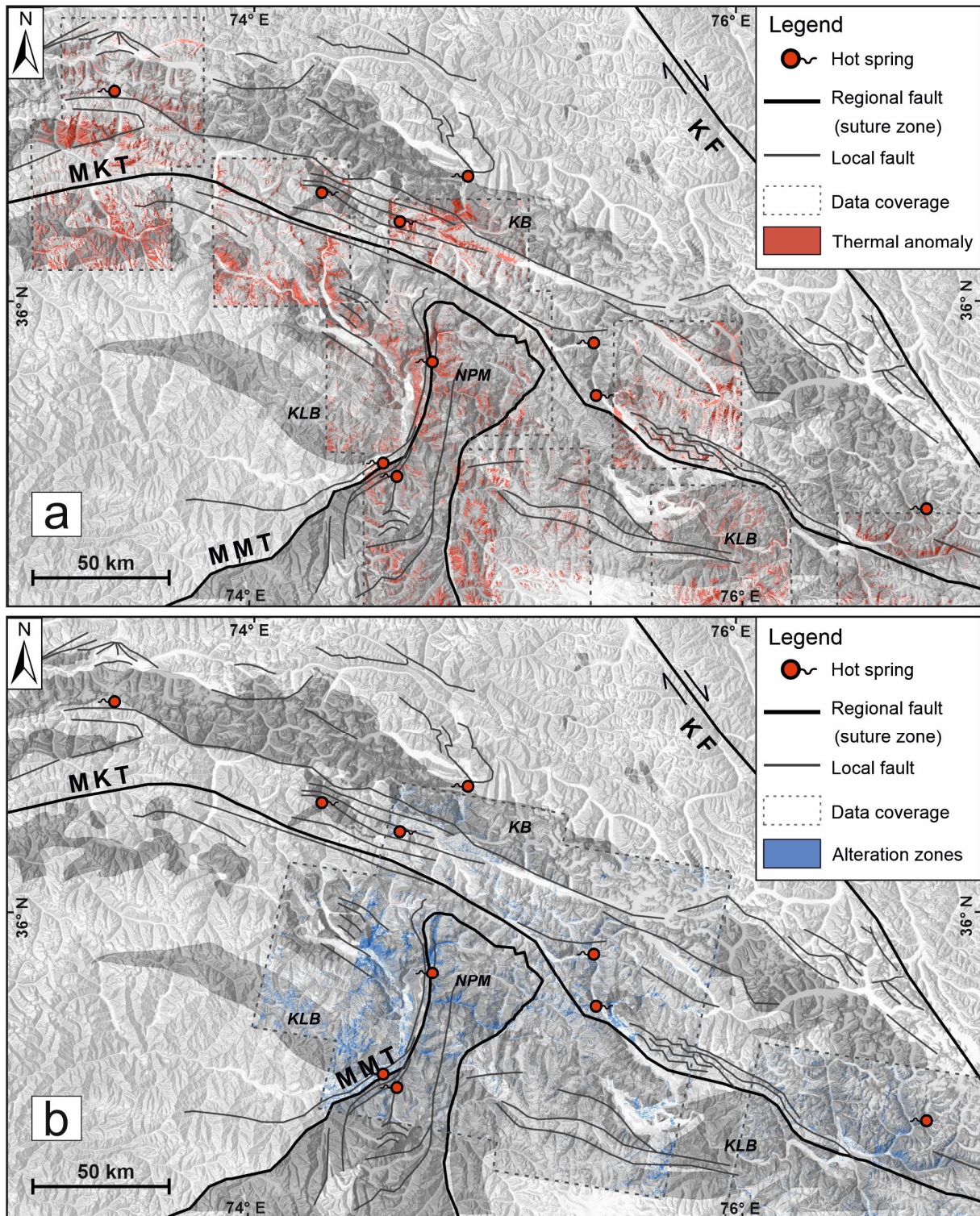
Figure 3.4 (a) Spatial distribution of thermal anomalies in the study area. The thermal anomalies only show pixels with positive values >1 SD from the results obtained after applying topographic correction on nighttime land surface temperature data. (b) Hydrothermal alterations in the study area. The filled grey polygons in the background indicate the lithological units of interest, i.e., granitoids and gneisses. Abbreviations are the same as in Figure 1.

3.3.2   Spatial distribution of thermal anomalies and alteration zones

The topographic correction was applied to nighttime thermal infrared data to remove the effect of altitude, aspect, and slope. A thermal anomaly image was obtained, having positive and negative thermal anomalies around the mean value of zero. The positive thermal anomalies were further filtered by selecting the data values >1 standard deviation to show the values with the highest surface temperature compared to the surroundings. Vegetation and snow were masked to minimize the identification of false anomalies. The thermal anomalies and hydrothermal alteration zones are shown in Figure 3.4. The potential high-temperature regions lie mostly along the valleys and batholiths, but false anomalies frequently occur in the results. However, despite this filter, the quality of results included high uncertainty, for which the reasons are discussed in the discussion section.

The results show detailed detection of alteration minerals (alunite, chlorite, epidote, illite, kaolinite, and sericite) overlapping to form clusters in alteration zones. However, the comparison between active hot springs and alteration zones does not show exact overlapping. These alteration zones commonly occur along faults, particularly along the western margin of NPM, MKT in Shigar and Saltoro valleys, and Hunza Valley (Fig 3.4b). Further details regarding alteration, lineament density, and thermal anomalies for specific locations are discussed in the following section.

3.3.3   Hydrothermal alteration zones

Using the eigenvector matrices of PCA bands calculated separately for alunite, chlorite, epidote, illite, kaolinite, and sericite were mapped in the Shigar, Raikot, Hunza, and Saltoro valleys. An appropriate threshold was applied to each PCA band selected for the corresponding mineral in order to obtain a classified map for that specific mineral. For example, kaolinite, as an argillic alteration indicator, has absorption in ASTER bands 1 and 6 and reflection in bands 4 and 7. Therefore, PC band 4's eigenvector loading showed the most difference in bands 6 and 7, indicating that the high pixel values in PC band 4 corresponded to kaolinite (Table 3.3). Lineament density and thermal anomaly data are also compared to understand the correlation between these three results.

In Shigar Valley (Fig 3.5a), alunite and muscovite are mapped close to MKT at the contact with Dassu gneiss and schist of the Karakoram metamorphic complex (KMC). Additionally, predominant alterations such as sericite, illite, and kaolinite are mapped in Dassu gneiss along the valley. Chlorite, epidote, and illite are mapped over Hemasil syenite. Alluvial fans and fluvial sediments also show deposition of alteration minerals eroded from nearby lithologies. The high

lineament density areas lie near MKT, faults in KMC, and over the Shigar plutonic complex (Ladakh batholith). Thermal anomalies show a broad correlation with high lineament zones, but false anomalies are found in river sediments and some moderate lineament areas (Fig 3.5b).

Table 3.3 Eigenvector values of principal components of ASTER bands selected according to target mineral's absorption and reflection characteristics. The bold-italic values show the most decorrelated eigenvector values, based on which that specific PC band is selected for a mineral. The presented eigenvector values are for one ASTER image, which can slightly differ from another image. Carbonate (calcite) and Mg-OH (chlorite) minerals have common absorption feature and are identified as single group through ASTER data.

Mineral	Eigenvectors	Band 1	Band 3	Band 5	Band 7	Sign
Alunite	PC1	-0.50455	-0.58786	-0.44561	-0.44864	
	PC2	-0.5672	-0.32618	0.550776	0.518214	
	PC3	-0.65002	0.737508	-0.17112	-0.06538	
	PC4	0.034569	-0.06411	***-0.68469***	***0.72519***	+

Mineral	Eigenvectors	Band 1	Band 2	Band 5	Band 8	
Chlorite (Calcite)	PC1	-0.56574	-0.56374	-0.45481	-0.39405	
	PC2	-0.43555	-0.41536	0.608264	0.517484	
	PC3	0.004489	-0.01076	-0.65033	0.759559	
	PC4	-0.70016	0.713831	***-0.01506***	***0.001359***	-

Mineral	Eigenvectors	Band 2	Band 5	Band 8	Band 9	
Epidote	PC1	-0.52877	-0.56229	-0.48709	-0.40863	
	PC2	-0.84875	0.352571	0.299254	0.256436	
	PC3	-0.0024	-0.74713	0.475203	0.464734	
	PC4	0.003625	0.036411	***-0.66886***	***0.742484***	-

Mineral	Eigenvectors	Band 1	Band 3	Band 5	Band 6	
Illite	PC1	-0.49873	-0.58244	-0.4488	-0.45892	
	PC2	-0.56465	-0.3435	0.518399	0.542623	
	PC3	-0.65757	0.736726	-0.11063	-0.11221	
	PC4	0.005365	0.002542	***-0.71945***	***0.694522***	-

Mineral	Eigenvectors	Band 1	Band 4	Band 6	Band 7	
Kaolinite	PC1	-0.41742	-0.58124	-0.50127	-0.48647	
	PC2	-0.90749	0.298423	0.232811	0.18223	
	PC3	0.047067	0.566296	0.097151	-0.8171	
	PC4	0.003066	0.50241	***-0.8277***	***0.249962***	+

Mineral	Eigenvectors	Band 1	Band 6	Band 7	Band 9	
Sericite (White mica)	PC1	-0.4984	-0.5536	-0.53984	-0.39205	
	PC2	-0.86652	0.338775	0.28681	0.228272	
	PC3	0.026007	0.736514	-0.65326	-0.17354	
	PC4	0.007916	-0.19055	***-0.44672***	***0.874111***	+

The Raikot Valley shows alunite, illite, and chlorite along the Raikot fault (Fig 3.6a). Kaolinite was mainly associated with leucogranite intrusions. Sericite and illite are common in orthogneiss, with scattered patches of alunite. High lineament density zones are associated

with faults, and hot springs are located in these zones (Fig 3.6b). However, thermal anomalies are mapped mostly over WNW-facing slopes, with one small anomaly close to a hot spring.

Epidote, sericite, and chlorite are present in the granodiorite of the Karakoram batholith (Hunza plutonic unit) in the Hunza Valley. Kaolinite is associated with mostly the granitic intrusions in the north part of the batholith (Fig 3.7a). Alunite is mapped at a hot spring and several other places where dikes cross-cut the metamorphic and plutonic lithologies. Alunite, illite and epidote were mapped at Sumayar pluton. Thermal anomalies have a uniform high pattern over HPU and Sumaryar pluton (Fig 3.7b). However, glacial moraines are also mapped as high thermal areas. A slight correlation between lineaments and thermal anomalies is present in this area.

Table 3.4 Results of semi-quantitative XRD analysis of samples from the study area.

Sample code	Qz	Kfs	Pl	Bt	Amp	Alu	Chl	Ep	Ilt-Ms-Ser	Kao	Cal-Dol	Jar	Tur
AST-8i	+++	++	+++						++				
RK-4i	+++	++	++	++			+		+				
RK-4i alt	+++	++	+++	++			+				+	+	
TTP-3	+++	+	++	+++			+						+
TTP-4	+++	++	++						+				
FM-4	+++	++	++						+				+
KOH-4	+++	+	++	++	+					+			
YK-2	+++		+++	+	++		+			+			
SGH-1	+++			+					++				
SGH-1 alt	+++	+	++						++			+	
SGH-9		++	+++	++				+	+				
KDS-1	+++	+++	+++	+			+		+				
HSH-5	++	+++	+++	++	+					+			
MT-1 alt	+++					++				++			
GL-alt	+++		+++	++									

+++: >25 %, ++: >10 % and +: <5 %

In Saltoro Valley, kaolinite was the most prominent alteration mineral observed associated with granitoids of Kande plutonic complex (KPC) and Hushe gneiss (Fig 3.8a). Hushe gneiss, in addition to the kaolinite, also shows alteration to sericite and illite. Alunite was mapped in KPC towards the north near the hot spring. A prominent thermal anomaly was mapped in KPC along the contact with Hushe gneiss (Fig 3.8b). However, the overall moderate lineament density lacked any correlation with thermal anomalies.

Table 3.4 and Figure 3.9 show a semi-quantitative XRD analysis of the samples collected from alteration zones. RK-4alt, collected from Raikot Valley in the NPM, consists of quartz, albite, orthoclase, and biotite as major components, while chlorite, calcite, and kaolinite are alteration products. From Hunza Valley, the sample MT-1alt collected from the alteration zone near the hot spring comprises quartz, kaolinite, and alunite. SGH-1alt, collected from the alteration zone in Shigar Valley, comprises quartz, albite, and white mica (illite / muscovite) as major constituents, while jarosite and anorthoclase are minor components. Granitoids from KPC in the Saltoro Valley comprise albite, microcline, quartz, and biotite as major components, while hornblende and kaolinite comprise minor mineralogy.
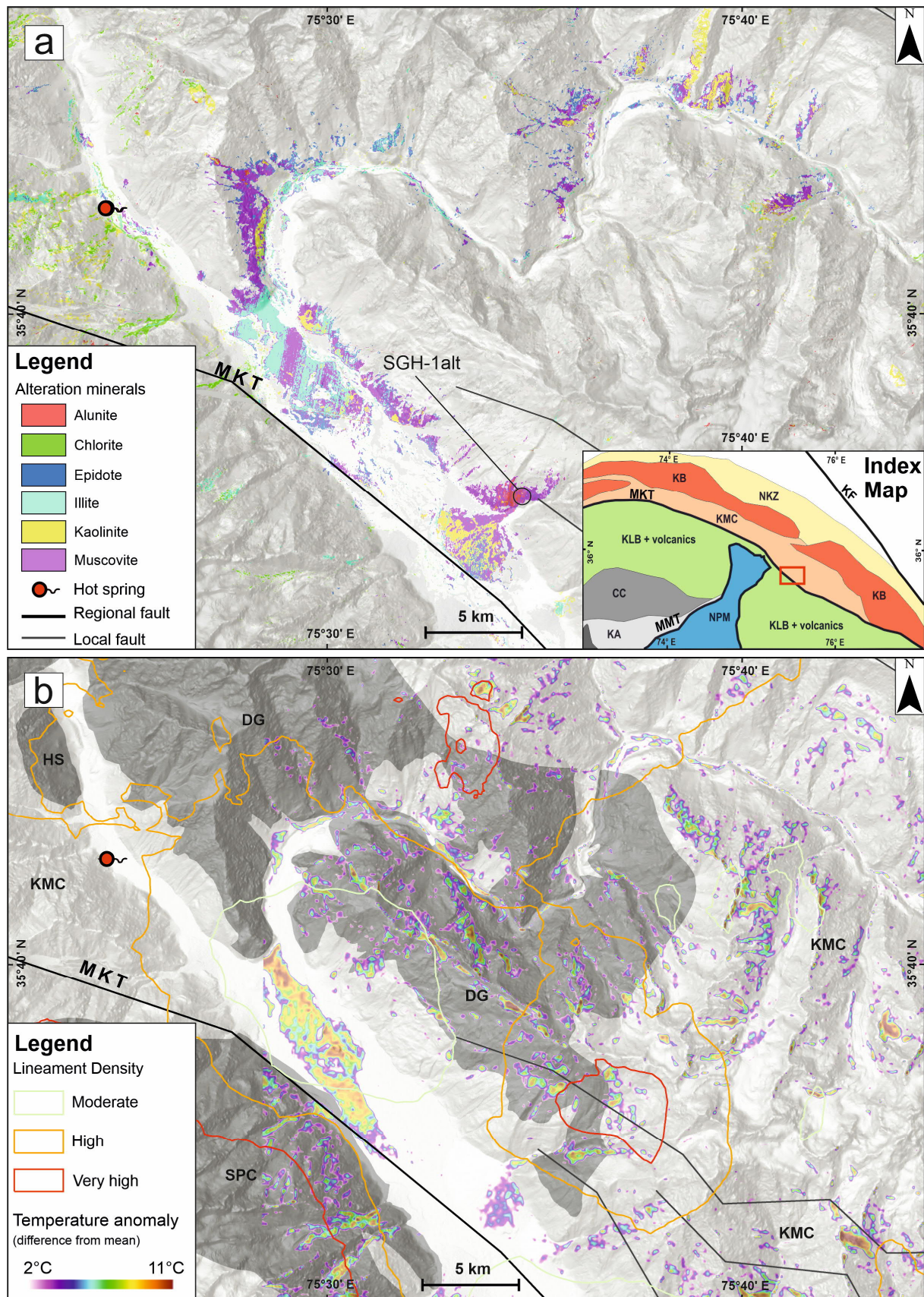
Figure 3.5 (a) Hydrothermal alteration in the Shigar Valley. SGH-1 alt shows the location of the altered sample analyzed using XRD. (b) Distribution of thermal anomalies and lineament density. DG-Dassu gneiss; KMC-Karakoram metamorphic complex; SPC-Shigar plutonic complex; HS-Hemasil syenite.
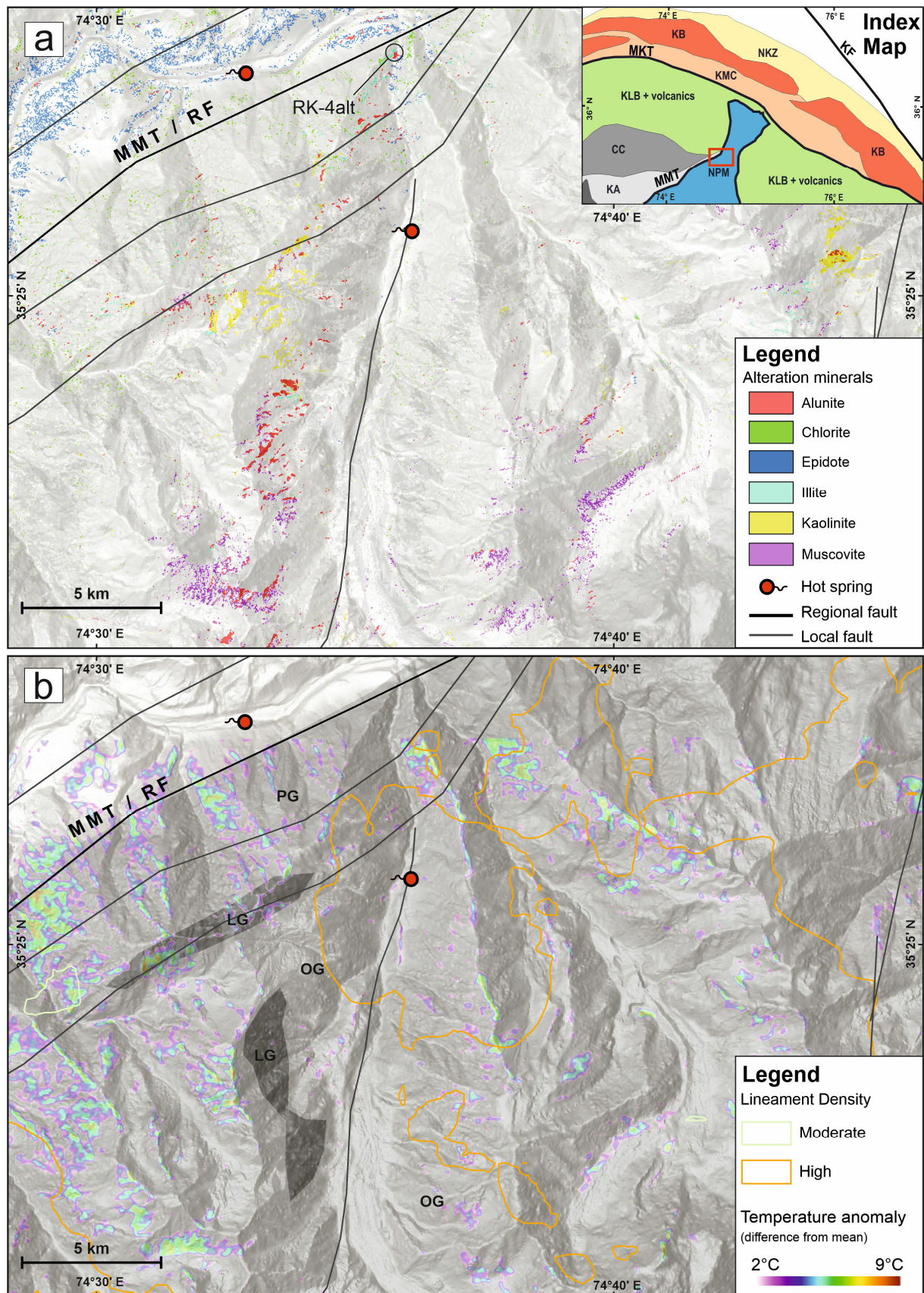
Figure 3.6 (a) Hydrothermal alteration in the Raikot Valley. RK-4 alt represents the location of the altered sample analyzed using XRD. (b) Distribution of thermal anomalies and lineament density. PG-Paragneiss; OG-Orthogneiss; LG-Leucogranite; RF-Raikot fault.
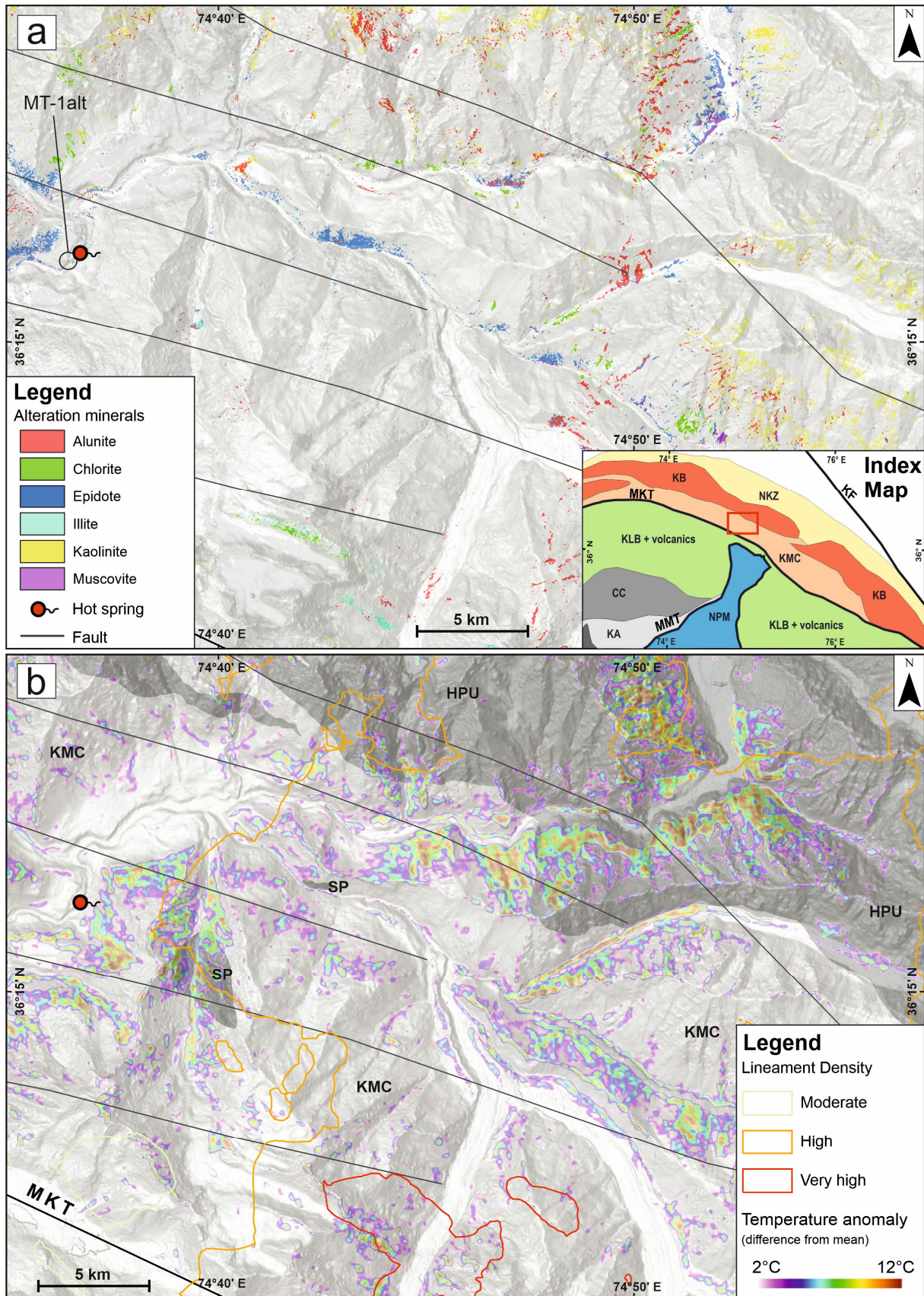
Figure 3.7 (a) Hydrothermal alteration in the Hunza Valley. MT-1 alt represents the location of the altered sample analyzed using XRD. (b) Distribution of thermal anomalies and lineament density. HPU-Hunza plutonic unit; KMC-Karakoram metamorphic complex; SP-Sumayar pluton.
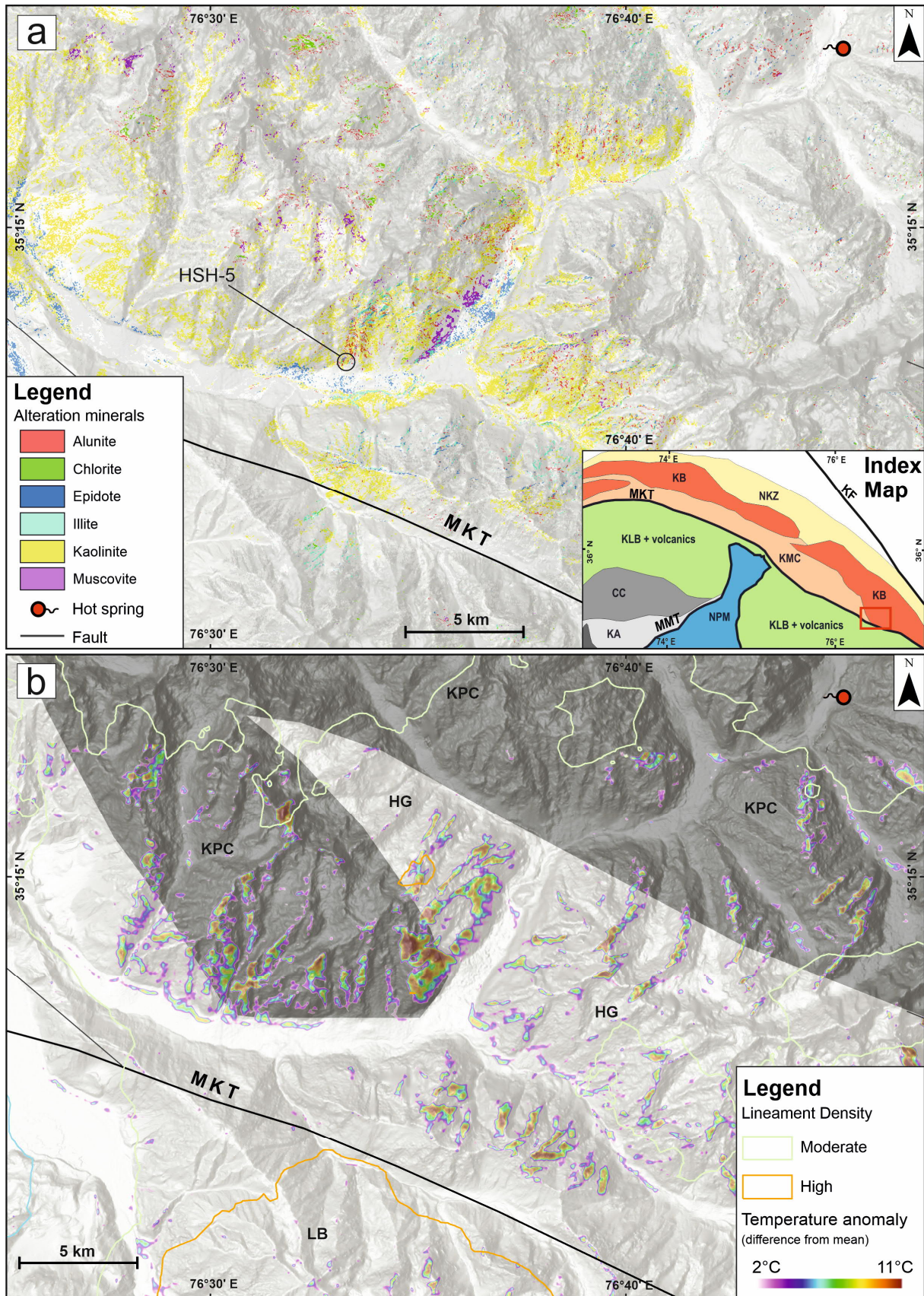
Figure 3.8 (a) Hydrothermal alteration in the Saltoro Valley. HSH-5 represents the location of the sample analyzed using XRD. (b) Distribution of thermal anomalies and lineament density. HG-Hushe gneiss; KPC-Kande plutonic complex; LB-Ladakh batholith.
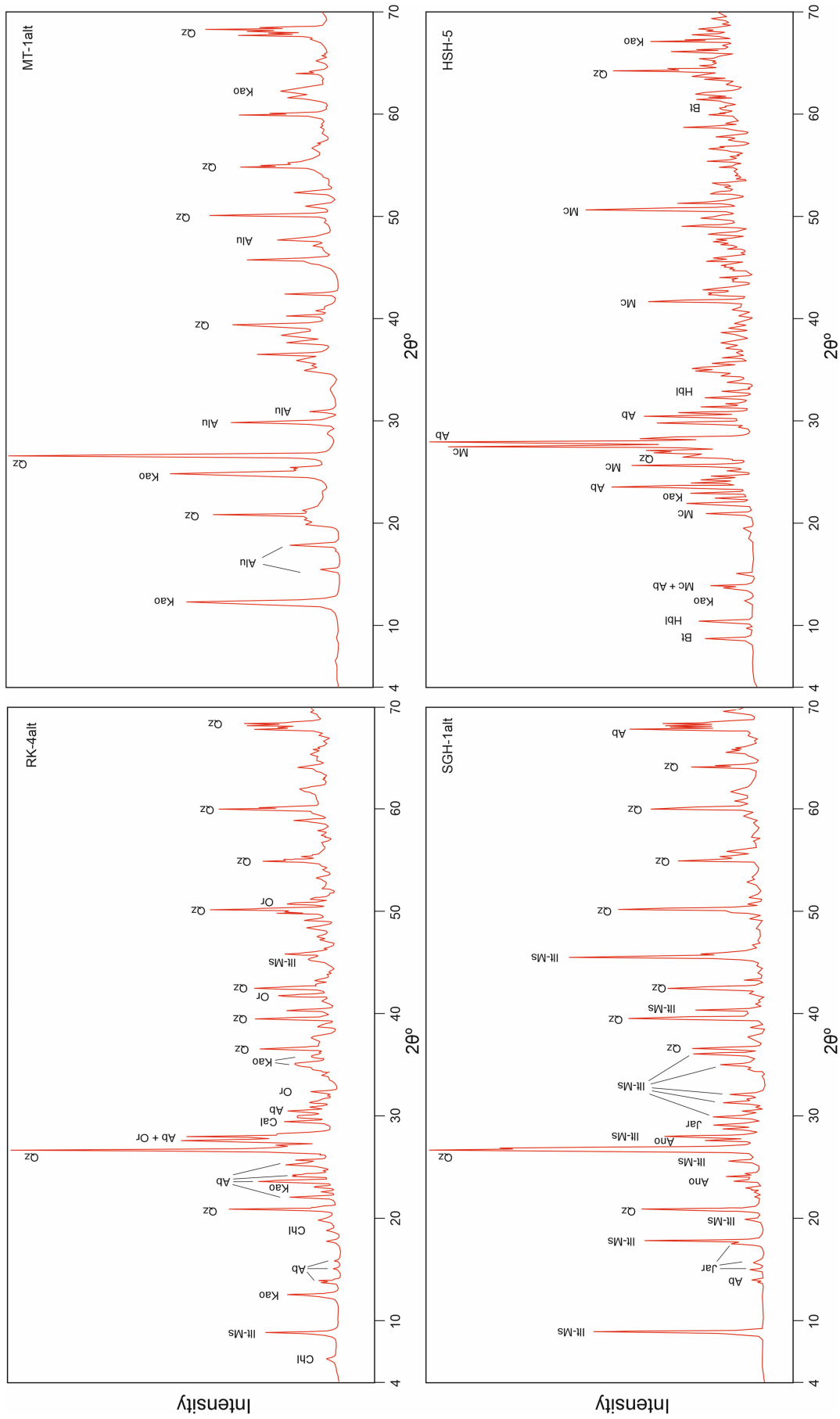
Figure 3.9 XRD patterns of altered samples from the study area. (Ab: albite, Alu: alunite, Ano: anorthoclase, Bt: biotite, Cal: calcite, Chl: chlorite, Hbl: hornblende, Ilt: illite, Jar: jarosite, Kao: kaolinite, Mc: microcline, Ms: muscovite, Or: orthoclase, Qz: quartz).

3.4   Discussion

The lineaments are broadly the manifestations of the joints, faults, and foliation trends on the ground (Sabins, 2007), created in response to the overall NNE tectonic stresses in the study area. These tectonic stresses act variably during folding, thrusting, and uplift and thus can create different sets of lineaments with different orientations. Except for NPM, most structures in the study area's western side (Gilgit, Hunza) have WNW to ESE orientation and show good agreement with the lineaments (Fig 3.3). Towards the east in the Shigar Valley, unlike NW-SE striking MKT, the ENE-WSE lineaments suggest shearing and drag folding along the thrust (Hanson, 1989). Within NPM, the NNE-SSW orientations of lineaments indicate the influence of metamorphic foliation (generally striking ± 10° N) and the faulted lithological contacts (Cronin et al., 1993).

Structural, lithological, and topographic factors control the variations in the lineament density (Nelson, 1985). The low lineament density is found in valleys and areas covered by alluvium, while the elevated regions with exposed lithology have high lineament density. Variable lithological properties such as mineralogy, fabric, compaction, porosity, and strata thickness can induce variable degrees of jointing (Hugman & Friedman, 1979; Marshak & Mitra, 1988). However, since the area is highly deformed due to tectonic collision, the overall lineament density is attributed to the structures, where intense folding and faulting can lead to high lineament density (Barbier et al., 2012; Awdal et al., 2013). The high lineament density zones along MMT and MKT suggest that in these high-strain zones, structural control on the lineaments is dominant (Watkins et al., 2015). The absence of prominent high-density zones in the Kande plutonic complex east of the study area is attributed to topographic factors (Fig 3.3), where cliffs, ice sheets, and glaciers hinder the detection of lineaments from satellite data (Ahmadi & Pekkan, 2021).

The idea behind using nighttime thermal infrared data was to minimize the effect of the sun on the surface, which would help identify the areas with high background (endogenic) temperatures associated with blind geothermal activity. The initial results indicated the high influence of topography in which temperature decreased with the elevation. The topographic correction aimed to remove this effect elevation and included aspect and slope correction for differential heating from the sun during the daytime (Ulusoy et al., 2012). To this extent, the results have shown that the topographic correction has significantly decreased the topographic influence over the surface temperature. From the identified thermal anomalies, few correlated with surface lithology, hydrothermal alteration, lineament density, and hot springs. However, the distribution of most of the thermal anomalies could not be interpreted solely as a

geothermal component because other environmental and physical factors can also significantly affect the temperature of a surface.

These factors include thermal inertia (dependent upon specific heat capacity and thermal conductivity), moisture content, atmospheric humidity, and differential solar heating of surfaces during daytime (Coolbaugh et al., 2007; Ramakrishnan et al., 2013). Moreover, the heterogeneous topographic shading and its variable influence on surface heating in cold and mountainous areas further increase the uncertainty (Zhang et al., 2018). Frequent or real-time ground-based monitoring of these factors, along with high temporal and spatial resolution satellite data, is required to reduce the effect of these highly variable factors. ASTER TIR product has a 90 m x 90 m pixel area and scarce data coverage in the study area, which increases the uncertainty in the results. While not addressed in this study, these limitations increased the uncertainty and reduced the usefulness of thermal anomaly results. However, this problem was partially addressed by analyzing thermal results with lineament, alteration, and background geology.

The alteration mineral maps (Fig 3.4 – 3.8) show the lithological control over the alteration minerals. Kaolinite has been mapped in Dassu gneiss (Shigar Valley), leucogranite (Raikot Valley), HPU (Hunza Valley), and KPC (Saltoro Valley). According to Fulignati (2020), kaolinite is an alteration product of aluminum silicates (feldspars) and represents an intermediate argillic alteration in acidic conditions (pH 4.5 – 6) at low temperatures (< 200 °C). Alunite (aluminum sulfate) can also be associated with kaolinite at higher temperatures (200 – 300 °C) and lower pH (2 – 4), termed advanced argillic alteration. Alunite has been mapped mostly in intensely altered zones in the Raikot, Shigar, and Hunza valleys. Illite forms due to alteration of K-feldspar and plagioclase above 200 – 300 °C up to 350 °C and represents phyllic to propylitic alteration conditions. Distribution of illite and sericite has been interpreted together as a representation of fine-grained (white) mica and was mapped in gneisses of NPM, Sumayar pluton (Hunza Valley) and contact between Hushe gneiss and KPC (Saltoro Valley). Chlorite and epidote also occur at similar temperatures (200 – 350 °C) through the alteration of mafic (Fe and Mg rich) minerals and are associated with metamorphism (both regional and contact) and hydrothermal alteration (Beaufort et al., 1992). They are mainly mapped in Hushe gneiss, HPU, KMC and lithologies of Kohistan, which are abundant in biotite, amphibole, and pyroxenes.

The popularity and utility of ASTER data in mapping hydrothermally alteration minerals are well established (Abrams & Yamaguchi, 2019; Eldosouky et al., 2017; Mars & Rowan, 2011, Rowan et al., 2006; Tangestani et al., 2008). However, the identification of alteration minerals

using satellite data cannot be directly linked to a fossil or active hydrothermal system without detailed analysis and verification (van der Meer et al., 2014). Therefore, comparison and integration with other datasets, such as thermal anomaly maps and lineaments, and field investigation are necessary for greater understanding. These remote sensing results provided helpful baseline information for the field investigations. For example, the alunite-sericite alteration at the contact between Dassu gneiss and schist in the Shigar Valley was confirmed in the field survey, and XRD analysis (of SGH-1 alt) corroborated the presence of illite-muscovite along with jarosite. The same was observed for the alunite-illite-chlorite alteration zone near the Raikot fault, where the XRD (of RK-4 alt) showed the presence of chlorite, kaolinite, calcite, and illite-muscovite. It can be noted that XRD results show kaolinite instead of alunite in contrast to remote sensing results. Alunite and kaolinite exhibit similar spectral characteristics in ASTER bands 5 and 6 due to the Al–OH absorption feature (Testa et al., 2018). Although this study employed different band sets for PCA of alunite (bands 1, 3, 5, and 7) and kaolinite (bands 1, 4, 6, and 7), both minerals are often present in argillic alteration. Their mixing could lead to difficulty in identification by ASTER data with 30m x 30m pixel resolution. Nonetheless, ASTER data proved its utility by identifying the zones of hydrothermal alteration, which can then be focused and studied in detail.

3.5 Conclusion

The Himalaya-Karakoram region of north Pakistan, with numerous hot springs, presents promising signs for geothermal energy. However, identifying and exploring geothermal resources in this vast, rugged, and inaccessible terrain is quite challenging. This study used a remote sensing approach to identify regions with high lineament density, surface temperature, and hydrothermal alteration. High lineament density is correlated with intense folding and faulting near major faults and suture zones. Thermal anomalies obtained after removing topographic effects showed some correlation with high lineament density and surface geothermal manifestations, but high uncertainty due to other environmental factors constrained their utility. Alteration minerals mapped in the area identified both previously known and unknown hydrothermal zones. These remote sensing-based results proved helpful in providing base information for field investigation, and the results were confirmed by XRD analysis. Given the results presented here, it is highly recommended to integrate remote sensing for geothermal exploration in an underexplored and topographically challenging area. The remote sensing results, in addition to providing base information for field surveys, can also be extrapolated to remote sites with confidence after field verification.

Chapter 4: Radiogenic heat production in the Nanga Parbat Massif, Kohistan and Karakoram

This chapter is based on the article published in Springer's Journal Geothermal Energy titled "Application of in-situ gamma spectrometry for radiogenic heat production estimation in the Western Himalaya, Kohistan, and Karakoram in northern Pakistan" (Anees et al. 2023) The abstract is not included here and the alphanumeric order of figures and tables may differ from the original article. Likewise, the formatting was adjusted to fit the layout of this work.

4.1 Introduction

Radioactive decay of radioelements, i.e., Uranium, Thorium, and Potassium (^{238}U, ^{235}U, ^{232}Th, and ^{40}K), is one of the most important heat generation processes in the Earth's crust. The information about variations in magnitude and distribution of radioelements is vital for geothermal assessments as it can significantly impact regional and local heat flow (Jaupart et al., 2016). Among crustal rocks, granitoids tend to have higher concentrations of radioelements and can enhance the geothermal gradient, which is favorable for geothermal exploration and development (Gnojek et al., 2018; McCay & Younger, 2017). Crustal evolution processes such as orogeny, subduction, and magmatic differentiation, which form large crystalline complexes of granitoids, are responsible for the heterogeneous distribution of radioelements (Artemieva et al., 2017). Thus, it is essential to estimate the variation in the distribution of radioelements across the various lithological units to constrain their contribution to the heat flow and its potential geothermal implications.

The Himalayas, Kohistan, and Karakoram Ranges collectively form the Tethyan collisional belt of the Indian and Eurasian plates in north Pakistan and surrounding regions (Kazmi & Jan, 1997). These ranges host hydrothermally active zones along and in the vicinity of tectonic sutures and intraplate thrust faults (e.g., Main Karakorum Thrust, Main Mantle Thrust, Main Boundary Thrust (Bakht, 2000; Fig 4.1). Previous studies have suggested various mechanisms for the origin of hydrothermal activity, including radioactive decay, shear heating along faults, residual heat from younger plutonic intrusions, plastic deformation, metamorphic heat due to tectonic collision, and rapid exhumation (Butler et al., 1997; Craw et al., 1997; Hochstein & Regenauer-Lieb, 1998; Chamberlain et al., 2002; Zaigham et al., 2009). The lack of borehole data hinders understanding the subsurface geothermal gradient and heat flow. Although some studies have numerically modeled subsurface geotherms in the context of exhumation and regional metamorphism while assuming standard petrophysical (heat production and thermal conductivity) values (Craw et al., 1994; Treloar, 1997), the magnitude and variations of heat

produced in the crust due to radioactive decay still need to be estimated for reliable geothermal modeling.
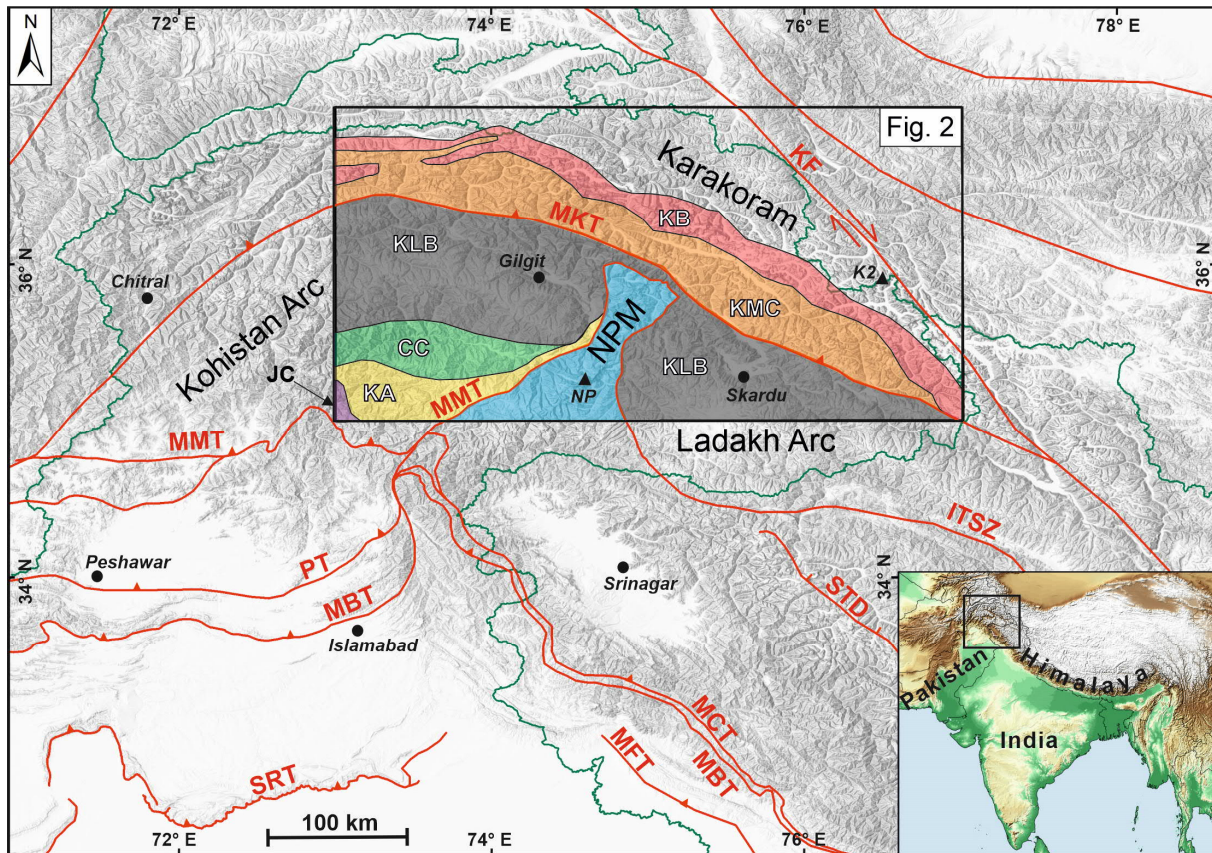
Figure 4.1 A generalized tectonic map of north Pakistan (overlaid on hill-shade terrain model) showing regional faults/sutures in the western Himalaya, Kohistan, and Karakoram. The political boundaries are shown with thin green lines. The black square in the inset figure (bottom right) shows the geographic location of Figure 4.1 in South Asia. The black box in the center shows the spatial extent of Figure 4.2 (study area) and regional geologic units of the Indian plate (NPM—Nanga Parbat Massif), Kohistan-Ladakh arcs (CC, JC, KA, KLB), and the Asian Plate (Karakoram—KB, KMC) (modified after Searle et al., 1999). Abbreviations: CC—Chilas Complex; ITSZ— Indus-Tsangpo Suture Zone; JC—Jijal Complex; KA—Kamila Amphibolite; KB—Karakoram Batholith; KF—Karakoram Fault; KLB—Kohistan-Ladakh Batholith (and volcanics); KMC—Karakoram Metamorphic Complex; MBT—Main Boundary thrust; MCT/PT—Main Central thrust / Panjal thrust; MFT—Main Frontal thrust; MKT—Main Karakoram thrust; MMT—Main Mantle thrust; NP—Nanga Parbat; SRT—Salt Range thrust; STD—South Tibet detachment.

This study aims to estimate the radiogenic heat production in prevailing crystalline lithologies using the concentration of radioelements (U, Th, and K) measured with a field gamma spectrometer. Furthermore, the intrinsic variations in radiogenic heat production associated with different rock types are examined to understand the factors controlling these variations and their potential geothermal implications. The results of this study provide better constraints for thermal modeling to explore the geothermal potential of the study area.

4.2   Methodology

4.2.1   In-situ gamma spectrometry

A portable gamma spectrometer called Exploranium GR-135G Plus (SAIC, Canada) was used to collect in-situ radioelement concentration data in the field. The instrument employs a Sodium Iodide (Thallium) 38 x 57mm detector, which can detect radionuclides with a gamma energy detection range from 0 to 3.0 MeV and uses 256 channels for spectral analysis (SAIC Exploranium, 2006). The instrument was calibrated every 24 hours with a Cesium 137 calibration source for greater accuracy. The data was acquired using the assay mode, which spectrally analyzes the gamma energies and calculates the concentrations of U (ppm), Th (ppm), and K (wt %) using the calibration coefficients stored in its memory. The instrument's precision (according to manufacturer) in assay mode for 120 seconds count time for a sample (with 2% K, 2ppm U, and 8ppm Th) in normal background is ±0.35%, ±1.5ppm, ±2.6ppm for K, U and Th, respectively (SAIC Exploranium, 2006).

A measurement time of 300 seconds was selected to obtain stable spectra. When in direct contact with an outcrop, the instrument collects the gamma rays emitted from 15 - 25 cm depth (depending upon density) within a 1 m circular disc. The instrument applies stripping and background corrections on the acquired spectrum and displays the concentrations of U and Th in ppm and K in wt % as output.

4.2.2   Data acquisition

The concentration of the radiogenic elements (U, Th, K) is commonly high in felsic rocks composing the upper continental crust (Jaupart & Mareschal, 2005); therefore, the granitoids, gneisses, and leucogranite intrusions were primarily targeted (Fig 4.2). The radioelement data from 158 readily accessible roadside fresh outcrops mainly located along the valleys was collected. In the Nanga Parbat massif, the Raikot valley, the Astore, and Skardu roads provide access to Proterozoic basement rocks (including migmatites) with young intrusive dikes (of centimeters to meters thickness) along shear zones (Fig 4.3b, c, d & e).

In the Gilgit and Ghizer valleys, the diorites (with varying composition), volcanogenic metasediments, and a few granitic outcrops represent the Kohistan batholith (Fig 4.3h). The readings for the Ladakh batholith were taken from the granites, granodiorites, and gneisses from the sections exposed around the Skardu and Khaplu cities in the northeastern part of the study area (Fig 4.2).

The data from the Karakoram batholith and metamorphic complex was acquired from western, central, and eastern Karakoram, corresponding to the Hunza, Shigar, Hushe, and Saltoro valleys. In Hunza valley, Hunza plutonic complex and Sumayar leucogranite comprise gneiss, granodiorites, diorites, granite, leucogranites and pegmatites (Fig 4.3i). Felsic gneisses (with pegmatites) of the Dassu gneissic dome and syenitic pluton of Hemasil were sampled from upper Shigar valley. In the Hushe and Saltoro valleys, the dioritic gneiss of the Hushe complex and hornblende granitoids of the Kande pluton (south of the Baltoro plutonic unit) represent the easternmost sampled locations of the Karakoram batholith for this study (Fig 4.2).

During the field campaign, several hot spring sites (some with boiling temperatures) and alteration zones (active and fossil zones with H_2S smell and sulphurised rocks) were observed, as shown in Figures 4.2, 4.3f, and 4.3g. These hydrothermal zones are mostly located near suture zones and faults, such as in the Raikot, Hunza, Shigar, and Saltoro valleys (Fig 4.2).

4.2.3 Data corrections and validation

Data acquisition using a portable gamma spectrometer ideally requires a relatively flat section of outcrop with minimal topographical features to meet 2π steradians or half space (flat) geometric condition between the instrument and the outcrop (McCay et al., 2014). However, finding an outcrop with a flat rock surface in the high-relief terrain is challenging, leading to gamma energy overestimation in valleys (Erdi-Krausz et al., 2003; McCay et al., 2014). Moreover, acquiring data along road outcrops (as is the case in the current study) means that each sampling point acquired additional gamma energy (from an area ranging between 2π to 3π steradians; Fig 4.3a), leading up to a 50 % overestimation in the concentrations of radioelements that needs to be corrected to obtain accurate values (McCay & Younger, 2017).

A geometric correction was applied to the data to overcome the overestimation due to possible geometric errors with the outcrop and the instrument. For this, at each sampling point, the average outcrop angle relative to the horizontal surface was noted, e.g., a completely vertical outcrop (with 3π geometry) was allotted a 90° angle while a flat space (or 2π geometry) horizontal outcrop with 0° angle and the rest plotting in between these two extremes (Fig 4.3a). Based on these angles, the correction factors ranging from 0.6667 to 1 were calculated, i.e., for a 90° angle outcrop that got one-third overestimation, the data values were multiplied by 0.6667 to reduce the values by one-third (or 33.33%). In contrast, all data values from an outcrop with a 0° angle were multiplied by one as it required no reduction. Correction factors for outcrops with angles between 0 and 90° are calculated using a similar linear relationship. In the end, all three values of radioelements are multiplied by their respective correction factors to obtain geometrically corrected values.
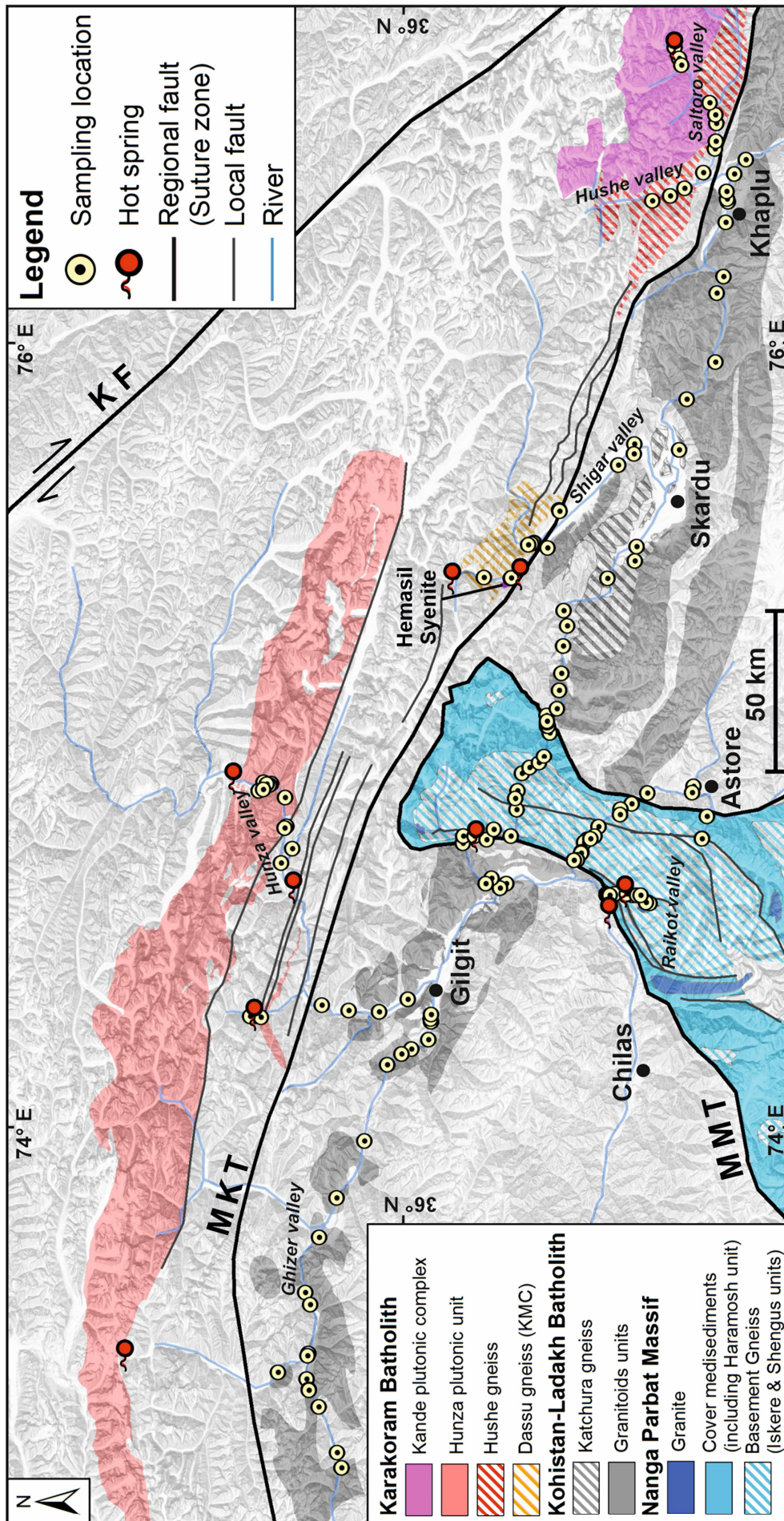
Figure 4.2 Map showing sampling locations, active hot springs, and the geological units sampled in the study (redrawn after Madin et al., 1989; Schneider et al., 1999; Searle & Khan, 1996). Abbreviations are the same as in Figure 4.1.
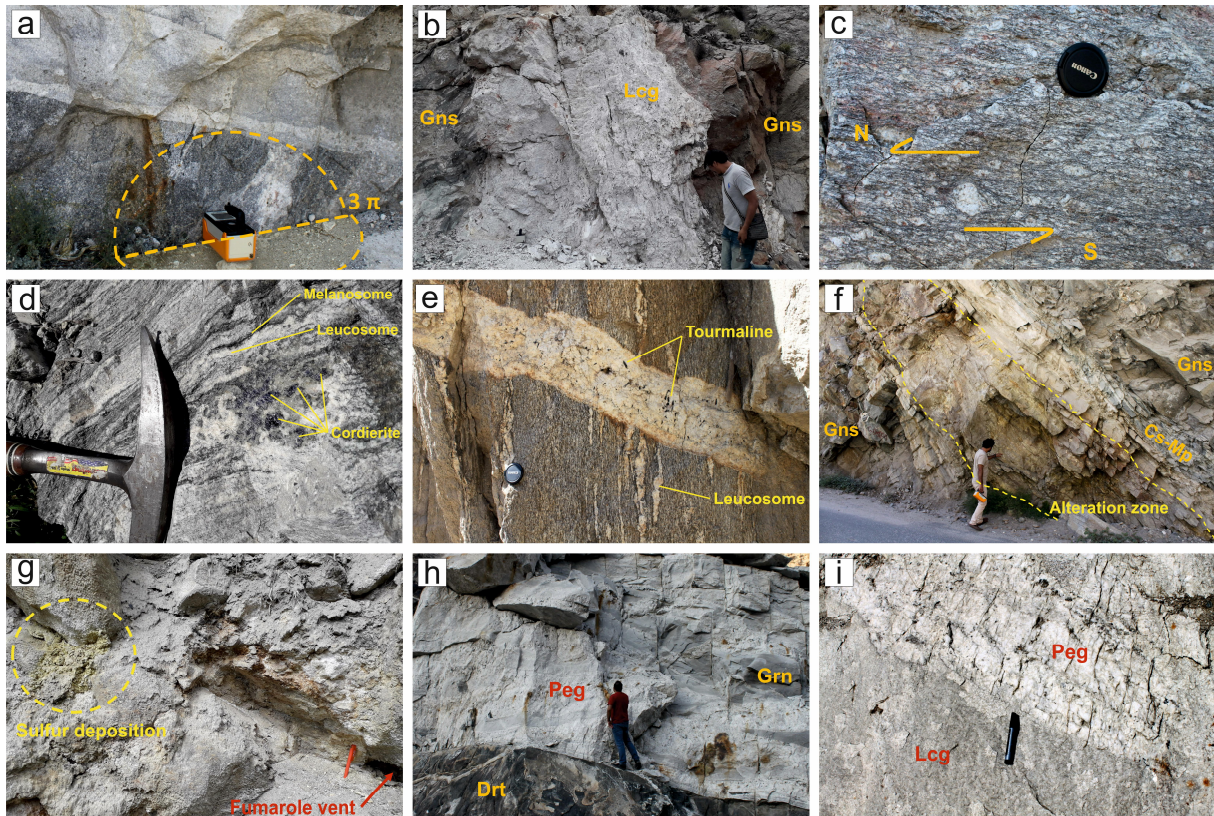
Figure 4.3 (a) Field gamma spectrometer acquiring U-Th-K data from an outcrop with 3π geometry (b) A leucogranite (Lcg) dike (with euhedral tourmaline crystals) intruding basement gneiss (Gns) along the Raikot shear zone in the Nanga Parbat Massif (NPM) (c) Sheared augen gneiss showing shear deformation in NPM along the Raikot fault (d) Cordierite in the migmatitc gneiss display HT-LP conditions in core of the Nanga Parbat during exhumation (e) Tourmaline bearing pegmatite dike cross cutting the gneissic fabric in NPM (f) Alteration zone (with sulfide smell) showing precipitation of secondary minerals in calc-silicate metapelite (Cs-Mp) along Astore road in NPM (g) Hydrothermal deposition of sulfur around the hot spring site at Murtazabad (north of MKT) in the Karakoram metamorphic complex (h) Pegmatite (Peg; with garnet and tourmaline) intruding granite (Grn) which is intruding diorite (Drt) of the Kohistan-Ladakh batholith at the confluence of the Indus and Gilgit rivers (i) Contact between leucogranite (Lcg) and two-mica Pegmatite (Peg) at the southern edge of the Karakoram batholith along Nagar valley.

An approach similar to altitude correction in airborne gamma spectrometry was followed to remove the possible overestimation of data due to topography. This correction assumed the additional gamma influence for the valleys < 500m wide (IAEA, 1991). The intensity of gamma radiation from the far side of valleys, calculated from the attenuation coefficient in the air for ~2MeV energies, exponentially decreases to ~50% at 130m and ~25% at 260m at STP conditions. Beyond 500m, the intensity of gamma rays will be < 10% of their original intensity and thus cannot significantly cause overestimation. The height and slope length ratio for the valley's far side is calculated using a digital elevation model up to 500m distance from the

sample location. The slope to height and intensity factors are multiplied by measured concentration values to calculate the overestimation from the opposite side of the valley, which was then subtracted from measured concentration values (Eq 4.1).

$$C_{TC} = C_{GC} - \left(C_{GC} \times I_{(d)} \times \frac{H}{S} \right) \qquad [4.1]$$

where, CGC is concentration U, Th and K after geometric correction, CTC is concentration after topographic correction, I(d) is the intensity of gamma radiation in the air at specific distance from the source, H is the height attained at the far side of valley against the slope length (S) at 500m from the sampling location.

For quality control of the field data, it was compared with a subset of 21 samples analyzed using a lab-based High Purity Germanium (HPGe) gamma spectrometer having superior resolution (of 1.85 keV) compared to NaI detectors (Younis et al., 2022). The comparison shows a strong positive correlation in Th and K values with R^2 of 0.93 and 0.86, respectively. In the case of U, although the correlation is strong ($R^2 = 0.88$), there is an average of ~6 ppm of overestimation. This was caused by the disequilibrium in the U decay series, which can occur due to the leaching of daughter products and radon escape from the decay chain (Erdi-Krausz et al., 2003). In the laboratory, secular equilibrium is achieved by storing samples in sealed containers for at least a month; however, disequilibrium (particularly in the U series) in the field is unavoidable. Therefore, to overcome this, a regression analysis was performed based on the slope equation between the lab and field data to recalculate the U concentration and remove the effect of disequilibrium.

4.2.4   Reliability of in situ gamma spectrometry

The in-situ gamma spectrometry through portable devices offers greater flexibility, better representation, and faster data collection than lab-based geochemical and gamma spectrometers. Additionally, they offer firsthand information at a reconnaissance scale, marking regions of interest for the follow-up detailed investigations. However, inevitable tradeoffs need to be considered depending on the nature of the study area. In the case of regions with higher topographic relief, such as narrow valleys with high mountains, it is expected to get the overestimation in concentrations of radioelements (McCay et al., 2014; Reinhart & Herrmann, 2019). These errors can be minimized by carefully documenting the geometric and topographic features at the sampling location during the field survey and applying suitable corrections as applied in this study.

Since the concentrations of Th and U are calculated by measuring the gamma radiations from their respective daughter products from respective series, the disequilibrium can provide false values of these elements. U is highly susceptible to disequilibrium due to the frequent mobility of parent radionuclides such as Radium and Radon (Minty, 1997). Weathering and groundwater can cause leaching in an oxidizing environment and concentration (precipitation) in reducing environment of soluble Radium (^{226}Ra) and U, respectively, causing under and overestimation (Dickson, 1985). Radon (^{222}Rn), a gas, escapes from the source into the atmosphere through joints and fractures, affecting the concentration of ^{214}Bi, which is used to calculate U concentration. In low-lying landscapes, a buildup of denser ^{222}Rn close to the surface can overestimate U (Minty & Wilford, 2004). Therefore, comparing a subset of field data with a lab-based gamma spectrometer is recommended. Correcting a larger field data set is possible using the correlation slope between two data sets in case of good correlation. However, one disadvantage of this technique is that it can also lead to underestimation at locations unaffected by U disequilibrium. Nonetheless, this method has been proven most effective in this study.

4.2.5   Radiogenic heat production

Radiogenic heat production (A) is calculated in µWm^{-3} using the following equation of Rybach (1988);

$$A = (9.52\, C_U + 2.56\, C_{Th} + 3.48\, C_K) \times \rho \times 10^{-5} \qquad\qquad [4.2]$$

where, ρ is the density of the rock given in kg/m^3, C_U, C_{Th}, and C_K is the concentration of Uranium (ppm), Thorium (ppm), and Potassium (wt %), respectively. The heat production constants in W/kg for U, Th, and K are 9.52, 2.56, and 3.48, respectively. They reflect the contribution of each of the radioelements to the radiogenic heat production, which is highest for Uranium, followed by Potassium and Thorium.

The densities were determined by hydrostatic weighing (buoyancy technique) on sample cubes as per the German industry standard (DIN 52102, 1988). The sample cubes were dried at 40°C until mass consistency and then fully saturated with demineralized water for 24 hours, after 24 hours of vacuum in a desiccator. Subsequent measurements of the wet and buoyancy weight (by weighing with an under-floor balance while submerging the sample in demineralized water) allow the calculation of the effective porosity, bulk, and matrix density. The bulk densities of 60 samples were estimated using this method, from which the average density values for similar rock types were calculated, which were then used for the field data points against which lab densities were unavailable.

4.3   Results

The main targets in this study were crystalline rock units of the Nanga Parbat Massif (NPM), Kohistan-Ladakh Batholith (KLB), and Karakoram Batholith (KB), ranging from granitoids and gneisses to metavolcanic units. The results here focus on the broad classification of the rock units (granite, granodiorite, gneiss, schist, etc.) rather than mineralogical variation or petrogenesis (e.g., biotite granite, orthogneiss, metadiorite, etc.). The results of this study are summarized in the following sections:

4.3.1   Radioelements concentration

The mean concentrations and standard deviation of U, Th, and K, along with Th/U and K/U ratios for different lithologies of NPM, KLB, and KB, are shown in Table 4.1.

The concentrations of radioelements in the NPM and KB range between 0.30 – 22.57 and 0.34 – 44.51 ppm for U, 0.66 – 86.17 and 1.96 – 154.00 ppm for Th, and 0.50 – 7.40 and 0.90 – 7.70 % for K. In KLB, the concentrations of U, Th, and K values are comparatively low, ranging between 0.12 – 4.53 ppm, 0.89 – 23.88 ppm, and 0.08 – 4.51 %, respectively. The mean concentrations of U, Th and K for the gneisses of NPM (8.78 ± 5.50 ppm, 30.42 ± 19.80 ppm, and 3.72 ± 0.97 %, respectively) tend to be high compared to KB (4.70 ± 2.60 ppm, 16.47 ± 8.66 ppm, and 3.63 ± 0.95 %, respectively) and KLB gneisses (2.73 ± 0.50 ppm, 13.54 ± 1.21 ppm, and 2.51 ± 0.38 %, respectively). The granites of NPM and KB have higher mean U concentrations (16.94 ± 7.85 and 15.81 ± 18.10 ppm, respectively) than KLB granites (2.96 ± 1.01 ppm). However, the mean Th concentration in KB granites is significantly high (61.32 ± 55.62 ppm) compared to NPM and KLB (20.70 ± 6.36 and 14.10 ± 5.30 ppm, respectively). The highest mean K value is found in the KB syenites (6.92 ± 0.67 %), surpassing the NPM granites and pegmatites (4.22 ± 0.65 % and 3.63 ± 0.71 %, respectively).

Figure 4.4 shows lithology-based relative concentrations of U, Th, and K in the NPM, KLB, and KB. In the NPM, gneisses differ from granites and pegmatites with a higher Th proportion (>0.6 in most samples), while the granites, pegmatite, and some gneisses have slightly higher U proportion (~0.4 – 0.5). The relative K content is higher in pegmatite than in the other rocks (Fig 4.4a). In contrast, the relative Th and U contents in most KLB rocks show minor variability (Fig 4.4b). The KB rocks display the most variable relative distribution of U, Th, and K contents, with a dominant Th proportion (>0.7) in granites and a dominant U proportion (~ 0.5) in pegmatites and leucogranites. The relative K proportion in syenites and pegmatites is higher than in other lithologies (Fig 4.4c).
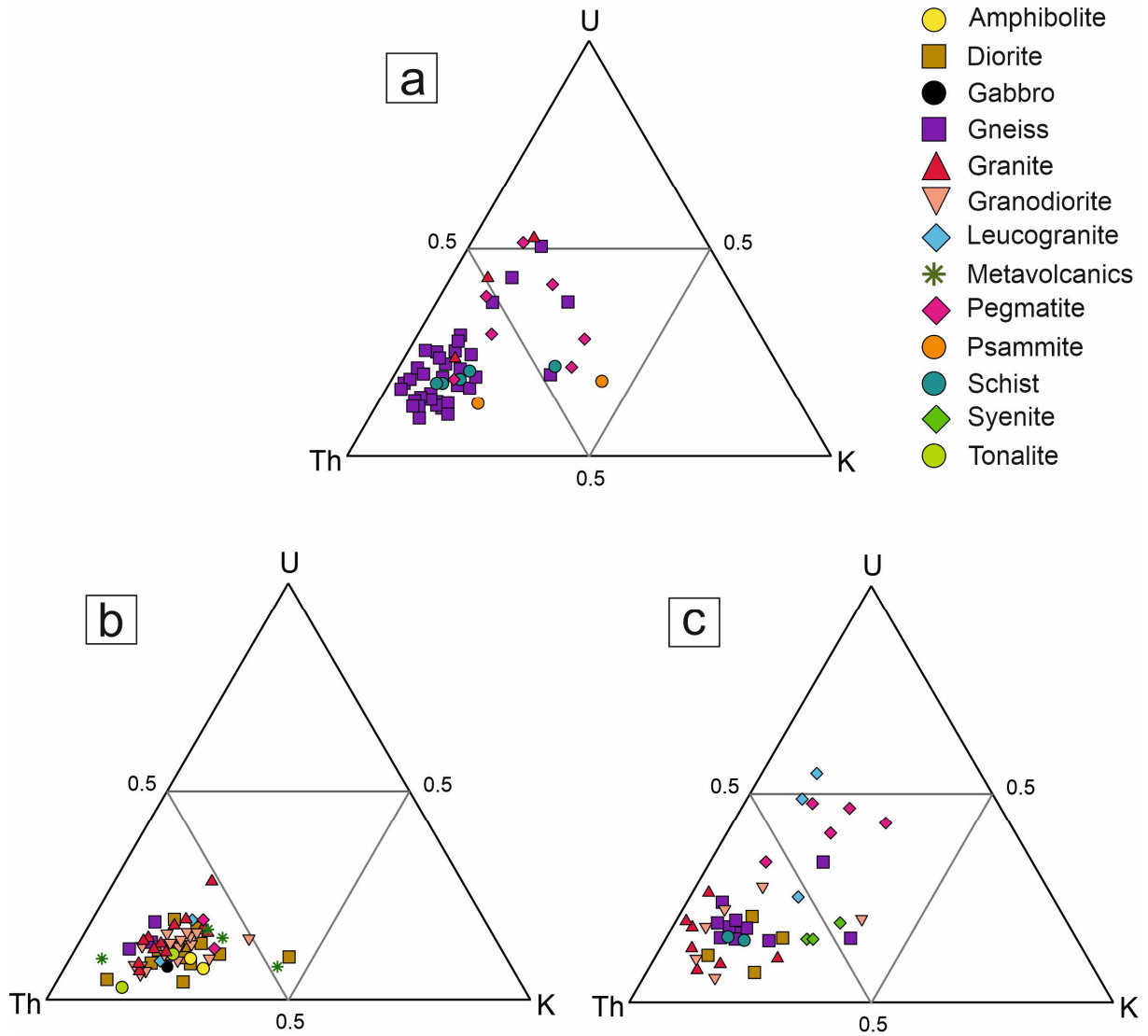
Figure 4.4 Ternary plots showing relative concentrations of U (ppm), Th (ppm) and K (wt %) within different lithologies; (a) Nanga Parbat Massif comprises Proterozoic basement gneisses (and schists) intruded by recent pegmatite and granites (b) Kohistan-Ladakh batholith is composed of Cretaceous granitoids and volcanic rocks with Tertiary pegmatitic leucogranites (c) Karakoram batholith represent Cretaceous and Tertiary granitoids with Proterozoic and Jurassic gneisses.
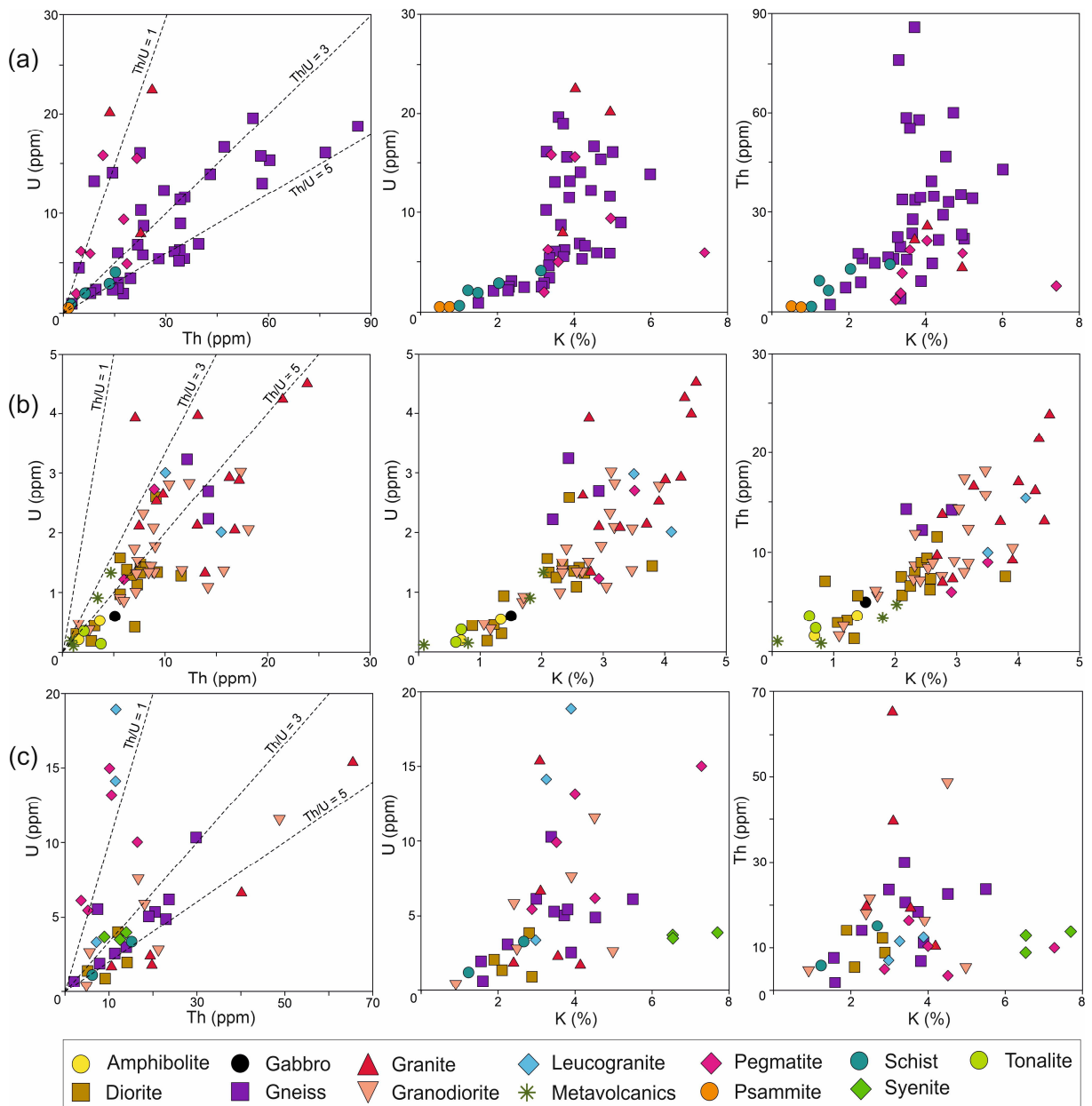
Figure 4.5 Plot of U versus Th and K, and Th versus K for different rock types in the study area inferred from in-situ gamma spectrometry (a) Nanga Parbat Massif (b) Kohistan-Ladakh batholith (c) Karakoram batholith. Note: Due to very high U (15.45 and 44.51 ppm) and Th (120.00 and 154.00 ppm) concentrations, two granite samples (from KB) plot outside the selected range in Fig 5c.

Table 4.1 Mean values of U (ppm), Th (ppm), and K (%), and Th/U and K/U ratios and their standard deviations for different lithologies from Nanga Parbat Massif, Kohistan-Ladakh and Karakoram batholiths

Lithology	N	eU (ppm)	eTh (ppm)	eK (%)	Th/U	K/U (10⁴)
Nanga Parbat Massif						
Gneiss	36	8.78 ± 5.50	30.42 ± 19.80	3.72 ± 0.97	3.97 ± 1.80	0.61 ± 0.35
Pegmatite	7	8.54 ± 5.33	12.35 ± 6.93	4.28 ± 1.50	1.71 ± 1.03	0.74 ± 0.53
Schist	5	2.38 ± 1.27	9.05 ± 5.41	1.78 ± 0.85	3.55 ± 0.90	0.85 ± 0.37
Granite	3	16.94 ± 7.85	20.70 ± 6.36	4.22 ± 0.65	1.55 ± 1.14	0.29 ± 0.15
Psammite	2	0.30 ± 0.01	1.13 ± 0.66	0.63 ± 0.18	3.76 ± 2.32	2.05 ± 0.52
Kohistan-Ladakh batholith						
Granodiorite	21	1.56 ± 0.73	9.31 ± 4.34	2.60 ± 0.75	6.31 ± 2.51	1.86 ± 0.52
Diorite	15	1.14 ± 0.61	6.60 ± 2.65	2.09 ± 0.78	6.98 ± 3.85	2.29 ± 1.25
Granite	12	2.96 ± 1.01	14.10 ± 5.30	3.63 ± 0.71	5.18 ± 2.32	1.33 ± 0.38
Metavolcanics	4	0.63 ± 0.59	2.54 ± 1.90	1.18 ± 0.90	5.43 ± 2.20	2.38 ± 2.07
Gneiss	3	2.73 ± 0.50	13.54 ± 1.21	2.51 ± 0.38	5.12 ± 1.32	0.93 ± 0.17
Tonalite	2	0.25 ± 0.15	2.95 ± 0.92	0.65 ± 0.07	15.73 ± 13.27	3.06 ± 1.59
Leucogranite	2	2.51 ± 0.70	12.76 ± 3.85	3.81 ± 0.44	5.51 ± 3.07	1.60 ± 0.62
Amphibolite	2	0.36 ± 0.25	2.56 ± 1.44	1.02 ± 0.47	7.49 ± 1.14	3.11 ± 0.83
Pegmatite	2	1.97 ± 1.07	7.47 ± 2.08	3.21 ± 0.41	4.12 ± 1.17	1.85 ± 0.79
Gabbro	1	0.60	5.08	1.51	8.53	2.53
Karakoram batholith						
Gneiss	11	4.70 ± 2.60	16.47 ± 8.66	3.34 ± 1.20	3.63 ± 0.95	0.93 ± 0.58
Granite	7	15.81 ± 18.10	61.32 ± 55.62	3.75 ± 1.04	7.04 ± 4.04	0.85 ± 0.85
Granodiorite	6	5.10 ± 4.05	19.15 ± 15.96	3.20 ± 1.54	5.58 ± 4.66	1.13 ± 0.94
Diorite	4	2.05 ± 1.28	10.20 ± 3.81	2.42 ± 0.49	5.94 ± 2.99	1.57 ± 1.07
Pegmatite	5	9.96 ± 4.20	9.20 ± 5.06	4.44 ± 1.71	0.93 ± 0.42	0.48 ± 0.17
Leucogranite	3	12.11 ± 7.99	10.04 ± 2.63	3.38 ± 0.47	1.18 ± 0.82	0.45 ± 0.39
Syenite	3	3.71 ± 0.15	11.87 ± 2.53	6.92 ± 0.67	3.19 ± 0.62	1.86 ± 0.11
Schist	2	2.29 ± 1.44	10.38 ± 6.51	1.97 ± 1.02	4.53 ± 0.01	0.89 ± 0.12

The detector indirectly calculates the concentrations of U-Th-K through gamma decay of their respective daughter elements. The instrument accuracy is 2%K, 2ppm U, and 8ppm Th, while its precision is K= ±0.35%, U= ±1.5ppm, Th= ±2.6ppm (SAIC Exploranium, 2006).
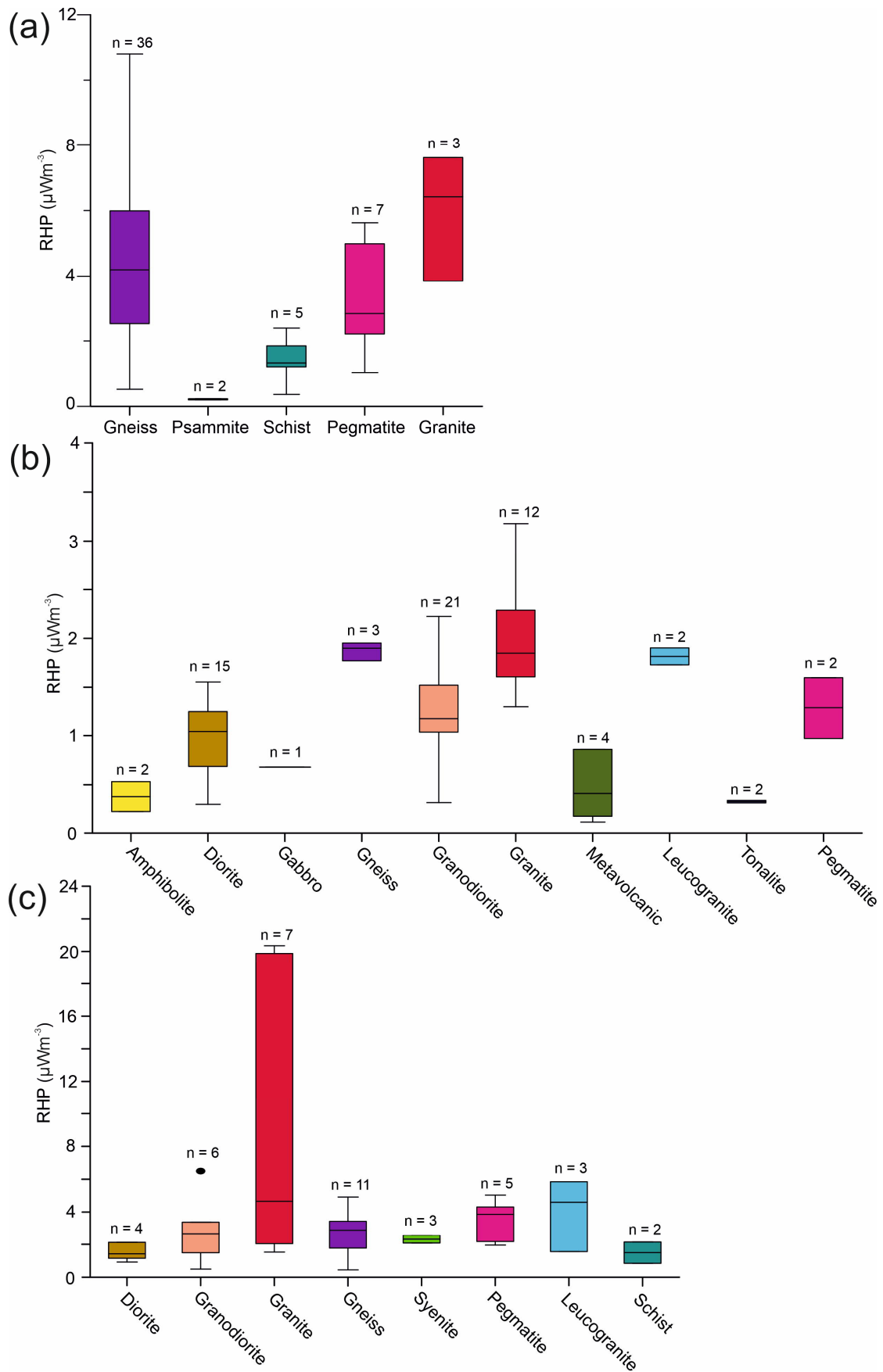
Figure 4.6 Lithology-wise variations in radiogenic heat production (μWm^{-3}) in the study area (a) Nanga Parbat Massif (b) Kohistan-Ladakh batholith (c) Karakoram batholith.

Table 4.2 Statistical overview of radiogenic heat production (μWm^{-3}) and density for lithologies within Nanga Parbat Massif, Kohistan-Ladakh, and Karakoram batholiths

Lithology	N	Density (g cm^{-3})	Min	Max	Mean	Median	SD±
Nanga Parbat Massif							
Gneiss	36	2.66	0.52	10.80	4.64	4.19	2.59
Pegmatite	7	2.63	1.03	5.63	3.33	2.84	1.61
Schist	5	2.76	0.37	2.39	1.43	1.33	0.75
Granite	3	2.61	3.84	7.62	5.96	6.42	1.92
Psammite	2	2.70	0.20	0.24	0.22	-	0.03
Kohistan-Ladakh batholith							
Granodiorite	21	2.65	0.32	2.22	1.26	1.17	0.49
Diorite	15	2.75	0.30	1.55	0.96	1.04	0.37
Granite	12	2.62	1.29	3.18	2.02	1.85	0.57
Metavolcanics	4	2.80	0.12	0.86	0.45	0.41	0.35
Gneiss	3	2.70	1.77	1.95	1.87	1.90	0.09
Pegmatite	2	2.69	0.97	1.60	1.28	-	0.44
Leucogranite	2	2.60	1.73	1.90	1.82	-	0.12
Tonalite	2	2.80	0.32	0.34	0.33	-	0.01
Amphibolite	2	2.62	0.23	0.53	0.38	-	0.21
Gabbro	1	2.84	0.68	0.68	-	-	-
Karakoram batholith							
Gneiss	11	2.65	0.42	4.92	2.61	2.89	1.25
Granite	7	2.63	1.53	20.35	8.47	4.66	8.31
Granodiorite	6	2.65	0.49	6.50	2.87	2.67	2.05
Pegmatite	5	2.72	1.95	5.03	3.46	3.86	1.34
Diorite	4	2.59	0.92	2.12	1.47	1.42	0.53
Leucogranite	3	2.62	1.56	5.85	4.00	4.59	2.20
Syenite	3	2.58	2.08	2.57	2.32	2.31	0.24
Schist	2	2.7	0.84	2.14	1.49	-	0.92

* Lowest and highest values are referred as min and max, respectively. SD—Standard deviation

Plots of U vs. Th, U vs. K, and Th vs. K for individual rock samples from the three domains show distinct correlations between radioelements for different lithologies (Fig 4.5). The granites and pegmatites of NPM have Th/U ratios ~1, while most gneisses and schists have ratios >3 (Fig 4.5a). In contrast, the Th/U ratio is slightly higher than 3 in most lithologies of KLB, with positive linear correlations between U, Th, and K concentrations (Fig 4.5b). U and Th show large variability compared to K in KB granites with distinctly higher Th/U ratio (≥ 5), in contrast to the younger leucogranites and pegmatites with Th/U < 1. The syenites do not show any correlation of Th and U with K (Fig 4.5c).

4.3.2 Radiogenic heat production

The lithological-wise distribution of minimum and maximum radiogenic heat production values, along with their mean, median, and standard deviations for NPM, KLB, and KB, are presented in Table 4.2. The radiogenic heat production data from the study area shows an overall variation from 0.1 to 20.3 μWm^{-3} with a mean and median of 2.8 and 1.9 μWm^{-3}, respectively. Based on tectonic affinity, the rocks of the NPM stand out from the rest with a mean of 4.0 ± 2.5 μWm^{-3} (median 3.9 μWm^{-3}) as compared to the KLB and KB with means of 1.2 ± 0.6 and

3.6 ± 4.1 µWm⁻³, respectively. This indicates that the tectonic affinity of rocks is the most significant factor controlling radiogenic heat production.

The NPM comprises Proterozoic basement gneisses with Tertiary granitic and pegmatitic intrusions. Radiogenic heat production values from 53 locations vary from a maximum of 10.8 to 0.2 µWm⁻³. The granites and gneisses show high heat production (mean 4.6 ± 2.5 and 5.9 ± 1.9 µWm⁻³, respectively), while schists and psammites have low mean values (1.4 ± 1.3 and 0.2 ± 0.1 µWm⁻³, respectively) (Fig 4.6a). The heat production in pegmatites varies between $1.0 – 5.6$ µWm⁻³ with a mean of 3.3 ± 1.6 µWm⁻³.

The KLB consists of various plutonic to volcanic units of the Cretaceous period with felsic to mafic composition with minor Tertiary intrusions. In KLB, the granites, granodiorites, gneisses, leucogranite, and pegmatites display higher mean values (2.0 ± 0.5, 1.2 ± 0.4, 1.8 ± 0.1, 1.8 ± 0.1, and 1.2 ± 0.4 µWm⁻³, respectively) than amphibolites, tonalites and metavolcanics (0.3 ± 0.2, 0.3 ± 0.1, and 0.4 ± 0.1 µWm⁻³, respectively) (Fig 4.6b). The heat production values in diorites vary between $0.3 – 1.5$ µWm⁻³ with a mean of 0.9 ± 0.3 µWm⁻³.

The typical lithologies in the KB, from which the data was collected, include Proterozoic and Jurassic gneisses, Cretaceous diorites and granodiorites, and Tertiary granites, leucogranites, and pegmatites. Granites display a wide range of radiogenic heat production values, with a maximum value of 20.3 µWm⁻³ and a highest mean of 8.4 ± 8.3 µWm⁻³ (Fig 4.6c). After granites, leucogranites and pegmatite show higher mean values (4.0 ± 2.2 and 3.4 ± 1.3 µWm⁻³, respectively) compared to gneisses, granodiorites, and syenites, while the diorites and schists show lower heat production (Fig 4.6c).

4.3.3 Spatial distribution and classification

Rocks exposed across the entire region exhibit a wide range of radiogenic heat production values due to variability in concentrations of radioelements. These variations can be controlled by various factors such as petrogenesis, age, rock type, and metamorphism (Artemieva et al., 2017; Jaupart & Mareschal, 2005). In this regard, the geographic locations of sampling points are used to identify and understand these spatial variations within NPM, KLB, and KB (Fig 4.7). The concentrations of U and Th within the NPM are primarily high, with the highest values in the core (mostly orthogneiss), while decreasing towards the flanks (mostly paragneiss). Values of K are higher in the west and gradually decrease eastward. U and Th in KLB are mostly low compared to NPM and KB and slightly increase in some scattered felsic outcrops. In KB, high U and Th concentrations in the east are associated with granites (containing hornblende), while

high K concertation in central and western parts is associated with syenites and pegmatites, respectively.

There are many classification schemes available for radiogenic heat production values, but they lack a consensus on the thresholds, and each one has established its thresholds depending on data and study area (Carson & Pittard, 2012; Gillespie et al., 2013; Huston et al., 2010; McCay & Younger, 2017; Siegel et al., 2012). For this study, the radiogenic heat production is classified into six classes, i.e., very low (< 1 µWm^{-3}), low ($1 - 2$ µWm^{-3}), moderate ($2 - 4$ µWm^{-3}), moderately high ($4 - 6$ µWm^{-3}), high ($6 - 8$ µWm^{-3}) and very high (> 8 µWm^{-3}).

In the NPM, most locations are moderately high to very high heat producing with few moderate and low values towards the northeast. Most of the sites in KLB are low heat producing with very low values (< 1 µWm^{-3}), mainly associated with outcrops north of Gilgit, along the Astore valley, and in the west of Skardu. There are a few scattered localities with moderate values in granite located east of Khaplu and in Ghizer Valley. KB is moderate to moderately high heat producing, with some locations in the Shigar and Saltoro valleys classified as high to very high heat producing (Fig 4.8a). The estimated weighted means for radiogenic heat production in NPM and KLB are 4.1 ± 2.0 and 1.0 ± 0.3 µWm^{-3}, respectively. For KB, the Kande pluton has the highest mean value of 7.4 ± 8.2 µWm^{-3}, followed by Dassu gneiss, Hunza plutonic unit, Hemasil syenite, and Hushe gneiss in decreasing order (Fig 4.8b).
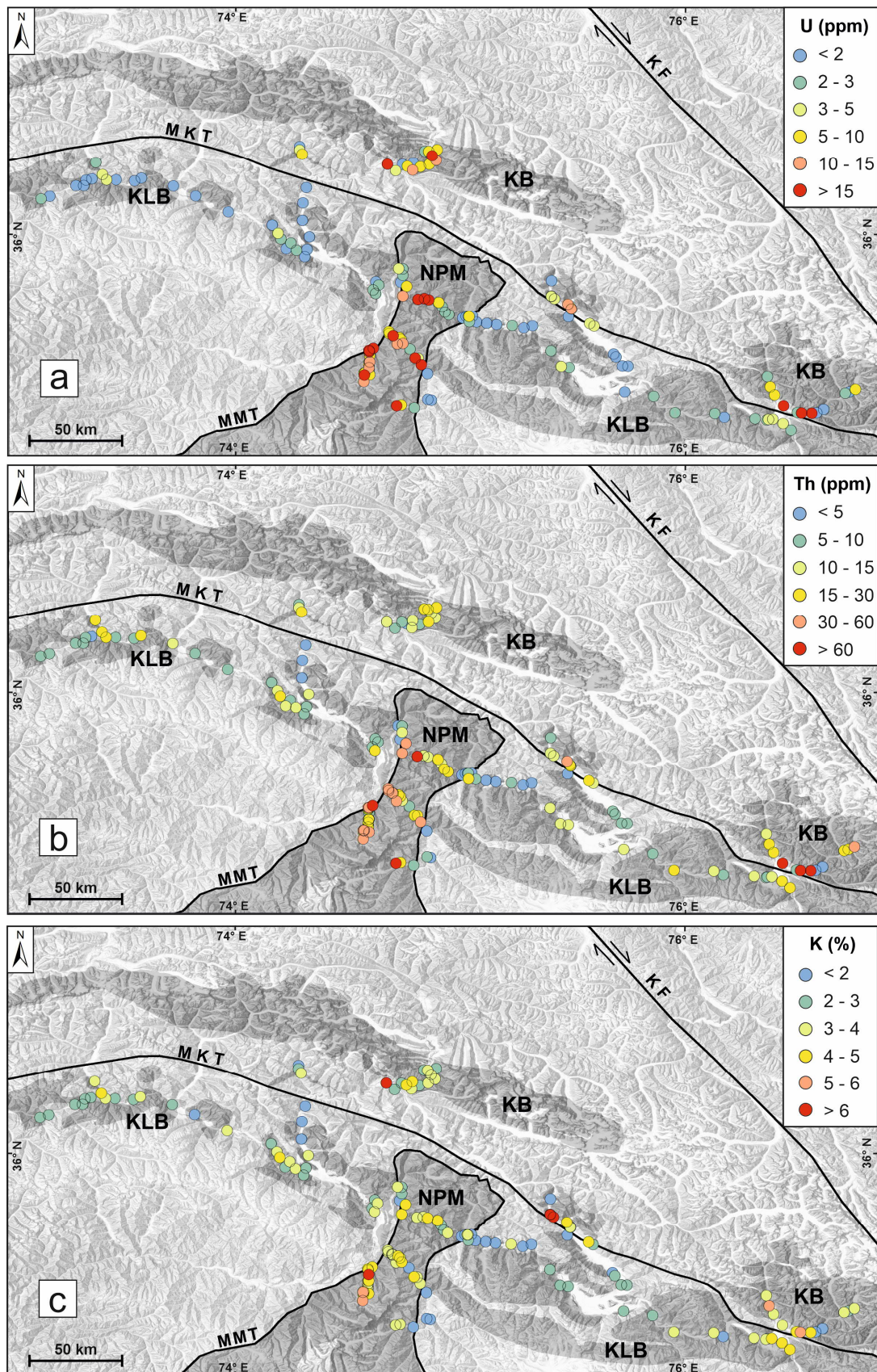
Figure 4.7 Spatial distribution of concentrations of radiogenic elements at each spot in the study area. (a) Concentrations of U (in ppm) (b) Concentrations of Th (in ppm) (c) Concentrations of K (in %). Abbreviations are the same as in Figure 4.1.
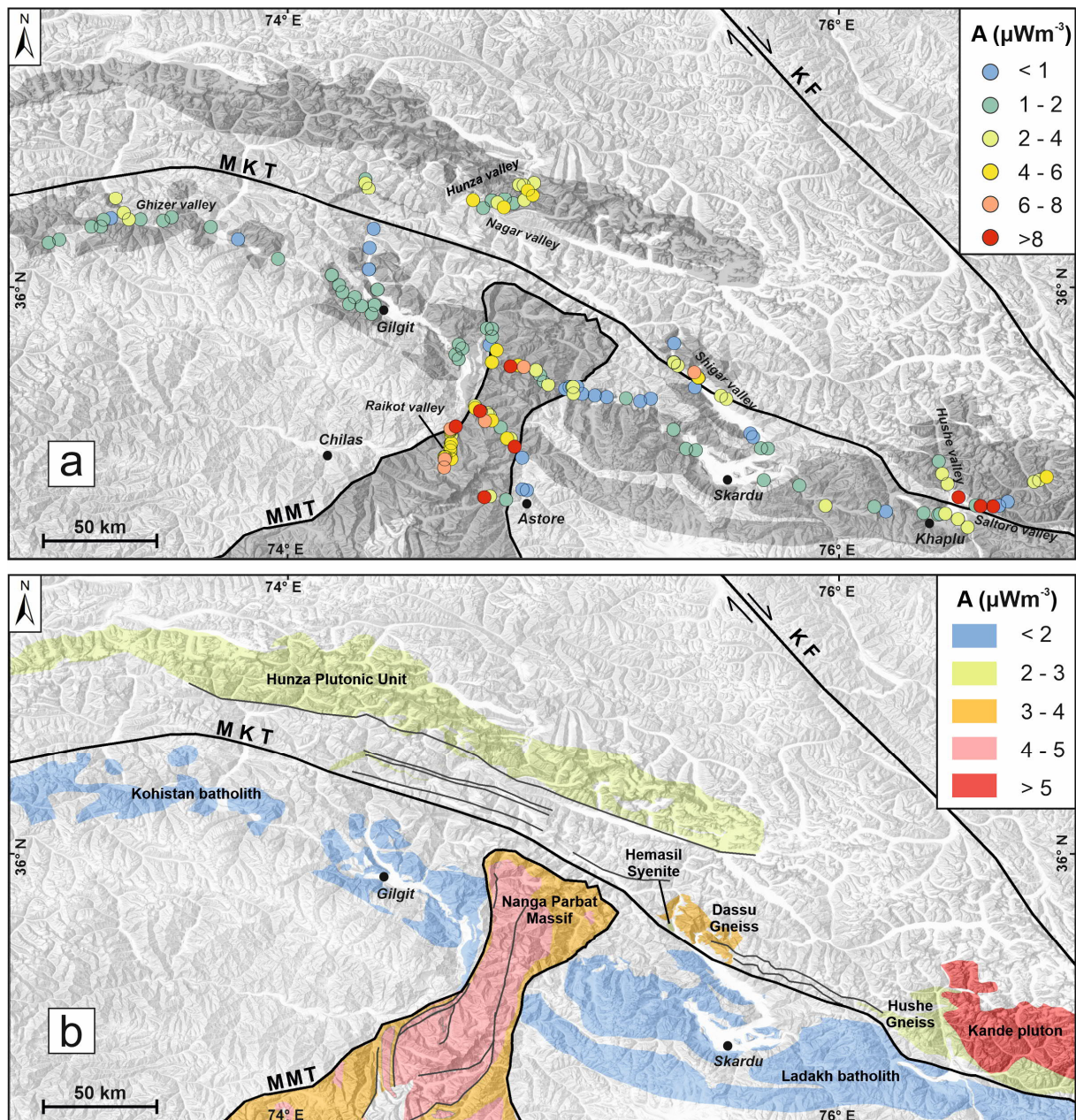
Figure 4.8 (a) Radiogenic heat production (µWm⁻³) for each sample in the Nanga Parbat Massif, Karakoram, and Kohistan-Ladakh batholiths (b) Mean values of radiogenic heat production (µWm⁻³) for the different (litho-) tectonic granitoid units in the study area. Weighted mean values are calculated from approximate lithological proportions for Nanga Parbat Massif (after Madin 1986) and Kohistan batholith (after Jagoutz & Schmidt, 2012). Simple mean values are used for lithological units of Karakoram (after Khan Searle & Khan, 1996).

4.4 Discussion

4.4.1 Variations in radioelement concentrations

Lithological variations are mainly responsible for the heterogeneous distribution of radioelement concentrations, which control the crustal heat production and tend to increase in rocks with felsic (SiO_2 abundant) composition (Jaupart & Mareschal, 2005; Kukkonen & Lahtinen, 2001). Radiogenic heat production depends directly upon concentrations of U, Th, and K in decreasing order (Rybach, 1988); therefore, rocks with minerals hosting these elements control its magnitude. Few studies suggested a negative correlation between radiogenic heat production, age, and metamorphism grade (McLaren et al., 2003; Vilà et al., 2010). However, the tectonic origin, setting, and chemical composition play more significant roles in controlling the radioelement concentration and heat production than the geological age (Kemp & Hawkesworth, 2003). The results indicate that granite, leucogranite, gneiss (pelitic and granitic), and pegmatite have a higher concentration of U, Th, K, and subsequent higher radiogenic heat productions than intermediate and mafic rocks such as granodiorite, tonalite, diorite, gabbro, and metavolcanics (Table 4.1). Commonly, in granites, K is abundant in alkali feldspars (orthoclase and microcline) and micas (muscovite); therefore, its concentration is naturally high in alkali-granite, syenite, and leucogranite. e.g., the Hemasil syenite in the Shigar Valley has the highest potassium concentration (> 6 wt %). U and Th commonly occur in accessory minerals (such as zircon, monazite, xenotime, apatite, and allanite), and peraluminous granitoids tend to be abundant in such minerals (Bea, 1996). The granitoids of the KLB and KB (except Tertiary granitic intrusions) are mostly metaluminous I-type and, therefore, have lower concentrations of U and Th than the peraluminous S-type Tertiary granitoids of the NPM and KB (Kande pluton).

A significant role of genetic association is observed, controlling the concentrations of radioelements. For example, the gneisses of NPM show enrichment in radioelements compared to the ones of KLB and KB. The NPM suggested as a metamorphosed and evolved component of the Indian continental crust (Butler, 2019; Treloar et al., 2019), shows similar radioelement signatures with the Besham complex as well as central and southern Indian shield rocks (Ahmad et al., 2021; Kumar et al., 2009; Ray et al., 2008; Ray et al., 2016). Such a widespread phenomenon has been observed globally in early to middle Proterozoic granitoids, which is attributed to large-scale orogenic and magmatic processes involving mantle plumes related to the assembling of continents before the formation of the supercontinent Nuna (Columbia) (Artemieva et al., 2017; Spencer et al., 2018).

The concentrations of incompatible radioelements (U and Th) can be affected by remobilization due to dehydration and fluid flow during metamorphism and partial melting, leading to their enrichment in leucogranites, pegmatites, and granites compared to their parent rocks. The average crustal ratios of Th/U and K/U are 4 and 1 x 104, respectively (Taylor & Mclennan, 1985; Jochum et al., 1983). Uranium is relatively more mobile compared to Thorium (Scott et al. 1992), due to which the U enrichment in Tertiary intrusions of NPM and KB (leucogranite and pegmatite) is observed, resulting in low Th/U and K/U (~1 and <0.5 x 104, respectively). By contrast, the Th/U ratio > 3 in the granite form KLB does not indicate mobilization of U. The granites from Kande pluton of KB with the highest concentration of radioelements suggest enrichment in localized zones and require further detailed investigations. At the same time, high Th/U ratios in these granites are >4, suggesting Th enrichment and possibly indicating a deep crustal source distinguishing them from anatectic Himalayan leucogranites (Mahar et al., 2014; Searle et al., 2010).

4.4.2   Implications on regional geothermal systems

The hydrothermal activity in the region generally manifests in the form of hot springs and alteration zones, mainly along the faults (Zaigham et al., 2009). The complex geodynamic and tectonic setting of the study area implies that multiple factors could control the heat flow and the geothermal gradient. While frictional heating is restricted to the perimeter of fault zones (Ai et al., 2021), rocks enriched in radioelements occur widely and could strongly affect geothermal gradient and surface heat flow (Jaupart et al., 2016; Pinet & Jaupart, 1987). Additionally, exhumation and denudation can rapidly exhume hot rocks to the surface and thus create a high near-surface geothermal gradient (Chamberlain et al. 2002; Zeitler et al. 2001).

The steaming geysers in NPM are believed to result from a high geothermal gradient created by the rapid tectonic uplift and young intrusions (Craw et al., 1997). Seismic and magnetotelluric studies have suggested a hot, weak crust that can generate partial melts upon decompression during uplift (Crowley et al., 2009; Meltzer et al., 2001; Park & Mackie, 2000). Although the rapid advection of hot "dry" rocks to the surface causing elevation of isotherms has been suggested to be the heat source for the geothermal system (Chamberlain et al., 2002), the results of this study suggest a significant additional contribution from radiogenic heat production, thus increasing the overall geothermal gradient.

The spatial proximity of hot springs to high heat-producing regions in the study area indicates hydrothermal fluid circulation in zones with enhanced geothermal gradients. These hot springs are commonly bounded to zones of enhanced permeability (such as faults) and are likely efficiently tapping the proximal zones of increased heat production. Furthermore, in contrast

to conduction, the interaction of topographic-driven deep groundwater flow with heat-producing hot rocks results in advective heat transport to the surface, which is more efficient and rapid near-surface heat transport process common in evolving orogens (Chamberlain et al., 1995; Wanner et al., 2020).

4.5 Conclusion

The study provides the first data set of radiogenic heat production of different lithological units in northern Pakistan's western Himalaya, Kohistan, and Karakoram regions. The radio-elemental concentrations in Nanga Parbat Massif are overall high (especially granites and gneisses), low in Kohistan-Ladakh batholith (but slightly higher in felsic lithologies), while intermediate in Karakoram batholith (except eastern granites). The lithological and genetic association of rocks are found to be controlling the distinct variations in radioelement patterns. High radioelement concentrations in the Nanga Parbat Massif are inherited from protoliths, which, upon partial melting, lead to U enrichment (Th/U ratio < 1) in granites and leucogranites. The high radiogenic heat production and Th in Proterozoic gneisses can be attributed to global paleo-tectonic crust-forming processes at that time. Overall, the Nanga Parbat Massif (with > 4 μWm^{-3}) is classified as high heat-producing, the Karakoram batholith (with 2 – 4 μWm^{-3}) as moderately heat-producing, and the Kohistan-Ladakh batholith (with < 2 μWm^{-3}) as low heat producing. The proximity of locations to high radiogenic heat production to the hot springs suggests its potential contribution towards the geothermal gradients in the study area on a local to regional scale.

Chapter 5: Petrological, geochemical and petrophysical characterization of outcrop analogs of potential geothermal reservoirs

This chapter is based on an article recently submitted to Elsevier's journal Geothermics entitled "Granitoids of the western Himalaya and Karakoram as potential geothermal reservoirs – A petrological, geochemical and petrophysical study" (Anees et al., submitted). The abstract is not included here and the alphanumeric order of figures and tables may differ from the original article. Likewise, the formatting was adjusted to fit the layout of this work.

5.1   Introduction

The Himalayan orogenic belt in northern Pakistan, formed as a response to the Indo-Eurasian tectonic collision, consists of the Karakoram and Kohistan terranes along with basement rocks of the Indian Plate (Fig. 5.1; Khan et al., 1998). This belt comprises several metasedimentary and meta-igneous crystalline complexes related to the Precambrian to Paleozoic basement and Mesozoic to Cenozoic magmatic events starting with the subduction of oceanic lithosphere and leading to the crustal thickening by continental-continental collision (Debon et al., 1987; Searle & Treloar, 2010; 2019). These terranes host EW-trending granitoid batholiths of several 100 km^2. High heat flow (> 100 mWm^{-2}) has been suggested across the belt, which is attributed to radioactive decay, thermal relaxation, and late magmatic processes in the thickened crust (Gokarn et al., 2002; Chandrasekharam & Bundschuh, 2008; Searle et al., 2009). Numerous hot springs occur along the entire Himalayan orogenic belt, in a zone stretching 3000 km long and 150 km wide from Pamir in the west to Tibet (West Yunnan) in the east, which has been termed the Himalayan geothermal province (Tong & Zhang, 1981; Hochstein & Zhongke, 1995; Craig et al., 2013). The source of geothermal heat is linked to the deep percolation of meteoric water and the interaction with hot, brittle, and dry crust (Hochstein & Regenauer-Lieb, 1998). Deep fluid circulation within crystalline complexes, along with regional sutures, resembles geothermal systems described for the Alps (Pastorelli et al., 2001).

Geothermal reservoir exploration requires numerical simulation for resource assessment, which requires information about vital parameters such as petrophysical properties and subsurface geology. Such data can be collected through geophysical surveys, boreholes, or from outcrop analogs of possible reservoir rocks (Held et al., 2014; Kana et al., 2015; Atef et al., 2016; Manning et al., 2007; Kruszewski et al., 2022; Brown, 2022; Weydt et al., 2018). In the unavailability of geophysical data and boreholes, the outcrop analogs provide the most accessible and valuable first-hand information to set thermophysical, hydraulic, and

mechanical parameters for numerical modeling. Moreover, extrapolation of such properties to the reservoir scale can be done to characterize further the geothermal parameters for resource estimation (Sass & Götz, 2012). On an outcrop scale, the changes of the rock due to the action of hydrothermal fluids, weathering, and deformation can be studied, which helps to distinguish between surface and deeper reservoir-scale processes.

In the past few decades, several studies have investigated hot spring sites in northern Pakistan (Shuja, 1986; Todaka et al., 1988; Bakht, 2000; Yousafzai et al., 2010). However, most of the literature either reports hot springs in the context of their regional geological settings or is limited to the overall chemical composition of thermal and groundwater. Some studies focused on fluid evolution and reservoir geothermometry (Ahmad et al., 2001; 2002). While the chemical geothermometers provide reservoir temperature estimates ranging between 100 to 225°C in north Pakistan (Ahmad et al., 2005), they cannot provide the depth and volumetric estimates required for resource assessment. Additionally, isotopes have suggested prolonged residence times of meteoric water, indicating deep infiltration and slow percolation (Ahmad et al., 2002). Information on thermophysical properties, geochemistry, heat production, and hydrothermal alteration is either limited or unavailable. Therefore, reliable reservoir property prediction and thermal modeling require comprehensive datasets of petrological, geochemical, and petrophysical rock properties (Reyer & Philipp, 2014; Rybach, 1988; Charléty et al., 2006; Sone & Zoback, 2013).

For this reason, an outcrop analog study in combination with a multi-parameter characterization (Bär et al., 2020; Weydt et al., 2022a & b) was carried out to better understand the thermophysical, geochemical, and petrographic properties of crystalline (mostly granitoids and gneisses) rocks of the western Himalaya orogenic belt (Fig. 5.1). The goal was to compile and establish a preliminary but extensive dataset of outcrop analogs for granitoid reservoirs in the study area. Compiling such data is necessary for numerical modeling and selecting suitable sites for further detailed and costly investigations.

5.2 Methodology

5.2.1 Field description and sampling

The samples were collected during the field gamma survey focused on the granitoids and gneisses with a high concentration of radiogenic elements. A few samples of intermediate to mafic and volcanic lithologies with low radiogenic elements were also collected to compare and develop a conceptual geothermal model. A total of 69 samples were collected from

outcrops of the Nanga Parbat Massif (NPM), the Kohistan-Ladakh batholith (KLB), and the Karakoram batholith (KB).
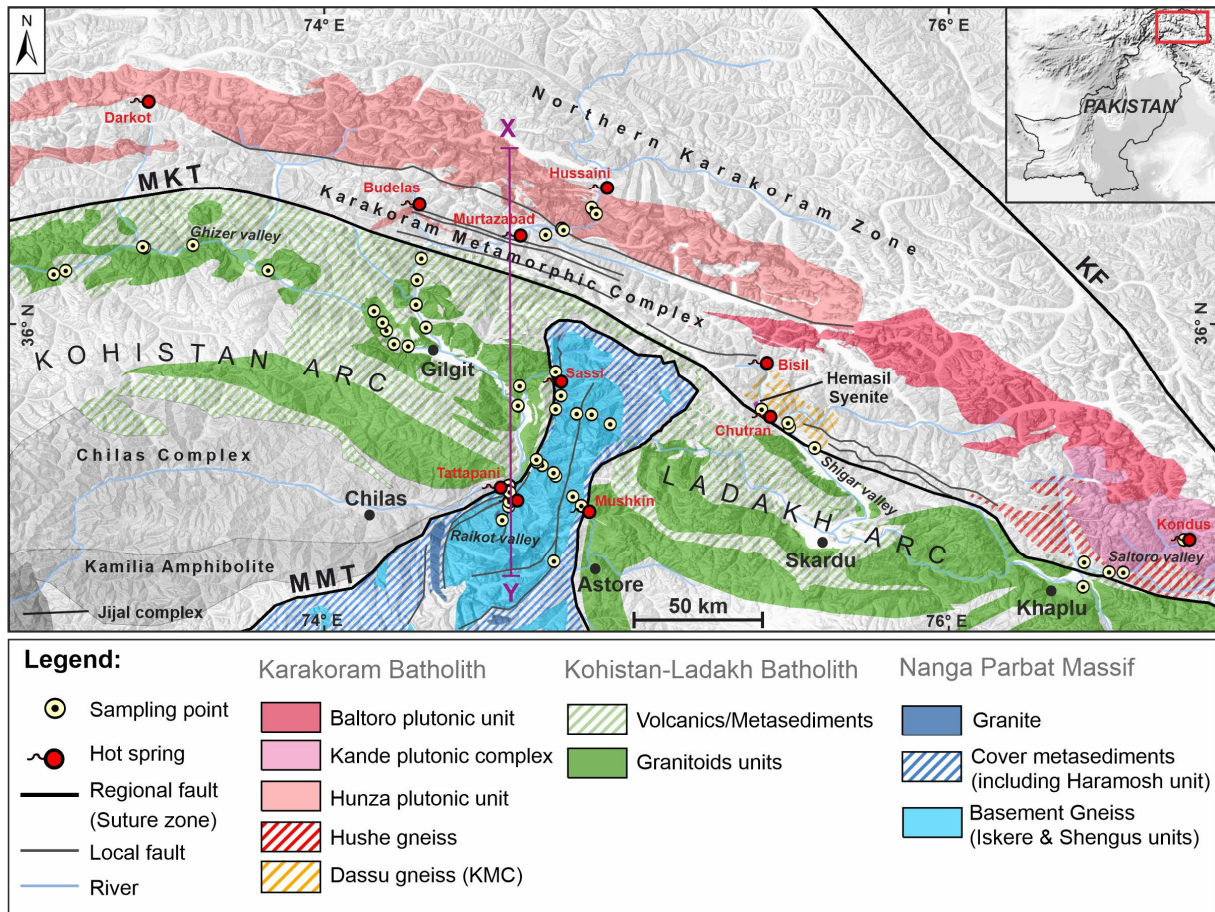
Figure 5.1 Geological map (overlaid on hill-shade terrain model) showing sampling locations, hot springs, and alteration zones along with the sampled geological units in this study (redrawn after Madin et al., 1989; Schneider et al., 1999; Searle & Khan, 1996). The index figure (top right) shows the geographic location of the study area within Pakistan. Abbreviations: KF—Karakoram Fault; MKT—Main Karakoram thrust; MMT—Main Mantle thrust. The purple line XY shows the location of the profile shown in Figure 5.11.
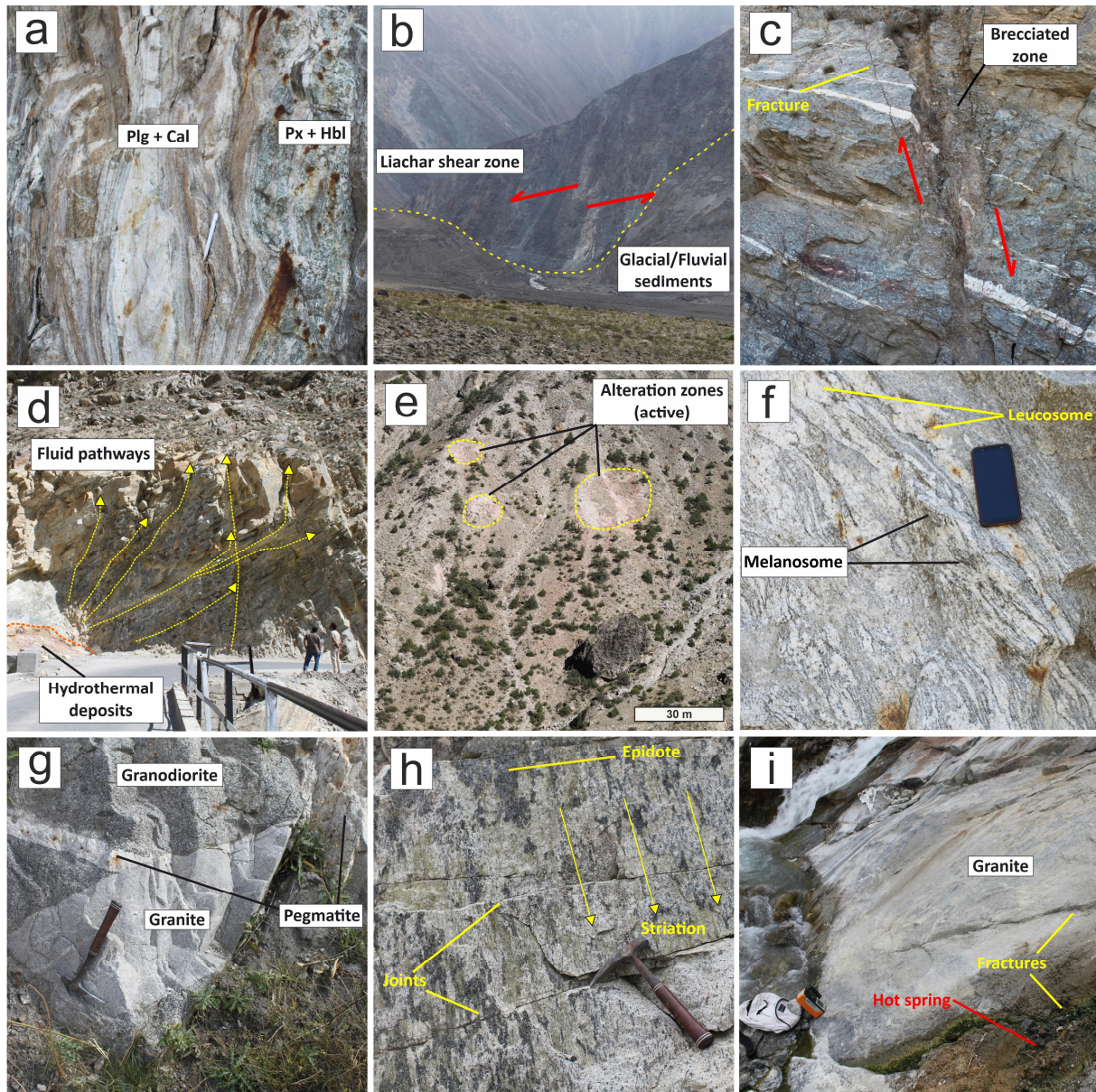
Figure 5.2 (a) Calc-silicate lens along MMT at the western margin of NPM showing leaching of iron oxides (b) Surface expression of strike-slip fault in seismically active Liachar shear zone (Butler et al., 2019) at the western margin of NPM (c) Normal fault within augen gneiss at the Raikot fault along the western margin of NPM. The fault-bounded brecciated zone shows alteration due to fluid flow (d) An altered gneissic outcrop along the Astore River showing evidence of a fossil hydrothermal system. The fluid flowed along foliation planes as well as fractures cross-cutting foliation (e) Alteration deposits around the active hydrothermal system at Tato village in Raikot valley (NPM) (f) Migmatitc gneiss displaying partial melting conditions in the core of the Nanga Parbat during exhumation (g) Contact between granodiorite, granite, and pegmatite in the Karakoram batholith in upper Hunza valley, showing late pegmatite intrusion along margins of granite (h) Epidote mineralization along fractures planes in Hemasil syenite at the southern edge of the Karakoram batholith along Shigar valley (i) Hot spring in Kondus valley (northeast of Saltoro valley) related to fractured porphyritic granite of the Kande pluton (Karakoram batholith).

From the NPM, gneiss, granite, and calc-silicate (Fig. 5.2a) samples were collected along the Raikot Valley, Rupal Valley, Astore River, and Indus River. In Raikot Valley, the augen gneiss with signs of intense shear deformation occurs along the margin of the NPM close to the MMT (Fig. 5.2b & c). Undeformed pegmatite dikes with tourmaline and muscovite were commonly observed cutting the gneissic foliation. At Tato village in Raikot valley, several hot springs, including a steaming geyser, were observed in glacial sediments. Around the hot springs, orange to yellowish colors in the area show signs of hydrothermal alteration of prior lithologies (Fig. 5.2e). The gneissic rocks near Tato village show a migmatitic texture (Fig. 5.2f) and are intruded by numerous pegmatite dikes with idiomorphic tourmaline, quartz, and muscovite crystals.

Further to the southeast along the valley, within the core of the massif, an undeformed leucogranite pluton with equigranular texture intrudes the host gneiss. Along the Astore River, which cuts down the NPM perpendicularly, several outcrops showed visible signs of hydrothermal alteration represented by yellowish alteration along the fracture planes and hydrogen sulfide smell from open fractures, indicating ongoing geothermal activity (Fig. 5.2d). Garnet-bearing gneisses were commonly observed at the eastern margin of NPM along the Astore River. In the Rupal valley, a biotite gneiss was sampled.

The samples from KLB were collected from Ghizer Valley, Gilgit city, Jaglot, and Khaplu. In Ghizer Valley, moving east to west, the leucogranite, granite, diorite, and gabbro were sampled. The lithologies around Gilgit city are mostly granitic to granodiorite with tonalitic units. Volcanic rocks were collected near the MKT, some 20 km north of Gilgit. The sampled outcrops at the Indus and Gilgit River confluence close to Jaglot comprise granites (mostly aplitic), which were intruded by biotite and muscovite-bearing pegmatites. Northeast of Jaglot on the Skardu road, granodiorite to diorite along the MMT at the contact with the NPM shows strong foliation. Towards the east, outcrops of granite to granodiorite with volcanic xenoliths are exposed east of Khaplu. A granite sample was collected approx. 10 km east of Khaplu from an outcrop with a volcanic dike and epidote veins along fracture planes.

From the KB, samples were collected from Hunza, Shigar, and Saltoro Valley. In the Hunza valley, the batholith mainly comprises granodiorites to diorite units with late aplitic to pegmatitic intrusions (Fig. 5.2g). The Sumayar leucogranite pluton, exposed at the southern margin of the KB, intrudes the gneiss of the metamorphic complex. Hydrothermal clay and sulfur deposits associated with fumaroles as evidence of recently active hot springs are observed along the road at Murtazabad in the southern Hunza valley. In Shigar Valley, the Dassu orthogneiss (dome), with peculiar K-feldspar augens, outcrops north of the MKT. This gneissic dome has

a muscovite-rich felsic core and biotite-rich flanks of granodioritic composition. The gneisses contain occasional lenticular marbles and are intruded by tourmaline-bearing pegmatitic dikes ranging from a few to tens of meters in size.

Further to the northwest along the MKT, the hot springs at Chutran village emerge from the fluvial deposits. Hemasil syenite, a relatively small plutonic body (4 x 2.5 km), is exposed north of Chutran (Villa et al., 1996). The pluton has two sets of fractures along which epidote veins formed (Fig. 5.2h). Another hot spring was observed further 15 km to the north at Bisil, which the locals exploit for domestic use. The hot spring emerged probably from the alluvium fan deposits. In the Saltoro Valley, the easternmost part of the study area, the granitoids of the Kande pluton commonly contain hornblende and biotite assemblages. About 20 km northeast of the Saltoro Valley, in the Kondus Valley, a cluster of hot springs occurs within fractured porphyritic granites, which are altered along fluid flow pathways (Fig. 5.2i).

5.2.2   Analytical methods

Optical and cathodoluminescence microscopy

Polarizing microscopy was carried out (for 63 samples) using a Zeiss Axio Imager A1m at the Geoscience Centre of the University of Goettingen (GZG) to describe textural features and major and accessory mineral phases. Additionally, alteration (especially in biotite, plagioclase, and K-feldspar) and their intensity were documented. The alteration intensity was characterized into three categories, i.e., weak, moderate, and strong (after Weydt et al., 2022b), in which weak represents only slight signs of alteration; moderate depicts variable impact and replacement of primary minerals, and strong means primary minerals are heavily altered and replaced by secondary minerals.

Cathodoluminescence microscopy (CL) is sensitive to slight variations in trace elements, which act as activators (Mn, Ti, and Fe) for luminescence and is used to observe features such as zoning, twinning, overgrowth, alteration, and the filling of micro-cracks that are not observable by traditional optical microscopy (Götze, 2012). At GZG, polished thin sections were first coated with a carbon layer and were then analyzed with a modified polarization microscope with a hot-cathode HC3-LM (Neuser et al., 1995), which bombards the thin section with accelerated electrons (14 keV) emitted from a heated filament (Pagel et al., 2000; Müller et al., 2000).

Bulk rock chemical analysis

Sixty-eight (68) samples were crushed and milled using a silicon ball mill down to 60 microns at GZG for chemical analysis of whole-rock major and trace elements. Major elements were analyzed using a Panalytical XRF spectrometer (at GZG and Masa Institute, Goettingen) with a measurement error of < 5%. For trace and REE elements, powdered samples were digested with a mixture of concentrated hydrofluoric and nitric acids in high-pressure vessels and subsequently analyzed with a ThermoFischer quadrupole inductively-coupled plasma mass spectrometer (at GZG).

Electron microprobe analysis

The electron microprobe at GZG was used to analyze accessory minerals in a syenite from the Kande pluton as a part of the Karakoram batholith with high U, Th, and other rare earth elements. The analyses were carried out using a JEOL JXA-iHP200F EPMA at the Goettingen laboratory for correlative Light and Electron Microscopy (GoeLEM – www.mineralogie.uni-goettingen.de, GZG). The instrument is equipped with five spectrometers for wavelength dispersive X-ray spectrometry. Quantitative analysis was performed at an acceleration voltage of 15 kV with a beam current of 20 nA. The counting times on peak/background positions were set to 15/5 s (Na, Si, Al, Fe, Ca), 30/15 s (Mg, P, Sr, Nb, Zr), and 60/ 30 s (Y, U, Th, La, Ce, Nd, Mn, Pr, Sm, Gd, Dy). San Carlos olivine (Si, Mg), albite (Na), hematite (Fe), rhodonite (Mn), wollastonite (Ca), TiO_2 (Ti), anorthite (Al), $ScPO_4$ (P), $SrTiO_3$ (Sr), YAG (Y), Hanchar (U, Th, Zr), Nb met (Nb), $LaPO_4$ (La), $CePO_4$ (Ce), $NdPO_4$ (Nd), $PrPO_4$ (Pr), $SmPO_4$ (Sm), $GdPO_4$ (Gd) and $DyPO_4$ (Dy) were used as reference materials for calibration. Before and after each analytical session, all standards were measured. Matrix correction was applied using the phi-rho algorithm. Quantitative line profiles in allanite were used to document chemical zoning at high spatial and analytical resolution. Additionally, single-point analyses were performed on different allanite, zircon, titanite, and apatite crystals. Two to three measurement points were set on each allanite grain to obtain representative core and rim compositions. SEM imaging was done using an acceleration voltage of 20 kV and a beam current of 2 nA to produce high-resolution back-scattered and secondary electron images.

Petrophysical measurements

For petrophysical measurements, 32 selected samples (out of 69) were cut into cubes (with dimensions ~8 x 5 x 4 cm) and oven-dried for 24 hours at average atmospheric pressure (0.1 MPa) and room temperature (21 ºC). The hydrostatic weighing method (after DIN 52102) was used to determine water absorption, effective porosity, bulk, and matrix density. Thermal

conductivity and thermal diffusivity were measured under dry conditions by an optical scanning technique using a thermal conductivity scanner at TU Darmstadt (Popov et al., 2016). The thermal conductivity scanner measures both parameters simultaneously (with a measurement error of 3% and 5% for thermal conductivity and diffusivity, respectively) by moving a sensor-mounted slide under samples placed between a reference pair and heated to an additional 4 °C with respect to ambient temperature (Lippman & Rauen, 2009). Each measurement was repeated three times to reduce uncertainty. A heat-flux differential scanning calorimeter (C80, Setaram Instrumentation, 2009) was used at the TU Darmstadt to determine specific heat capacity. The samples were crushed to gravel size, continuously heated to 200°C, and cooled to room temperature for 24 hours, resulting in respective temperature curves for all samples. The specific heat capacity for each sample was determined by analyzing its respective temperature curve with an accuracy of 1% (Setaram Instrumentation, 2009). For volumetric heat capacity, the calculated specific heat capacity values were multiplied by the respective bulk density of the samples.

5.3 Results

5.3.1 Optical and Cathodoluminescence microscopic observations
Nanga Parbat Massif

Rocks from NPM are classified based on petrographical observations into gneisses, granites (mostly leucogranite), pegmatites, and calcsilicate. Most of the samples from NPM comprise medium to coarse-grained gneisses of metapelites and meta-granitic origin with biotite-quartz-plagioclase-K-feldspar as typical mineral assemblages. The intensity and style of deformation vary depending upon their location within the massif; e.g., the samples along the western margin show sheared fabric with K-feldspar augen gneiss. The gneisses show textural and mineralogical variations and are further classified in this study based on their primary mineralogy into biotite gneiss and garnet-mica gneiss (Table 5.1).

The biotite gneisses are primarily composed of K-feldspar, quartz, plagioclase, and biotite with muscovite, apatite, zircon, monazite, tourmaline, epidote, and opaque minerals as accessory phases. Sometimes, muscovite occurs as major mineral assemblage along biotite with sporadic garnet and sillimanite. In thin sections, K-feldspar typically is porphyroblastic, with myrmektic margins and alteration to kaolinite. Quartz shows subgrain formation in the strain zones and exhibits intense undulatory extinction. Plagioclase is subhedral to anhedral, with kink twining, and mostly shows sericitic alteration along cleavage planes. In CL, plagioclase appears with yellowish-green core reddish margins with a slight alteration to calcite. While in highly deformed samples, CL shows light to dark yellowish green plagioclase altered to bluish

albite (Fig. 5.3f). Biotite with greenish to reddish brown pleochroism is oriented parallel to foliation and shows a grain size reduction and increased chloritization with intense deformation. It commonly contains the inclusions of epidote, zircon, and apatite. Opaques are Fe-bearing minerals that show oxidization to limonite in deformed zones (Table 5.1).

The garnet-mica gneisses comprise quartz, K-feldspar, and plagioclase as primary assemblage with garnet, muscovite, biotite, and aluminosilicate (sillimanite and kyanite) as minor minerals. Garnet appears anhedral and cracked, while kyanite forms subhedral grain clusters with small replacements by quartz and feldspar. Sillimanite occurs as elongated subhedral grains parallel to foliation. Slight sericitization and chloritization of feldspars and biotite are present. Apatite, zircon, and rutile (as inclusion in quartz) are found as accessory minerals. Two different varieties of plagioclase are observed in CL: unaltered blue and reddish-green with a calcic alteration. Sillimanite and kyanite appear dark red in CL.

Calc-silicate rocks in NPM mainly occur in shear zones as banded alternating layers of greenish pyroxene, whitish carbonate, and plagioclase. In the thin section, coarse to very coarse plagioclase and clinopyroxene (diopside) with amphibole (tremolite), calcite, and quartz occur as major assemblages. Secondary calcite and quartz occur in veinlets and intergranular spaces. Epidote, titanite, and apatite are accessory minerals (Table 5.1).

The granites within the massif occur as equigranular undeformed plutons with pegmatitic dikes cross-cutting the basement gneisses along the margins of the massif. In thin section, the equigranular granites primarily comprise K-feldspar, plagioclase, and quartz. At the same time, biotite and tourmaline are sometimes present as major phases (Fig. 5.3). Plagioclase crystals are euhedral to subhedral with well-developed zoning. Fluorite occurs as a secondary phase within intergranular spaces and cores of plagioclase (Fig. 5.3g). The pegmatites exhibit similar mineralogy with muscovite as a major assemblage. Tourmaline, muscovite, and biotite are often a few cm in size. The plagioclase in CL appears bright green with calcite (orange) and albite (blue) patches (Fig. 5.3l). Overall, the granites show weak to moderate alteration, while pegmatites typically show moderate alteration in plagioclase and biotite.

Table 5.1 Summary of petrographic observations. Abbreviations of mineral names are after Whitney and Evans (2010).

Lithology	Mineralogy			Alteration Intensity within		
	Major (> 5 %)	Accessory (< 5 %)	Alteration	Pl	Bt	Kfs
Nanga Parbat Massif						
Bt Gneiss	Kfs, Qz, Pl, Bt, ± Ms	Ms, Ap, Zrn, ± Opq,± Mnz, ± Tur, ± Ep, ± Grt, ± Sil	Chl, Ser, ± Lm	Weak to Moderate	Weak to Moderate	Weak
Garnet Mica Gneiss	Qz, Kfs, Pl	Grt, Ms, Bt, Sil, Ky, Ap, Zrn, Rt	Chl, Ser	Weak	Weak	Weak
Calc-silicate	Pl, Px, Amp, Cal, Qz	Ep, Ttn, Ap	Cal			
Granite	Kfs, Pl, Qz, ± Bt, ± Tur	± Fl, ± Ms, Ap, ± Grt, Zrn, ± Ep, ± Mnz, ± Opq	Ser, Chl	Weak to Moderate	Weak to Moderate	
Pegmatite	Kfs, Qz, Pl, Ms, Tur, Bt	± Grt, Ap, ± Opq, Zrn, ± Mnz	Ser, Chl	Moderate	Moderate	
Karakoram Batholith						
Granite	Kfs, Pl, Qz, ± Bt, ± Ms	± Opq, ± Ap, ± Zrn, ± Ttn, ± Grt	± Ser, ± Chl	Moderate	Moderate	
Bt-Ms Gneiss	Pl, Qz, Kfs, Bt, Ms	Ap, ± Ep, ± Zrn, ± Grt, ± Opq	Ser, Chl	Weak to Moderate	Weak to Moderate	
Mica Schist	Qz, Kfs, Bt, Ms	Grt, Ttn, Ep, Zrn, Opq				
Quartz monzonite	Qz, Kfs, Pl, Bt, ± Amp	± Opq, ± Ttn, Ep, ± Czo, Ap, Zrn, ± Aln, ± Ms, ± Tur	± Cal, Ser, ± Chl	Weak	Weak	
Syenite	Kfs, Qz, Pl, ± Amp, ± Bt, ± Ep	± Aln, ± Bt, Opq, ± Grt, ± Ttn, ± Ep, Ap, ± Zrn	± Cal, ± Ser, ± Chl ± Ab	Weak to Moderate	Moderate	Weak
Granodiorite	Pl, Qz, ± Kfs, Bt, ± Amp	± Px, ± Ms, Ep, ± Ttn, Opq, ± Ap, Zrn, ± Grt	± Ser, ± Chl	Moderate	Moderate	
Diorite	Pl, Qz, Bt, Kfs, Amp	Ep, Ttn, Opq, Ap, Zrn				
Kohistan Batholith						
Granodiorite	Pl, Qz, Kfs, Bt, ± Amp	± Px, ± Opq, ± Ttn, Ep, Ap, Zrn	Chl, Ser	Moderate	Moderate	Weak to Moderate
Meta-granodiorite	Pl, Qz, Bt	Opq, Amp, Zo, Grt, Zrn				
Diorite	Pl, Amp	Opq, Bt, Ep, Ap, Zrn	Chl, Ser, Cal, Ep	Strong	Strong	Moderate
Granite	Pl, Kfs, Qz, ± Bt	± Ms, ± Ttn, ± Ep, ± Ap, ± Zrn, ± Grt, ± Amp	Chl, Ser	Weak to Moderate	Weak to Moderate	
Tonalite	Qz, Pl, Kfs, ± Bt	± Px, ± Ap, ± Ep, ± Amp	± Ser	Weak		
Quartz monzonite	Pl, Qz, Bt, Kfs, Amp	Ttn, Ap, Ep, Px				
Monzodiorite	Pl, Amp, Bt	Opq, Ep, Ttn, Ap	Chl, Ser	Moderate	Moderate	
Volcanic	Qz, Amp, Pl	± Bt, ± Ep, ± Opq, ± Ttn	Chl			
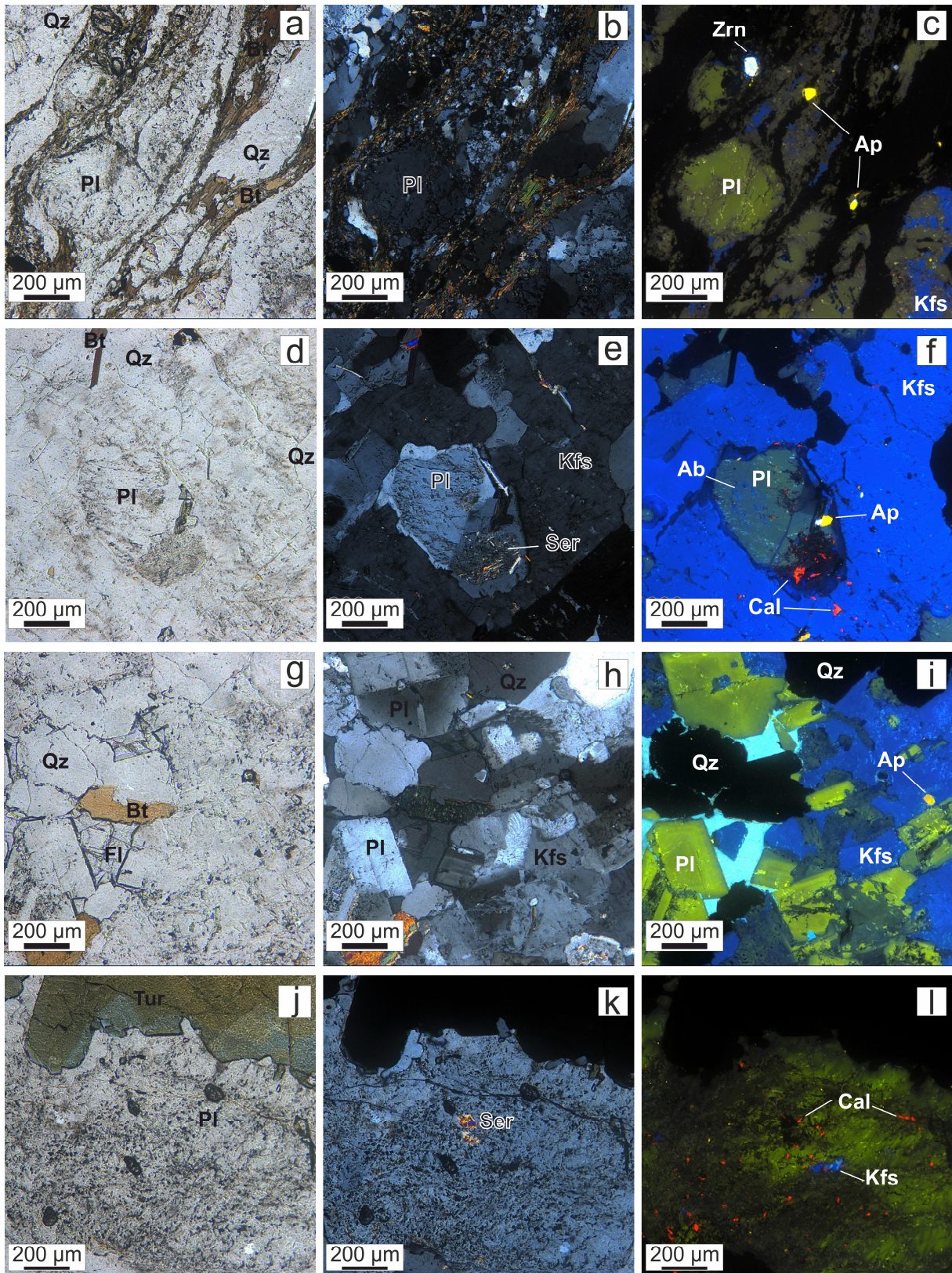
Figure 5.3 Transmitted (a, d, j, g), Polarizing (b, e, h, k) and cathodoluminescence (c, f, i, l) microphotographs illustrating primary and alteration mineralogy in gneiss (RK-4i & NP-8; a-f), granite (FM-4; g-i) and pegmatitic granite (NP-10; j-l) from the Nanga Parbat Massif. Abbreviations of mineral names are after Whitney and Evans (2010).
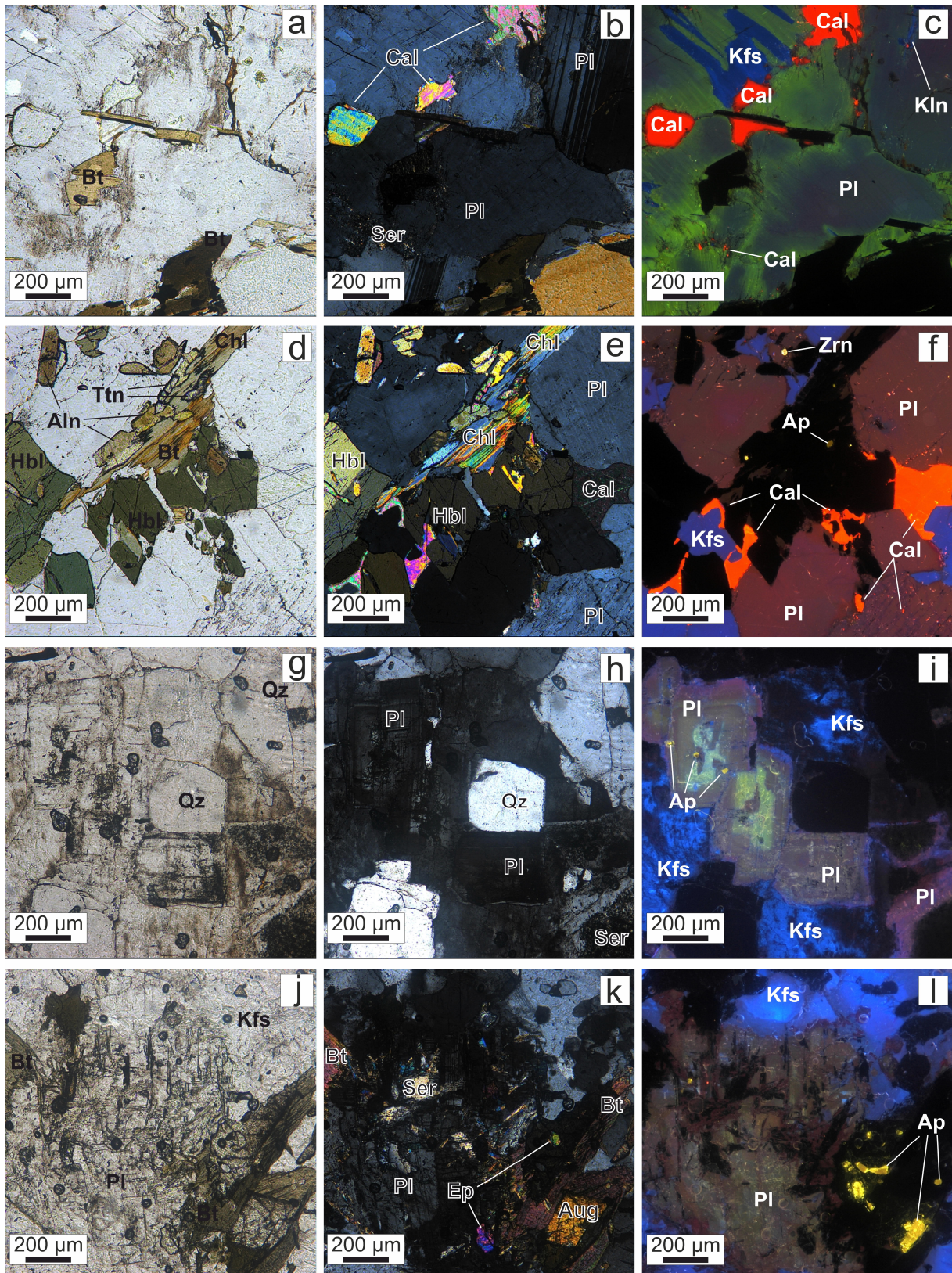
Figure 5.4 Transmitted (a, d, j, g), polarizing (b, e, h, k) and cathodoluminescence (c, f, i, l) microphotographs illustrating primary and alteration mineralogy in syenite (SGH-9 & HSH-5; a-f) from Karakoram batholith and granodiorite (JT-2 & TH-1; g-l) from the Kohistan batholith. Abbreviations of mineral names are after Whitney and Evans (2010).

Kohistan-Ladakh batholith

Samples from KLB comprise granite, quartz monzonite, granodiorite, meta-granodiorite, diorite, monzodiorite, tonalite, and volcanics comprising dacite and basalt (Fig 5.4g-l; Table 5.1). The granites are aplitic to coarse-grained and mainly composed of plagioclase, K-feldspar, and quartz, with biotite as essential minerals in some samples. Muscovite and amphibole are minor phases with other accessory minerals such as titanite, apatite, epidote, apatite, zircon, and garnet. Some samples contain microcline, which is mostly unaltered. Granite shows weak to moderate sericitic and chloritic alteration in plagioclase and biotite, respectively. In quartz-monzonite, plagioclase, quartz, biotite, K-feldspar, and amphibole comprise the essential mineralogy, while titanite, apatite, epidote, and pyroxene occur as accessory minerals. The granodiorites primarily comprise plagioclase, quartz, K-feldspar, and biotite, while pyroxene, opaque, titanite, epidote, apatite, and zircon comprise the accessory mineralogy. Granodiorites show moderate alteration in plagioclase and biotite and weak to moderate alteration in K-feldspar, which appears bright blue with patches of reddish alteration under CL (Fig 5.4l). A meta-diorite sample with strong foliation collected close to the western margin of NPM comprises plagioclase, quartz, and biotite, along with amphibole, opaque, and zoisite as accessory minerals.

Diorite and monzodiorite samples contain plagioclase, amphibole, and biotite along with opaque, titanite, apatite, and pyroxene as accessory minerals and show moderate to strong alteration with secondary minerals such as sericite, calcite, epidote, and chlorite (Table 5.1). In CL, plagioclase appears yellowish-green to greenish-red, altered to calcite. K-feldspars have bright blue luminescent in CL and contain small patches of calcite. Tonalite shows weak alteration and primarily consists of quartz, plagioclase with varying K-feldspar and biotite, and minor pyroxene, apatite, epidote, and amphibole. Out of volcanic samples, basalt has amphibole, plagioclase, and quartz as essential minerals, while dacite is composed of quartz, plagioclase, amphibole, and biotite. Both samples show minor alterations.

Karakoram batholith

Samples from Kande pluton are classified as syenite, quartz monzonite, and granite. The syenites and quartz monzonite have K-feldspar, plagioclase, quartz, biotite, and amphibole as major minerals, while allanite, zircon, apatite, epidote, titanite, and opaque are present as accessory minerals (Fig. 5.4d-f). Myrmekite can be observed along the margins of K-felspar phenocrysts. Calcite is present as an alteration product within plagioclase and amphibole. Biotite shows weak to moderate alteration into chlorite, while sericite is present in the core of moderately altered plagioclase. In CL, plagioclase has a bluish-red core with a pinkish-red

margin, showing slight calcic alteration and albitization along cleavage planes. K-felspars have mostly deep blue luminescence with slightly altered reddish margins. The granite has a porphyritic texture and comprises plagioclase, K-feldspar, quartz, and biotite as primary minerals, with apatite, titanite, zircon, and opaques as accessory minerals. Biotite shows strong chloritization, while plagioclase shows moderate sericitization.

In Shigar Valley, samples include biotite-muscovite gneiss, syenite, and granodiorite. The Bt-Ms gneiss primarily comprises plagioclase, quartz, K-feldspar, biotite, and muscovite, with apatite, epidote, zircon, garnet, and opaque as accessory minerals. Myrmekites are present on the margins of K-feldspar augens reaching up to 3cm in size. Plagioclase and biotite show weak to moderate alteration into sericite and chlorite. The syenites belong to the Hemasil pluton and consist of K-feldspar, plagioclase, quartz, biotite, and epidote. Trace mineralogy comprise clionzoisite, zircon, apatite, epidote, titanite and opaque minerals. Calcite is a secondary phase filling intergranular space (Fig. 5.4b, c). Biotite and plagioclase are strongly altered into chlorite and sericite, respectively. Plagioclase also show albitic rims. In CL, plagioclase has a reddish-green core with a yellowish-green margin and shows calcic alteration along fractured margins (Fig. 5.4c). Granodiorite has quartz, plagioclase, K-feldspar, and biotite as major assemblages, with muscovite, apatite, epidote, zircon, garnet, and opaque as minor and accessory minerals (Table 5.1). Plagioclase and biotite show moderate alteration.

The samples collected from Hunza Valley comprise granite, quartz monzonite, granodiorite, and diorite (Table 5.1). The granites comprise K-feldspar, plagioclase, and quartz, including muscovite in leucogranite and biotite in aplite. Garnet and muscovite are accessory minerals in pegmatite, while leucogranite contains apatite and zircon alongside garnet. Plagioclase and biotite are strongly altered in aplite but weakly in leucogranite and pegmatite. Plagioclase in leucogranites shows yellowish to reddish-green luminescence in CL with reddish margins and is slightly altered to calcite along cleavage planes. Quartz monzonite sample (with weak foliation) has quartz, K-feldspar, biotite, and plagioclase as primary mineralogy and is cut by a tourmaline-bearing quartz vein parallel to foliation. Titanite, muscovite, apatite, epidote, zircon and secondary calcite comprise trace mineralogy. The granodiorites and diorite samples contain plagioclase, quartz, K-feldspar, biotite, and amphibole as major mineral assemblages with pyroxene, epidote, titanite, opaque, apatite, and zircon as the accessory phase. Biotite shows weak alteration to chlorite, while plagioclase alteration is negligible.

5.3.2   Whole rock geochemistry

Major element geochemistry

Using Total Alkali vs. Silica classification (after Middlemost, 1994), we classify the granitoids based on their SiO_2 vs $Na_2O + K_2O$ concentrations (Fig. 5.5a).

Overall, most rocks from all three domains have a granitic composition. In the NPM, the SiO_2 concentration varies between 65 and 77 wt% and the $Na_2O + K_2O$ content between 6 and 9 wt%, corresponding to granite, quartz monzonite, and granodiorite. Calc-silicate lenses contain 53 and 1.5 wt% SiO_2 and $Na_2O + K_2O$, respectively, corresponding to a mafic (gabbroic diorite) composition. In the KLB, the SiO_2 content varies between 51 and 78 wt% and $Na_2O + K_2O$ between 2 and 8 wt%, classifying the plutonic rocks as granite, granodiorite, monzonite, diorite, monzodiorite, and volcanics as dacite and basalt. In the KB, the SiO_2 concentrations range between 59 and 78 wt%, and the $Na_2O + K_2O$ concentration ranges between 5.5 and 12 wt%, classifying the samples as granite, syenite, granodiorite, quartz monzonite, and diorite (Fig. 5.5a).

The CIPW normative feldspar (Albite-Anorthite-Orthoclase) diagram (after O'Connor 1965) shows that most of the NPM and the KB samples plot in the granite field, while the samples from the KLB are distributed among granite, granodiorite and tonalite fields (Fig. 5.5b). According to the Shand index (Shand, 1943), the NPM rocks are peraluminous, with most corresponding to S-type and a few to I-type granitoids (Fig. 5.5c). The KLB contains both meta and peraluminous rocks classified as I-type granitoids. Granitoids from the KB show a broad variation between meta and peraluminous compositions and contain both I and S-type granitoids. Frost's 2001 classification shows rocks from the NPM primarily as alkali-calcic, except those with lower alkalic and calc-alkalic composition, while the KLB is calc-alkalic to calcic (Fig. 5.5d). In the KB, granitoids vary between calc-alkalic and alkalic compositions.

The Harker variation diagrams (Harker, 1909) are used to demonstrate the correlations between major element oxides with increasing SiO_2 concentration. We noticed negative correlations for Al_2O_3, CaO, MgO, Fe_2O_3, P_2O_5, TiO_2, and MnO and a weak correlation for K_2O and Na_2O (Fig. 5.6). In the NPM, the gneisses and granites follow typical decreasing trends for Al_2O_3, CaO, MgO, Fe_2O_3, TiO_2 and MnO with increasing SiO_2 concentration, except for P_2O_5, K_2O, and Na_2O where a clear correlation is lacking. Calc-silicate in the NPM shows higher CaO and MgO concentrations (19 and 5.4 wt.%, respectively) and lower K_2O and Na_2O (0.37 and 0.21 wt.%, respectively) compared to other rock types in the NPM (Fig. 5.6 d & e). Tonalite and meta-granodiorite (shown as gneiss in Fig. 5.6) show low concentrations of K_2O vs. SiO_2 compared to granites and granodiorites within the KLB. Syenite and quartz monzonite

from the KB show distinct lower SiO_2 (59–61 wt%) versus higher Al_2O_3, Na_2O, and K_2O concentrations than other rock types (Fig. 5.6).

Trace element geochemistry

Figure 5.7 shows primitive mantle-normalized trace-element (McDonough & Sun, 1995) and chondrite-normalized REE patterns (Boynton, 1984). Overall, rocks from the NPM exhibit enrichment in trace (Rb, Th, Nb, Ta) and LREE (La, Ce, Pr, Nd) relative to the KB and KLB (Fig 5.7a & b). In contrast, the KLB rocks are depleted with most trace and REEs but do not show a negative Eu anomaly.

Within the NPM, gneisses show slightly higher enrichment in Th, Ba, Nb, Ta, Sr, and Sm compared to granites, which display higher Rb and U concentrations and relative depletion in large-ion lithophile elements such as Sr and Ba (Fig. 5.7c). The chondrite-normalized REE plot shows enrichment of light rare earth elements (LREE) in gneisses, while the granites show enrichment in HREE with negative Eu anomalies in both rock types (Fig. 5.7d). In the KLB, the granites show enrichment in Rb, Th, and U while depletion in Nb, Ce, Sr, and Nd compared to granodiorites and diorites (Fig. 5.7e). The tonalites and volcanic rocks show an overall depletion trend in trace elements compared to other rock types. Quartz monzonites, granodiorites, and diorites from KLB show relatively higher LREE and lower HREE than granites, tonalites, and volcanics (Fig. 5.7f). In KB, the syenites distinctly show higher Ba, Th, Pb, Pr, Sr, Nd, and Sm compared to granites with higher U and Ta, while lower Ba, Th, La, Ce, Sr, Nd, and Sm (Fig. 5.7g). In the chondrite-normalized REE plot, gneisses, syenites, quartz monzonite, and granodiorites show enriched LREE compared to granites. Granites show highly variable HREE patterns (Fig. 5.7h).
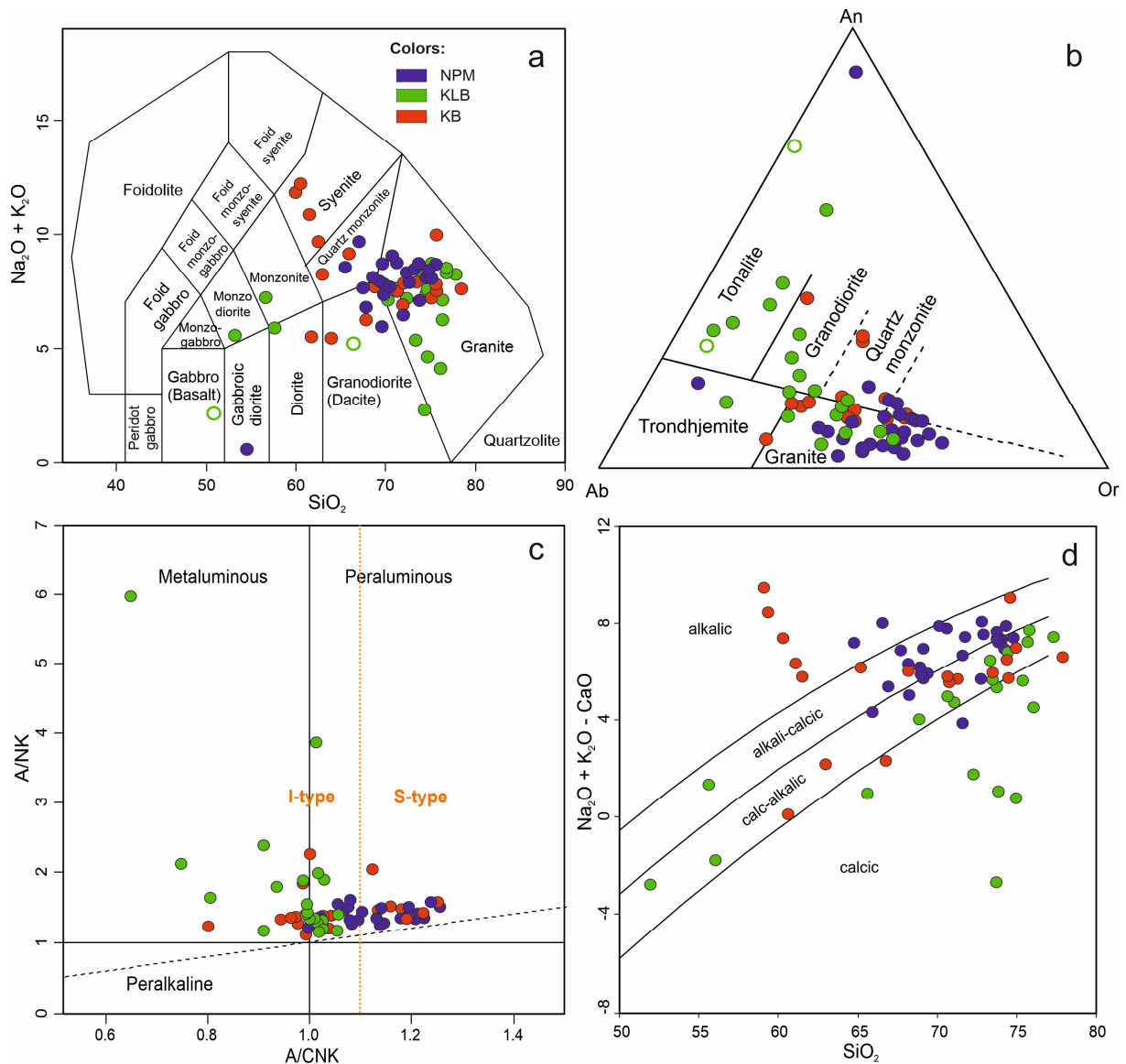
Figure 5.5 (a) Total alkali versus silica diagram (after Middlemost, 1994) showing the classification of plutonic and volcanic rocks (b) CIPW Normative feldspar differentiation diagram (O'Connor, 1965) (c) Shand's index diagram (1943) (d) Tectonic discrimination of granitoids (Frost et al., 2001). Gneisses are used in all classifications for compositional comparison with other granitoids. Hallow green circles show volcanic samples (in a & b).
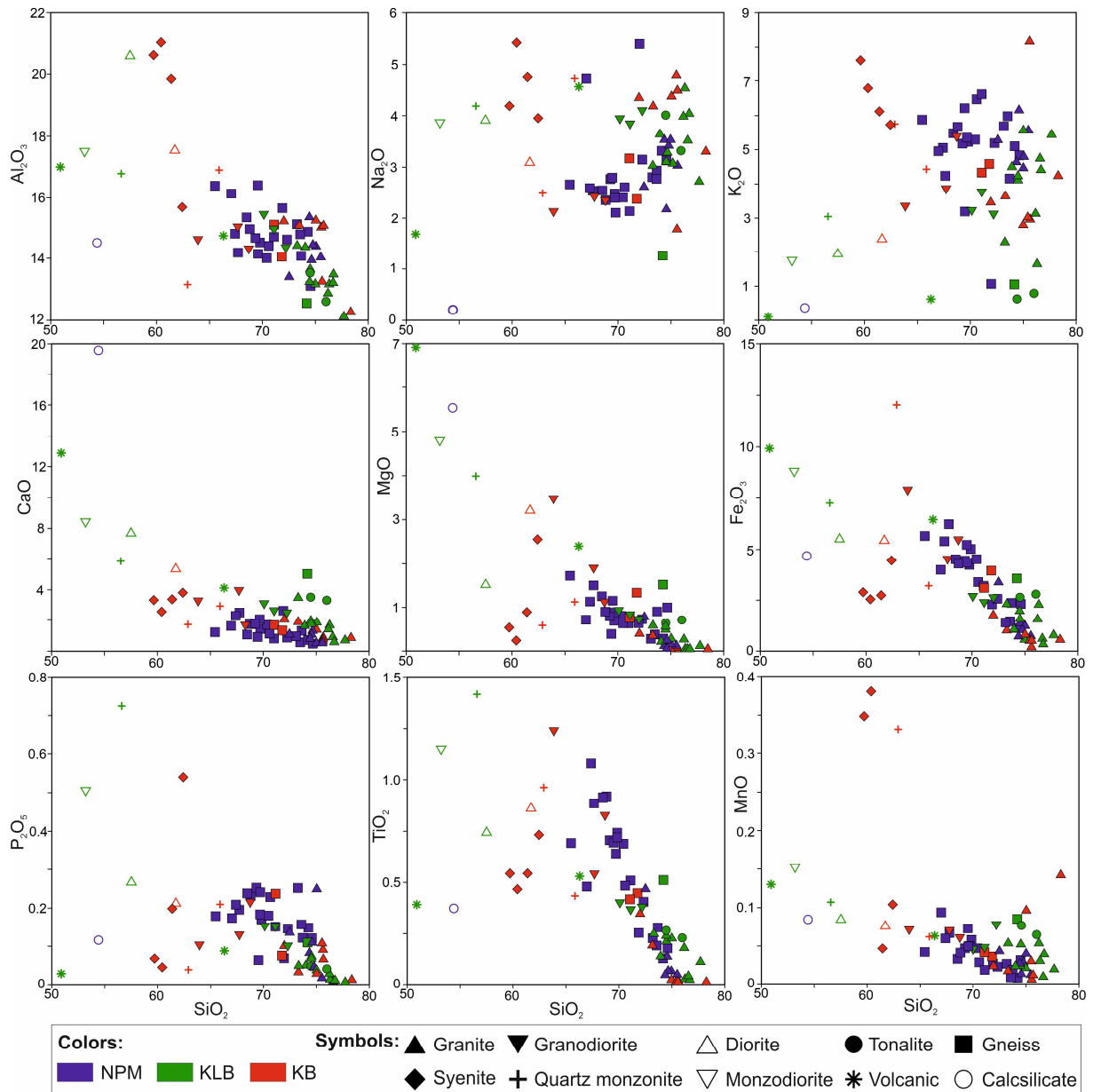
Figure 5.6 Harker diagrams of major-element vs. silica concentrations
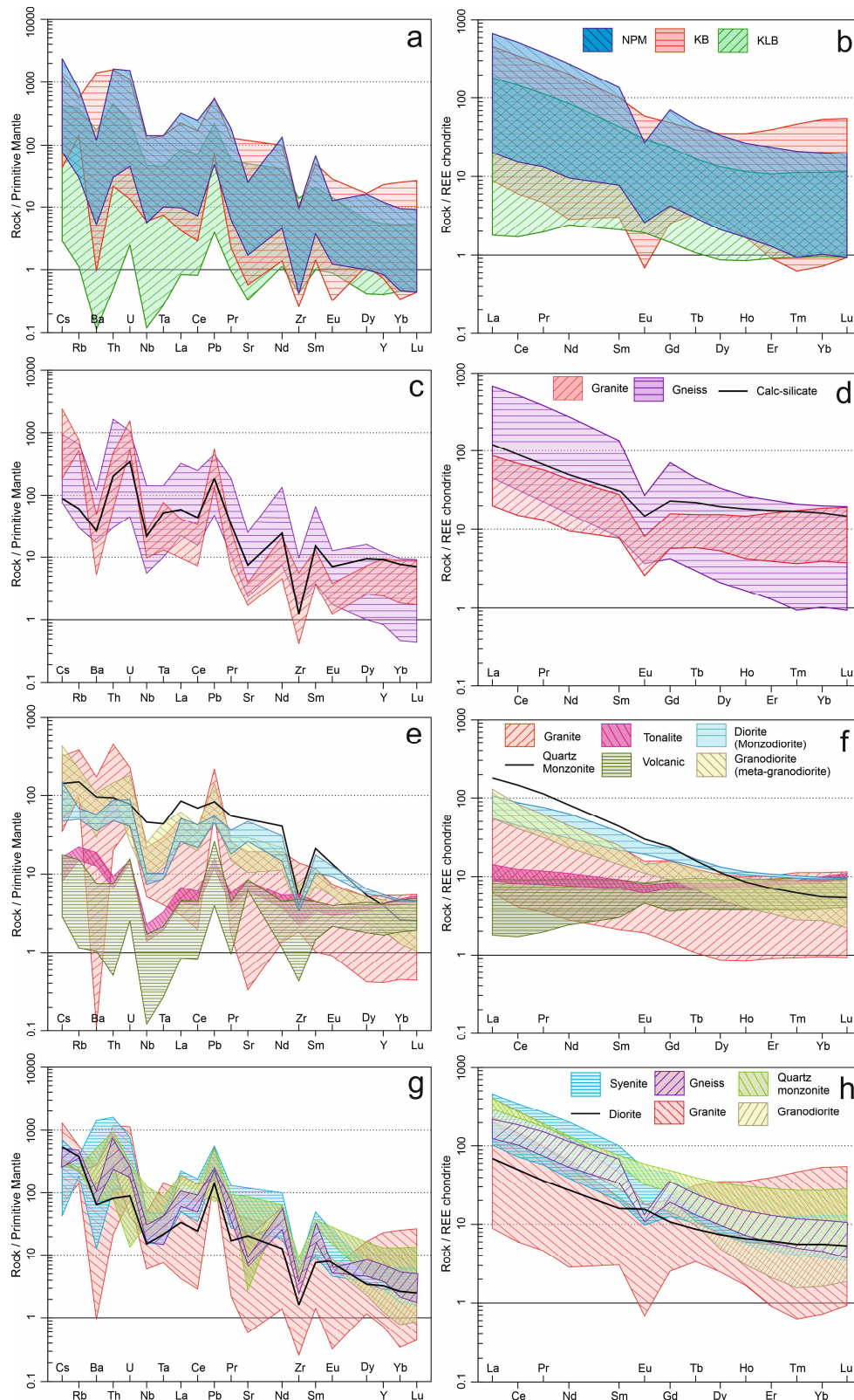
Figure 5.7 Primitive mantle-normalized (after McDonough & Sun, 1995) and chondrite-normalized (after Boynton, 1984) showing overall trace element and rare earth element (REE) patterns (a & b) in Nanga Parbat Massif, Kohistan-Ladakh batholith, and Karakoram batholith. Follow-up figures show intra-domain trace and REE comparison within different lithological units for the NPM (c & d), KLB (e & f), and KB (g & h), respectively.
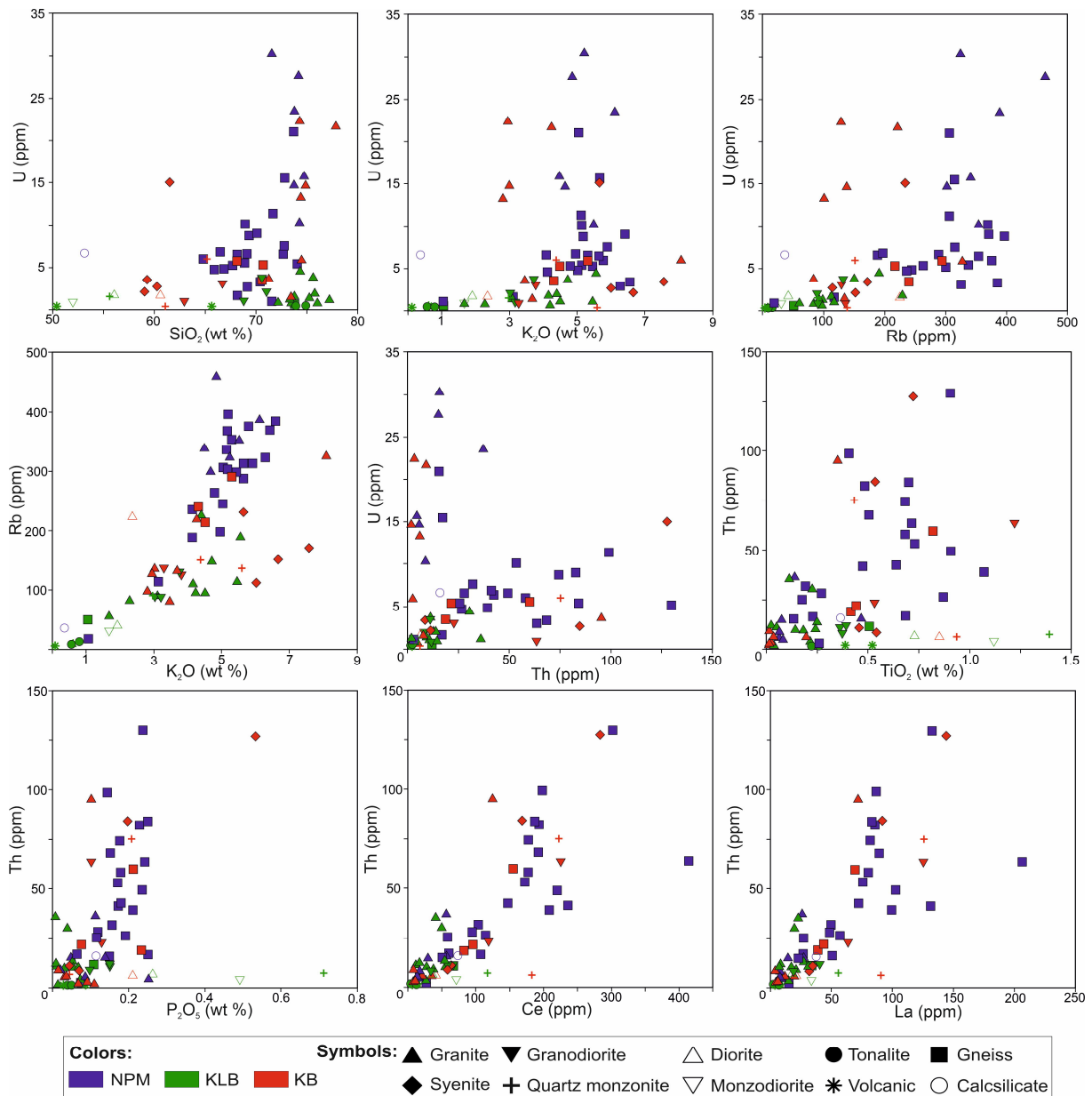
Figure 5.8 Cross plots of U and Th vs. selected major, trace and REE element concentrations

Radioelements show a wide range, with the highest concentrations of U and Th in NPM ranging from 0.9 – 30.46 ppm (10.02 ppm mean) and 2.37 – 129.63 ppm (41.18 ppm mean), respectively. KB has slightly lower concentrations of radioelements (compared to NPM), which range between 0.27 – 22.45 ppm (7.46 ppm mean) and 1.75 – 127.45 ppm (36.27 ppm mean) for U and Th, respectively. In contrast, U and Th concentrations in KLB range between 0.05 – 4.58 ppm (1.48 ppm mean) and 0.04 – 36.06 ppm (9.74 ppm mean), respectively. Figure 5.8 shows several cross plots to illustrate the relationship of U, Rb, and Th with some major and rare earth elements. The U vs. SiO_2 plot shows increasing concertation of U with increasing SiO_2, which corresponds to most granites and gneisses of NPM and KB. The granites of the KLB also have slightly higher U concentrations than other decreasingly less felsic lithologies. However, overall, they have significantly lower U concentrations (< 5 ppm) than the NPM and KLB. U vs. K_2O, U vs. Rb, and Rb vs. K_2O plots show that in the NPM, granites, and gneisses with high K_2O correlate positively with high Rb, which correlates with high U concentration. U vs. Th indicates no correlation in the granites from the NPM and KB, while a weak positive correlation is in the case of NPM's gneisses and KLB's granites. Th vs. TiO_2, Th vs. P_2O_5, Th vs. Ce, and Th vs. La plots show a positive correlation in the case of KB's syenites, gneisses, granodiorites, and NPM's gneisses (Fig. 5.8).

5.3.3 EPMA analysis of allanite

The EPMA of allanites from the Kande pluton of Karakoram batholith reveals their average major composition as SiO_2 (33.65 wt%), Al_2O_3 (18.34 wt%), CaO (15.49 wt%), and Fe_2O_3 (15.20 wt %) (Fig 5.9). Additionally, the REE elements show significant concentrations of UO_2 (0.13 wt%), ThO_2 (2.80 wt%), La_2O_3 (3.33 wt%), Ce_2O_3 (5.98 wt%), and Nd_2O_3 (1.95 wt%). In a semi-quantitative comparison, the EPMA of zircons shows SiO_2 (32.08 wt%), ZrO_2 (57.81 wt%), TiO_2 (10.07 wt%) and CaO (3.25 wt %) as major oxides while the concentration of REE oxides UO_2 (0.21 wt%), ThO_2 (0.16 wt%), La_2O_3 (0.32 wt%), Ce_2O_3 (0.36 wt%) and Nd_2O_3 (0.14 wt%) indicate significate decrease as opposed to allanite. Titanite contains SiO_2 (29.90 wt%), Fe_2O_3 (1.13 wt%), TiO_2 (36.16 wt%), and CaO (27.97 wt %) as major oxides and significantly low values of REE (Supplementary data 2). Similarly, the analysis of apatite also shows insignificant REE within its crystal lattice.

SEM-EDS imaging of allanite shows zoning with bright core and dark margins, indicating variation in concentration of REE elements (Fig. 5.9). The same was confirmed by EPMA analysis, which revealed an increase in the concentration of Th, Ce, La, and Nd towards the bright core.

5.3.4   Petrophysical properties

The thermophysical parameters, along with porosity, density, and water absorption of 30 samples, are shown in Table 5.2. The petrophysical results overall show high variability, with bulk density, porosity, thermal conductivity, and thermal diffusivity ranging from 2.58 – 3.0 g cm^{-3}, 0.7 – 3.5 %, 1.48 – 3.37 W m^{-1} K^{-1} and 0.68 – 1.95·10^{-6} m^2 s^{-1}, respectively. Porosity decreases with an increase in bulk density and tends to increase in altered and deformed samples slightly. The thermal conductivity and thermal diffusivity show a higher scattering when correlating with bulk density, which slightly reduces when correlating with porosity (Fig. 5.10). In contrast, the thermal conductivity and thermal diffusivity show a strong positive correlation with increasing SiO$_2$ content, with SiO$_2$ enriched granite and gneiss displaying enhanced the thermal conductivity and diffusivity (Fig. 5.10 f & i). Overall, Fig. 5.10 indicates that mineral composition and porosity play an important role in controlling thermal conductivity and thermal diffusivity. The specific heat capacity dataset instead shows a small variation (744 to 767 J kg^{-1} K^{-1}) with the averages for the KB, KLB, and NPM are 755, 754, 752 J kg^{-1} K^{-1}, respectively (Fig 5.10c). The volumetric heat capacity shows an increasing trend towards higher density (Table 5.2).

Thermal conductivity and thermal diffusivity in NPM gneiss vary between 1.52 – 2.78 W m^{-1} K^{-1} and 0.77 – 1.38·10^{-6} m^2 s^{-1}, respectively (Fig 5.10a). The highest thermal conductivity and thermal diffusivity (3.37 W m^{-1} K^{-1} and 1.95·10^{-6} m^2 s^{-1}, respectively) were found in pegmatite (RK-4ii). The porosity is slightly higher in granite (1.5 – 2.2 %) compared to gneiss (0.9 – 1.7 %) and calc-silicate (1.0 %), while the bulk density is slightly lower (2.58 – 2.59 g cm^{-3}). Calc-silicates have higher thermal conductivity, thermal diffusivity, and bulk density (2.73 W m^{-1} K^{-1}, 1.19 10^{-6} m^2 s^{-1} and 3 g cm^{-3}, respectively) than granite (excluding pegmatite) and most gneisses.

In KLB, the thermal conductivity in granite ranges between 2.00 – 2.42 W m-1 K-1, which is slightly higher than granodiorite (2.03 W m^{-1} K^{-1}), but lower than meta-granodiorite (2.91 W m^{-1} K^{-1}) and comparable to tonalite and dacite (2.39 and 2.13 W m^{-1} K^{-1}, respectively). Dacite showed the lowest porosity (0.6 %) and highest bulk density (2.79 g cm^{-3}) within the KLB. From the KB, the syenite and quartz monzonite (of Kande pluton) show significantly decreased thermal conductivity and diffusivity (1.48 – 1.71 W m^{-1} K^{-1} and 0.68 – 0.76 ·10^{-6} m^2 s^{-1}, respectively). The diorite (from Hunza) with higher porosity and matrix density (3.52 % and 2.78 g cm^{-3}), with thermal conductivity and diffusivity of 1.52 W m^{-1} K^{-1} and 0.77 10^{-6} m^2 s^{-1}, respectively (Table 5.2).
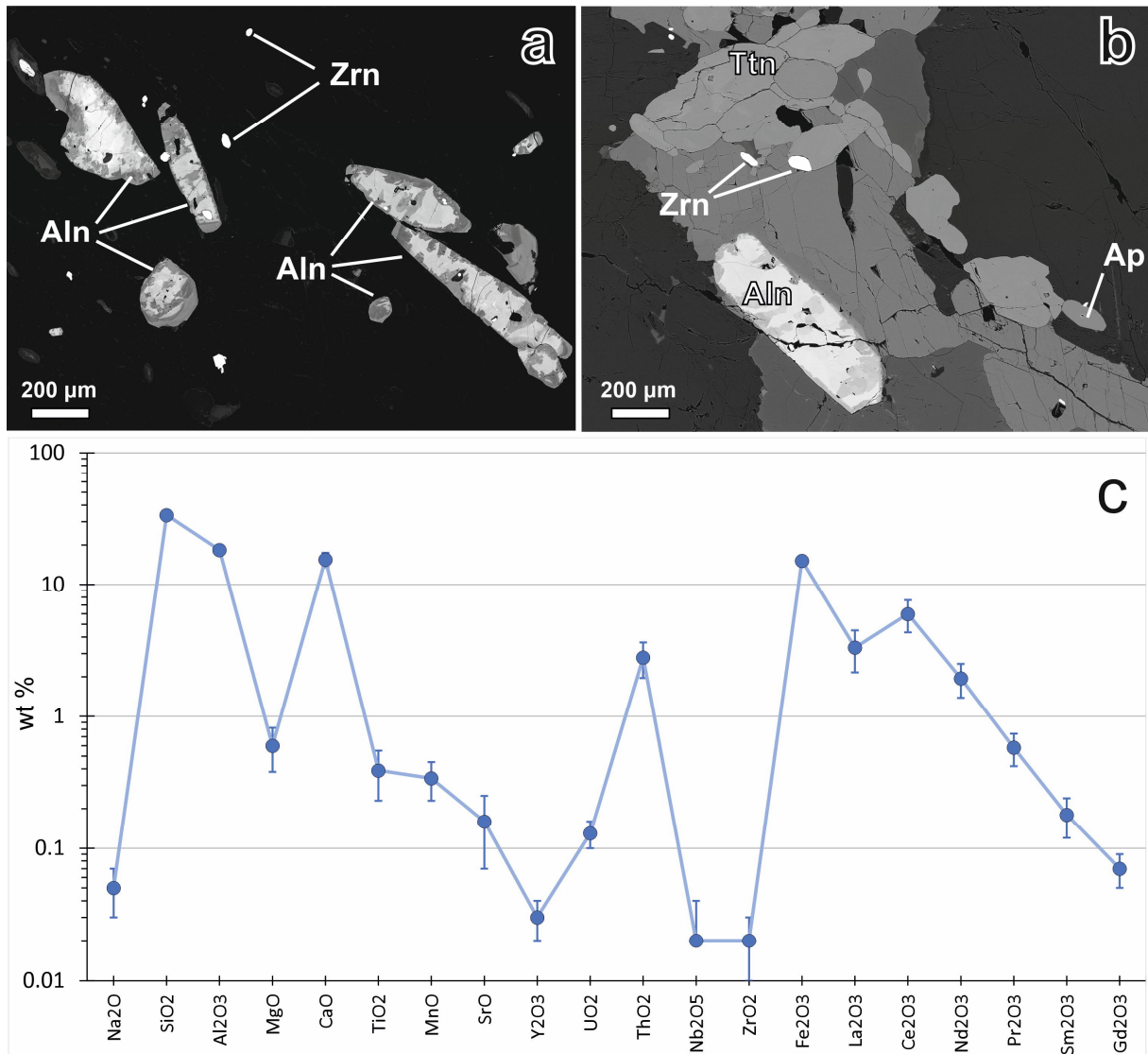
Figure 5.9 (a &b) Back-scattered electron microscope images of allanites showing zonation along with other accessory minerals in syenite (HSH-5) from Kande pluton of Karakoram batholith (c) EPMA point analysis of allanites (n=54) showing mean chemical composition. Abbreviations: Aln—Allanite, Ap—Apatite, Hbl—Hornblende, Pl—Plagioclase, Ttn—Titanite, Zrn—Zircon.

Table 5.2 Petrophysical properties samples at laboratory conditions.

Sample ID	Lithology	WA	φ	ρ_m	ρ_b	λ	α	c_p	c_{vol}
Nanga Parbat Massif									
TTP-3	Gneiss	0.62	1.7	2.75	2.70	2.65	1.14	749.6	2023.92
TTP-5	Gneiss	0.38	1.0	2.70	2.67	2.78	1.07	752.7	2009.71
AST-4	Gneiss	0.50	1.3	2.69	2.66	1.78	0.77	755.2	2008.83
AST-6	Gneiss	0.39	1.0	2.67	2.64	1.98	1.08	750.3	1980.79
AST-8ii	Gneiss	0.47	1.2	2.65	2.62	2.72	1.38	748.7	1961.59
AST-16	Gneiss	0.52	1.4	2.69	2.65	2.03	1.18	750.9	1989.89
RK-9	Gneiss	0.53	1.4	2.70	2.66	1.99	0.89	746.9	1986.75
NP-6	Gneiss	0.47	1.3	2.71	2.67	2.17	0.95	748	1997.16
NP-8	Gneiss	0.36	0.9	2.64	2.62	2.20	1.12	752.3	1971.03
NP-12	Gneiss	0.55	1.4	2.65	2.62	2.12	1.16	758.5	2070.71
TAR-1	Gneiss	0.51	1.4	2.72	2.68	1.93	0.87	755.6	2025.01
RK-4ii	Granite	0.60	1.5	2.64	2.59	3.37	1.95	754.5	1954.16
FM-4	Granite	0.87	2.2	2.64	2.58	1.86	1.09	749.3	1933.19
NP-2	Calcsilicate	0.34	1.0	3.03	3.00	2.73	1.19	751.3	2253.90
Average (± SD)		**0.51** **(± 0.13)**	**1.3** **(± 0.3)**	**2.71** **(± 0.10)**	**2.67** **(± 0.10)**	**2.31** **(± 0.45)**	**1.13** **(± 0.27)**	**751.70** **(± 3.18)**	**2011.90** **(± 74.83)**
Kohistan-Ladakh Batholith									
CG-1	Granite	0.56	1.5	2.66	2.62	2.30	1.08	752.8	1972.34
CG-2	Granite	0.46	1.2	2.65	2.62	2.00	1.00	748.3	1960.55
GB-1	Granite	0.56	1.5	2.71	2.67	2.17	0.88	755.7	2016.20
KPL-2	Granite	0.57	1.5	2.69	2.65	2.42	1.43	744.3	1972.40
GRT-1	Tonalite	0.33	0.9	2.72	2.69	2.39	1.14	755.2	2054.14
DR-1	Dacite	0.23	0.6	2.79	2.77	2.13	1.00	760.4	2106.31
JT-2	Granodiorite	0.61	1.6	2.71	2.66	2.03	0.79	758.5	2032.78
KOH-4	Meta-gd	0.26	0.7	2.76	2.74	2.91	1.18	753.3	2064.04
Average (± SD)		**0.45** **(± 0.14)**	**1.2** **(± 0.4)**	**2.71** **(± 0.04)**	**2.68** **(± 0.05)**	**2.29** **(± 0.27)**	**1.06** **(± 0.18)**	**753.56** **(± 4.91)**	**2022.34** **(± 48.43)**
Karakoram Batholith									
SGH-2	Gneiss	0.39	1.0	2.69	2.66	2.14	0.79	746.4	1985.42
SGH-4	Gneiss	0.46	1.2	2.70	2.66	2.39	1.23	758.4	2017.34
SGH-6	Gneiss	0.47	1.3	2.71	2.68	1.97	1.01	748.1	2004.91
KB-1	Granite	0.33	0.9	2.64	2.62	2.31	1.31	743.3	1945.69
KB-6	Granite	0.58	1.5	2.66	2.62	2.44	1.13	764.7	2000.41
KDS-1	Granite	0.52	1.3	2.66	2.63	2.11	1.05	755.7	1987.49
SGH-9	Syenite	0.54	1.4	2.66	2.62	1.66	0.75	764.3	2002.47
HSH-5	Syenite	0.77	2.0	2.69	2.64	1.48	0.68	747.8	1974.19
HSH-2	Q-monzonite	0.81	2.1	2.69	2.64	1.71	0.76	751.3	1983.43
KB-4ii	Diorite	1.31	3.5	2.78	2.68	1.52	0.77	767.1	2055.83
Average (± SD)		**0.62** **(± 0.27)**	**1.6** **(± 0.7)**	**2.69** **(± 0.04)**	**2.65** **(± 0.02)**	**1.97** **(± 0.34)**	**0.95** **(± 0.21)**	**754.71** **(± 8.14)**	**1995.72** **(± 27.43)**

Abbreviations: WA = water absorption (wt%), ρ_m = matrix density (g cm^{-3}), ρ_b = bulk density (g cm^{-3}), φ = porosity (%), λ = thermal conductivity (W m^{-1} K^{-1}), α = thermal diffusivity (10^{-6} m^2 s^{-1}), c_p = specific heat capacity (J kg^{-1} K^{-1}), c_{vol} = volumetric heat capacity (KJ m^{-3} K^{-1})
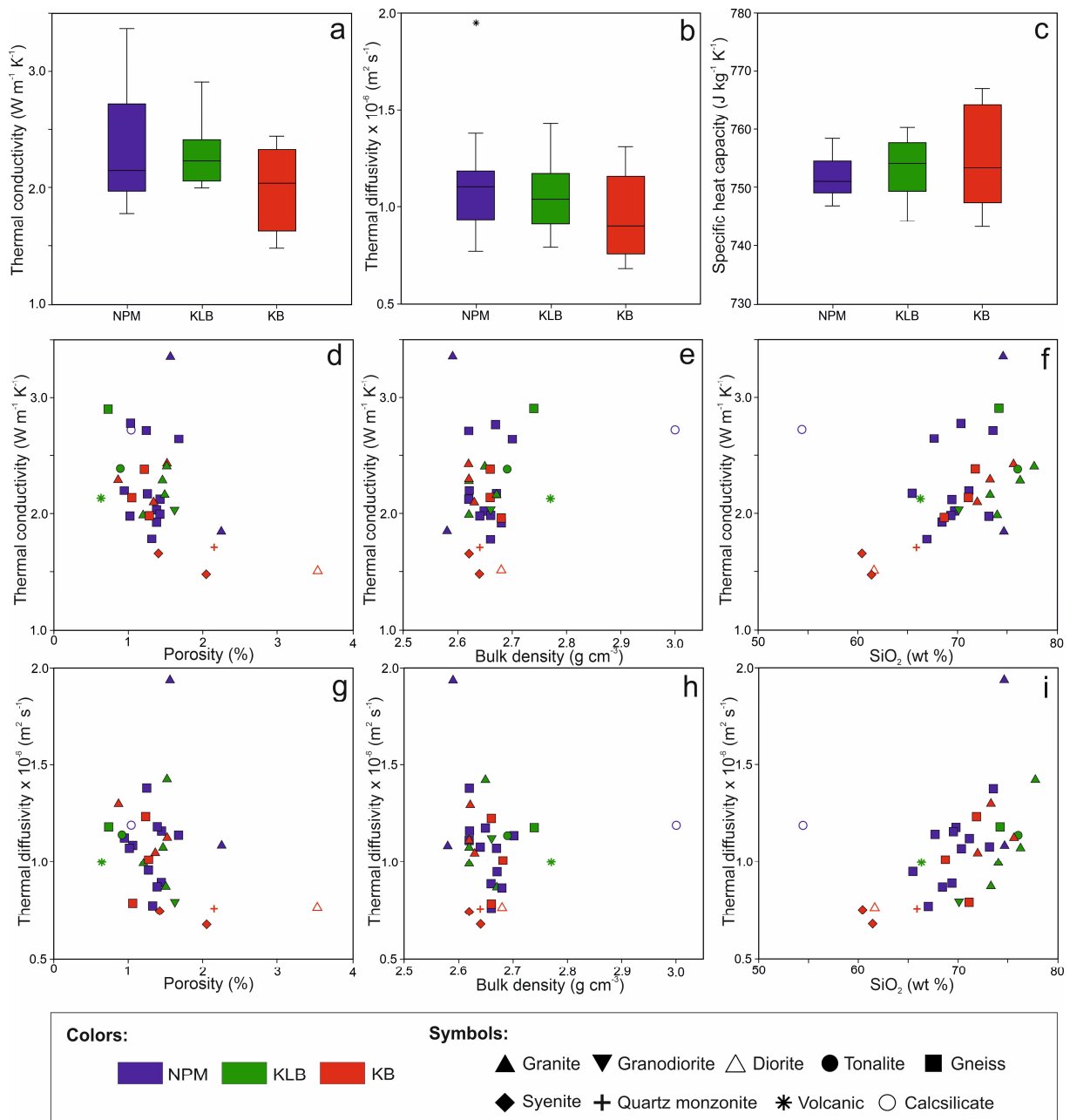
Figure 5.10 Box plots showing ranges of thermal conductivity, thermal diffusivity and specific heat capacity in Nanga Parbat Massif, Kohistan-Ladakh Batholith, and Karakoram Batholith. Scatter plots showing the relationship of thermal conductivity (d-f) and thermal diffusivity (g-i) with porosity, bulk density, and silica concentration.

5.4 Discussion

5.4.1 Petrogenesis, geochemical evolution and hydrothermal alteration

The petrogenesis of the NPM, KLB, and KB are well established, with the NPM belonging to a metamorphosed part of the Proterozoic Indian basement and sedimentary cover (Whittington et al., 2000). The KLB formed as a late granitoid intrusive during the Cretaceous with an intra-oceanic island arc during the closing of the Tethyan Ocean (Jagoutz & Schmidt, 2012). The KB formed like an Andean-type margin due to magmatism (pre-Himalayan phase: Jurassic to Cretaceous) caused by subducting oceanic crust under the continental plate (Rex et al., 1988; Crawford & Searle, 1992). Bulk chemical analysis in this study indicates a granitic affinity of most rocks, mostly I-type calc-alkaline orthogneiss with alkaline S-type granites in the NPM and I-type calc-alkaline to calcic in KLB. The KB shows the most heterogeneity, with the eastern parts comprising younger post-collision S-type alkaline rocks (Hemasil and Kande plutons) and the western parts comprising older pre-collision I-type calc-alkaline rocks (Hunza pluton).

The enrichment of the LREE in gneiss and depletion in granite from the NPM and KB (Fig. 5.7) indicates partial melting in which immobile LREE remained behind in the protolith (Rollinson, 2014). In contrast, the syenites of the KB show enrichment in both LREE and HREE, suggesting a different magmatic process (Searle & Hacker, 2019). The granites show negative Ba, Sr, and Eu anomalies, commonly induced by fractional crystallization in plagioclase and K-feldspar (Miller & Mittlefehldt, 1984; Wu et al., 2020). Granites from the NPM show higher depletion in Eu than those from the KLB and KB, indicating higher fractionation rates (Koljonen & Rosenberg, 1974). The petrographical observations also show zoned plagioclase in the younger granites, suggesting compositional variations within the magma during crystallization (Fig. 5.3i). Additionally, high Rb/Sr and their negative correlation with Sr and Ba in the granites from the KB and NPM (along with some migmatitic gneisses) indicate muscovite breakdown during dehydration melting along with fractionation of feldspars (Harris et al., 1995; Weinberg & Hasalová, 2015).

The alteration grade positively correlates to the loss on ignition (LOI) and can be used to characterize granite alteration (Klee et al., 2021). The petrographic observations demonstrated varying sericitization (white mica) of plagioclase and chloritization of biotite, which correlates with high LOI values in samples with moderate and strong alteration, inferring the interaction of thermal fluids with the surrounding rock (see Appendix 2). In the NPM, biotite in gneisses shows weak to moderate replacement by chlorite along with similar alteration of plagioclase by sericite. Additionally, the deformed samples show stronger alteration and signs of oxidation

of Fe-minerals in hand specimens and thin sections. Pyroxene in calc-silicate rocks shows alteration into hornblende with partial replacement by epidote, which points to a crystallization temperature around 220°C (Traineau et al., 1991), suggesting a higher temperature (pyropyllitic) alteration. Pegmatites and granites show weak to moderate alteration, suggesting the interaction with late magmatic fluid after crystallization. Calcite, while mainly observed in intergranular spaces and veinlets, was also sometimes found to be replacing plagioclase cores due to Ca release ("filled plagioclase"). K-feldspars show only weak alteration in gneiss along fracture zones, suggesting low temperature (argillic) alteration (130 to 220°C) due to fluid circulation in these permeable zones (Fulignati, 2020). K-feldspar in granites and pegmatite commonly show slight alteration. Granodiorite, diorite and monzodiorite from the KLB show moderate to strong alteration forming biotite and plagioclase. Epidote is found in diorite as an alteration product of amphibole, probably indicating metasomatic reactions with late magmatic fluids (Shcherbakova et al., 2021). Similarly, syenite from the KB also contains epidote and amphibole, suggesting a similar process. Additionally, calcite both within plagioclase and filling intergranular spaces indicates low-temperature (~150°C) interaction with CO_2-rich fluid (Morad et al., 2010; Leichmann et al., 2003).

The NPM formed during late-stage orogenic activity and the geomorphological response to the interaction between fluvial erosion and decompression melting, causing fast exhumation (Guevara et al., 2022; Butler, 2019; Whitney et al., 2004). The rocks of the NPM are genetically identical to those from the lesser Himalayas but are metamorphosed to upper amphibolite facies with intense deformation and younger intrusions (Whittington et al., 1999). The gneiss commonly contains biotite, K-feldspar, plagioclase, and quartz, which show weak to moderate alteration. Alteration increases in intensely deformed zones, suggesting interaction with hydrothermal fluids. In granites, tourmaline and fluorite suggest a late-stage interaction of available B, Cl, and F in the system (Laurs et al., 1998). The boiling geysers formed due to the deep infiltration of meteoric waters through fractures and the interaction with young solidified, dry, but still hot granitic intrusions in the subsurface (Chamberlain et al., 2002). With the uplift and evolution of the massif, fluid pathways might have shifted over time, as indicated by several inactive alteration zones.

5.4.2   Radiogenic characteristics of Granitoids

The granitoids and gneisses of the NPM and KB contain significantly high concentrations of U and Th, which are incorporated in accessory minerals such as zircon, monazite, allanite, rutile, titanite, and apatite (see Appendix 2). Scatter plots of U and Th with different trace and major elements are used to understand their host minerals and behavior during rock evolution. The

correlation of U vs. SiO_2 and K_2O indicates that granites of the NPM and KB contain high U concentrations, which is not the case with the KLB granites despite similar SiO_2 and K_2O contents. In a continent-continent collision setting, the magmatic processes show a high degree of fractionation, resulting in igneous rocks with high concentrations of SiO_2 and incompatible elements (such as U and Th; Slagstad, 2008). In addition, positive correlations of U with Rb and Rb with K_2O indicate that U and Rb, being incompatible elements, upon partial melting, become enriched in the K-rich melt (Singh et al., 2023); thus, the granites formed by partial melting also contain high concentrations of these elements.

The high U and low Th concentrations in granite suggest the mobilization of U during melt generation, while Th is retained in the protolith (Scott et al., 1992). In contrast, the gneiss of the NPM shows an overall positive correlation, suggesting negligible mobilization of radioelements. Positive correlations in Th vs. TiO_2, P_2O_5, Ce, and La plots indicate monazite, titanite, apatite, rutile, and allanite as accessory phases containing Th (Bea, 1996). The high concentrations of Th (75 – 127 ppm) and REE in syenite and granite from the Kande pluton from the KB correlate positively with Ce and La, which can be explained by the presence of allanite (Fig. 5.4 & 5.8). In EPMA, point analysis confirmed allanite containing a significant concentration of Th and other REEs (Fig. 5.9).

5.4.3 Petrophysical Characteristics

The complex and highly variable geological settings are also reflected in the thermophysical parameters obtained from outcrop analogs in the study area. Mineralogical similarities often lead to lithology-specific clusters in the data plots, while secondary processes caused by metamorphism, deformation, and alteration typically lead to high variability in the thermophysical properties (Julia et al., 2014; Navelot et al., 2018; Weydt et al., 2022b). A broad negative correlation between porosity vs. thermal conductivity and diffusivity suggests that higher porosity decreases thermal conductivity and diffusivity. A general decrease in thermal conductivity with increasing matrix porosity was also observed by Weinert et al. (2021), where thermal conductivity varied by more than 1 W m^{-1} K^{-1} depending on the porosity (< 1% up to 9% in granitic rocks from the Mid-German crystalline high). Likewise, Weydt et al. (2022a) reported an average reduction of thermal conductivity of ~0.5 W m^{-1} K^{-1} in altered granitoids close to (metamorphic) contact zones with increasing porosity (~9%) compared to fresh/weakly altered samples (1.8 %). Similar trends were observed by Géraud et al. (2010), Stanék (2013), and Weydt et al. (2022a), who reported increased matrix porosities associated with alteration and fracturing. For example, Stanék (2013) reported 1-2% and 2- 3.5% porosity increases due to clay and chlorite-dominated alteration, respectively. Géraud et al. (2010) examined granitic

core samples (Upper Rhine Graben, Germany) affected by hydrothermal alteration (illite-hematite, hematite, and hematite-chlorite dominated alteration), which showed porosities in the range of ~2 to 13%, while the pristine rocks showed porosities of less than 1%.

Thermal conductivity and diffusivity show a positive correlation with SiO_2. Quartz has a comparatively high thermal conductivity of ~7.7 W m^{-1} K^{-1} (Clauser & Huenges, 1995); therefore, the samples with higher SiO_2 content show higher thermal conductivities (Goes et al., 2020). Similarly, the syenite from the KB shows low thermal conductivity and diffusivity due to their low SiO_2 (60-62 wt %). Besides quartz, secondary (alteration) minerals such as calcite (~3.6 W m^{-1} K^{-1}), hematite (~11.3 W m^{-1} K^{-1}), epidote (~2.5-3.1 W m^{-1} K^{-1}), and chlorite (~3.1-5.3 W m^{-1} K^{-1}) with higher thermal conductivities can enhance the bulk thermal conductivity of a rock (Clauser & Huenges, 1995; and reference therein). The higher thermal conductivity (2.73 W m^{-1} K^{-1}) in calc-silicate is attributed to high CaO (19.12 wt%) and MgO (5.39 wt%) due to the presence of calcite ($CaCO_3$) and diopside ($MgCaSi_2O_6$). Higher thermal conductivities (2.78 & 2.74 W m^{-1} K^{-1}, respectively) in biotite gneiss (TTP-5) of the NPM and meta-granodiorite of the KLB (KOH-4) compared to granites can be associated with chlorite and epidote, respectively (Fig. 5.10). However, further detailed studies are needed to draw definitive conclusions about the relationship between porosity and thermal conductivity and the influence of alteration on the rock properties.

5.4.4   Conceptual model and implications for geothermal exploration

The spatial distribution of hot springs in the study area implies structural and geological controls on the overall geothermal heat flow. Figure 5.11 shows a generalized conceptual model of the study area, which considers the background geothermal heat flow on a lithospheric scale and the near-surface hot springs controlled by local and regional structures. Subduction of the Indian lithosphere under the Kohistan Island Arc and Karakoram Block (of the Asian Plate) since Eocene times initiated the thickening of the crust, which presently ranges between 70 to 80 km (Kumar et al., 2019). This thick and radiogenically fertile continental crust may undergo initial melting (Bea, 2012) and form low-velocity zones in the mid to lower crust (Shah et al., 2018; Meltzer et al., 2001), which upon exhumation to the surface as migmatic gneisses may evolve to leucogranite and pegmatite (Crawford & Windley, 1990). Additionally, the lithospheric slab break-off from the Indian lithosphere caused asthenospheric upwelling, resulting in deep fluid flow, which initiated voluminous alkaline magmatism in Karakoram (ca. 4000 km^2 Baltoro batholith and Hemasil syenite) during the Miocene (Awais et al., 2022; Searle et al., 1992). The high uplift rates at Nanga Parbat and Karakoram exhumed the radiogenically enriched basement gneiss to the near-surface and caused isothermal upwelling (Craw et al.,

1994; Crowley et al., 2009; Schärer et al., 1990). A high geothermal background heat flow of > 100 mWm-2 is estimated from the radiogenically thick upper crust (Chapter 6), which would further increase when rapidly exhuming Nanga Parbat and Miocene magmatism in Karakoram batholith are considered.

Regarding the geothermal background, the fault systems and high topographic relief (ranging between 1000 to 8000 m) control the meteoric fluid flow by providing permeable zones for local precipitation to infiltrate several kilometers deep from the topographically elevated regions (located mostly in the NPM and KB). This deep percolation with longer residence time (Ahmad et al., 2002) resulted in more intense fluid-rock interaction and heat transfer from hot rocks to the fluid, which was heated up to boiling temperatures. These deep geothermal fluids, driven by hydraulic head, ascend to the surface (discharging into valleys) along fault zones and associated fractures (Fig. 5.11). These thermal fluids altered susceptible minerals in gneiss and granite (notably plagioclase and biotite) and further enhanced the fracture-related porosity.

The granitoids enriched with radioelements show a dry hot-rock potential similar to the Cornwall granite in the UK (Beamish & Busby, 2016), where reservoir temperatures of 180 °C were encountered at 5 km depth (Reinecker et al., 2021). The exhumation rates of > 2 mm/year are typical at the NPM and KB (Zeitler et al., 2001; Korinkova et al., 2014), which in the extreme case of Nanga Parbat may increase the geothermal gradient up to 100 °C/km (?) (Craw et al., 1994). Such reservoirs with natural fracture systems potentially offer high temperatures at depths of ~2-3 km and are sufficient to sustain electric power production (Jiang et al., 2023). Due to decreasing fracture-dominated permeability away from fault zones and with increasing depth, these reservoirs could be engineered in order to induce the permeability or be installed with advanced closed-loop heat exchangers for better heat recovery and less risk of induced seismicity (Budiono et al., 2022).

The investigation of outcrop analogs has provided basic parameters for a better understanding and modeling. The reconnaissance nature of the present study constrained the coverage of all units. However, it provided a representative overview of the geothermal regime and heterogeneity of geochemical and petrophysical characteristics of granitoids and gneisses. Detailed and site-specific investigations are necessary to assess geothermal potential for exploitation. While the hot spring sites are relatively straightforward for direct-use applications (Lund & Toth, 2021), additional parameters such as output enthalpy, flow rate, seasonal variation, and fluid chemistry are necessary for the assessment of future geothermal energy development (Barbier, 2002; Moeck, 2014). Moreover, geophysical surveys (e.g., electrical resistivity, gravity, and magnetic) and local stress fields would provide more information

required for subsurface reservoir volume estimation, numerical simulation, and economic evaluation (Ciriaco et al., 2020; Kana et al., 2015; Kruszewski et al., 2021).

5.5 Conclusions

This study presents the first dataset of petrographic, geochemical, and petrophysical rock properties of mainly granitoids and gneisses of the western Himalayan orogenic belt. Polarized and CL microscopic observations were used to characterize mineralogy, alteration intensity, and affected minerals. Whole rock geochemical analysis was used for chemical classification and to assert the changes in trace elements (in response to orogenic evolution) and their relationship with alteration and petrophysical properties. The granitoids and gneisses show weak to moderate alteration of biotite, K-feldspar, and plagioclase, which increases towards intensely deformed zones.

Geochemical results indicate that the gneiss and granites of the NPM are mostly peraluminous alkaline S-type, enriched in REEs and radioactive elements, indicating partial melting and high fractionation. The granitoids of the KB, due to their different magmatic histories, are more diverse, ranging from syenite to granite, I-type to S-type, and alkaline to calc-alkaline in composition. They also show an overall enrichment in REEs and radiogenic elements, which, in the case of syenite, are primarily present in allanite. The KLB granitoids are calc-alkaline I-type and show depletion of REEs and radiogenic elements. Petrophysical measurements reveal low matrix porosities (0.64–3.52%), with primarily average thermal conductivities (1.48 – 3.37 W m^{-1} K^{-1}) and thermal diffusivities (0.68–1.95 10^{-6} m^2 s^{-1}), with slight variation in specific heat capacities (744 – 767 J kg^{-1} K^{-1}). The NPM displays higher average thermal conductivity, thermal diffusivity, and lower porosity than the KB, while the KLB falls between these two.
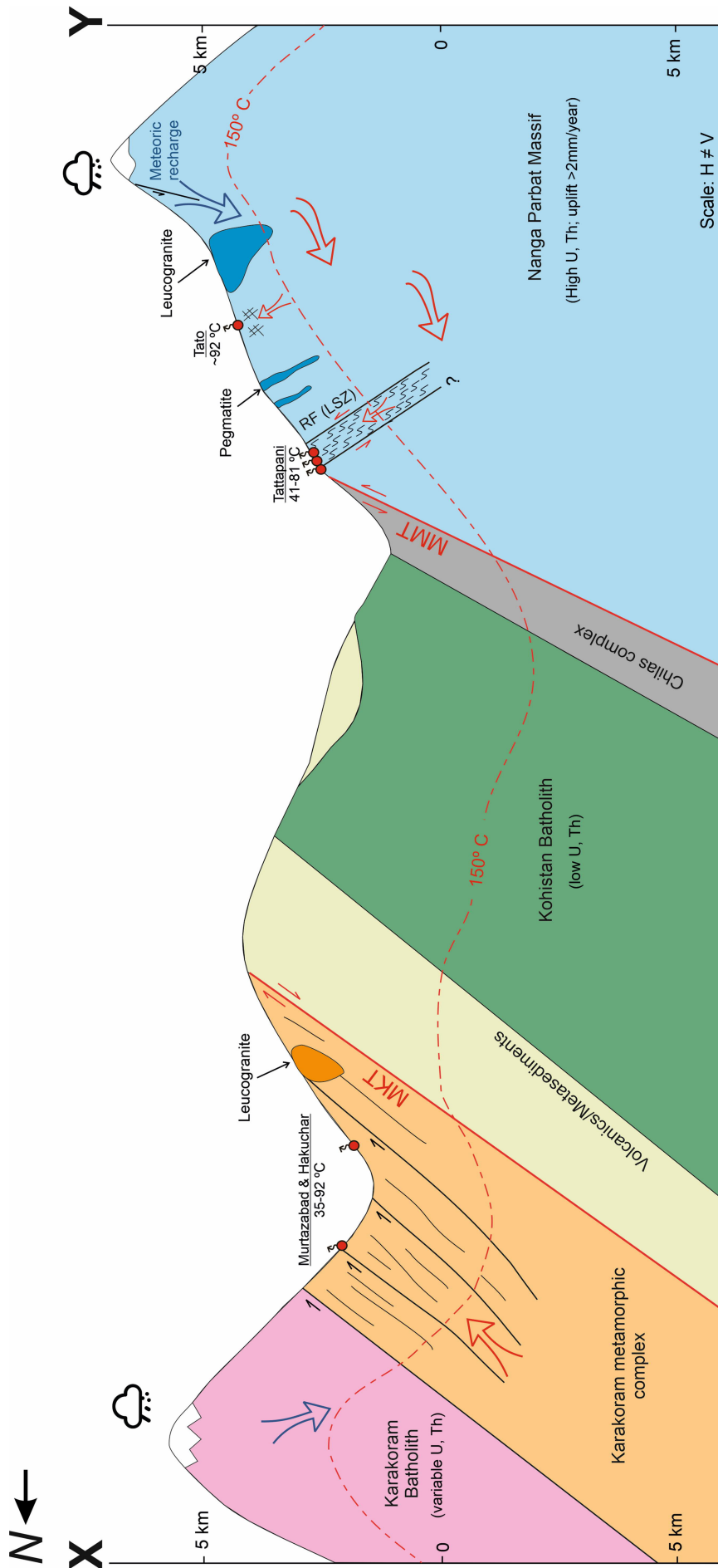
Figure 5.11: Conceptual model (horizontally not to scale) for XY line on Fig.5.1 showing the subsurface fluid pathways of hot springs of Raikot and Hunza valleys. The shape of the isotherm depicts the effects of radiogenic heat production, exhumation, and topography. Blue arrows represent the percolation of meteoric water, which gets heated in the subsurface before discharging as hot springs (red arrows). Abbreviations: MKT—Main Karakoram thrust; MMT—Main Mantle thrust; RF (LSZ)—Raikot Fault (Liachar shear zone).

The proposed conceptual model considers the batholith granitoids and gneissic complexes as potential reservoirs and establishes the basic parameters for understanding and developing future geothermal modeling. Variable alteration intensity in plagioclase and biotite shows fluid circulation within these rocks, weakening them and allowing new fluids to circulate. Water from glaciers and snow in high-altitude regions percolates several kilometers deep due to high relief and fractures created along the fault/sutures. High concentrations of radiogenic elements within these rocks and high rock uplift rates also increase the geothermal gradient by heat production and advection. The fluids following permeable fracture zones in these thermally conductive rocks are heated to boiling temperatures and may discharge as geysers and fumaroles along river and stream banks. These hot fluids interact with the host rocks and cause alteration, which increases their porosity.

Due to the reconnaissance scope of the study, the focus was on a regional perspective, and the results were synthesized to evaluate the geothermal parameters broadly. Moreover, these analog samples differ from in-situ reservoir conditions regarding temperature, pressure, and fluid properties. Nonetheless, they provide vital information for a large-scale regional model that can be used for overall characterization and numerical modeling. The information presented here provides a basis for developing local reservoir models, which focus on estimating fault/fracture zone properties and the feedback effect of hydrothermal fluids on the host rocks via alteration-induced porosity increase compared to unaltered rocks.

Chapter 6: Geothermal implications of the thermal structure of lithosphere in northern Pakistan

A journal publication of this chapter is planned in the near-future with some modifications.

6.1 Introduction

Shallow regions of high heat flow are primarily associated with active volcanism concentrated along plate boundaries and represent conventional geothermal resources (Stober & Bucher, 2021). Recently, areas of exposed crystalline basement have started receiving the attention of the geothermal community as unconventional geothermal resources (Genter et al., 2010; Ledésert et al., 2022; Rosberg & Erlström, 2021). Crystalline rocks such as gneiss and granite usually possess high concentrations of radiogenic elements and high heat production, which enhances their surface heat flow, thus making them a potential target as hot-dry rock geothermal resources (Hills et al., 2004; Moska et al., 2023; Stober & Bucher, 2021). In HDR systems, the temperatures can rise to as much as 240°C at a depth of 3.5 km for high heat-producing granitic basement ($3.8 - 8.7$ µWm^{-3}) in the case of Cooper Basin in Australia (Beardsmore, 2005; Hillis et al., 2004; Meixner et al., 2012). Crystalline basement and granitic intrusions typically form the cores of orogenic belts. The larger volume and greater accessibility of these rocks at the surface, coupled with the overall orogenic heat flow in these settings, make them viable targets for geothermal exploration (Gnojek et al., 2018; McCay & Younger, 2017; Wanner et al., 2019).

The Himalaya-Karakoram orogen lacks surface heat flow data, hindering understanding of subsurface geothermal gradients. Additionally, it also needs a comprehensive study on the thermal state of the lithosphere to constrain background heat flow, which has to be coupled with radiogenic heat flow. Although high heat flow (> 100 mWm^{-2}) is estimated from geothermal fields to the east of this region (Craig et al., 2013; Shanker, 1988), they might not be representative of background heat flow due to advective heat transport in these hydrothermal dominated systems. Information about the structure and physical properties of a lithosphere is crucial for developing a thermal model (Goes et al., 2020). However, even without accurate geophysical data and reliable thermophysical parameters, thermal modeling with varying parameters can be employed to obtain broad estimates of lithospheric thermal structure.

This chapter focuses on the estimation of the thermal state of the lithosphere in Himalaya, Kohistan, and Karakoram using 1D and 2D thermal models. The modeling includes the surface radiogenic heat production data and literature-based geophysical and thermal parameters for

a preliminary model. The impact of variable radiogenic heat production in the crustal layer and their respective thickness in the complex tectonic settings of the study area are investigated. Additionally, the effect of exhumation on the crustal geotherms and surface heat flow is tested. Based on the 1D model and petrophysical parameters from this work (in Chapter 5), a pseudo-2D thermal model is produced along a cross-section line to show the configuration of isotherms in the top 10 km of the upper crust and its geothermal implications.

6.2   Lithospheric and crustal structure

The present-day lithospheric structure in the study area is the result of subduction and suturing of different continental terrains during the India-Eurasia convergence and collision. Subsequent crustal thickening during the Himalayan orogeny was to a large degree achieved by the internal shortening of the Indian Plate and its underthrusting under Kohistan and Karakoram. The Moho depth, which is 30 – 40 km in the Indian Shield (Acton et al., 2010), increases to 50 – 60 km beneath the Himalayan front and reaches 70 to 80 km under the mountain range (Rai et al., 2006; Hazarika et al., 2014; Priestley et al., 2019). The leading edge of the Indian Plate is estimated to have subducted to more than 90 km depth under Kohistan and Ladakh (Kufner et al., 2016). Precise constraints on the depth and structure of the lithosphere-asthenosphere boundary are not available, except for variable 150 – 250 km estimates (Li & Mashele, 2009; Kumar et al., 2022; Jadoon et al., 2021). Kind & Yuan (2010) and Zhao et al. (2010) have suggested that the Indian lithospheric mantle does not follow the surface trace of major suture zones and probably decouples from the crust due to the wedging in of Asian lithospheric mantle.

Bhukta et al. (2006) and Guerra et al. (1983) have subdivided the Himalayan crystalline crust in northern Pakistan into four layers based on P-wave velocities. The base of the Himalayan orogen is upper to mid-crustal metamorphic rocks corresponding to the mid-Archean to neo-Proterozoic shields of Indian cratonic blocks, which are underlain by the granulitic lower crust (Grujic et al., 2011; Warren et al., 2011). The crustal structure of the Kohistan arc terrane is tilted to the north due to the India-Eurasia collision with upper crustal granitoids and volcanics exposed in the north, and mid- to lower crust amphibolites and granulites in the south. The present thickness of Kohistan above the underthrusting Indian Plate is probably 10 to 25 km (Malinconico, 1986; Burg et al., 2006; Burg & Bouihol, 2019).
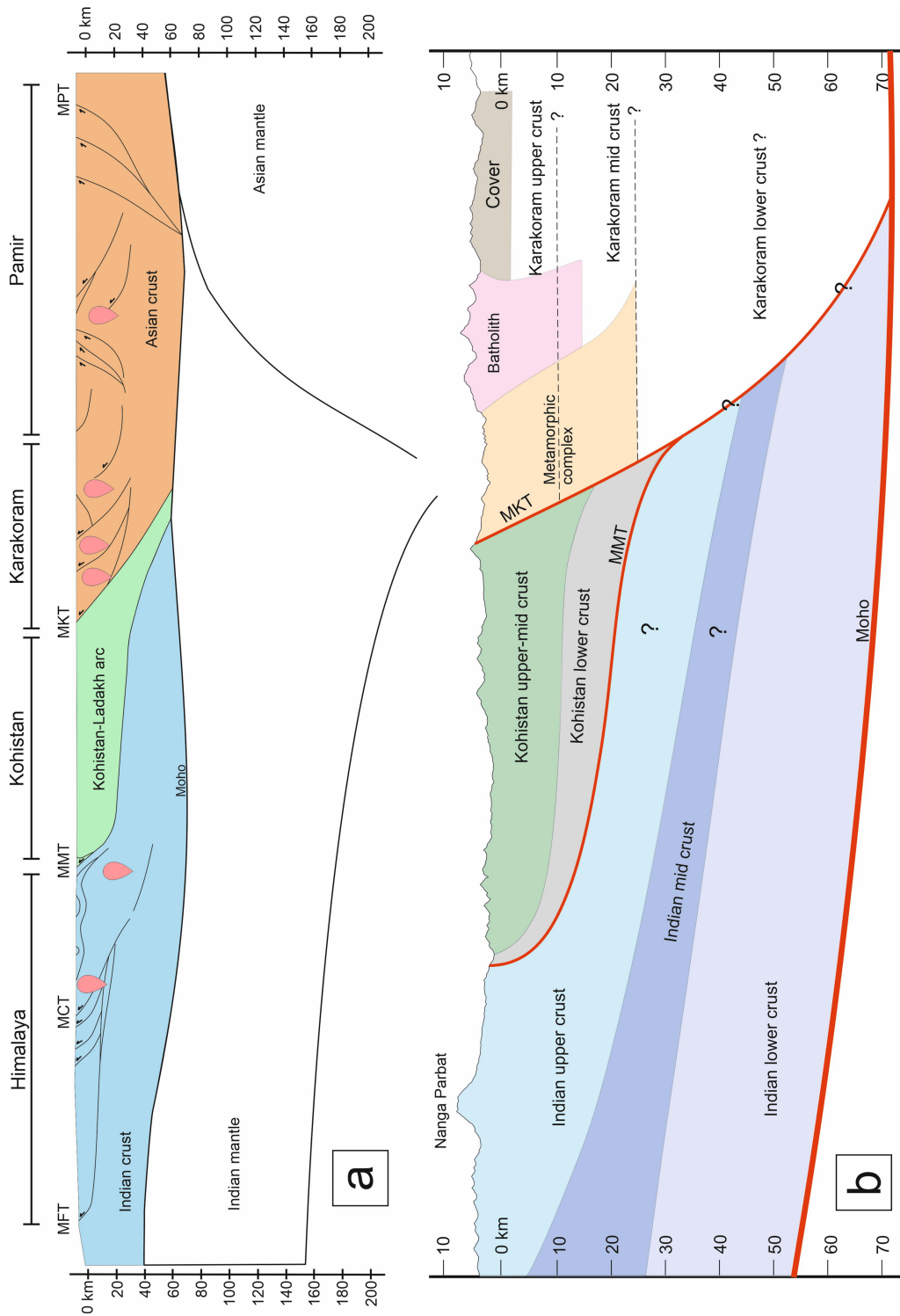
Figure 6.1 (a) Regional lithospheric structure of Himalaya, Karakoram, and Pamir orogenic belt (after Mechie et al., 2012). (b) Crustal scale N-S cross-section of Nanga Parbat Massif, Kohistan, and Southern Karakoram (modified after Searle et al., 2010). The structure of the crust is based on various cross-sections for literature (Bhukta et al., 2006; Burg et al., 2006; Searle et al., 1989; Burg & Bouihol, 2019). Abbreviations: MBT-Main Boundary Thrust; MCT-Main Central Thrust; MFT-Main Frontal Thrust; MKT-Main Karakoram Thrust; MMT-Main Mantle Thrust; MPT-Main Pamir Thrust.

Wittlinger et al. (2009) suggested the subduction of the Indian lower crust under the Asian plate as far north as Tibet and Pamir, which is corroborated by Kumar et al. (2022) and Zhao et al. (2010). In contrast to the Pamir, where the geometry of subducting Asian crust has been explained (Li et al., 2018; Schneider et al., 2019), the crustal structure due to the underthrusting of the Indian plate under the Karakoram and western Tibet remains to be resolved. According to Searle & Hacker 2019, the crust of the Karakoram comprises unradiogenic felsic and mafic granulitic lower crust and a radiogenically fertile gneissic middle crust. Priestley et al. (2008) also suggested cold and dry granulitic Indian crust under western Tibet. The fate of the upper and mid-Indian crust under the Karakoram is unclear, but it is believed to be left behind due to lateral material transfer, which forms the Himalayas (Razi et al., 2014).

6.3   1D steady-state conductive thermal model

6.3.1   Mathematical solution

A non-linear, steady state, one dimensional conductive heat transfer equation (after Hindle, 2023) is solved as;

$$(k(u)u')' = q \qquad\qquad [6.1]$$

where u is temperature, $k(u)$ is a temperature-dependent thermal conductivity, and q is radiogenic heat production. u, and q are both functions of depth.

Temperature-dependent thermal conductivity is modeled according to the suggestion of Jaupart et al. (2016). We also include a temperature-dependent radiative heat transfer component of thermal conductivity at temperatures >1000°K (Jaupart and Mareschal 2005). The equations describing temperature-dependent thermal conductivity and radiative heat transfer are;

$$k_u = 2.26 - \frac{618.251}{u} + k_o \cdot \left(\frac{355.576}{u} - 0.30247\right) \qquad\qquad [6.2]$$

$$k_r = 0.37e^{-9} \cdot u^3, u \geq 1000°K \qquad\qquad [6.3]$$

where k_o is the measured thermal conductivity of the rock under surface conditions, and k_r describes the effect of radiative heat transfer on thermal conductivity at high temperatures. Hence, for equation [6.1];

$$k(u) = k_u + k_r \qquad\qquad [6.4]$$

The equation is solved with Dirichlet boundary conditions of fixed temperatures at the top and base of the lithosphere. The model incorporates an arbitrary number of layers for which values of both k_o and q can be defined. To deal with abrupt changes in coefficients, a finite difference scheme of "half station" is used (Hindle and Besson, 2023 and references therein). A tri-diagonal matrix algorithm and a fixed-point iteration scheme is used to solve the non-linear problem.

6.3.2   Modelling scenarios and results

Effect of LAB depth

Previous studies have used Moho heat flow as a lower boundary condition to model crustal geotherms over parts of the Indian craton (Kumar et al., 2007; 2009). However, due to the thicker lithosphere and dynamic orogenic setting in the study area, the lithosphere-asthenosphere boundary (LAB) with 1300°C temperature is used as a bottom boundary condition. While the Moho is estimated to range between 60-70 km in the study area (Priestley et al., 2019), there is no consensus on the depth of LAB, with estimates ranging between 150 to 250 km (Li & Mashele, 2009; Kumar et al., 2022; Jadoon et al., 2021). The effect of this 100 km variation on the geotherms was tested with three models with LAB depths of 150, 200, and 250 km, respectively (Fig 6.2a). The geotherms increased with shallower LAB (150 km), but its effects on upper crustal temperatures and heat flow were negligible (Fig 6.2a). Therefore, LAB-2 with an intermediate depth of 200 km is selected for the rest of the models.

Effect of thickness of heat producing layer

There is a general agreement in the literature over a decreasing trend in heat production with depth (Jaupart et al. 2016 and references therein). However, the vertical and horizontal heterogeneity, especially in the upper crust, hinders putting stratigraphic control on the heat production distribution (Vilà et al., 2010). For the surface radiogenic heat production, multiple scenarios are assumed with variable thicknesses (5, 10, and 15 km) of a heat-producing layer (HPL) of 4 μWm^{-3} (as a weighted mean of NPM) to estimate crustal (mainly upper crustal) temperature ranges. The crust is assumed to consist of a 25 km thick upper crust (including HPL) and a 45 km thick lower crust. Standard heat production values of 0.02, 0.4, and 2 μWm^{-3} are taken for the mantle lithosphere, lower crust, and upper crust, respectively (Hasterok & Chapman, 2011). The temperature at the upper boundary is assumed to be 10ºC and 1300ºC

at the lower boundary (McKenzie et al., 2005). Temperature-dependent thermal conductivity and radiative heat transfer were also incorporated into the modeling (Jaupart et al., 2016; Jaupart & Mareschal, 2005). The effect of this non-linear thermal conductivity on the geotherms and the heat flow is shown in Appendix D.

Figure 6.2b shows that in the upper crust, a change of 10 km in the thickness of HPL significantly affects the geotherms in contrast to a 100 km change in lithospheric thickness. The calculated temperatures for the three HPL cases show variations ranging from 337 to 430°C at 10 km, further increasing between 578 to 686°C at 20 km. Similarly, the heat flow calculated at the surface is 84, 94, and 103 mW m−2 for HPL of 5, 10, and 15 km thick, respectively. This suggests that a thickened HPL significantly increases upper crustal temperature and surface heat flow.
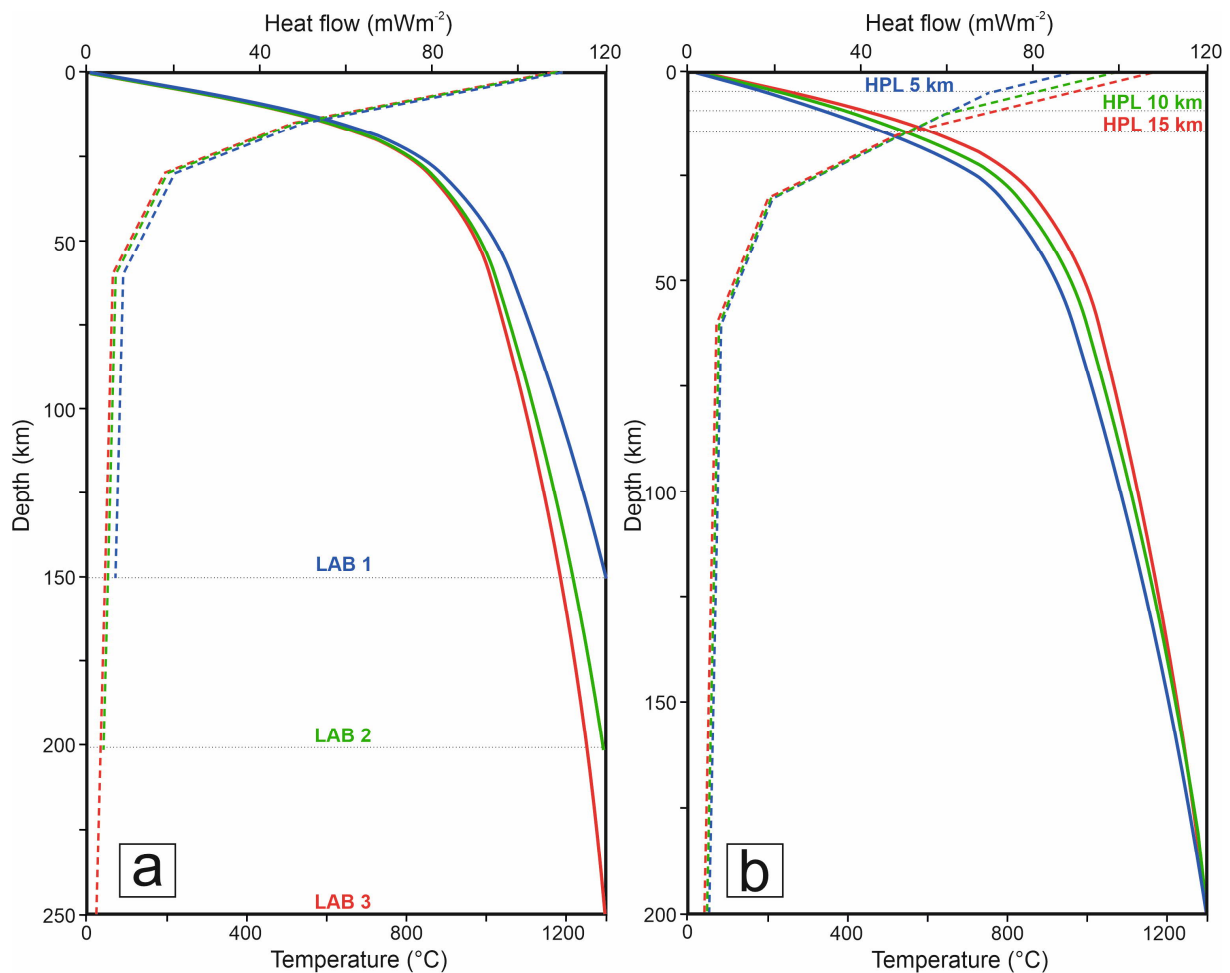
Figure 6.2 1D steady-state conductive geotherms showing the effect of thickness of lithospheric and heat-producing layer in the upper crust (a) The geotherms show variations in temperature and heat flow with varying lithospheric thickness from 150 to 250 km. (b) The geotherms show variations in temperature and heat flow with varying thicknesses of heat producing layer in the upper crust from 5 to 15 km.

Table 6.1 Parameters used for the steady-state conductive thermal model of Nanga Parbat Massif. Ind-1 and Ind-2, respectively, refer to high and low heat-producing crustal layers. BG refers to basement gneiss, which is present in the core of NPM and has high surface RHP.

	Crustal depth range (km)	Radiogenic heat production (μWm^{-3})	Thermal Conductivity ($Wm^{-1}K^{-1}$)
Model 1			
Upper crust (Ind-1)	0 - 20	4.0	2.3
Mid crust (Ind-2)	20 - 30	2.0	2.5
Lower crust	30 - 60	0.4	2.6
Model 2			
Upper crust (Ind-1)	0 - 15	4.0	2.3
Mid crust (Ind-2)	15 - 30	2.0	2.5
Lower crust	30 - 60	0.4	2.6
Model 3			
Upper crust (Ind-1)	0 - 10	4.0	2.3
Mid crust (Ind-2)	10 - 30	2.0	2.5
Lower crust	30 - 60	0.4	2.6
Model 4			
Upper crust (Ind-1)	0 - 5	4.0	2.3
Mid crust (Ind-2)	5 - 30	2.0	2.5
Lower crust	30 - 60	0.4	2.6
Model 5			
Upper crust (BG)	0 - 5	5.33	2.3
Mid crust (Ind-2)	5 - 30	2.0	2.5
Lower crust	30 - 60	0.4	2.6
Model 6			
Upper crust (BG)	0 - 10	5.33	2.3
Mid crust (Ind-2)	10 - 30	2.0	2.5
Lower crust	30 - 60	0.4	2.6
Model 7			
Upper crust (BG)	0 - 10	5.33	2.3
Mid crust (Ind-2)	10 - 30	1.0	2.5
Lower crust	30 - 60	0.4	2.6

The following sections present the results of various thermal models for the Nanga Parbat Massif, Kohistan and Karakoram.

Nanga Parbat Massif (NPM)

For the NPM with a 60 km thick upper crust, a 30 km lower crust of granulitic composition is assumed to have radiogenic heat production of 0.4 μWm^{-3} and thermal conductivity of 2.6 $Wm^{-1}K^{-1}$ (Roy & Mareschal, 2011). In Models 1 to 4, the thickness of the heat-producing upper crust with 4 μWm^{-3} is reduced from 20 km to 5 km, while the crust with 2 μWm^{-3} increases from 10 to 25 km (Table 6.1). Models 5 and 6 assume a highly enriched upper crust (5.33 μWm^{-3}) with thicknesses of 5 and 10 km, respectively. Model 7 assumes a 10 km thick enriched upper crust (5.33 μWm^{-3}) but a 20 km thick slightly depleted midcrust.

The results show that the temperature difference between modeled scenarios reaches 200°C at depths of 20 to 40 km, with the highest temperature for model 1 with 20 km thick upper crust

with 4 µWm^{-3} (Fig 6.3). Model 2-6 (with 2 µWm^{-3} mid crust) do not show considerable variation among them despite the change in thickness and magnitude of heat production of the upper crust. The surface heat flow values range between 100-120 mWm-2 for models 1, 2, and 6, while they are between 85-100 mWm-2 for models 2, 3, 4, and 7.
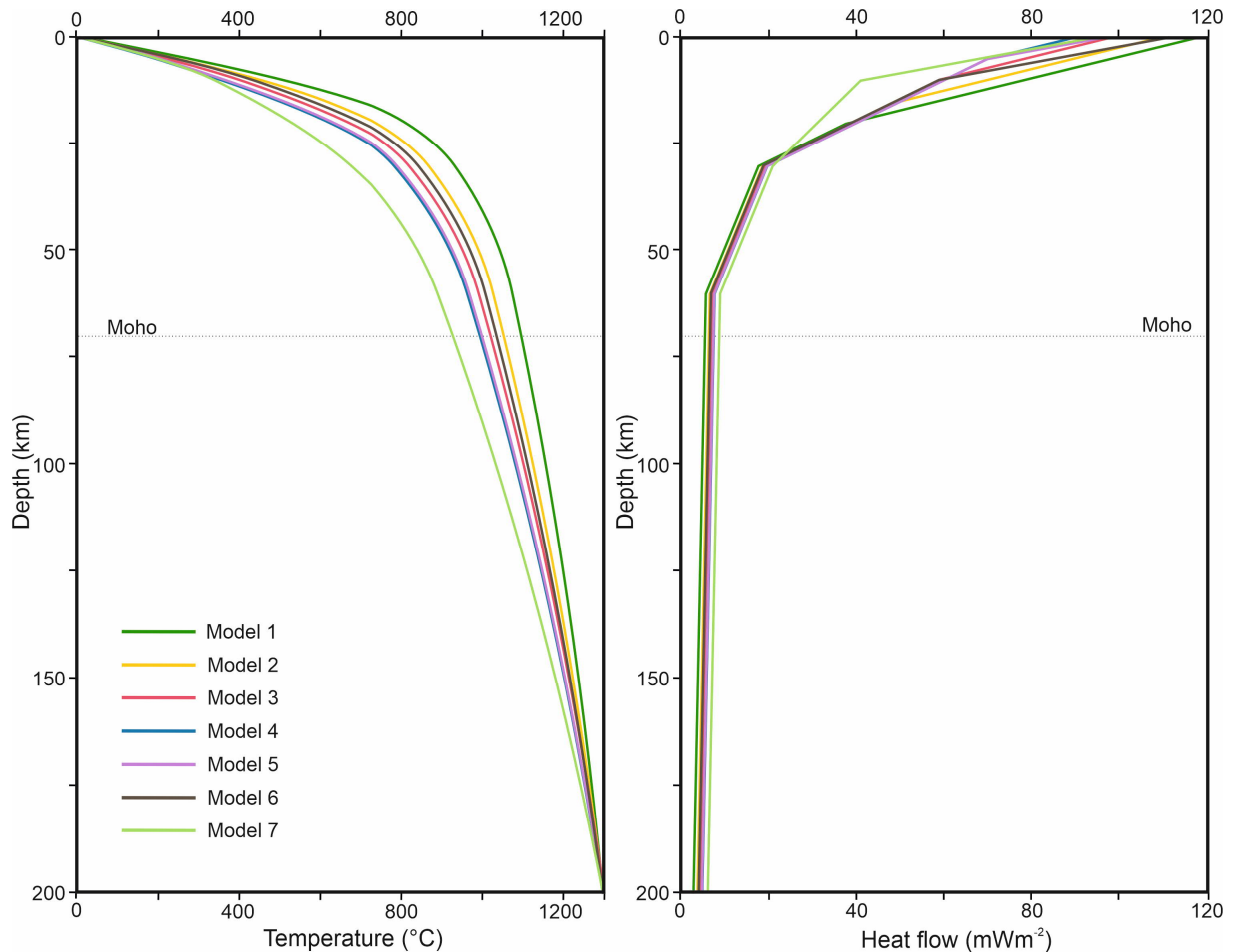
Figure 6.3 1D steady-state conductive geotherms and heat flow plots for different modeling scenarios with varying parameters in the Nanga Parbat Massif.

Kohistan

The crustal thickness under the northern Kohistan arc is estimated at 70 km (Priestley et al., 2019). While the stratigraphic thickness of the arc is estimated to be 50 – 55 km (Petterson, 2019; Jagoutz & Schmidt, 2012), the present-day structural thickness estimates range between 10 to 25 km (Malinconico, 1986; Petterson, 2019). It is assumed that the upper crust comprises a 20 km thick Kohistan arc. Table 6.2 shows modeling parameters for crustal layers with variable thickness and radiogenic heat production for 7 different scenarios. In Models 1 to 5, the upper crust is assumed to comprise felsic (Kohistan batholith) and mafic (amphibolite-granulite) components, each with 10 km thickness. The weighted average radiogenic heat production of Kohistan batholith is 1 µWm^{-3}, and 0.08 µWm^{-3} for the mafic layer (Mukai et al., 1999).

Indian crust, exposed on the surface at NPM in the south, is subducted under the Kohistan arc towards the north and lies at mid to lower crustal depths (Searle & Hacker, 2019). The lower crust for all models is assumed to be similar to the case of NPM, i.e., 30 km thick with 0.4 μWm^{-3}. For the mid-crustal region, two basements of Indian origin (Ind-1 & Ind-2) with different radiogenic heat production are assumed. For model 1, Ind-1 and Ind-2 are assumed to be 10 km each with RHP of 4 and 2 μWm^{-3}, respectively. For model 2, Ind-1 is reduced to 5 km, while Ind-2 is increased to 15 km. Model 3 assumes only Ind-2 (20 km thick) at mid-crustal level. The geotherms for models 1 and 2 show high temperatures ($\geq 1100°C$) and surface heat flow ranging between 65 – 85 mWm^{-2} (Fig 6.4)

The geotherms for models 4 and 5, respectively, show the effect of decreasing RHP to 50 and 25% for mid-crustal layers. The results show a decrease of 25% in RHP of mid-crust (model 5 & 6), and the Moho temperatures and surface heat flow drop below 950°C and 55 mWm^{-2}, respectively. The geotherms for models 4 and 7 (with a 50% RHP decrease) indicate Moho temperatures between 1000–1050°C. Models 6 and 7, while keeping lower RHP in mid-crustal layers, assume a 5 km increase in the felsic layer of Kohistan and a 5 km decrease in the mafic layer. The surface heat flow in these models shows an increase of ~5 mWm^{-2} (Fig 6.4).
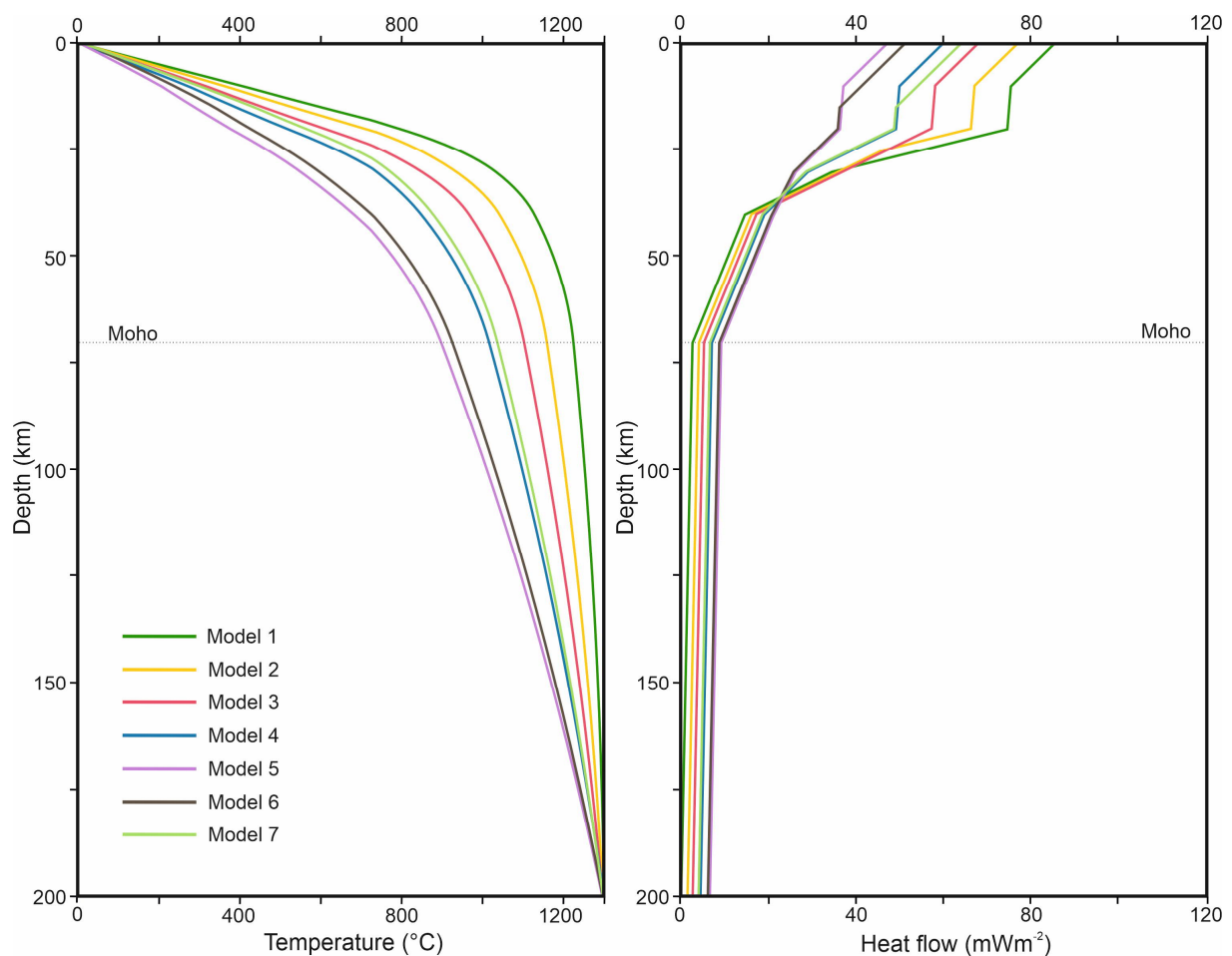
Figure 6.4 1D steady-state conductive geotherms and heat flow plots for the Kohistan arc.

Table 6.2 Parameters used for the steady-state conductive thermal model of Kohistan arc. Koh-F and Koh-M, respectively, refer to the upper felsic and lower mafic Kohistan crust overlying the Indian crust.

	Crustal depth range (km)	Radiogenic heat production (μWm^{-3})	Thermal Conductivity ($Wm^{-1}K^{-1}$)
Model 1			
Upper crust:			
Koh-F	0 - 10	1.0	2.3
Koh-M	10 - 20	0.08	3.0
Mid crust:			
Ind-1	20 - 30	4.0	2.3
Ind-2	30 - 40	2.0	2.5
Lower crust	40 - 70	0.4	2.6
Model 2			
Upper crust:			
Koh-F	0 - 10	1.0	2.3
Koh-M	10 - 20	0.08	3.0
Mid crust:			
Ind-1	20 - 25	4.0	2.3
Ind-2	25 - 40	2.0	2.5
Lower crust	40 - 70	0.4	2.6
Model 3			
Upper crust:			
Koh-F	0 - 10	1.0	2.3
Koh-M	10 - 20	0.08	3.0
Mid crust:			
Ind-2	25 - 40	2.0	2.5
Lower crust	40 - 70	0.4	2.6
Model 4			
Upper crust:			
Koh-F	0 - 10	1.0	2.3
Koh-M	10 - 20	0.08	3.0
Mid crust:			
Ind-1	20 - 30	2.0	2.3
Ind-2	30 - 40	1.0	2.5
Lower crust	40 - 70	0.4	2.6
Model 5			
Upper crust:			
Koh-F	0 - 10	1.0	2.3
Koh-M	10 - 20	0.08	3.0
Mid crust:			
Ind-1	20 - 30	1.0	2.3
Ind-2	30 - 40	0.5	2.5
Lower crust	40 - 70	0.4	2.6
Model 6			
Upper crust:			
Koh-F	0 - 15	1.0	2.3
Koh-M	15 - 20	0.08	3.0
Mid crust:			
Ind-1	20 - 30	1.0	2.3
Ind-2	30 - 40	0.5	2.5
Lower crust	40 - 70	0.4	2.6
Model 7			
Upper crust:			
Koh-F	0 - 15	1.0	2.3
Koh-M	15 - 20	0.08	3.0
Mid crust:			
Ind-1	20 - 30	2.0	2.3
Ind-2	30 - 40	1.0	2.5
Lower crust	40 - 70	0.4	2.6

Table 6.3 Parameters used for the steady-state conductive thermal model of Karakoram. KB-Karakoram batholith, KMC-Karakoram metamorphic complex, DG-Dassu gneiss, HG-Hushe gneiss.

	Crustal depth range (km)	Radiogenic heat production (μWm^{-3})	Thermal Conductivity ($Wm^{-1}K^{-1}$)
Model 1			
Upper crust (KB)	0 - 15	2.5	2.3
Mid crust (KMC)	15 - 25	1.0	2.5
Lower crust	25 - 70	0.2	2.6
Model 2			
Upper crust			
KB	0 - 15	2.5	2.3
KMC	15 - 30	1.0	2.5
Mid crust			
Ind-1	30 - 40	2.0	2.3
Ind-2	40 - 50	1.0	2.5
Lower crust	50 - 70	0.4	2.6
Model 3			
Upper crust			
KB	0 - 15	2.5	2.3
KMC	15 - 30	1.0	2.5
Mid crust			
Ind-1	30 - 40	1.0	2.3
Ind-2	40 - 50	0.5	2.5
Lower crust	50 - 70	0.2	2.6
Model 4			
Upper crust (KB)	0 - 10	2.5	2.3
Mid crust (DG)	10 - 30	3.15	2.5
Lower crust	30 - 70	0.2	2.6
Model 5			
Upper crust (KB)	0 - 10	2.0	2.3
Mid crust (DG)	10 - 30	2.5	2.5
Lower crust	30 - 70	0.2	2.6
Model 6 (KB-Kande pluton)			
Upper crust	0 - 10	5.0	2.0
Mid crust (HG)	10 - 30	2.0	2.3
Lower crust	30 - 70	0.2	2.6
Model 7			
Upper crust (KB)	0 - 10	2.5	2.3
Mid crust (HG)	10 - 30	2.0	2.5
Lower crust	30 - 70	0.2	2.6

<u>Karakoram</u>

Table 6.3 shows modeling parameters for crustal layers with variable thickness and radiogenic heat production for 7 scenarios to accommodate the present-day uncertainty in the crustal structure of Karakoram. The total crust thickness of 70 km is taken after Priestley et al. (2019), with a lower depleted crust (0.2 μW^{-3}) for all models except model 2. For model 1, the 15 km thick upper crust comprises Karakoram batholith (KB), while the 10 km mid-crust comprises Karakoram metamorphic complex (KMC) with RHP values of 2.5 and 1 μWm^{-3}, respectively. Model 1 also assumes a 45 km thick lower depleted crust, and the modeled geotherm gives a lower Moho temperature of 850°C with a surface heat flow of ~65 mWm^{-2} (Fig 6.5).
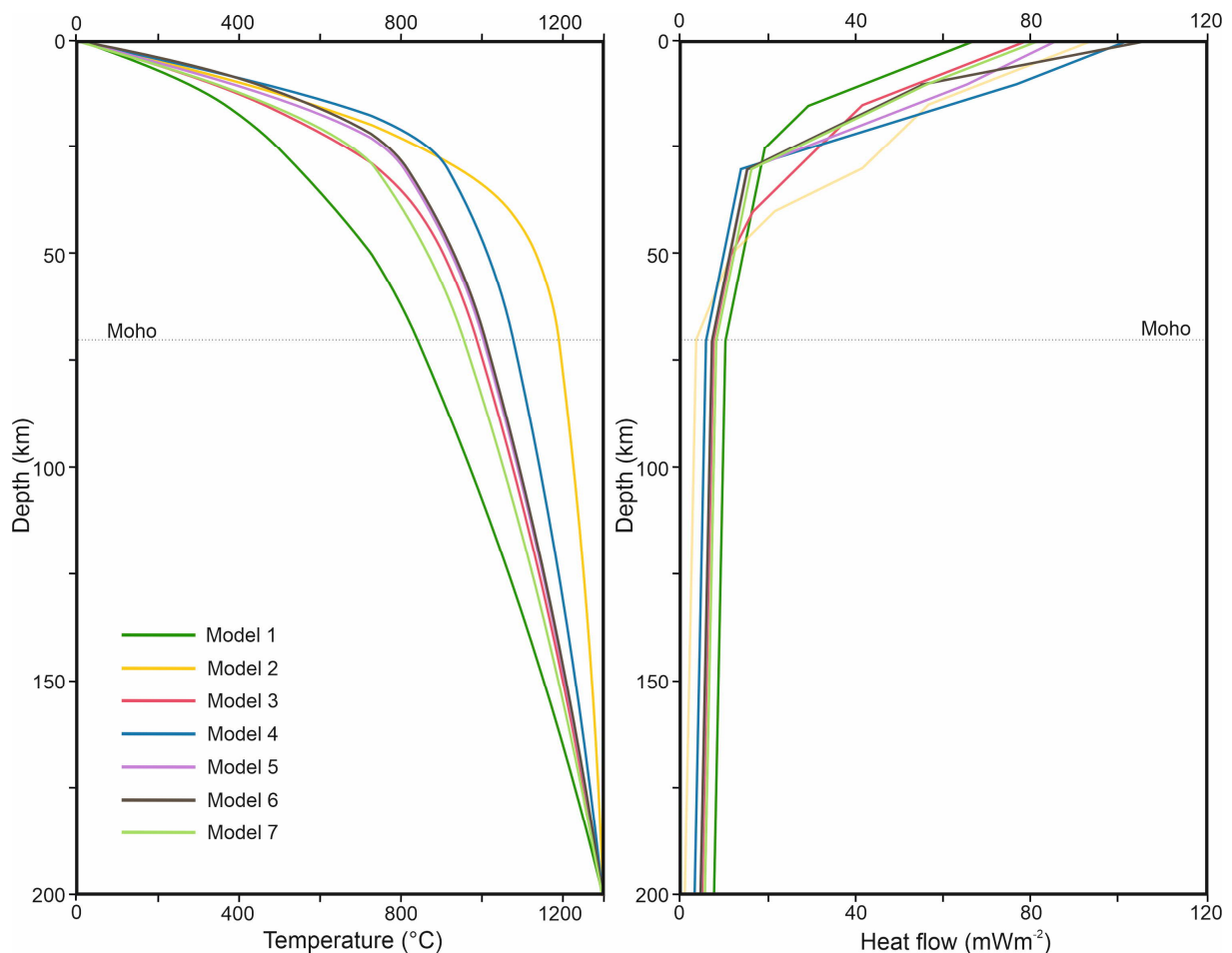
Figure 6.5 1D steady-state conductive geotherms and heat flow plots for different modeling scenarios with varying parameters in the Karakoram.

Model 2 assumes a 30 km upper crust with KB and KMC, each 15 km thick, and a 20 km mid-crust comprising Ind-1 and Ind-2 with RHP of 2 and 1 μWm^{-3}, respectively. The lower crust for this model is 20 km thick with RHP of 0.4 μWm^{-3}. The respective geotherm shows exceptionally hot Moho (~ 1200°C). Therefore, for model 3, the RHP of mid-crust is reduced by 50% (1 and 0.5 μWm^{-3}), while the rest of the parameters are the same as in model 2. The geotherm for this model gives a 200°C lower Moho temperature (ca. 1000°C).

For models 4 and 5, mid-crust (20 km) comprises Dassu gneiss (DG) with RHP of 3.15 (surface RHP) and 2.5 μWm^{-3}, respectively. The lower crust is assumed to be 40 km thick with RHP of 0.2 μWm^{-3} (model 4 to 7). The respective geotherms for models 4 and 5 show Moho temperatures between 1000 – 1100°C and surface heat flow 85 – 103 mWm^{-2}.

Model 6 assumes the upper crust (10 km) comprising of Kande pluton with the mean surface RHP 5 μWm^{-3} and mid-crust (20 km) comprising of Hushe gneiss (HG) with RHP of 2 μWm^{-3}. For Model 7, RHP is assumed to be half (2.5 μWm^{-3}) of model 6, while other parameters are kept the same. The results show that while the Moho temperatures lie between 950 – 1000°C,

the surface heat flow is significantly higher in model 6 (~105 mWm⁻²) than in model 7 (~80 mWm⁻²).

6.4   1D transient advective-conductive thermal model

6.4.1   Mathematical solution

A non-linear, transient, one dimensional heat diffusion equation is solved as;

$$\rho c \frac{\partial u}{\partial t} = (k(u)u')' + q \qquad [6.5]$$

where u is temperature, $k(u)$ is a temperature-dependent thermal conductivity, and q is radiogenic heat production. u, and q are both functions of depth. This can be rearranged into a recursive, linear system as follows;

$$\rho c \frac{u_{r+1}-u_r}{\delta t} = (k(u)u')' + q \qquad [6.6]$$

where r is the recursive time step. Spatial discretisation is then done in fully implicit form as;

$$\frac{u_{r+1}-u_r}{\delta t} = A_r u_{r+1} + q_{r+1} \qquad [6.7]$$

where $A_r = A(u_r)$ is a linearised form of the coefficient matrix dependent on the value of u for the preceding time step. The equation [6.7] can rearranged as;

$$(I - \delta t A_r)u_{r+1} = u_r + \delta t q_{r+1} \qquad [6.8]$$

or

$$Au = q$$

The equation is solved with Dirichlet boundary conditions of fixed temperatures at the top and base of the model. A tri-diagonal matrix algorithm is used to recursively solve the equation [6.8].

6.4.2   Modelling scenario

To model the transient effect of exhumation on the geotherms in a dynamic orogenic belt, the ideal initial condition should start before the collision. One way is to assume the present-day cratonic India as the pre-collision initial state of the Indian margin. This way, it can be started by subducting the Indian passive margin with cover sediments under the Kohistan at 50 Ma, increasing the crustal thickness. However, there would be too much uncertainty involved with the dynamic and kinematic conditions happening between 50 and 10 Ma before the start of the fast exhumation episode (Zeitler, 1985). Additionally, it is possible that in a period of ~35 Ma, crustal geotherms have been re-equilibrated and achieved a steady state condition (Fairley, 2016). Figure 6.6 shows zircon fission track data from Zeitler (1985) with very young cooling ages in (< 5 Ma) NPM and Karakoram in contrast to Kohistan (> 10 Ma), which suggests very fast exhumation (7 mm y^{-1}). However, Whittington (1996) suggested slow exhumation between 50 to 10 Ma followed by constant exhumation of 3 to 4 mm y^{-1} in the last 10 Ma.
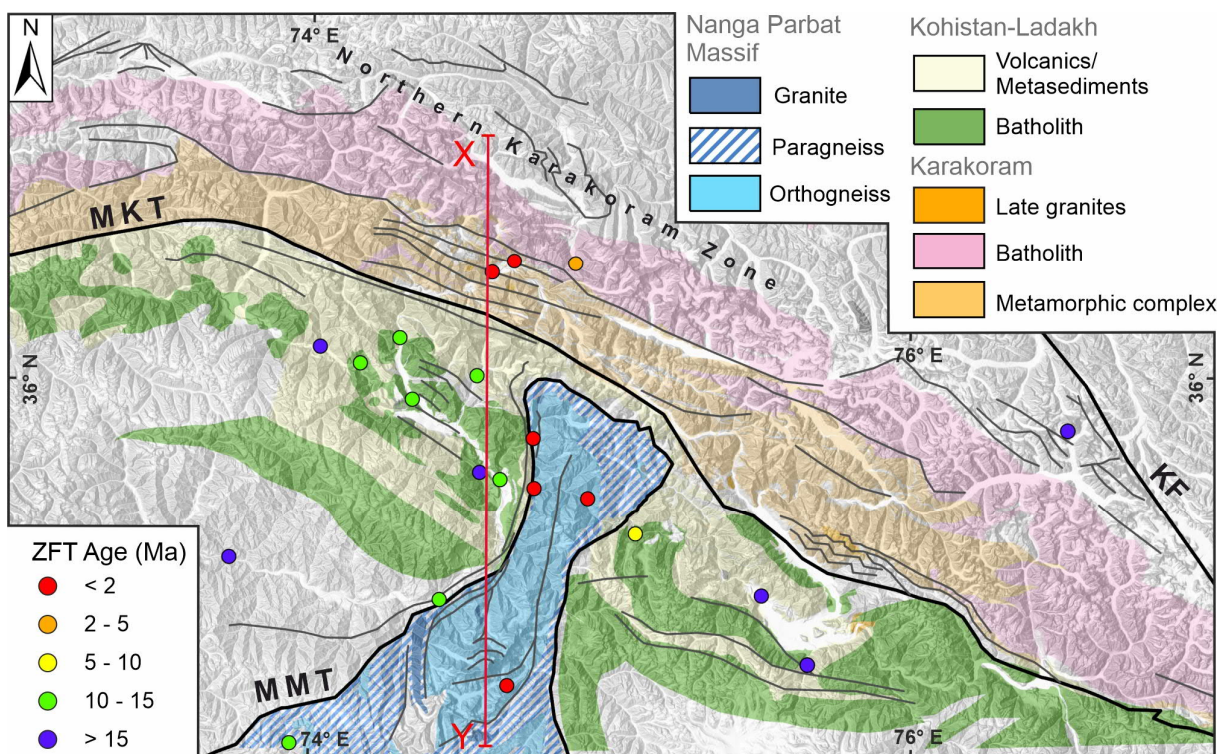

Figure 6.6 Zircon fission track cooling ages (after Zeitler, 1985) in the study area. Young cooling ages show fast exhumation in Nanga Parbat Massif and Karakoram compared to Kohistan. XY line shows the surface profile of 2D models in Figs 6.8 - 6.10.

For this study, the Nanga Parbat is opted an endmember example with the objective to test the effect of exhumation on the geotherms in combination with low and high radiogenic heat production scenarios (Table 6.4). To match metamorphic conditions, a 25 km crust of NPM comprising two layers was assumed with an initial thickness of 20 km for the top and 5 km for the bottom. Two cases of low and high RHP were assumed. For the high RHP scenario, RHP values for the top and bottom layers were set to 4 and 2 μWm^{-3}, respectively. For low RHP cases, values of 1 and 0.5 μWm^{-3} were set respectively for the top and bottom layers. Thermal conductivity, density, and specific heat capacity for the top layer were assumed to be 2.3 $Wm^{-1}K^{-1}$, 2700 kg m^{-3}, and 750 J kg$^{-1}K^{-1}$, respectively. For the bottom layer, values of 2.5 $Wm^{-1}K^{-1}$, 2800 kg m^{-3}, and 1000 J kg$^{-1}K^{-1}$ were assumed for thermal conductivity, density, and specific heat capacity. The top boundary condition is set to 10°C, and the temperature at the bottom is set to 800°C, as per high temperature migmatitic conditions (Guevara et al., 2022). A conductive heat transfer was solved through a finite difference method with bottom-to-top heat advection implicitly achieved through the vertical moving column at speeds corresponding to the respective exhumation rates (Appendix D). The total run time was set to 10 Ma with a 1000-year interval. Through the run time, the crustal thickness was maintained at 25 km by removing (thinning) the top layer and adding (thickening) the bottom at a rate corresponding to the exhumation.

Figure 6.7 and Table 6.5 show the transient effect of low and high RHP scenarios with exhumation rates varying between 1 to 3 mm y^{-1}. Overall, the geotherms after 10 Ma show significantly higher temperatures than the initial condition, and at 3 mm y^{-1}, the geotherm in the model with high RHP got inverted at 20 km. The model with higher RHP shows even higher temperatures with an increased exhumation rate. However, the geotherms of low RHP models catch up to the high RHP models when the exhumation rate in low RHP models is 1 mm y^{-1} higher compared to high RHP models. At 10 km depth, the geotherms of the low RHP model increase by a mean factor of 1.22, while the geotherms of the high RHP model increase by a mean factor of 1.14 for every 1 mm y^{-1} increase in exhumation.

Similarly, the surface heat flow values also increase with increasing exhumation. For the low RHP models, the surface heat flow values increase from 75 mWm^{-2} for initial conditions to 100, 160, and 220 mWm^{-2} for exhumation rates of 1, 2, and 3 mm y^{-1}, respectively. The heat flow for the high RHP models increased from 110 mWm^{-2} to 135, 180, and 250 mWm^{-2} for respective increase in exhumation (Fig 6.7).

Table 6.4 Parameters used for the 1D transient advective-conductive thermal model to test the effect of exhumation of geotherms and heat flow.

	Crustal depth range (km)	Radiogenic heat production (μWm^{-3})	Thermal Conductivity ($Wm^{-1}K^{-1}$)	Specific heat capacity (J $kg^{-1} K^{-1}$)	Density (kg m^{-3})
Model 1 (High RHP)					
Layer 1	0 – 20	4.0	2.3	750	2700
Layer 2	20 – 25	2.0	2.5	1000	2800
Model 2 (Low RHP)					
Layer 1	0 – 20	1.0	2.3	750	2700
Layer 2	20 – 25	0.5	2.5	1000	2800

Table 6.5 Results of Temperature (°C) at 10 km for 1D transient advective-conductive thermal model against varying exhumation rates for 10 Ma.

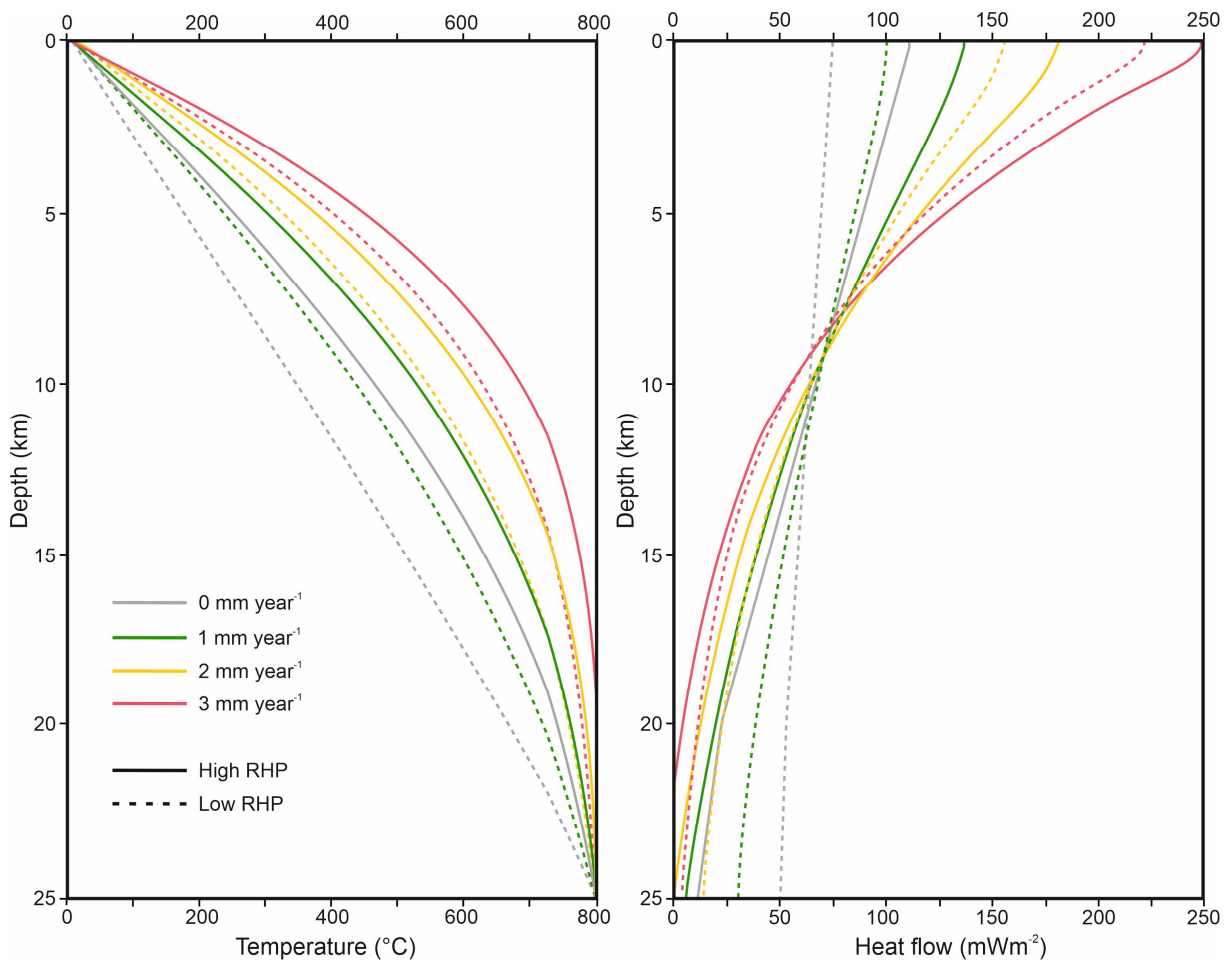|	for exhumation rate				Mean increment factor (per 1 mm y^{-1})
	0 mm y^{-1}	1 mm y^{-1}	2 mm y^{-1}	3 mm y^{-1}	
High RHP model	464	528	611	686	1.14
Low RHP model	348	437	545	630	1.22

Figure 6.7 1D transient advective-conductive geotherms and heat flow plots showing the effect of variable exhumation (after 10 Ma) for low and high RHP models.

6.5   2D thermal model

2D thermal modeling is carried out to understand the near-surface lateral distribution of isotherms. Two-dimensional conductive heat transfer is modeled using finite element method-based COMSOL Multiphysics software. A geological model (up to 10 km below sea level) was created along a profile incorporating all the representative lithologies and topographic variations (Fig 6.8). The geological model was assigned petrophysical properties calculated from outcrop analogs (see Appendix). Using the equation of Jaupart et al. (2016) for temperature-dependent thermal conductivity, an analytical function was introduced in COMSOL to convert the input thermal conductivity values. The triangular finite element mesh was created with 72643 elements with an area of 2255 km^2 (Fig 6.8).

For the boundary conditions, the left and right sides are assumed to be thermally insulated, while a constant 10°C top is set for the top surface. For the basal boundary (at 10 km bsl), the laterally variable temperatures were calculated from 1D steady-state and transient models. Table 6.6 shows the bottom temperatures for NPM, Kohistan, and Karakoram with three different scenarios. The upper half of the table is based on steady-state geotherms for high, moderate, and low RHP. The bottom half of the table shows the basal temperatures based on the transient model, including the effect of exhumation and RHP.

Figure 6.9 shows 2D thermal models obtained with the steady-state basal temperature input calculated for low, high, and moderate RHP. The isotherms shift upward with an increase in basal temperature to accommodate an approximate 100°C temperature increase in each model with higher RHP. The isotherms get compressed toward the surface, with the near-surface isotherms following the topographic profile in all three cases. The effect of topography is most evident in NPM and Karakoram, where isotherms are compressed under valleys and expanded under peaks due to high relief. At NPM, the 150 and 200°C isotherms lie at sea level for low RHP and high RHP models, respectively. The isotherms rise from 100 to 150°C at sea level under Karakoram, increasing from 50 to 100°C in Kohistan.

Figure 6.10 shows 2D thermal models based on basal temperature input calculated for variable exhumation and RHP (Table 6.6). The results clearly show that with focused high exhumation, the temperature increase is higher in the vertical direction compared to the lateral direction. In comparison, the moderate to high RHP models (despite low exhumation) show greater lateral spread of isotherms. At sea level, the isotherms under NPM and Karakoram batholith are surprisingly around the same range for models 1 and 2 with contrasting scenarios. The

isotherms in Kohistan react more due to RHP-based basal temperature than the exhumation ones.

Table 6.6 Input bottom temperatures (°C) for 2D thermal models at 10 km below sea level calculated from 1D models.

	Temperatures (°C) at 10 km from 1D steady-state conduction model		
	Model 1 Low RHP	Model 2 Moderate RHP	Model 3 High RHP
NPM	343	405	506
Kohistan	211	299	413
Karakoram	274	385	461
	Temperatures (°C) at 10 km from 1D transient advective-conductive model		
	Model 1 High exhumation-Low RHP	Model 2 Low exhumation-High RHP	Model 3 Low exhumation-Moderate RHP
NPM- core	623 (at 3 mm y^{-1})	657 (at 2 mm y^{-1})	564 (at 2 mm y^{-1})
NPM-side	510 (at 2 mm y^{-1})	577 (at 1 mm y^{-1})	478 (at 1 mm y^{-1})
Kohistan	257 (at 1 mm y^{-1})	432 (at 0.5 mm y^{-1})	318 (at 0.5 mm y^{-1})
KMC	407 (at 2 mm y^{-1})	482 (at 0.5 mm y^{-1})	410 (at 0.5 mm y^{-1})
KB	497 (at 3 mm y^{-1})	525 (at 1 mm y^{-1})	454 (at 1 mm y^{-1})

Geological model

Finite element mesh
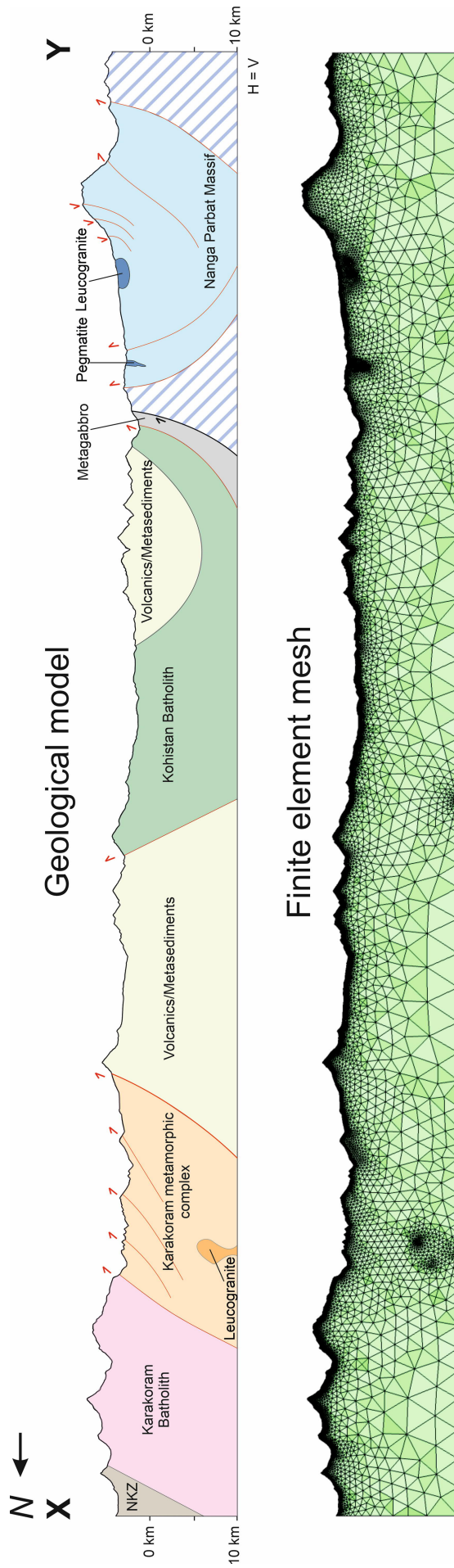
Figure 6.8 Geological model of the XY profile in Fig 6.6 showing the subsurface geological structure of the major lithological units up to 10 km below sea level (modified after Searle & Khan, 1996). A two-dimensional triangular mesh containing 72643 elements created in COMSOL for the thermal modeling.
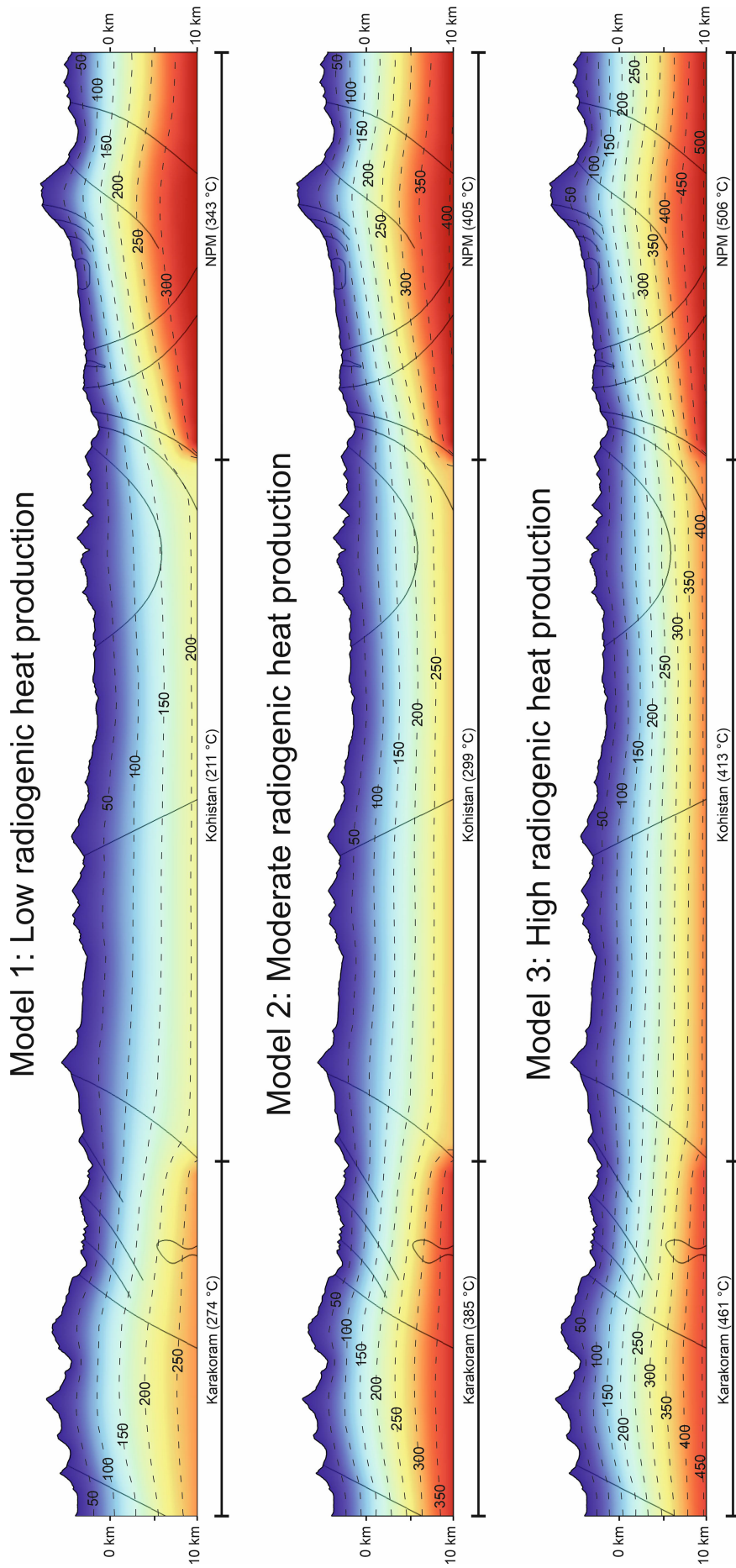
Figure 6.9 2D steady-state conduction thermal models with basal temperature input from 1D steady-state conduction models, which assume low, moderate, and high RHP scenarios for Nanga Parbat Massif, Kohistan, and Karakoram.
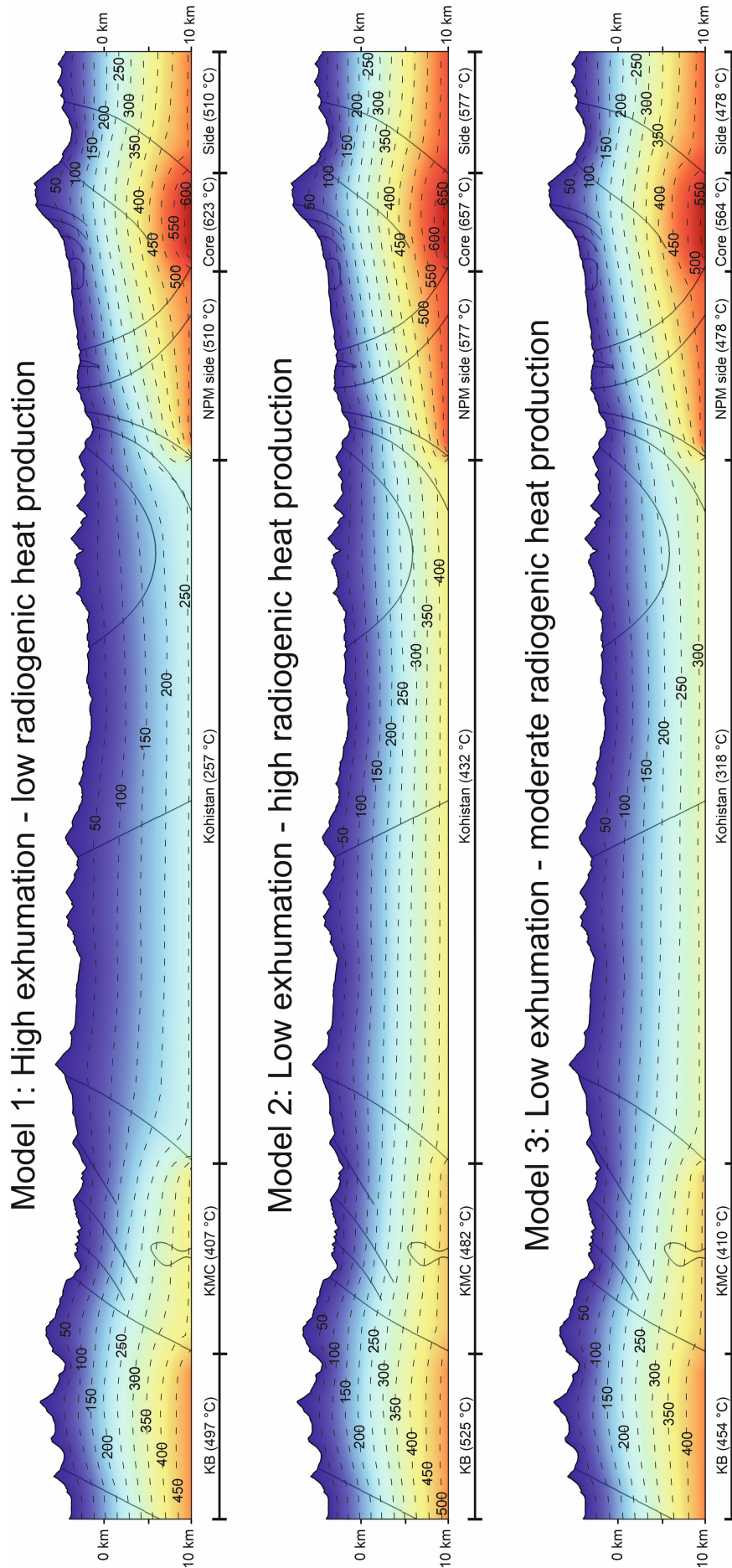
Figure 6.10 2D steady-state conduction thermal models with basal temperature input from 1D transient advective-conductive models, which test high and low exhumation and incorporate them with low, moderate, and high RHP scenarios for Nanga Parbat Massif, Kohistan, and Karakoram.

6.6   Discussion

6.6.1   Thermal modeling of lithosphere and radiogenic heat production

The tectonic and geodynamic settings of the Himalaya, Kohistan, and Karakoram orogens greatly influence the thermal regime of the study area. The subduction and thrusting in the Indian plate caused crustal thickening and subsequent exhumation due to thrust imbrication. The added crustal thickness increases the total radiogenic heat production in the crust (Jaupart et al., 2016), while the exhumation causes heat advection by moving hot rocks to the surface (Jamieson et al., 2002). Additionally, the crustal thickening also involves the formation of melts at mid to lower crustal depths, which get transported to upper crustal depth in the form of plutons (Jamieson et al., 2011). Such orogens have a deep Moho and shallow Curie depth (580 °C isotherm) and thus indicate high background heat flow (Gao et al., 2017; 2021).

Information about the structure and physical properties of a lithosphere is crucial for developing a thermal model. Thermal modeling of the lithosphere is usually coupled with surface heat flow measurements based on deep boreholes to avoid the transient effects of circulating groundwater and environment (Fuchs et al., 2022). Steady-state thermal models are mainly used for stable cratonic interiors, which have relatively horizontal crustal stratification with reasonable constraints from geophysical data (Furlong & Chapman, 2013). However, in evolving orogens, neither the surface heat flow data (if present) is reliable nor the deep geophysical estimates. In this study, the multiple models with variable parameters take this uncertainty into account to approximate the thermal state of the lithosphere.

Radiogenic heat production (RHP) is the most significant parameter in the crust that controls the crustal geotherms (Hasterok & Chapman, 2011). Despite the availability of surface constraints on RHP, uncertainty about its variation with depth is the main reason for the wide range of results. It has been suggested that the heat-producing elements in the crust are not redistributed at temperatures below solidus (McKenzie & Priestley, 2016). Alessio et al. (2018), Weller et al. (2020), and Yakymchuk and Brown (2019) suggested that Th is retained in the accessory minerals during partial melting and compensates for the removal of other heat-producing elements. A global comparison of metamorphic grade and RHP also shows no correlation (Hasterok et al., 2018). The results of Chapter 4 agree with the suggestions of these authors and show the presence of high Th in migmatitic gneiss. However, attempting to assign surface RHP values to mid-crustal layers resulted in exceptionally hot and unrealistic geotherms (Fig 6.3 – 6.5). This implies the existence of some mechanism by which, beyond a certain depth, the RHP gets reduced and vice versa.

6.6.2   Crustal Differentiation

Perry et al. (2006a) proposed a crustal differentiation index (D_I) to indicate vertical stratification in the crust in response to the enrichment of upper crustal layers. They derived D_I through a ratio of mean surface heat production (A_o) and total mean crustal heat production (A_c) as follows;

$$D_I = \frac{A_o}{A_c}$$

$$A_c = \frac{Q_s - Q_m}{h}$$

where, Q_s is the surface heat flow, Q_m is the heat flow from the mantle, and h is the crustal thickness.

In the absence of surface heat flow data, the values calculated from 1D steady-state models are incorporated for the calculation of D_I. For the NPM, the total mean crustal heat production (1.5 µWm^{-3}) is obtained by removing the mean mantle heat flow (8 mWm^{-2}) from the mean surface heat flow (100 mWm^{-2}) and dividing it by total crustal thickness (60 km). The ratio of total mean crustal heat production (1.5 µWm^{-3}) and mean surface heat production (4.6 µWm-3) provides a D_I of 3. Similarly, the D_I for Kohistan and Karakoram were calculated to be 1.1 and 2, respectively.

Figure 6.11 shows a plot of differentiation index (D_I) vs. bulk mean crustal heat production (A_c) for NPM, Kohistan, and Karakoram and compares them with the Indian (Bundelkhand and Dharwar) and North American (Trans-Hudson, Grenville, and Appalachians) cratons (Perry et al., 2006a; Podugu et al., 2017). The plot shows a positive correlation between D_I and mean crustal heat production, with D_I > 1 suggesting radiogenic radioelement enrichment in the upper crust, possibly due to magmatic differentiation (Perry et al., 2006a). The higher D_I in the NPM (3) and Karakoram batholith (2) is comparable to the Appalachians (2.5), indicating enrichment of radioelements in the upper crust. In comparison, the Kohistan batholith shows low D_I (1.1), which is on par with the Dharwar craton, Grenville Province and Trans-Hudson Orogen. However, the Kohistan batholith shows higher average crustal heat production compared to these Indian and North American terranes, which can probably be attributed to the subducting enriched Indian crust under it.

The D_I values of the NPM and Bundelkhand craton are equally high, but the significantly higher average crustal heat production in the NPM (1.5 µWm^{-3}) compared to the Bundelkhand craton (0.41 – 0.68 µWm^{-3}) can be associated with the imbrication and crustal thickening. Doubling the crustal thickness also doubles its average crustal heat production, which results in high temperatures at mid to lower crust depths. This induces the onset of crustal melting, in which radioelements are redistributed by migrating upwards in the upper crust, thus stabilizing the temperatures in the lower crust (Perry et al., 2006a). This is also corroborated by modeling results, where higher RHP (≥ 2 µWm^{-3}) layers in the mid-crust resulted in exceptionally hot geotherms (Fig 6.3 – 6.6). It should be noted that, in the absence of surface heat flow measurements, the estimations of differentiation index and average crustal heat production should be considered preliminary.
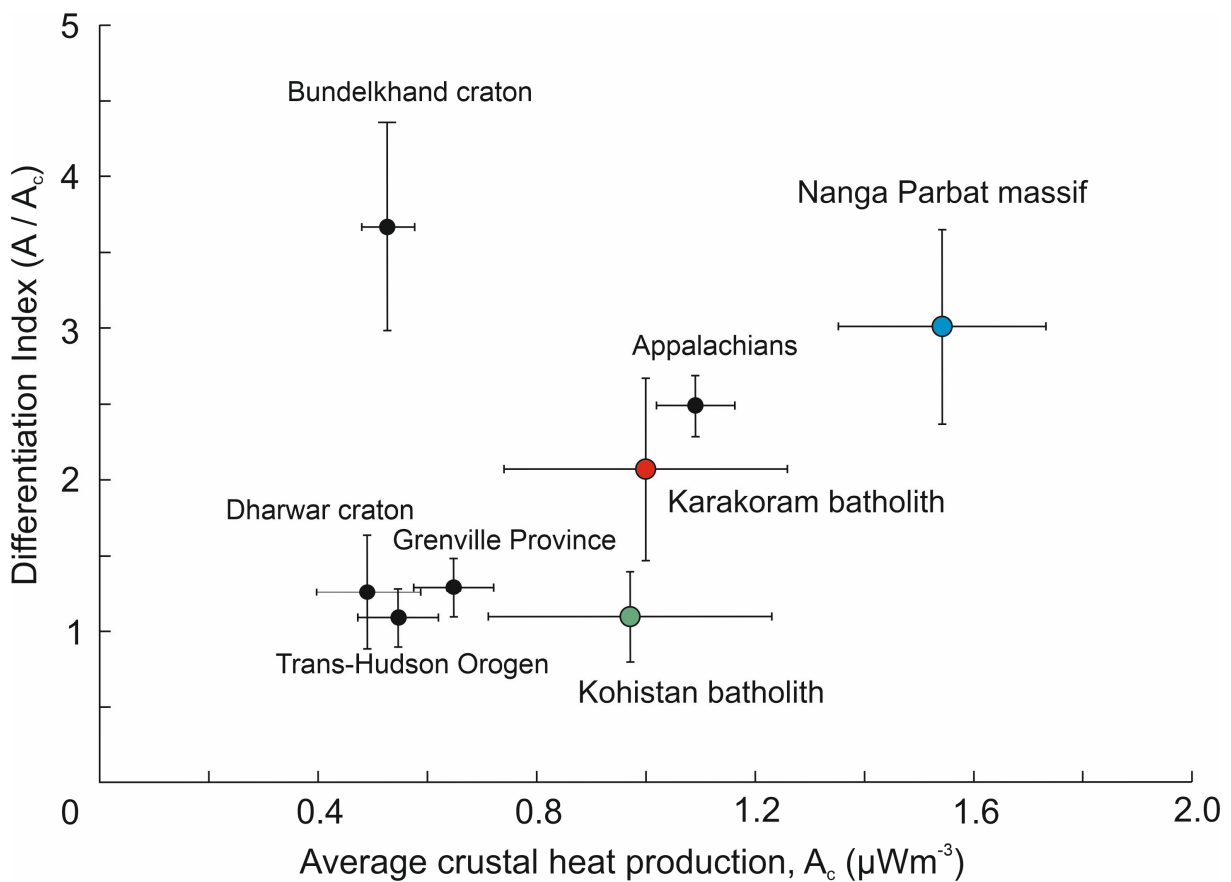
Figure 6.11 Plot of differentiation index (D_I) vs. average crustal heat production (A_c) for the Nanga Parbat Massif, Kohistan and Karakoram batholith in comparison with Indian cratonic regions (after Podugu et al., 2017) and North American geological provinces (after Perry et al., 2006a).

6.6.3   Upper crustal heat flow and geothermal implications

It is evident from 1D modeling results that the surface heat flow depends on the concentrations of heat-producing elements in and thickness of the heat-producing layer in the upper crust.

While the 1D transient models indicate a stronger influence of exhumation, the 2D model reveals its limited lateral influence compared to RHP. In the NPM, a high thermal regime is due to the combination of exhumation and RHP, which together create the high near-surface geothermal gradient. Additionally, the near-surface temperatures are greatly influenced by topographic relief, which explains the distribution of hot springs.

These hot springs commonly occur in zones of enhanced permeability (such as faults) and are likely to tap the proximal zones of increased heat production efficiently. Furthermore, in contrast to conduction, the interaction of topographic-driven deep groundwater flow with heat-producing hot rocks results in advective heat transport to the surface, which is a more efficient and rapid near-surface heat transport process common in evolving orogens (Chamberlain et al., 1995; Wanner et al., 2020).

The geothermal regime in the NPM and Karakoram can be characterized as medium to high enthalpy. Adopting the more conservative estimates of exhumation rate and moderate RHP, the isotherms of > 100 °C lie at sea level, 1200 to 2500 m beneath the floors of deep valleys. The Indus and Astore river cut across the NPM and lie 1150 to 2500 m above sea level, so the isotherms under these valleys would be closest to the surface with possible access to > 200°C within 3 km from the surface. On the other hand, the subsurface groundwater aquifers in the high-relief areas carry water with elevated temperatures due to longer and deeper flow paths. Therefore, the main geothermal plays could be both petrothermal (hot-dry rock) and hot aquifer (hydrothermal) in this area.

6.6.4   Modeling limitations

The presented thermal models explore the potential role of heat production and provide first-order estimates on crustal geotherms and surface heat flow by incorporating the uncertainty associated with limited data and heterogeneous parameters. For this, the intra-layer RHP values are assumed to be constant. However, as discussed earlier (in section 6.6.1), assigning the surface RHP value to a mid-crustal layer causes unrealistic temperature increases. Therefore, the RHP values at the mid-crustal level were adjusted to get reasonable geotherms following models of stratified continental crust (Rudnick & Gao, 2003; Hacker et al., 2015).

In the ongoing active collisional settings, several dynamic and transient factors also contribute to the heat production in the crust—for example, uplift, shear heating, partial melting and melt migration, crustal thickening, and paleoclimate. The shear heating, while playing an important role in orogenic evolution (Burg & Gerya, 2005; Wang et al., 2013), is restricted to the fault

zones (Ai et al., 2021) and on the crustal scale, its contribution in comparison to radiogenic heat is negligible (Fagereng & Biggs, 2019; Rowe & Griffith, 2015). The migration of melts to the upper crust due to mid-crustal anatexis can cause heat advection, but in the current case, it would affect only a small area and is neglected in the modeling. While the crustal thickening increases the total radiogenic content of the crustal volume, it is also neglected due to its longer time scales.

The lateral and vertical lithological variations, along with deformation intensity, greatly influence the rock properties and can significantly affect local heat flow (Abdulagatova et al., 2020; Weinert et al., 2020). The thermophysical parameters for the 2D model, while based on outcrop analogs, do not represent deep conditions affected by temperature, pressure, and fluids. The fluid circulation and rock permeability are also not considered in the model. Percolation of cold meteoric water leads to hydrothermal cooling and disturbs the conductive geotherms in the shallow regions (Cao et al., 2019). In contrast, in regions around hot springs, the hot fluid causes the advection of deeper heat to the near surface and, thus, also disturbs the conductive heat flow (Bächler et al., 2003; Koltzer et al., 2019). Hence, the regions with higher deformation and fracture-related permeability are highly likely to be affected by advective heat flow.

6.7 Conclusion

This chapter explored the role of radiogenic heat production and exhumation on the crustal geotherms and the effect of these processes on surface heat flow. Given the limited information on the crustal structure and the considerable uncertainty involving other parameters, various models have been tested for different scenarios. The crustal-scale thermal models have revealed that the surface radiogenic heat production cannot be extrapolated to mid-crust depth in the case of a subducting or under-thrusting layer. The magnitude of heat production and thickness of the heat-producing layer mainly control surface heat flow. Exhumation transports heat faster to the surface and results in higher surface heat flow, even in an upper crust with low RHP. However, the lateral influence of exhumation is restricted to the proximity of the uplifting block. In contrast, the RHP has a more significant lateral influence on the crustal temperatures. The shape and spacing of the near-surface isotherms are greatly influenced by topography. The isotherms get upwarped and expanded under mountains and compressed beneath valleys. Deep valleys are thus the most suitable place to access the high temperatures in the subsurface with relatively shallow drilling.

Chapter 7: Summary and outlook

7.1 Key findings

This thesis aimed to assess the geothermal potential of crystalline units of the Himalayas, Kohistan, and Karakoram region and identify the promising sites for future detailed exploration and development. The absence of reliable data and inaccessible terrain favored remote sensing to map the surface hydrothermal alteration, high lineament densities, and thermal anomalous zones. Field surveys, aided by remote sensing results, were carried out for radioelement measurements using a portable gamma spectrometer and sample collection for lab analysis. The lab analysis included petrographic observations, geochemistry, and petrophysical properties to characterize the effect of fluid flow on rock properties and to provide the physical parameters for thermal models. Thermal modeling was carried out to test the effects of radiogenic heat production and of exhumation on crustal temperatures and surface heat flow. The key findings of this thesis are summarized as follows:

The remote sensing methodology has successfully identified areas with high lineament density, anomalous surface temperature, and hydrothermal alteration. High lineament density is associated with intense folding and faulting near regional faults and suture zones. Thermal anomalies (obtained after removing topographic effects) show a slight correlation with high lineament density and surface geothermal manifestations, but high uncertainty due to other environmental factors constrained their utility. Alteration minerals are mapped in the areas with active and fossil hydrothermal activity. These remote sensing-based results proved helpful in providing base information for field investigation, and the results were confirmed by XRD analysis. It is recommended to employ remote sensing for geothermal exploration in an underexplored and topographically challenging area. In addition to providing base information for field surveys, the remote sensing results can also be extrapolated to remote sites with confidence after field verification.

In-situ gamma spectrometry revealed that the radio-elemental concentrations in the Nanga Parbat Massif (NPM) are overall high (especially granites and gneisses), low in the Kohistan-Ladakh batholith (KLB) (but slightly higher in felsic lithologies), and intermediate in the Karakoram batholith (KB) (except eastern granites). The lithological and genetic association of rocks are found to be controlling the distinct variations in radioelement concentrations. High radioelement concentrations in the Nanga Parbat Massif are inherited from protoliths, which, upon partial melting, lead to U enrichment (Th/U ratio < 1) in granites and leucogranites. The high radiogenic heat production and Th in Proterozoic gneisses can be attributed to global

paleo-tectonic crust-forming processes at that time. Overall, the Nanga Parbat Massif (with > 4 µWm^{-3}) is classified as high heat-producing, the Karakoram batholith (with 2 – 4 µWm^{-3}) as moderately heat-producing, and the Kohistan-Ladakh batholith (with < 2 µWm^{-3}) as low heat-producing. The proximity of locations of high radiogenic heat production to the hot springs suggests its potential contribution to the geothermal gradients in the study area on a local to regional scale.

The granitoids and gneisses (at macro to microscopic scale) show weak to moderate alteration of biotite, K-feldspar, and plagioclase, which increases towards intensely deformed zones. Geochemical results indicate that the gneiss and granites of the NPM are mostly peraluminous alkaline S-type, enriched in REEs and radioactive elements, indicating partial melting and high fractionation. The granitoids of the KB, due to their different magmatic histories, are more diverse, ranging from syenite to granite, I-type to S-type, and alkaline to calc-alkaline in composition. They also show an overall enrichment in REEs and radiogenic elements, which, in the case of syenite, are primarily present in allanite. In comparison to NPM and KB, the KLB granitoids are calc-alkaline I-type and show depletion of REEs and radiogenic elements. Petrophysical measurements reveal low matrix porosities (0.64–3.52%), with primarily average thermal conductivities (1.48–3.37 W m^{-1} K^{-1}) and thermal diffusivities (0.68–1.95 10^{-6} m^2 s^{-1}), with slight variation in specific heat capacities (744–767 J kg^{-1} K^{-1}). The NPM displays higher average thermal conductivity, thermal diffusivity, and lower porosity than the KB, while the KLB falls between these two.

The role of radiogenic heat production and exhumation on the crustal geotherms and its implication on surface heat flow have been explored. Given the limited information on the crustal structure and the considerable uncertainty involving the parameters, various models for different scenarios are tested. The crustal-scale thermal models revealed that the surface radiogenic heat production cannot be extrapolated to mid-crust depth in the case of a subducting or under-thrusting layer. The magnitude of heat production and thickness of the heat producing layer mainly control surface heat flow. Exhumation transports heat faster to the surface and results in higher surface heat flow, even in an upper crust with low RHP. However, the lateral influence of exhumation is restricted to the proximity of the uplifting block. In contrast, the RHP has a more significant lateral influence on the crustal temperatures. The spacing of the near-surface isotherms is greatly influenced by topography. Isotherm distances get expanded under mountains and compressed in valleys. Deep valleys are therefore the most suitable place to access the high temperatures in the subsurface with relatively shallow drilling.

The proposed conceptual model considers the batholith granitoids and gneissic complexes as potential reservoirs and establishes the basic parameters for understanding and developing future exploration and geothermal modeling. Variable alteration intensity in plagioclase and biotite shows fluid circulation within these rocks, weakening them and allowing new fluids to circulate. Water from glaciers and snow in high-altitude regions percolates several kilometers deep due to high relief and fractures created along the faults and shear zones. High concentrations of radiogenic elements within these rocks and high rock uplift rates also increase the geothermal gradient by heat production and advection. The fluids following permeable fracture zones in these thermally conductive rocks are heated to boiling temperatures and may discharge as geysers and fumaroles along river and stream banks.

To conclude, a cost-effective methodology involving a combination of multi-scale and multi-method studies has been extremely helpful in characterizing the basic geothermal framework in an under-explored and remote area. The findings presented in this work improve understanding of the region's geothermal regime on a larger scale. The concepts elaborated here could be extended to the whole Himalayan geothermal belt due to its comparable geological settings. The data generated by this work provides a basis for developing local reservoir models, which focus on estimating fault/fracture zone properties and the feedback effect of hydrothermal fluids on the host rocks via alteration-induced porosity increase compared to unaltered rocks.

7.2   Potential geothermal targets

The multi-method findings of this thesis are compiled in a map to identify the promising zones of geothermal potential for further exploration and development (Fig 7.1). The Nanga Parbat region, central Karakoram, and eastern Karakoram are potential geothermal target regions.
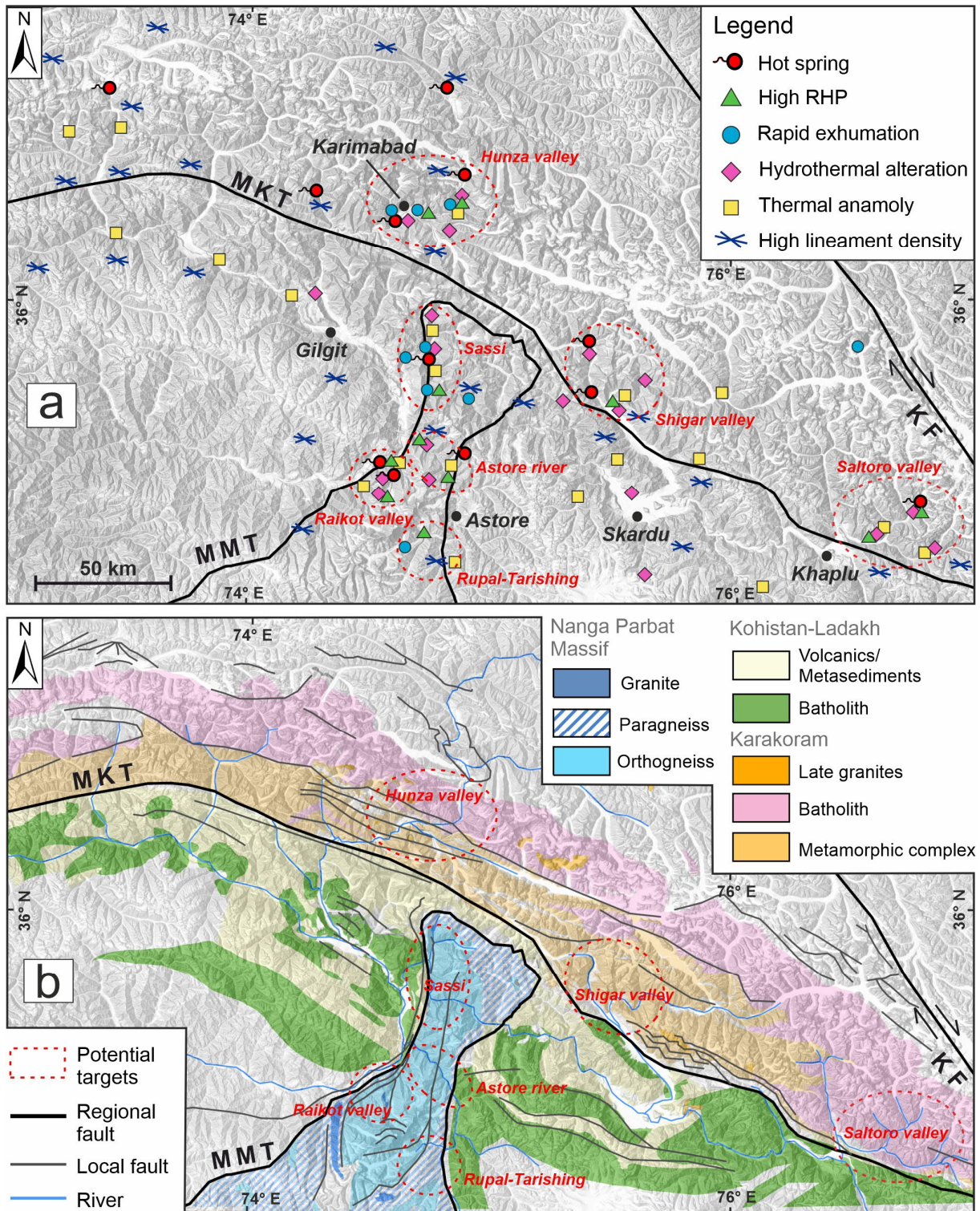
Figure 7.1 (a) Compilation map shows areas with high RHP, rapid exhumation, hydrothermal alteration, thermal anomalies, and high lineament density. These multi-method results form clusters (dashed red circles) mostly near hot springs. (b) Geological map showing potential geothermal targets identified in this thesis and recommended for detailed exploration and exploitation.

Nanga Parbat region

The radioelement-enriched and rapidly exhuming hot rocks make the Nanga Parbat region an attractive geothermal prospect. The results of this thesis point towards the concentration of geothermal activity in the Raikot Valley, Astore River, Rupal-Tarishing, and Sassi. Due to extreme relief and high exhumation, the Raikot Valley is deeply incised and shows numerous signs of active and fossil hydrothermal systems. In addition, the RHP and exhumation in the core are high (~ 5 μWm^{-3} and ~ 3 mm y^{-1}, respectively), and isotherms are significantly upwarped. A steaming geyser (at Tato village in upper Raikot Valley) is located close to the core of the NPM, suggesting interaction with shallow, hot migmatites and young granitic intrusions (Craw et al., 1994). In the Raikot Valley and Sassi, hot spring clusters are linked to the seismically active Raikot fault, which provides an escape channel for deeply infiltrated meteoric waters. Due to low matrix porosity, the fluid flow is controlled by fault-induced fractures, which could act as hydrothermal reservoirs underlying the topographic lows (close to rivers) and potentially offer high temperatures (> 100°C) at depths of ~2 – 3 km below the surface (Fig 5.11). The Astore River completely cuts through high RHP (~ 4.5 μWm^{-3}) gneisses of the NPM. There are few hydrothermal alteration areas, active hot springs directly discharging into the river. The narrow valley greatly restricts the accessibility here. The Rupal-Tarishing area is mainly covered with glacial sediments, but underlying gneisses have high RHP (~ 6 μWm^{-3}), which, combined with exhumation, could also induce high subsurface temperatures.

Central Karakoram

In the central Karakoram, the Hunza and Shigar valleys display indications of geothermal potential. Karakoram batholith and metamorphic complex in Hunza Valley has moderate heat production (~ 2 μWm^{-3}) and numerous intruded dikes and stocks of radiogenic (~ 4 μWm^{-3}) young granites. Along these intrusions, hydrothermal alterations are common in country rocks. The batholith forms a topographic high, has high lineament density, and acts as the recharge zone for hot springs. The imbricate thrusts in the metamorphic complex provide pathways for hydrothermal water, manifested by hot springs at the surface (Fig 5.11). Ahmed et al. (2001) estimated the subsurface reservoir temperature to be > 150 °C between 2000 to 4000 m below the surface. Hot spring sites in the upper Shigar Valley (Basha Valley) are in proximity to heat-producing (~ 3 μWm^{-3}) felsic gneiss of the Karakoram metamorphic complex intruded by numerous pegmatitic dikes and a syenitic body. Close to the MKT, the hydrothermal alteration and increased lineament density are more prominent. This metamorphic complex with high RHP (possibly young cooling age) could have a higher subsurface temperature.

The Kande pluton of the Karakoram batholith showed the highest RHP (~ 7 μWm^{-3}) values. The elevated location of hot springs with a relatively low flow rate is probably an effect of shallow meteoric flow due to a network of smaller fractures instead of deep faults. Surface thermal anomalies, hydrothermal alteration and dense lineaments all point towards warm fractured rock surfaces with thermal imprints. High surface heat flow (> 100 mWm^{-2}) is predicted if the Kande pluton is 10 km thick. Although there is an average relief of 2000 to 4000 m, the morphology of the pluton does not favor abundant meteoric circulation. The pluton has the potential of a hot-dry rock system with high enough temperature (> 100°C) at depths of ~2 – 3 km for geothermal exploitation. Such a reservoir (with a low matrix porosity of 1.3 – 2.1%) could be engineered to induce permeability and enhance fluid flow rate for better heat recovery and economic viability.

7.3 Potential geothermal applications

The hot springs in the area range from low to intermediate enthalpy, suggesting an excellent direct-use potential for domestic applications. The hot springs with high flow rates and surface temperatures > 50°C would be sufficient for space heating during prolonged winters. In the Shigar Valley, the hot springs (Chutran and Bisil) have decent flow rates and are already being exploited for domestic use at a limited scale, which needs to be upscaled to integrate all households in the community. The subsurface hydrothermal aquifers of these hot springs could also be accessed in these areas to meet the more extended demand. Many local industries (such as fish farming and agriculture) are severely affected during winter. The shallow aquifers (< 500m) in most areas would be at > 50°C, enough to keep these industries running during sub-freezing winters. The hot spring locations could also have the potential to be developed as tourist resorts, including saunas, which would further promote tourism in the region.

Temperatures above 100°C are suitable for electric power production, which are most likely to be encountered by high-temperature hot springs in the Raikot, Hunza, and Saltoro valleys. Installation of small and efficient power plants would benefit remote communities from where they are forced to migrate in harsh winters. The deeply incised valleys along the margins of the NPM are the likely candidates for the deep and hot subsurface rocks. They could have sufficiently high temperatures (100 – 200 °C) at depths of ~2 – 3 km to sustain geothermal power plants to meet the demand of urban areas. The Kande Pluton in the Salotor Valley would be another likely candidate for a HRD resource. HDR resources are usually engineered (EGS-Enhance/engineered geothermal systems) for artificial permeability enhancement by fracturing

or stimulation to increase deep permeability for transmitting fluids at required rates (Schulz et al., 2022). Additionally, such reservoirs could be exploited with advanced closed-loop heat exchangers for better heat recovery and lower risk of induced seismicity (Budiono et al., 2022).

7.4 Recommendations for future geothermal exploration

Immediate application of the results of this thesis is limited by the availability of local geophysical and geological data. Such data are essential to constrain the depth, thickness and extent of geothermal reservoirs and to develop 3D geological and geothermal models, all to be used in reservoir estimation. However, the investigation of outcrop analogs has provided basic parameters for a better understanding and initial modeling, but the reconnaissance nature of the present study precluded the coverage of all units. Based on the results from surface data and thermal models, detailed and site-specific investigations would be the next step to assess the geothermal potential for exploitation.

For the development of geothermal resources in the region, short (< 5 years), medium (5 – 10 years) and long-term (> 10 years) strategies are proposed. The short-term strategy should focus on developing hot spring sites for direct-use applications. It would involve an assessment of parameters such as output enthalpy, flow rate, seasonal variation, and fluid chemistry (Barbier, 2002; Moeck, 2014). Accordingly, this would require a feasibility study to determine the best direct-use application based on demand and resource capacity. Lower cost, ease of access, and short operational time would be the key benefits of this short-term plan (Sharmin et al., 2023). Moreover, the success of this plan would garner more acceptance and support in the community and attract investment for medium and long-term strategies.

The medium-term geothermal development plan should focus on exploiting subsurface hydrothermal reservoirs. The exploration should start with the detailed mapping (1:10,000) of the identified geothermal targets for developing geological models. Geochemical and petrophysical data based on extensive sampling of outcrop analog samples should be compiled. Gravity and resistivity surveys would then be carried out to acquire information on deep structures and conductive zones. Incorporating subsurface data and petrophysical parameters in the geological model would help reservoir characterization and modeling. Reservoir models then provide a baseline on which numerical simulations could run with combinations of multiple parameters and scenarios. Drilling should initiate from shallow hydrothermal reservoirs to provide vital information from core samples and well logs about reservoir conditions (pressure and temperature) that are important for updating reservoir

models. Depending upon a prospect's capacity, it could be used for industrial applications or electric power production.

The long-term strategy should focus on developing deep HDR as EGS systems. Exploration for HDR geothermal resources should expand beyond hot spring areas and incorporate intensive large-scale geophysical and geological surveys. The geophysical surveys should be airborne for greater coverage. These airborne surveys should include gamma spectrometry, gravity, and magnetics to provide information on the area's radioelement distribution, density structure, and magnetization (Curie depth), respectively. This data would allow the establishment of 3D geological and thermal models, which would then require calibration from the surface heat flow measurements (from boreholes or deep mines). Although the thermal models presented in Chapter 6 indicate the promising potential of such resources in the Nanga Parbat and Karakoram regions, the enormous financial risks, complex geodynamic settings, and lack of technical expertise would make implementing this strategy challenging. Nonetheless, assuming short and medium-term plans are successfully implemented, one can be optimistic that this strategy would also be adopted. In this regard, worldwide successful examples of exploitation of HDR reservoirs in Upper Rhine Graben and Cornwall provide guidelines and valuable lessons for exploration and development (Ledesert et al., 2022).

References

Abdulagatova, Z. Z., Kallaev, S. N., Omarov, Z. M., Bakmaev, A. G., Grigor'ev, B. A., & Abdulagatov, I. M. (2020). Temperature effect on thermal-diffusivity and heat-capacity and derived values of thermal-conductivity of reservoir rock materials. Geomechanics and Geophysics for Geo-Energy and Geo-Resources, 6(1), 8. https://doi.org/10.1007/s40948-019-00131-2

Abrams, M., & Yamaguchi, Y. (2019). Twenty years of ASTER contributions to lithologic mapping and mineral exploration. Remote Sensing, 11(11), 1394.

Acton, C. E., Priestley, K., Gaur, V. K., & Rai, S. S. (2010). Group velocity tomography of the Indo-Eurasian collision zone. Journal of Geophysical Research: Solid Earth, 115(B12), 2009JB007021. https://doi.org/10.1029/2009JB007021

Aghahosseini, A., & Breyer, C. (2020). From hot rock to useful energy: A global estimate of enhanced geothermal systems potential. Applied Energy, 279, 115769.

Ahmad, M., Akram, W., Ahmad, N., Tasneem, M. A., Rafiq, M., & Latif, Z. (2002). Assessment of reservoir temperatures of thermal springs of the northern areas of Pakistan by chemical and isotope geothermometry. Geothermics, 31(5), 613–631.

Ahmad, M., Akram, W., Hussain, S. D., Sajjad, M. I., & Zafar, M. S. (2001). Origin and subsurface history of geothermal water of Murtazabad area, Pakistan—Isotopic evidence. Applied Radiation and Isotopes, 55(5), 731–736.

Ahmad, M., Rafiq, M., Iqbal, N., Akram, W., Tasneem, M. A., & Ali, M. (2005). Investigation of major geothermal fields of Pakistan using isotope and chemical techniques. Proceedings of the World Geothermal Congress, Antalya, Turkey, 24–29.

Ahmad, T., Arif, M., Qasim, M., & Sajid, M. (2021). Petrology of granitoids from Indus syntaxis, northern Pakistan: Implications for Paleo-Proterozoic A-type magmatism in north-western Indian Plate. Geochemistry, 81(1), 125693.

Ahmadi, H., & Pekkan, E. (2021). Fault-based geological lineaments extraction using remote sensing and GIS—a review. Geosciences, 11(5), 183.

Ai, Y., Zhang, J., Dong, M., Wang, B., & Fang, G. (2021). Heat generation effects from shear friction along Xianshui river strike-slip fault in western Sichuan, China. Geothermics, 89, 101936.

Alessio, K. L., Hand, M., Kelsey, D. E., Williams, M. A., Morrissey, L. J., & Barovich, K. (2018). Conservation of deep crustal heat production. Geology, 46(4), 335–338.

Allen, T., & Chamberlain, C. P. (1991). Metamorphic evidence for an inverted crustal section, with constraints on the Main Karakorum Thrust, Baltistan, northern Pakistan. Journal of Metamorphic Geology, 9(4), 403–418.

Anees, M., Kley, J., Leiss, B., Hindle, D., Wajid, A. A., Wagner, B., Shah, M. M., & Luijendijk, E. (2023). Application of in-situ gamma spectrometry for radiogenic heat production estimation in the Western Himalaya, Kohistan, and Karakoram in northern Pakistan. Geothermal Energy, 11(1), 29. https://doi.org/10.1186/s40517-023-00273-3

Anees, M., Sosa, G., van den Kerkhof, A., Leiss, B., Kley, J., Shah, M. M., & Weydt, L. M. (2023). Granitoids of the western Himalaya and Karakoram as potential geothermal reservoirs – A petrological, geochemical and petrophysical study (submitted).

Arnorsson, S. (2000). Isotopic and chemical techniques in geothermal exploration, development and use. Sampling methods, data handling, interpretation. International Atomic Energy Agency (IAEA), Vienna, Austria.

Arnórsson, S., Bjarnason, J. Ö., Giroud, N., Gunnarsson, I., & Stefánsson, A. (2006). Sampling and analysis of geothermal fluids. Geofluids, 6(3), 203–216. https://doi.org/10.1111/j.1468-8123.2006.00147.x

Artemieva, I. M., Thybo, H., Jakobsen, K., Sørensen, N. K., & Nielsen, L. S. (2017). Heat production in granitic rocks: Global analysis based on a new data compilation GRANITE2017. Earth-Science Reviews, 172, 1–26.

Atef, H., Abd El-Gawad, A. M. S., Abdel Zaher, M., & Farag, K. S. I. (2016). The contribution of gravity method in geothermal exploration of southern part of the Gulf of Suez–Sinai region, Egypt. NRIAG Journal of Astronomy and Geophysics, 5(1), 173–185.

Awais, M., Liu, X.-C., Qasim, M., & Wu, F.-Y. (2022). U (-Th)–Pb age and petrogenesis of Shigar leucogranites, Karakoram Metamorphic Complex, North Pakistan. Geological Journal, 57(10), 4052–4073.

Awdal, A. H., Braathen, A., Wennberg, O. P., & Sherwani, G. H. (2013). The characteristics of fracture networks in the Shiranish Formation of the Bina Bawi Anticline; comparison with the Taq Taq Field, Zagros, Kurdistan, NE Iraq. Petroleum Geoscience, 19(2), 139–155. https://doi.org/10.1144/petgeo2012-036

Bächler, D., Kohl, T., & Rybach, L. (2003). Impact of graben-parallel faults on hydrothermal convection—-Rhine Graben case study. Physics and Chemistry of the Earth, Parts A/B/C, 28(9–11), 431–441.

Badshah, M. S., Gnos, E., Jan, M. Q., & Afridi, M. I. (2000). Stratigraphic and tectonic evolution of the northwestern Indian plate and Kabul Block. Geological Society, London, Special Publications, 170(1), 467–476. https://doi.org/10.1144/GSL.SP.2000.170.01.25

Bakht, M. S. (2000). An overview of geothermal resources of Pakistan. Proceedings of the World Geothermal Congress, 77–83.

Bär, K., Arbarim, R., Turan, A., Schulz, K., Mahmoodpour, S., Leiss, B., Wagner, B., Sosa, G., Ford, K., & Trullenque, G. (2020). Database of Petrophysical and Fluid Properties and Recommendations for Model Parametrization of the Four Variscan Reservoir Types. MEET Report, Deliverable D, 5.

Barbier, E. (2002). Geothermal energy technology and current status: An overview. Renewable and Sustainable Energy Reviews, 6(1), 3–65. https://doi.org/10.1016/S1364-0321(02)00002-3

Barbier, M., Leprêtre, R., Callot, J.-P., Gasparrini, M., Daniel, J.-M., Hamon, Y., Lacombe, O., & Floquet, M. (2012). Impact of fracture stratigraphy on the paleo-hydrogeology of the Madison Limestone in two basement-involved folds in the Bighorn basin, (Wyoming, USA). Tectonophysics, 576–577, 116–132. https://doi.org/10.1016/j.tecto.2012.06.048

Bard, J. P. (1980). The Kohistan sequence: Crust and mantle of an island arc. Proc. Int. Committe Geodyn., Group 6 Meet., 13, 87–93.

Bea, F. (1996). Residence of REE, Y, Th and U in granites and crustal protoliths; implications for the chemistry of crustal melts. Journal of Petrology, 37(3), 521–552.

Bea, F. (2012). The sources of energy for crustal melting and the geochemistry of heat-producing elements. Lithos, 153, 278–291.

Beamish, D., & Busby, J. (2016). The Cornubian geothermal province: Heat production and flow in SW England: estimates from boreholes and airborne gamma-ray measurements. Geothermal Energy, 4(1), 1–25.

Beardsmore, G. R. (2005). Thermal modelling of the hot dry rock geothermal resource beneath GEL99 in the Cooper Basin. Proceedings World Geothermal Congress, Antalya, Turkey, 24–29 April.

Beaufort, D., Patrier, P., Meunier, A., & Ottaviani, M. M. (1992). Chemical variations in assemblages including epidote and/or chlorite in the fossil hydrothermal system of Saint Martin (Lesser Antilles). Journal of Volcanology and Geothermal Research, 51(1–2), 95–114.

Beck, R. A., Burbank, D. W., Sercombe, W. J., Khan, A. M., & Lawrence, R. D. (1996). Late Cretaceous ophiolite obduction and Paleocene India-Asia collision in the westernmost Himalaya. Geodinamica Acta, 9(2–3), 114–144. https://doi.org/10.1080/09853111.1996.11105281

Bertini, G., Casini, M., Gianelli, G., & Pandeli, E. (2006). Geological structure of a long-living geothermal system, Larderello, Italy. Terra Nova, 18(3), 163–169. https://doi.org/10.1111/j.1365-3121.2006.00676.x

Bertrand, J.-M., Kienast, J.-R., & Pinardon, J.-L. (1988). Structure and metamorphism of the Karakorum gneisses in the Braldu-Baltoro Valley (North Pakistan). Geodinamica Acta, 2(3), 135–150.

Bhukta, S. K., Sain, K., & Tewari, H. C. (2006). Crustal Structure Along the Lawrencepur-Astor Profile in the Northwest Himalayas. Pure and Applied Geophysics, 163(7), 1257–1277. https://doi.org/10.1007/s00024-006-0070-x

Borneman, N. L., Hodges, K. V., Van Soest, M. C., Bohon, W., Wartho, J.-A., Cronk, S. S., & Ahmad, T. (2015). Age and structure of the Shyok suture in the Ladakh region of northwestern India: Implications for slip on the Karakoram fault system: AGE OF SHYOK SUTURE. Tectonics, 34(10), 2011–2033. https://doi.org/10.1002/2015TC003933

Bouilhol, P., Jagoutz, O., Hanchar, J. M., & Dudas, F. O. (2013). Dating the India–Eurasia collision through arc magmatic records. Earth and Planetary Science Letters, 366, 163–175.

Boynton, W. V. (1984). Cosmochemistry of the rare earth elements: Meteorite studies. In Developments in geochemistry (Vol. 2, pp. 63–114). Elsevier.

Brookfield, M. E., & Reynolds, P. H. (1981). Late Cretaceous emplacement of the Indus suture zone ophiolitic melanges and an Eocene-Oligocene magmatic arc on the northern edge of the Indian plate. Earth and Planetary Science Letters, 55(1), 157–162.

Brown, C. S. (2022). Regional geothermal resource assessment of hot dry rocks in Northern England using 3D geological and thermal models. Geothermics, 105, 102503.

Budiono, A., Suyitno, S., Rosyadi, I., Faishal, A., & Ilyas, A. X. (2022). A Systematic Review of the Design and Heat Transfer Performance of Enhanced Closed-Loop Geothermal Systems. Energies, 15(3), Article 3. https://doi.org/10.3390/en15030742

Burbank, D. W., & Beck, R. A. (1989). Early Pliocene uplift of the Salt Range; Temporal constraints on thrust wedge development, northwest Himalaya, Pakistan. In L. L. Malinconico Jr. & R. J. Lillie (Eds.), Tectonics of the western Himalayas (Vol. 232, p. 0). Geological Society of America. https://doi.org/10.1130/SPE232-p113

Burg, J., Jagoutz, O., Dawood, H., & Hussain, S. S. (2006). Precollision tilt of crustal blocks in rifted island arcs: Structural evidence from the Kohistan Arc. Tectonics, 25(5), 2005TC001835. https://doi.org/10.1029/2005TC001835

Burg, J. -P., & Gerya, T. V. (2005). The role of viscous heating in Barrovian metamorphism of collisional orogens: Thermomechanical models and application to the Lepontine Dome in the Central Alps. Journal of Metamorphic Geology, 23(2), 75–95. https://doi.org/10.1111/j.1525-1314.2005.00563.x

Burg, J.-P., & Bouilhol, P. (2019). Timeline of the South Tibet–Himalayan belt: The geochronological record of subduction, collision, and underthrusting from zircon and monazite U–Pb ages. Canadian Journal of Earth Sciences, 56(12), 1318–1332.

Burtman, V. S., & Molnar, P. (1993). Geological and geophysical evidence for deep subduction of continental crust beneath the Pamir.

Butler, R. W. (2019). Tectonic evolution of the Himalayan syntaxes: The view from Nanga Parbat. Geological Society, London, Special Publications, 483(1), 215–254.

Butler, R. W., Harris, N. B., & Whittington, A. G. (1997). Interactions between deformation, magmatism and hydrothermal activity during active crustal thickening: A field example from Nanga Parbat, Pakistan Himalayas. Mineralogical Magazine, 61(404), 37–52.

Butler, R. W., & Prior, D. J. (1988). Tectonic controls on the uplift of the Nanga Parbat Massif, Pakistan Himalayas. Nature, 333(6170), 247–250.

Butler, R. W., Prior, D. J., & Knipe, R. J. (1989). Neotectonics of the Nanga Parbat syntaxis, Pakistan, and crustal stacking in the Northwest Himalayas. Earth and Planetary Science Letters, 94(3–4), 329–343.

Cao, W., Lee, C.-T. A., Yang, J., & Zuza, A. V. (2019). Hydrothermal circulation cools continental crust under exhumation. Earth and Planetary Science Letters, 515, 248–259.

Carosi, R., Montomoli, C., Langone, A., Turina, A., Cesare, B., Iaccarino, S., Fascioli, L., Visonà, D., Ronchi, A., & Rai, S. M. (2015). Eocene partial melting recorded in peritectic garnets from kyanite-gneiss, Greater Himalayan Sequence, central Nepal. Geological Society, London, Special Publications, 412(1), 111–129. https://doi.org/10.1144/SP412.1

Carson, C. J., & Pittard, M. (2012). A reconnaissance crustal heat production assessment of the Australian Antarctic Territory (AAT) (Record 2012/63). Geoscience Australia.

Chamberlain, C. P., Koons, P. O., Meltzer, A. S., Park, S. K., Craw, D., Zeitler, P., & Poage, M. A. (2002). Overview of hydrothermal activity associated with active orogenesis and metamorphism: Nanga Parbat, Pakistan Himalaya. American Journal of Science, 302(8), 726–748.

Chamberlain, C. P., Zeitler, P. K., Barnett, D. E., Winslow, D., Poulson, S. R., Leahy, T., & Hammer, J. E. (1995). Active hydrothermal systems during the recent uplift of Nanga Parbat, Pakistan Himalaya. Journal of Geophysical Research: Solid Earth, 100(B1), 439–453.

Chandrasekharam, D., & Bundschuh, J. (2008). Low-enthalpy geothermal resources for power generation. CRC press.

Charléty, J., Cuenot, N., Dorbath, C., & Dorbath, L. (2006). Tomographic study of the seismic velocity at the Soultz-sous-Forêts EGS/HDR site. Geothermics, 35(5–6), 532–543.

Chen, Z., Du, J., Zhou, X., Yi, L., Liu, L., Xie, C., Cui, Y., & Li, Y. (2014). Hydrochemistry of the Hot Springs in Western Sichuan Province Related to the Wenchuan 8.0 Earthquake. The Scientific World Journal, 2014. https://www.hindawi.com/journals/tswj/2014/901432/

Ciriaco, A. E., Zarrouk, S. J., & Zakeri, G. (2020). Geothermal resource and reserve assessment methodology: Overview, analysis and future directions. Renewable and Sustainable Energy Reviews, 119, 109515.

Clauser, C., & Huenges, E. (1995). Thermal conductivity of rocks and minerals. Rock Physics and Phase Relations: A Handbook of Physical Constants, 3, 105–126.

Coolbaugh, M. F., Kratt, C., Fallacaro, A., Calvin, W. M., & Taranik, J. V. (2007). Detection of geothermal anomalies using advanced spaceborne thermal emission and reflection radiometer (ASTER) thermal infrared images at Bradys Hot Springs, Nevada, USA. Remote Sensing of Environment, 106(3), 350–359.

Coward, M. P., Rex, D. C., Asif Khan, M., Windley, B. F., Broughton, R. D., Luff, I. W., Petterson, M. G., & Pudsey, C. J. (1986). Collision tectonics in the NW Himalayas. Geological Society, London, Special Publications, 19(1), 203–219.

Craig, J., Absar, A., Bhat, G., Cadel, G., Hafiz, M., Hakhoo, N., Kashkari, R., Moore, J., Ricchiuto, T. E., & Thurow, J. (2013). Hot springs and the geothermal energy potential of Jammu & Kashmir State, NW Himalaya, India. Earth-Science Reviews, 126, 156–177.

Craw, D., Chamberlain, C. P., Zeitler, P. K., & Koons, P. O. (1997). Geochemistry of a dry steam geothermal zone formed during rapid uplift of Nanga Parbat, northern Pakistan. Chemical Geology, 142(1–2), 11–22.

Craw, D., Koons, P. O., Winslow, D., Chamberlain, C. P., & Zeitler, P. (1994). Boiling fluids in a region of rapid uplift, Nanga Parbat massif, Pakistan. Earth and Planetary Science Letters, 128(3–4), 169–182.

Crawford, M. B., & Searle, M. P. (1992). Field relationships and geochemistry of pre-collisional (India-Asia) granitoid magmatism in the central Karakoram, northern Pakistan. Tectonophysics, 206(1–2), 171–192.

Crawford, M. B., & Windley, B. F. (1990). Leucogranites of the Himalaya/Karakoram: Implications for magmatic evolution within collisional belts and the study of collision-related leucogranite petrogenesis. Journal of Volcanology and Geothermal Research, 44(1–2), 1–19.

Cronin, V. S., Schurter, G. J., & Sverdrup, K. A. (1993). Preliminary Landsat lineament analysis of the northern Nanga Parbat-Haramosh Massif, northwest Himalaya. Geological Society, London, Special Publications, 74(1), 193–206. https://doi.org/10.1144/GSL.SP.1993.074.01.14

Crósta, A. P., De Souza Filho, C. R., Azevedo, F., & Brodie, C. (2003). Targeting key alteration minerals in epithermal deposits in Patagonia, Argentina, using ASTER imagery and principal component analysis. International Journal of Remote Sensing, 24(21), 4233–4240. https://doi.org/10.1080/0143116031000152291

Crowley, J. L., Waters, D. J., Searle, M. P., & Bowring, S. A. (2009). Pleistocene melting and rapid exhumation of the Nanga Parbat massif, Pakistan: Age and P–T conditions of accessory mineral growth in migmatite and leucogranite. Earth and Planetary Science Letters, 288(3–4), 408–420.

Debon, F., Le Fort, P., Dautel, D., Sonet, J., & Zimmermann, J. L. (1987). Granites of western Karakorum and northern Kohistan (Pakistan): A composite Mid-Cretaceous to upper Cenozoic magmatism. Lithos, 20(1), 19–40.

Diamond, L. W., Wanner, C., & Waber, H. N. (2018). Penetration depth of meteoric water in orogenic geothermal systems. Geology, 46(12), 1063–1066.

Dickson, B. (1985). Radium isotopes in saline seepages, south-western Yilgarn, Western Australia. Geochimica et Cosmochimica Acta, 49(2), 361–368.

DIN 52102. (1988). Determination of absolute density, dry density, compactness and porosity of natural stone and mineral aggregates, German Standard DIN. Deutsches Institut für Normung, Berlin.

DiPietro, J. A., Hussain, A., Ahmad, I., & Khan, M. A. (2000). The main mantle thrust in Pakistan: Its character and extent. Geological Society, London, Special Publications, 170(1), 375–393.

DiPietro, J. A., & Pogue, K. R. (2004). Tectonostratigraphic subdivisions of the Himalaya: A view from the west. Tectonics, 23(5), 2003TC001554. https://doi.org/10.1029/2003TC001554

Eldosouky, A. M., Abdelkareem, M., & Elkhateeb, S. O. (2017). Integration of remote sensing and aeromagnetic data for mapping structural features and hydrothermal alteration zones in Wadi Allaqi area, South Eastern Desert of Egypt. Journal of African Earth Sciences, 130, 28–37.

Erdi-Krausz, G., Matolin, M., Minty, B., Nicolet, J. P., Reford, W. S., & Schetselaar, E. M. (2003). Guidelines for radioelement mapping using gamma ray spectrometry data. International Atomic Energy Agency (IAEA).

Faccenda, M., Gerya, T. V., & Chakraborty, S. (2008). Styles of post-subduction collisional orogeny: Influence of convergence velocity, crustal rheology and radiogenic heat production. Lithos, 103(1–2), 257–287.

Fagereng, Å., & Biggs, J. (2019). New perspectives on 'geological strain rates' calculated from both naturally deformed and actively deforming rocks. Journal of Structural Geology, 125, 100–110.

Fairley, J. P. (2016). Models and modeling: An introduction for Earth and environmental scientists. John Wiley & Sons.

Faisal, S., Larson, K. P., Camacho, A., & Coutand, I. (2018). Cooling, exhumation, and deformation in the Hindu Kush, NW Pakistan: New constraints from preliminary 40Ar/39Ar and fission track analyses. Journal of Asian Earth Sciences, 158, 415–427.

Fraser, J. E., Searle, M. P., Parrish, R. R., & Noble, S. R. (2001). Chronology of deformation, metamorphism, and magmatism in the southern Karakoram Mountains. Geological Society of America Bulletin, 113(11), 1443–1455.

Frost, B. R., Barnes, C. G., Collins, W. J., Arculus, R. J., Ellis, D. J., & Frost, C. D. (2001). A geochemical classification for granitic rocks. Journal of Petrology, 42(11), 2033–2048.

Fuchs, S., Förster, A., & Norden, B. (2022). Evaluation of the terrestrial heat flow in Germany: A case study for the reassessment of global continental heat-flow data. Earth-Science Reviews, 235, 104231.

Fulignati, P. (2020). Clay minerals in hydrothermal systems. Minerals, 10(10), 919.

Furlong, K. P., & Chapman, D. S. (2013). Heat Flow, Heat Generation, and the Thermal State of the Lithosphere. Annual Review of Earth and Planetary Sciences, 41(1), 385–410. https://doi.org/10.1146/annurev.earth.031208.100051

Furlong, K. P., Kirby, E., Creason, C. G., Kamp, P. J., Xu, G., Danišík, M., Shi, X., & Hodges, K. V. (2021). Exploiting thermochronology to quantify exhumation histories and patterns of uplift along the margins of Tibet. Frontiers in Earth Science, 9, 688374.

Gaetani, M. (1997). The Nonh Karakoram in the framework of the Cimmerian blocks. Him. Geol, 18, 33–48.

Gaetani, M., Angiolini, L., Nicora, A., Sciunnach, D., Le Fort, P., Tanoli, S., & Khan, A. (1996). Reconnaissance geology in Upper Chitral, Baroghil and Karambar districts (northern Karakorum, Pakistan). Geologische Rundschau, 85(4), 683–704.

Gaetani, M., Garzanti, E., Jadoul, F., Nicora, A., Tintori, A., Pasini, M., & Khan, K. S. A. (1990). The north Karakorum side of the Central Asia geopuzzle. Geological Society of America Bulletin, 102(1), 54–62.

Gaetani, M., Jadoul, F., Erba, E., & Garzanti, E. (1993). Jurassic and Cretaceous orogenic events in the North Karakoram: Age constraints from sedimentary rocks. Geological Society, London, Special Publications, 74(1), 39–52. https://doi.org/10.1144/GSL.SP.1993.074.01.04

Gansser, A. (1980). The significance of the Himalayan suture zone. Tectonophysics, 62(1–2), 37–52.

Gao, G., Kang, G., Li, G., Bai, C., & Wu, Y. (2017). An analysis of crustal magnetic anomaly and Curie surface in west Himalayan syntaxis and adjacent area. Acta Geodaetica et Geophysica, 52(3), 407–420. https://doi.org/10.1007/s40328-016-0179-z

Gao, G., Lu, Q., Wang, J., & Kang, G. (2021). Constraining crustal thickness and lithospheric thermal state beneath the northeastern Tibetan Plateau and adjacent regions from gravity, aeromagnetic, and heat flow data. Journal of Asian Earth Sciences, 212, 104743.

Gao, Z., Liu, J., Li, F., Wang, M., Feng, J., & Wu, G. (2019). Hydrochemical characteristics and temporal variations of geothermal water quality in Tangtou, Shandong, China. Water, 11(8), 1643.

Garzanti, E., Baud, A., & Mascle, G. (1987). Sedimentary record of the northward flight of India and its collision with Eurasia (Ladakh Himalaya, India). Geodinamica Acta, 1(4–5), 297–312. https://doi.org/10.1080/09853111.1987.11105147

Genter, A., Evans, K., Cuenot, N., Fritsch, D., & Sanjuan, B. (2010). Contribution of the exploration of deep crystalline fractured reservoir of Soultz to the knowledge of enhanced geothermal systems (EGS). Comptes Rendus Geoscience, 342(7–8), 502–516.

Géraud, Y., Rosener, M., Surma, F., Place, J., Le Garzic, E., & Diraison, M. (2010). Physical properties of fault zones within a granite body: Example of the Soultz-sous-Forêts geothermal site. Comptes Rendus Geoscience, 342(7–8), 566–574.

Ghani, H., Zeilinger, G., Sobel, E. R., & Heidarzadeh, G. (2018). Structural variation within the Himalayan fold and thrust belt: A case study from the Kohat-Potwar Fold Thrust Belt of Pakistan. Journal of Structural Geology, 116, 34–46.

Gillespie, M. R., Crane, E. J., & Barron, H. F. (2013). Deep geothermal energy potential in Scotland (Commissioned Report CR/12/131; p. 129). British Geological Survey.

Gnojek, I., Sedlak, J., Rapprich, V., Skacelova, Z., Mlcoch, B., Krentz, O., & Casar-Garcia, R. (2018). Structure of the Carboniferous Altenberg-Teplice Caldera (Eastern part of the Krusne hory/Erzgebirge Mts.) revealed by combined airborne and ground gamma-ray spectrometry. Journal of Geosciences, 63(1), 3–20.

Goes, S., Hasterok, D., Schutt, D. L., & Klöcking, M. (2020). Continental lithospheric temperatures: A review. Physics of the Earth and Planetary Interiors, 306, 106509. https://doi.org/10.1016/j.pepi.2020.106509

Gokarn, S. G., Gupta, G., Rao, C. K., & Selvaraj, C. (2002). Electrical structure across the Indus Tsangpo suture and Shyok suture zones in NW Himalaya using magnetotelluric studies. Geophysical Research Letters, 29(8), 92–1.

Götze, J. (2012). Application of cathodoluminescence microscopy and spectroscopy in geosciences. Microscopy and Microanalysis, 18(6), 1270–1284.

Green, O. R., Searle, M. P., Corfield, R. I., & Corfield, R. M. (2008). Cretaceous-Tertiary Carbonate Platform Evolution and the Age of the India-Asia Collision along the Ladakh Himalaya (Northwest India). The Journal of Geology, 116(4), 331–353. https://doi.org/10.1086/588831

Grujic, D., Warren, C. J., & Wooden, J. L. (2011). Rapid synconvergent exhumation of Miocene-aged lower orogenic crust in the eastern Himalaya. Lithosphere, 3(5), 346–366.

Guerra, I., Luongo, G., Maistrello, M., & Scarascia, S. (1983). Deep seismic sounding along the profile Lawrencepur-Sango Sar (Nanga Parbat). Bull. Geofis. Teor. Appl, 25, 211–219.

Guevara, V. E., Smye, A. J., Caddick, M. J., Searle, M. P., Olsen, T., Whalen, L., Kylander-Clark, A. R. C., Jercinovic, M. J., & Waters, D. J. (2022). A modern pulse of ultrafast exhumation and diachronous crustal melting in the Nanga Parbat Massif. Science Advances, 8(31), eabm2689. https://doi.org/10.1126/sciadv.abm2689

Hacker, B. R., Kelemen, P. B., & Behn, M. D. (2015). Continental Lower Crust. Annual Review of Earth and Planetary Sciences, 43(1), 167–205. https://doi.org/10.1146/annurev-earth-050212-124117

Hanson, C. R. (1989). The northern suture in the Shigar valley, Baltistan, northern Pakistan. In L. L. Malinconico Jr. & R. J. Lillie (Eds.), Tectonics of the western Himalayas (Vol. 232, p. 0). Geological Society of America. https://doi.org/10.1130/SPE232-p203

Harker, A. (1909). The Natural History of Igneous Rocks. Journal of Geology, 17(5), 488–489.

Harris, N., Ayres, M., & Massey, J. (1995). Geochemistry of granitic melts produced during the incongruent melting of muscovite: Implications for the extraction of Himalayan leucogranite magmas. Journal of Geophysical Research: Solid Earth, 100(B8), 15767–15777.

Haselwimmer, C., & Prakash, A. (2013). Thermal Infrared Remote Sensing of Geothermal Systems. In C. Kuenzer & S. Dech (Eds.), Thermal Infrared Remote Sensing (Vol. 17, pp. 453–473). Springer Netherlands. https://doi.org/10.1007/978-94-007-6639-6_22

Hasterok, D., & Chapman, D. S. (2011). Heat production and geotherms for the continental lithosphere. Earth and Planetary Science Letters, 307(1–2), 59–70.

Hasterok, D., Gard, M., & Webb, J. (2018). On the radiogenic heat production of metamorphic, igneous, and sedimentary rocks. Geoscience Frontiers, 9(6), 1777–1794.

Hazarika, D., Sen, K., & Kumar, N. (2014). Characterizing the intracrustal low velocity zone beneath northwest India–Asia collision zone. Geophysical Journal International, 199(3), 1338–1353.

Held, S., Genter, A., Kohl, T., Kölbel, T., Sausse, J., & Schoenball, M. (2014). Economic evaluation of geothermal reservoir performance through modeling the complexity of the operating EGS in Soultz-sous-Forêts. Geothermics, 51, 270–280.

Hillis, R., Hand, M., Mildren, S., Reid, P., Reynolds, S., & Nelson, E. (2004). Hot dry rock geothermal exploration in Australia. ASEG Extended Abstracts, 2004(1), 1–4.

Hindle, D. (2023). Steady-nl-heat [Computer software]. https://doi.org/10.5281/zenodo.7875952

Hindle, D., & Besson, O. (2023). A corrected finite-difference scheme for the flexure equation with abrupt changes in coefficient. Solid Earth, 14(2), 197–212. https://doi.org/10.5194/se-14-197-2023

Hochstein, M. P., & Regenauer-Lieb, K. (1998). Heat generation associated with collision of two plates: The Himalayan geothermal belt. Journal of Volcanology and Geothermal Research, 83(1), 75–92. https://doi.org/10.1016/S0377-0273(98)00018-3

Hochstein, M. P., & Zhongke, Y. (1995). The Himalayan Geothermal Belt (Kashmir, Tibet, West Yunnan). In M. Yamano & M. L. Gupta (Eds.), Terrestrial Heat Flow and Geothermal Energy in Asia, IUGG Monograph, Oxford-IBH Publishing Co, New Delhi (pp. 331–386).

Huenges, E. (Ed.). (2010). Geothermal Energy Systems: Exploration, Development, and Utilization (1st ed.). Wiley. https://doi.org/10.1002/9783527630479

Hugman Iii, R. H. H., & Friedman, M. (1979). Effects of texture and composition on mechanical behavior of experimentally deformed carbonate rocks. AAPG Bulletin, 63(9), 1478–1489.

Huston, D. L., Ayling, B., Connolly, D., Huston, D. L., Lewis, B., Mernagh, T. P., Schofield, A., Skirrow, R. S., & van der Wielen, S. E. (2010). An assessment of the uranium and geothermal potential of north Queensland ([Record 2010/14]). Geoscience Australia.

IAEA. (1991). Airborne Gamma Ray Spectrometer Surveying; Technical Reports Series No. 323 [Technical Reports Series No. 323]. International Atomic Energy Agency.

Jadoon, I. A. K., Ding, L., Jadoon, S.-R. K., Bhatti, Z. I., Shah, S. T. H., & Qasim, M. (2021). Lithospheric Deformation and Active Tectonics of the NW Himalayas, Hindukush, and Tibet. Lithosphere, 2021(1), 7866954. https://doi.org/10.2113/2021/7866954

Jagoutz, O., & Schmidt, M. W. (2012). The formation and bulk composition of modern juvenile continental crust: The Kohistan arc. Chemical Geology, 298, 79–96.

Jamieson, R. A., & Beaumont, C. (2011). Coeval thrusting and extension during lower crustal ductile flow – implications for exhumation of high-grade metamorphic rocks. Journal of Metamorphic Geology, 29(1), 33–51. https://doi.org/10.1111/j.1525-1314.2010.00908.x

Jamieson, R. A., Beaumont, C., Nguyen, M. H., & Lee, B. (2002). Interaction of metamorphism, deformation and exhumation in large convergent orogens. Journal of Metamorphic Geology, 20(1), 9–24. https://doi.org/10.1046/j.0263-4929.2001.00357.x

Jan, M. Q., & Howie, R. A. (1981). The mineralogy and geochemistry of the metamorphosed basic and ultrabasic rocks of the Jijal complex, Kohistan, NW Pakistan. Journal of Petrology, 22(1), 85–126.

Jaupart, C., & Mareschal, J. C. (2005). Constraints on crustal heat production from heat flow data. In H. D. Holland & K. K. Turekian (Eds.), The Crust (Rudnick RL ed) (Treatise on Geochemistry, Vol. 3, pp. 65–84). Elsevier-Pergamon.

Jaupart, C., Mareschal, J.-C., & Iarotsky, L. (2016). Radiogenic heat production in the continental crust. Lithos, 262, 398–427. https://doi.org/10.1016/j.lithos.2016.07.017

Jiang, S., Zhang, K., Moore, J., & McLennan, J. (2023). Lessons learned from hydrothermal to hot dry rock exploration and production. Energy Geoscience, 100181. https://doi.org/10.1016/j.engeos.2023.100181

Jochum, K. P., Hofmann, A. W., Ito, E., Seufert, H. M., & White, W. M. (1983). K, U and Th in mid-ocean ridge basalt glasses and heat production, K/U and K/Rb in the mantle. Nature, 306(5942), 431–436.

Julia, F., Vladimir, L., Sergey, R., & David, Z. (2014). Effects of hydrothermal alterations on physical and mechanical properties of rocks in the Kuril–Kamchatka island arc. Engineering Geology, 183, 80–95.

Kana, J. D., Djongyang, N., Danwe Raïdandi, Njandjock Nouck, P., & Abdouramani Dadjé. (2015). A review of geophysical methods for geothermal exploration. Renewable and Sustainable Energy Reviews, 44, 87–95. https://doi.org/10.1016/j.rser.2014.12.026

Kapp, P., & DeCelles, P. G. (2019). Mesozoic–Cenozoic geological evolution of the Himalayan-Tibetan orogen and working tectonic hypotheses. American Journal of Science, 319(3), 159–254.

Kazmi, A. H., & Jan, M. Q. (1997). Geology and tectonics of Pakistan. Graphic publishers.

Kazmi, A. H., Lawrance, R. D., Dawood, H., Snee, L. W., & Hussain, S. S. (1984). Geology of The Indus Suture Zone In The Mingora-Swat Shangla Area Of Swat, N. Pakistan. Journal of Himalayan Earth Sciences, 17.

Kemp, A. I. S., & Hawkesworth, C. J. (2003). Granitic perspectives on the generation and secular evolution of the continental crust. In Treatise on Geochemistry (Vol. 3, pp. 349–410). Elsevier.

Khan, M. A., Treloar, P. J., Khan, M. A., Khan, T., Qazi, M. S., & Jan, M. Q. (1998). Geology of the Chalt–Babusar transect, Kohistan terrane, N. Pakistan: Implications for the constitution and thickening of island-arc crust. Journal of Asian Earth Sciences, 16(2–3), 253–268.

Kind, R., & Yuan, X. (2010). Seismic Images of the Biggest Crash on Earth. Science, 329(5998), 1479–1480. https://doi.org/10.1126/science.1191620

Klee, J., Potel, S., Ledésert, B. A., Hébert, R. L., Chabani, A., Barrier, P., & Trullenque, G. (2021). Fluid-rock interactions in a Paleo-geothermal reservoir (Noble Hills Granite, California, USA). Part 1: Granite pervasive alteration processes away from fracture zones. Geosciences, 11(8), 325.

Koljonen, T., & Rosenberg, R. J. (1974). Rare earth elements in granitic rocks. Lithos, 7(4), 249–261.

Koltzer, N., Scheck-Wenderoth, M., Bott, J., Cacace, M., Frick, M., Sass, I., Fritsche, J.-G., & Bär, K. (2019). The effects of regional fluid flow on deep temperatures (Hesse, Germany). Energies, 12(11), 2081.

Korinkova, D., Svojtka, M., & Kalvoda, J. (2014). Rate of erosion and exhumation of crystalline rocks in the Hunza Karakoram defined by apatite fission track analysis. Acta Geodyn. Geomater, 11, 235–253.

Kruse, F. A. (2004). Comparison of ATREM, ACORN, and FLAASH atmospheric corrections using low-altitude AVIRIS data of Boulder, CO. Summaries of 13th JPL Airborne Geoscience Workshop, Jet Propulsion Lab, Pasadena, CA, 1–10. https://citeseerx.ist.psu.edu/document?repid=rep1&type=pdf&doi=e70b97543dce6ce2e388ded9f0f9c7226c224162

Kruszewski, M., Hofmann, H., Alvarez, F. G., Bianco, C., Haro, A. J., Garduño, V. H., Liotta, D., Trumpy, E., Brogi, A., & Wheeler, W. (2021). Integrated stress field estimation and implications for enhanced geothermal system development in Acoculco, Mexico. Geothermics, 89, 101931.

Kruszewski, M., Montegrossi, G., Parisio, F., & Saenger, E. H. (2022). Borehole observation-based in situ stress state estimation of the Los Humeros geothermal field (Mexico). Geomechanics for Energy and the Environment, 32, 100392.

Kufner, S.-K., Schurr, B., Sippl, C., Yuan, X., Ratschbacher, L., Ischuk, A., Murodkulov, S., Schneider, F., Mechie, J., & Tilmann, F. (2016). Deep India meets deep Asia: Lithospheric indentation,

delamination and break-off under Pamir and Hindu Kush (Central Asia). Earth and Planetary Science Letters, 435, 171–184.

Kukkonen, I. T., & Lahtinen, R. (2001). Variation of radiogenic heat production rate in 2.8–1.8 Ga old rocks in the central Fennoscandian shield. Physics of the Earth and Planetary Interiors, 126(3–4), 279–294.

Kumar, N., Aoudia, A., Guidarelli, M., Babu, V. G., Hazarika, D., & Yadav, D. K. (2019). Delineation of lithosphere structure and characterization of the Moho geometry under the Himalaya–Karakoram–Tibet collision zone using surface-wave tomography. Geological Society, London, Special Publications, 481(1), 19–40.

Kumar, P. S., Menon, R., & Reddy, G. K. (2007). The role of radiogenic heat production in the thermal evolution of a Proterozoic granulite-facies orogenic belt: Eastern Ghats, Indian Shield. Earth and Planetary Science Letters, 254(1–2), 39–54.

Kumar, P. S., Menon, R., & Reddy, G. K. (2009). Heat production heterogeneity of the Indian crust beneath the Himalaya: Insights from the northern Indian Shield. Earth and Planetary Science Letters, 283(1–4), 190–196.

Kumar, P., Yuan, X., Kumar, M. R., Kind, R., Li, X., & Chadha, R. K. (2007). The rapid drift of the Indian tectonic plate. Nature, 449(7164), 894–897.

Kumar, V., Rai, S. S., Hawkins, R., & Bodin, T. (2022). Seismic Imaging of Crust Beneath the Western Tibet-Pamir and Western Himalaya Using Ambient Noise and Earthquake Data. Journal of Geophysical Research: Solid Earth, 127(6), e2021JB022574.

Laurs, B. M., Dilles, J. H., Wairrach, Y., Kausar, A. B., & Snee, L. W. (1998). Geological setting and petrogenesis of symmetrically zoned, miarolitic granitic pegmatites at Stak Nala, Nanga Parbat-Haramosh Massif, northern Pakistan. The Canadian Mineralogist, 36(1), 1–47.

Ledésert, B. A., Hébert, R. L., Trullenque, G., Genter, A., Dalmais, E., & Hérisson, J. (Eds.). (2022). Enhanced Geothermal Systems and other Deep Geothermal Applications throughout Europe: The MEET Project. MDPI. https://doi.org/10.3390/books978-3-0365-6053-3

Leichmann, J., Broska, I., & Zachovalová, K. (2003). Low-grade metamorphic alteration of feldspar minerals: A CL study. Terra Nova, 15(2), 104–108. https://doi.org/10.1046/j.1365-3121.2003.00467.x

Li, A., & Mashele, B. (2009). Crustal structure in the Pakistan Himalaya from teleseismic receiver functions. Geochemistry, Geophysics, Geosystems, 10(12). https://doi.org/10.1029/2009GC002700

Li, W., Chen, Y., Yuan, X., Schurr, B., Mechie, J., Oimahmadov, I., & Fu, B. (2018). Continental lithospheric subduction and intermediate-depth seismicity: Constraints from S-wave velocity structures in the Pamir and Hindu Kush. Earth and Planetary Science Letters, 482, 478–489.

Lippmann, E., & Rauen, A. (2009). Measurements of Thermal Conductivity (TC) and Thermal Diffusivity (TD) by the Optical Scanning Technology. Lippmann and Rauen GbR, Schaufling, Germany, 49.

Lu, S.-M. (2018). A global review of enhanced geothermal system (EGS). Renewable and Sustainable Energy Reviews, 81, 2902–2921.

Lund, J. W., & Toth, A. N. (2021). Direct utilization of geothermal energy 2020 worldwide review. Geothermics, 90, 101915. https://doi.org/10.1016/j.geothermics.2020.101915

Madin, I. P. (1986). Structure and neotectonics of the northwestern Nanga Parbat-Haramosh massif [Master Thesis, Oregon State University]. https://ir.library.oregonstate.edu/concern/graduate_thesis_or_dissertations/2b88qh67s?locale=en

Madin, I. P., Lawrence, R. D., & Ur-Rehman, S. (1989). The northwestern Nanga Parbat–Haramosh Massif; Evidence for crustal uplift at the northwestern corner of the Indian Craton. In L. L. Malinconico Jr. & R. J. Lillie (Eds.), Tectonics of the western Himalayas (Vol. 232, pp. 169–182). Geological Society of America Special Papers.

Mahar, M. A., Mahéo, G., Goodell, P. C., & Pavlis, T. L. (2014). Age and origin of post collision Baltoro granites, south Karakoram, North Pakistan: Insights from in-situ U–Pb, Hf and oxygen isotopic record of zircons. Lithos, 205, 341–358.

Malinconico, L. L. (1986). The structure of the Kohistan-arc terrane in northern Pakistan as inferred from gravity data. Tectonophysics, 124(3–4), 297–307.

Manning, D. A. C., Younger, P. L., Smith, F. W., Jones, J. M., Dufton, D. J., & Diskin, S. (2007). A deep geothermal exploration well at Eastgate, Weardale, UK: A novel exploration concept for low-enthalpy resources. Journal of the Geological Society, 164(2), 371–382.

Mars, J. C., & Rowan, L. C. (2011). ASTER spectral analysis and lithologic mapping of the Khanneshin carbonatite volcano, Afghanistan. Geosphere, 7(1), 276–289.

Marshak, S., & Mitra, G. (1988). Basic methods of structural geology. New Jersey: Prentice Hall.

Martin, C. R., Jagoutz, O., Upadhyay, R., Royden, L. H., Eddy, M. P., Bailey, E., Nichols, C. I. O., & Weiss, B. P. (2020). Paleocene latitude of the Kohistan–Ladakh arc indicates multistage India–Eurasia collision. Proceedings of the National Academy of Sciences, 117(47), 29487–29494. https://doi.org/10.1073/pnas.2009039117

McCay, A. T., Harley, T. L., Younger, P. L., Sanderson, D. C., & Cresswell, A. J. (2014). Gamma-ray spectrometry in geothermal exploration: State of the art techniques. Energies, 7(8), 4757–4780.

McCay, A. T., & Younger, P. L. (2017). Ranking the geothermal potential of radiothermal granites in Scotland: Are any others as hot as the Cairngorms? Scottish Journal of Geology, 53(1), 1–11.

McDonough, W. F., & Sun, S.-S. (1995). The composition of the Earth. Chemical Geology, 120(3–4), 223–253.

McKenzie, D., Jackson, J., & Priestley, K. (2005). Thermal structure of oceanic and continental lithosphere. Earth and Planetary Science Letters, 233(3), 337–349. https://doi.org/10.1016/j.epsl.2005.02.005

McKenzie, D., & Priestley, K. (2016). Speculations on the formation of cratons and cratonic basins. Earth and Planetary Science Letters, 435, 94–104.

McLaren, S., Sandiford, M., Hand, M., Neumann, N., Wyborn, L., & Bastrakova, I. (2003). The hot southern continent: Heat flow and heat production in Australian Proterozoic terranes. In R. R. Hillis & R. D. Müller (Eds.), Evolution and Dynamics of the Australian Plate (Vol. 372, pp. 157–168). Geological Society of America.

Mechie, J., Yuan, X., Schurr, B., Schneider, F., Sippl, C., Ratschbacher, L., Minaev, V., Gadoev, M., Oimahmadov, I., & Abdybachaev, U. (2012). Crustal and uppermost mantle velocity structure along a profile across the Pamir and southern Tien Shan as derived from project TIPAGE wide-angle seismic data. Geophysical Journal International, 188(2), 385–407.

Meigs, A. J., Burbank, D. W., & Beck, R. A. (1995). Middle-late Miocene (> 10 Ma) formation of the Main Boundary thrust in the western Himalaya. Geology, 23(5), 423–426.

Meixner, A. J., Kirkby, A. L., Lescinsky, D. T., & Horspool, N. (2012). The Cooper Basin 3D map version 2: Thermal modelling and temperature uncertainty (Record 60; p. 52). Geoscience Australia.

Meltzer, A., Sarker, G., Beaudoin, B., Seeber, L., & Armbruster, J. (2001). Seismic characterization of an active metamorphic massif, Nanga Parbat, Pakistan Himalaya. Geology, 29(7), 651–654.

Middlemost, E. A. (1994). Naming materials in the magma/igneous rock system. Earth-Science Reviews, 37(3–4), 215–224.

Miller, C. F., & Mittlefehldt, D. W. (1984). Extreme fractionation in felsic magma chambers: A product of liquid-state diffusion or fractional crystallization? Earth and Planetary Science Letters, 68(1), 151–158.

Minty, B. R. S. (1997). Fundamentals of airborne gamma-ray spectrometry. AGSO Journal of Australian Geology and Geophysics, 17, 39–50.

Minty, B., & Wilford, J. (2004). Radon effects in ground gamma-ray spectrometric surveys. Exploration Geophysics, 35(4), 312–318.

Moeck, I. S. (2014). Catalog of geothermal play types based on geologic controls. Renewable and Sustainable Energy Reviews, 37, 867–882. https://doi.org/10.1016/j.rser.2014.05.032

Morad, S., El-Ghali, M. a. K., Caja, M. A., Sirat, M., Al-Ramadan, K., & Mansurbeg, H. (2010). Hydrothermal alteration of plagioclase in granitic rocks from Proterozoic basement of SE Sweden. Geological Journal, 45(1), 105–116. https://doi.org/10.1002/gj.1178

Moska, R., Labus, K., Kasza, P., & Moska, A. (2023). Geothermal Potential of Hot Dry Rock in South-East Baltic Basin Countries—A Review. Energies, 16(4), Article 4. https://doi.org/10.3390/en16041662

Muhammad, S., & Haq, A. (2022). Spatial distribution of radon contamination in hot springs water and its cancer and non-cancer risks in the Hunza-Nagar valley, Pakistan.

Mukai, M., Yamaguchi, T., Komura, K., Furumoto, M., & Nagao, T. (1999). Measurement of radioactive heat generation in rocks by means of gamma ray spectrometry Vertical distribution of heat source in the island arc crust. Proceedings of the Japan Academy, Series B, 75(7), 181–185.

Müller, A., Seltmann, R., & Behr, H.-J. (2000). Application of cathodoluminescence to magmatic quartz in a tin granite–case study from the Schellerhau Granite Complex, Eastern Erzgebirge, Germany. Mineralium Deposita, 35, 169–189.

Najman, Y., Jenks, D., Godin, L., Boudagher-Fadel, M., Millar, I., Garzanti, E., Horstwood, M., & Bracciali, L. (2017). The Tethyan Himalayan detrital record shows that India–Asia terminal collision occurred by 54 Ma in the Western Himalaya. Earth and Planetary Science Letters, 459, 301–310.

Nakata, T. (1989). Active faults of the Himalaya of India and Nepal. Geological Society of America Special Paper, 232(1), 243–264.

Navelot, V., Géraud, Y., Favier, A., Diraison, M., Corsini, M., Lardeaux, J.-M., Verati, C., de Lepinay, J. M., Legendre, L., & Beauchamps, G. (2018). Petrophysical properties of volcanic rocks and impacts of hydrothermal alteration in the Guadeloupe Archipelago (West Indies). Journal of Volcanology and Geothermal Research, 360, 1–21.

Nelson, A. E. (1985). Major tectonic features and structural elements in the northwest part of the Greenville Quadrangle, Georgia (Report 1643; Bulletin). US Geological Survey; USGS Publications Warehouse. https://pubs.usgs.gov/publication/b1643

Neuser, R. D., Reinecke, T., & Schertl, H.-P. (1995). Low temperature cathodoluminescence of selected minerals from high pressure metamorphic rocks. Bochumer Geol. Und Geotech. Arb, 44, 119–123.

O'Connor, J. T. (1965). A classification for quartz-rich igneous rocks based on feldspar ratios. US Geological Survey, Professional Papers 525B, B79–B84.

O'leary, D. W., Friedman, J. D., & Pohn, H. A. (1976). Lineament, linear, lineation: Some proposed new standards for old terms. Geological Society of America Bulletin, 87(10), 1463–1469.

Pagel, M., Barbin, V., Blanc, P., & Ohnenstetter, D. (2000). Cathodoluminescence in geosciences: An introduction. Springer.

Palin, R. M., Searle, M. P., Waters, D. J., Horstwood, M. S. A., & Parrish, R. R. (2012). Combined thermobarometry and geochronology of peraluminous metapelites from the Karakoram metamorphic complex, North Pakistan; New insight into the tectonothermal evolution of the Baltoro and Hunza Valley regions. Journal of Metamorphic Geology, 30(8), 793–820.

Park, S. K., & Mackie, R. L. (2000). Resistive (dry?) lower crust in an active orogen, Nanga Parbat, northern Pakistan. Tectonophysics, 316(3–4), 359–380.

Pastorelli, S., Marini, L., & Hunziker, J. (2001). Chemistry, isotope values (δD, δ18O, δ34SSO4) and temperatures of the water inflows in two Gotthard tunnels, Swiss Alps. Applied Geochemistry, 16(6), 633–649.

Perry, H. K. C., Jaupart, C., Mareschal, J. -C., & Bienfait, G. (2006). Crustal heat production in the Superior Province, Canadian Shield, and in North America inferred from heat flow data. Journal of Geophysical Research: Solid Earth, 111(B4), 2005JB003893. https://doi.org/10.1029/2005JB003893

Petterson, M. G. (2010). A review of the geology and tectonics of the Kohistan island arc, north Pakistan. Geological Society, London, Special Publications, 338(1), 287–327.

Petterson, M. G. (2019). The plutonic crust of Kohistan and volcanic crust of Kohistan–Ladakh, north Pakistan/India: Lessons learned for deep and shallow arc processes. Geological Society, London, Special Publications, 483(1), 123–164. https://doi.org/10.1144/SP483.4

Petterson, M. G., Crawford, M. B., & Windley, B. F. (1993). Petrogenetic implications of neodymium isotope data from the Kohistan batholith, North Pakistan. Journal of the Geological Society, 150(1), 125–129.

Petterson, M. G., & Treloar, P. J. (2004). Volcanostratigraphy of arc volcanic sequences in the Kohistan arc, North Pakistan: Volcanism within island arc, back-arc-basin, and intra-continental tectonic settings. Journal of Volcanology and Geothermal Research, 130(1–2), 147–178.

Petterson, M. G., & Windley, B. F. (1985). RbSr dating of the Kohistan arc-batholith in the Trans-Himalaya of north Pakistan, and tectonic implications. Earth and Planetary Science Letters, 74(1), 45–57.

Petterson, M. G., & Windley, B. F. (1991). Changing source regions of magmas and crustal growth in the Trans-Himalayas: Evidence from the Chalt volcanics and Kohistan batholith, Kohistan, northern Pakistan. Earth and Planetary Science Letters, 102(3–4), 326–341.

Pinet, C., & Jaupart, C. (1987). A thermal model for the distribution in space and time of the Himalayan granites. Earth and Planetary Science Letters, 84(1), 87–99.

Poage, M. A., Chamberlain, C. P., & Craw, D. (2000). Massif-wide metmorphism and fluid evolution at Nanga Parbat, northern Pakistan. American Journal of Science, 300(6), 463–482.

Podugu, N., Ray, L., Singh, S. P., & Roy, S. (2017). Heat flow, heat production, and crustal temperatures in the Archaean Bundelkhand craton, north-central India: Implications for thermal regime beneath the Indian shield. Journal of Geophysical Research: Solid Earth, 122(7), 5766–5788. https://doi.org/10.1002/2017JB014041

Popov, Y., Beardsmore, G., Clauser, C., & Roy, S. (2016). ISRM suggested methods for determining thermal properties of rocks from laboratory tests at atmospheric pressure. Rock Mechanics and Rock Engineering, 49, 4179–4207.

Priestley, K., Ho, T., & Mitra, S. (2019). The crustal structure of the Himalaya: A synthesis. Geological Society, London, Special Publications, 483(1), 483–516. https://doi.org/10.1144/SP483-2018-127

Priestley, K., Jackson, J., & McKenzie, D. (2008). Lithospheric structure and deep earthquakes beneath India, the Himalaya and southern Tibet. Geophysical Journal International, 172(1), 345–362.

Rai, S. S., Priestley, K., Gaur, V. K., Mitra, S., Singh, M. P., & Searle, M. (2006). Configuration of the Indian Moho beneath the NW Himalaya and Ladakh. Geophysical Research Letters, 33(15), 2006GL026076. https://doi.org/10.1029/2006GL026076

Ramakrishnan, D., Bharti, R., Singh, K. D., & Nithya, M. (2013). Thermal inertia mapping and its application in mineral exploration: Results from Mamandur polymetal prospect, India. Geophysical Journal International, 195(1), 357–368.

Ray, L., Nagaraju, P., Singh, S. P., Ravi, G., & Roy, S. (2016). Radioelemental, petrological and geochemical characterization of the Bundelkhand craton, central India: Implication in the Archaean geodynamic evolution. International Journal of Earth Sciences, 105, 1087–1107.

Ray, L., Roy, S., & Srinivasan, R. (2008). High radiogenic heat production in the Kerala Khondalite block, Southern Granulite province, India. International Journal of Earth Sciences, 97(2), 257–267.

Raz, U., & Honegger, K. (1989). Magmatic and tectonic evolution of the Ladakh block from field studies. Tectonophysics, 161(1–2), 107–118.

Razi, A. S., Levin, V., Roecker, S. W., & Huang, G. D. (2014). Crustal and uppermost mantle structure beneath western Tibet using seismic traveltime tomography. Geochemistry, Geophysics, Geosystems, 15(2), 434–452. https://doi.org/10.1002/2013GC005143

Reinhardt, N., & Herrmann, L. (2019). Gamma-ray spectrometry as versatile tool in soil science: A critical review. Journal of Plant Nutrition and Soil Science, 182(1), 9–27.

Rex, A. J., Searle, M. P., Tirrul, R., Crawford, M. B., Prior, D. J., Rex, D. C., Barnicoat, A., Bertrand, J. -m., Shackleton, R. M., Dewey, J. F., & Windley, B. F. (1997). The geochemical and tectonic evolution of the central Karakoram, North Pakistan. Philosophical Transactions of the Royal Society of London. Series A, Mathematical and Physical Sciences, 326(1589), 229–255. https://doi.org/10.1098/rsta.1988.0086

Reyer, D., & Philipp, S. L. (2014). Empirical relations of rock properties of outcrop and core samples from the Northwest German Basin for geothermal drilling. Geothermal Energy Science, 2(1), 21–37.

Robinson, D. M., DeCelles, P. G., Garzione, C. N., Pearson, O. N., Harrison, T. M., & Catlos, E. J. (2003). Kinematic model for the Main Central thrust in Nepal. Geology, 31(4), 359–362.

Rollinson, H. R. (2014). Using geochemical data: Evaluation, presentation, interpretation. Routledge.

Rosberg, J.-E., & Erlström, M. (2021). Evaluation of deep geothermal exploration drillings in the crystalline basement of the Fennoscandian Shield Border Zone in south Sweden. Geothermal Energy, 9(1), 20. https://doi.org/10.1186/s40517-021-00203-1

Rowan, L. C., Schmidt, R. G., & Mars, J. C. (2006). Distribution of hydrothermally altered rocks in the Reko Diq, Pakistan mineralized area based on spectral analysis of ASTER data. Remote Sensing of Environment, 104(1), 74–87.

Rowe, C. D., & Griffith, W. A. (2015). Do faults preserve a record of seismic slip: A second opinion. Journal of Structural Geology, 78, 1–26.

Roy, S., & Mareschal, J.-C. (2011). Constraints on the deep thermal structure of the Dharwar craton, India, from heat flow, shear wave velocities, and mantle xenoliths. Journal of Geophysical Research, 116(B2), B02409. https://doi.org/10.1029/2010JB007796

Rudnick, R. L., & Gao, S. (2003). Vol. 3: The Crust, 3.01–The Composition of the Continental Crust. Treatise on Geochemistry, 1–64.

Rybach, L. (1988). Determination of Heat Production Rate. In R. Haenel, L. Rybach, & L. Stegena (Eds.), Handbook of terrestrial heat-flow density determination (pp. 9–57). Springer.

Sabins, F. F. (1999). Remote sensing for mineral exploration. Ore Geology Reviews, 14(3–4), 157–183.

Sabins, F. F. (2007). Remote sensing: Principles and applications. Waveland Press. https://books.google.com/books?hl=en&lr=&id=nVgfAAAAQBAJ&oi=fnd&pg=PP2&dq=Sabins,+1996+remote+sensing&ots=geu2pwuWi0&sig=DpurOCPPzJonIjCBiEqAFVJJai4

SAIC Exploranium. (2006). Exploranium GR-135G Plus The Identifier System Manual, Revision 1.0. SAIC, Canada. https://www.aseg.org.au/sites/default/files/Exploranium_GR-135G%20Plus%20System%20Manual.pdf

Sass, I., & Götz, A. E. (2012). Geothermal reservoir characterization: A thermofacies concept. Terra Nova, 24(2), 142–147.

Schärer, U., Copeland, P., Harrison, T. M., & Searle, M. P. (1990). Age, cooling history, and origin of post-collisional leucogranites in the Karakoram Batholith; a multi-system isotope study. The Journal of Geology, 98(2), 233–251.

Schneider, D. A., Edwards, M. A., Kidd, W. S. F., Asif Khan, M., Seeber, L., & Zeitler, P. K. (1999). Tectonics of Nanga Parbat, western Himalaya: Synkinematic plutonism within the doubly vergent shear zones of a crustal-scale pop-up structure. Geology, 27(11), 999–1002.

Schneider, F. M., Yuan, X., Schurr, B., Mechie, J., Sippl, C., Kufner, S. -K., Ratschbacher, L., Tilmann, F., Oimahmadov, I., Gadoev, M., Minaev, V., Abdybachaev, U., Orunbaev, S., Ischuk, A., & Murodkulov, S. (2019). The Crust in the Pamir: Insights From Receiver Functions. Journal of Geophysical Research: Solid Earth, 124(8), 9313–9331. https://doi.org/10.1029/2019JB017765

Schulz, K. E., Bär, K., & Sass, I. (2022). Lab-Scale Permeability Enhancement by Chemical Treatment in Fractured Granite (Cornubian Batholith) for the United Downs Deep Geothermal Power Project, Cornwall (UK). Geosciences, 12(1), 35.

Scott, R. D., MacKenzie, A. B., & Alexander, W. R. (1992). The interpretation of 238U-234U-230Th-226Ra disequilibria produced by rock-water interactions. Journal of Geochemical Exploration, 45(1–3), 323–343.

Searle, M. P. (2015). Mountain Building, Tectonic Evolution, Rheology, and Crustal Flow in the Himalaya, Karakoram, and Tibet. In G. Schubert (Ed.), Treatise on Geophysics (Second Edition) (pp. 469–511). Elsevier. https://doi.org/10.1016/B978-0-444-53802-4.00121-4

Searle, M. P., Cottle, J. M., Streule, M. J., & Waters, D. J. (2009). Crustal melt granites and migmatites along the Himalaya: Melt source, segregation, transport and granite emplacement mechanisms. Earth and Environmental Science Transactions of the Royal Society of Edinburgh, 100(1–2), 219–233.

Searle, M. P., Crawford, M. B., & Rex, A. J. (1992). Field relations, geochemistry, origin and emplacement of the Baltoro granite, central Karakoram. Earth and Environmental Science Transactions of The Royal Society of Edinburgh, 83(3), 519–538.

Searle, M. P., & Hacker, B. R. (2019). Structural and metamorphic evolution of the Karakoram and Pamir following India–Kohistan–Asia collision. Geological Society, London, Special Publications, 483(1), 555–582.

Searle, M. P., & Khan, M. A. (1996). Geological map of north Pakistan and adjacent areas of northern Ladakh and western Tibet (Western Himalaya, Salt Ranges, Kohistan, Karakoram, Hindu Kush) [Map]. Oxford University.

Searle, M. P., Khan, M. A., Fraser, J. E., Gough, S. J., & Jan, M. Q. (1999). The tectonic evolution of the Kohistan-Karakoram collision belt along the Karakoram Highway transect, north Pakistan. Tectonics, 18(6), 929–949.

Searle, M. P., Parrish, R. R., Thow, A. V., Noble, S. R., Phillips, R. J., & Waters, D. J. (2010). Anatomy, age and evolution of a collisional mountain belt: The Baltoro granite batholith and Karakoram Metamorphic Complex, Pakistani Karakoram. Journal of the Geological Society, 167(1), 183–202.

Searle, M. P., Rex, A. J., Tirrul, R., Rex, D. C., Barnicoat, A., & Windley, B. F. (1989). Metamorphic, magmatic, and tectonic evolution of the central Karakoram in the Biafo-Baltoro-Hushe regions of northern Pakistan. In L. L. Malinconico Jr. & R. J. Lillie (Eds.), Tectonics of the western Himalayas (Vol. 232, p. 0). Geological Society of America.

Searle, M. P., & Tirrul, R. (1991). Structural and thermal evolution of the Karakoram crust. Journal of the Geological Society, 148(1), 65–82.

Searle, M. P., & Treloar, P. J. (2010). Was Late Cretaceous–Paleocene obduction of ophiolite complexes the primary cause of crustal thickening and regional metamorphism in the Pakistan Himalaya? Geological Society, London, Special Publications, 338(1), 345–359.

Searle, M. P., & Treloar, P. J. (2019). Introduction to Himalayan tectonics: A modern synthesis. In Geological Society, London, Special Publications (Vol. 483, Issue 1, pp. 1–17). The Geological Society of London.

Setaram Instrumentation. (2009). K/C80-1A C80 Commissioning. Setaram Instrumentation KEP Technologies, Caluire, France, 52, 1005.

Shah, S. T. H., Zhao, J., Xiao, Q., Bhatti, Z. I., Khan, N. G., Zhang, H., Deng, G., & Liu, H. (2018). Electrical resistivity structures and tectonic implications of Main Karakorum Thrust (MKT) in the western Himalayas: NNE Pakistan. Physics of the Earth and Planetary Interiors, 279, 57–66.

Shand, S. J. (1943). The eruptive rocks (2nd ed.). Wiley New York.

Shanker, R. (1988). Heat-flow map of India and discussions on its geological and economic significance. Indian Minerals, 42(2), 89–110.

Sharmin, T., Khan, N. R., Akram, M. S., & Ehsan, M. M. (2023). A State-of-the-art Review on for Geothermal Energy Extraction, Utilization, and Improvement Strategies: Conventional, Hybridized, and Enhanced Geothermal Systems. International Journal of Thermofluids, 100323.

Shcherbakova, T. F., Terekhov, E. N., & Kuklei, L. N. (2021). Metasomatic Epidote in Amphibolite-Replacing Rocks: An Indicator of Tectonic Processes Related to the Exhumation of Rocks of the Belomorian Belt. Petrography and Geochemistry. Geochemistry International, 59(12), 1157–1169. https://doi.org/10.1134/S0016702921120053

Shuja, T. A. (1986). Geothermal areas in Pakistan. Geothermics, 15(5–6), 719–723.

Siegel, C., Bryan, S., Purdy, D., Allen, C., Schrank, C., Uysal, T., Gust, D., & Beardsmore, G. (2012). Evaluating the role of deep granitic rocks in generating anomalous temperatures in south-west Queensland. Geological Survey of Queensland: Digging Deeper 10 Seminar Extended Abstracts [Queensland Geological Record 2012/14], 95–102.

Singh, A., & Harrison, A. (1985). Standardized principal components. International Journal of Remote Sensing, 6(6), 883–896. https://doi.org/10.1080/01431168508948511

Singh, B. (1993). Geological set up of a part of the Ladakh Granitoid Complex, Ladakh Himalaya. Journal of Himalayan Geology, 4(1), 57–62.

Singh, P., Sethy, P. C., Singh, A. K., Singhal, S., Maurya, A. K., & Giri, S. R. (2023). Geochemistry and U–Pb zircon geochronology of the Jutogh Thrust sheet, Himachal Pradesh, NW-Himalaya: Implications to the petrogenesis and regional tectonic setting. Geological Journal, 58(1), 131–149. https://doi.org/10.1002/gj.4583

Slagstad, T. (2008). Radiogenic heat production of Archaean to Permian geological provinces in Norway. Norwegian Journal of Geology/Norsk Geologisk Forening, 88(3).

Sone, H., & Zoback, M. D. (2013). Mechanical properties of shale-gas reservoir rocks—Part 2: Ductile creep, brittle strength, and their relation to the elastic modulus. Geophysics, 78(5), D393–D402.

Spencer, C. J., Murphy, J. B., Kirkland, C. L., Liu, Y., & Mitchell, R. N. (2018). A Palaeoproterozoic tectono-magmatic lull as a potential trigger for the supercontinent cycle. Nature Geoscience, 11(2), 97–101.

Stanek, M. (2013). Structural and petrophysical characterisation of granite: Intended for radioactive waste stocking [PhD Thesis, University of Strasbourg]. https://publication-theses.unistra.fr/public/theses_doctorat/2013/Stanek_Martin_2013_ED413.pdf

Stober, I., & Bucher, K. (2021). Geothermal Energy: From Theoretical Models to Exploration and Development (2nd ed.). Springer International Publishing. https://doi.org/10.1007/978-3-030-71685-1

Suzen, M. L., & Toprak, V. (1998). Filtering of satellite images in geological lineament analyses: An application to a fault zone in Central Turkey. International Journal of Remote Sensing, 19(6), 1101–1114. https://doi.org/10.1080/014311698215621

Tahirkheli, R. K. (1979). Geology of Kohistan and adjoining Eurasian and Indo-Pakistan continents, Pakistan. Geol. Bull. Univ. Peshawar, 11(1), 1–30.

Tahirkheli, R. K. (1983). Geological evolution of Kohistan island arc on the southern flank of the Karakoram-Hindu Kush in Pakistan. Bollettino Geofisica Terica Ed Applicata, 25, 351–364.

Taillefer, A., Soliva, R., Guillou-Frottier, L., Le Goff, E., Martin, G., & Seranne, M. (2017). Fault-related controls on upward hydrothermal flow: An integrated geological study of the Têt fault system, Eastern Pyrénées (France). Geofluids, 2017. https://www.hindawi.com/journals/geofluids/2017/8190109/abs/

Tangestani, M. H., Mazhari, N., Agar, B., & Moore, F. (2008). Evaluating Advanced Spaceborne Thermal Emission and Reflection Radiometer (ASTER) data for alteration zone enhancement in a semi-arid area, northern Shahr-e-Babak, SE Iran. International Journal of Remote Sensing, 29(10), 2833–2850. https://doi.org/10.1080/01431160701422239

Taylor, S. R., & McLennan, S. M. (1985). The continental crust, its composition and evolution: An examination of the geochemical record preserved in sedimentary rocks. Blackwell Scientific, Oxford.

Testa, F. J., Villanueva, C., Cooke, D. R., & Zhang, L. (2018). Lithological and hydrothermal alteration mapping of epithermal, porphyry and tourmaline breccia districts in the Argentine Andes using ASTER imagery. Remote Sensing, 10(2), 203.

Thannoun, R. G. (2013). Automatic extraction and geospatial analysis of lineaments and their tectonic significance in some areas of Northern Iraq using remote sensing techniques and GIS. International Journal of Enhanced Research in Science Technology & Engineering Bulletin, 2(2), 1–11.

Thigpen, J. R., Ashley, K. T., Mako, C., Law, R. D., & Spencer, B. (2021). Interplay Between Crustal-Scale Thrusting, High Metamorphic Heating Rates, and the Development of Inverted Thermal-

Metamorphic Gradients: Numerical Models and Examples from the Caledonides of Northern Scotland. Tectonics, 40(11), e2021TC006716. https://doi.org/10.1029/2021TC006716

Thussu, J. L. (2002). Geothermal energy resources of India (69; Speical Publications, p. 210). Geological Survey of India.

Todaka, N., Shuja, T. A., Jamiluddin, S., Khan, N. A., Pasha, M. A., & Iqbal, M. (1988). A preliminary study for Geothermal Development Project in Pakistan. Geological Survey of Pakistan, 4–47.

Tong, W., & Zhang, J. (1981). Characteristics of geothermal activities in Xizang plateau and their controlling influence on plateau's tectonic model. Geological and Ecological Studies of the Quinghai-Xizang Plateau, 841–846.

Tóth, J. (2009). Gravitational systems of groundwater flow: Theory, evaluation, utilization. Cambridge University Press. https://books.google.com/books?hl=en&lr=&id=_MHtUgv0ciIC&oi=fnd&pg=PR7&dq=Toth,+2009+geothermal&ots=OP8U5JuhgE&sig=RWKxgsYMeMalWweAriUZGuVRhL0

Traineau, H., Genter, A., Cautru, J. P., Fabriol, H., & Chevremont, P. (1991). Petrography of the granite massif from drill cutting analysis and well log interpretation in the geothermal HDR borehole GPK1 (Soultz, Alsace, France). Geothermal Science and Technology, 3(1–4), 1–29.

Treloar, P. J. (1997). Thermal controls on early-Tertiary, short-lived, rapid regional metamorphism in the NW Himalaya, Pakistan. Tectonophysics, 273(1–2), 77–104.

Treloar, P. J., Brodie, K. H., Coward, M. P., Jan, M. Q., Khan, M. A., Knipe, R. J., Rex, D. C., & Williams, M. P. (1990). The evolution of the Kamila shear zone, Kohistan, Pakistan. In M. H. Salisbury & D. M. Fountain (Eds.), Exposed cross-sections of the continental crust (Vol. 317, pp. 175–214). Springer.

Treloar, P. J., & Izatt, C. N. (1993). Tectonics of the Himalayan collision between the Indian Plate and the Afghan Block: A synthesis. Geological Society, London, Special Publications, 74(1), 69–87. https://doi.org/10.1144/GSL.SP.1993.074.01.06

Treloar, P. J., Palin, R. M., & Searle, M. P. (2019). Towards resolving the metamorphic enigma of the Indian Plate in the NW Himalaya of Pakistan. Geological Society, London, Special Publications, 483(1), 255–279.

Treloar, P. J., Petterson, M. G., Jan, M. Q., & Sullivan, M. A. (1996). A re-evaluation of the stratigraphy and evolution of the Kohistan arc sequence, Pakistan Himalaya: Implications for magmatic and tectonic arc-building processes. Journal of the Geological Society, 153(5), 681–693.

Treloar, P. J., Potts, G. J., Wheeler, J., & Rex, D. C. (1991). Structural evolution and asymmetric uplift of the Nanga Parbat syntaxis, Pakistan Himalya. Geologische Rundschau, 80, 411–428.

Ulusoy, İ., Labazuy, P., & Aydar, E. (2012). STcorr: An IDL code for image-based normalization of lapse rate and illumination effects on nighttime TIR imagery. Computers & Geosciences, 43, 63–72.

van der Meer, F. D., van der Werff, H. M., van Ruitenbeek, F. J., Hecker, C. A., Bakker, W. H., Noomen, M. F., Van Der Meijde, M., Carranza, E. J. M., De Smeth, J. B., & Woldai, T. (2012). Multi-and hyperspectral geologic remote sensing: A review. International Journal of Applied Earth Observation and Geoinformation, 14(1), 112–128.

van der Meer, F., Hecker, C., van Ruitenbeek, F., van der Werff, H., de Wijkerslooth, C., & Wechsler, C. (2014). Geologic remote sensing for geothermal exploration: A review. International Journal of Applied Earth Observation and Geoinformation, 33, 255–269.

Vilà, M., Fernández, M., & Jiménez-Munt, I. (2010). Radiogenic heat production variability of some common lithological groups and its significance to lithospheric thermal modeling. Tectonophysics, 490(3–4), 152–164.

Villa, I. M., Lemennicier, Y., & Le Fort, P. (1996). Late Miocene to Early Pliocene tectonometamorphism and cooling in south-central Karakorum and Indus-Tsangpo suture, Chogo Lungma area (NE Pakistan). Tectonophysics, 260(1–3), 201–214.

Wajid, A. A., Anees, M., Alam, S. U., Gorchani, J. K., Shahzad, K., Israr, A., & Shafique, M. (2021). Lineament mapping for a part of the Central Sulaiman Fold–Thrust Belt (SFTB), Pakistan. Arabian Journal of Geosciences, 14(15), 1438. https://doi.org/10.1007/s12517-021-07784-y

Wang, Y., Zhou, L., & Zhao, L. (2013). Cratonic reactivation and orogeny: An example from the northern margin of the North China Craton. Gondwana Research, 24(3–4), 1203–1222.

Wanner, C., Diamond, L. W., & Alt-Epping, P. (2019). Quantification of 3-D Thermal Anomalies from Surface Observations of an Orogenic Geothermal System (Grimsel Pass, Swiss Alps). Journal of Geophysical Research: Solid Earth, 124(11), 10839–10854. https://doi.org/10.1029/2019JB018335

Wanner, C., Waber, H. N., & Bucher, K. (2020). Geochemical evidence for regional and long-term topography-driven groundwater flow in an orogenic crystalline basement (Aar Massif, Switzerland). Journal of Hydrology, 581, 124374.

Warren, C. J., Grujic, D., Kellett, D. A., Cottle, J., Jamieson, R. A., & Ghalley, K. S. (2011). Probing the depths of the India-Asia collision: U-Th-Pb monazite chronology of granulites from NW Bhutan. Tectonics, 30(2), 2010TC002738. https://doi.org/10.1029/2010TC002738

Watkins, H., Butler, R. W. H., Bond, C. E., & Healy, D. (2015). Influence of structural position on fracture networks in the Torridon Group, Achnashellach fold and thrust belt, NW Scotland. Journal of Structural Geology, 74, 64–80. https://doi.org/10.1016/j.jsg.2015.03.001

Weinberg, R. F., & Hasalová, P. (2015). Water-fluxed melting of the continental crust: A review. Lithos, 212, 158–188.

Weinert, S., Bär, K., & Sass, I. (2020). Thermophysical rock properties of the crystalline Gonghe Basin Complex (Northeastern Qinghai–Tibet-Plateau, China) basement rocks. Environmental Earth Sciences, 79(3), 77. https://doi.org/10.1007/s12665-020-8808-9

Weinert, S., Bär, K., & Sass, I. (2021). Database of petrophysical properties of the Mid-German Crystalline Rise. Earth System Science Data, 13(3), 1441–1459.

Weller, O. M., Jackson, S., Miller, W. G. R., St-Onge, M. R., & Rayner, N. (2020). Quantitative elemental mapping of granulite-facies monazite: Textural insights and implications for petrochronology. Journal of Metamorphic Geology, 38(8), 853–880. https://doi.org/10.1111/jmg.12552

Weydt, L. M., Bär, K., & Sass, I. (2022). Petrophysical characterization of the Los Humeros geothermal field (Mexico): From outcrop to parametrization of a 3D geological model. Geothermal Energy, 10(1), 1–48.

Weydt, L. M., Lucci, F., Lacinska, A., Scheuvens, D., Carrasco-Núñez, G., Giordano, G., Rochelle, C. A., Schmidt, S., Bär, K., & Sass, I. (2022). The impact of hydrothermal alteration on the physiochemical characteristics of reservoir rocks: The case of the Los Humeros geothermal field (Mexico). Geothermal Energy, 10(1), 20.

Wheeler, J., Treloar, P. J., & Potts, G. J. (1995). Structural and metamorphic evolution of the Nanga Parbat syntaxis, Pakistan Himalayas, on the Indus gorge transect: The importance of early events. Geological Journal, 30(3–4), 349–371.

Whitney, D. L., & Evans, B. W. (2010). Abbreviations for names of rock-forming minerals. American Mineralogist, 95(1), 185–187.

Whitney, D. L., Teyssier, C., & Fayon, A. K. (2004). Isothermal decompression, partial melting and exhumation of deep continental crust. Geological Society, London, Special Publications, 227(1), 313–326.

Whittington, A., Foster, G., Harris, N., Vance, D., & Ayres, M. (1999). Lithostratigraphic correlations in the western Himalaya—An isotopic approach. Geology, 27(7), 585–588.

Whittington, A. G. (1996). Exhumation overrated at Nanga Parbat, northern Pakistan. Tectonophysics, 260(1–3), 215–226.

Whittington, A., Harris, N. B. W., Ayres, M. W., & Foster, G. (2000). Tracing the origins of the western Himalaya: An isotopic comparison of the Nanga Parbat massif and Zanskar Himalaya. Geological Society, London, Special Publications, 170(1), 201–218.

Wittlinger, G., Farra, V., Hetényi, G., Vergne, J., & Nábělek, J. (2009). Seismic velocities in Southern Tibet lower crust: A receiver function approach for eclogite detection. Geophysical Journal International, 177(3), 1037–1049.

Wu, F.-Y., Liu, X.-C., Liu, Z.-C., Wang, R.-C., Xie, L., Wang, J.-M., Ji, W.-Q., Yang, L., Liu, C., & Khanal, G. P. (2020). Highly fractionated Himalayan leucogranites and associated rare-metal mineralization. Lithos, 352, 105319.

Yakymchuk, C., & Brown, M. (2019). Divergent behaviour of Th and U during anatexis: Implications for the thermal evolution of orogenic crust. Journal of Metamorphic Geology, 37(7), 899–916. https://doi.org/10.1111/jmg.12469

Yalcin, M., Kilic Gul, F., Yildiz, A., Polat, N., & Basaran, C. (2020). The mapping of hydrothermal alteration related to the geothermal activities with remote sensing at Akarcay Basin (Afyonkarahisar), using Aster data. Arabian Journal of Geosciences, 13(21), 1166. https://doi.org/10.1007/s12517-020-06083-2

Yang, K., Browne, P. R. L., Huntington, J. F., & Walshe, J. L. (2001). Characterising the hydrothermal alteration of the Broadlands–Ohaaki geothermal system, New Zealand, using short-wave infrared spectroscopy. Journal of Volcanology and Geothermal Research, 106(1–2), 53–65.

Younis, H., Ahmad, F., Anees, M., Atiq, A., Shakeel, N., Adil, M., Mehboob, K., Alhawsawi, A. M., Khan, R., & Khubrani, A. M. (2022). Gamma radioactivity and Environmental radiation risks of Granitoids in Central and Western Gilgit-Baltistan, Himalayas, North Pakistan. Results in Physics, 37, 105509.

Yousafzai, A., Eckstein, Y., & Dahl, P. S. (2010). Hydrochemical signatures of deep groundwater circulation in a part of the Himalayan foreland basin. Environmental Earth Sciences, 59, 1079–1098.

Zaigham, N. A., Nayyar, Z. A., & Hisamuddin, N. (2009). Review of geothermal energy resources in Pakistan. Renewable and Sustainable Energy Reviews, 13(1), 223–232.

Zeitler, P. K. (1985). Cooling history of the NW Himalaya, Pakistan. Tectonics, 4(1), 127–151. https://doi.org/10.1029/TC004i001p00127

Zeitler, P. K., Chamberlain, C. P., & Smith, H. A. (1993). Synchronous anatexis, metamorphism, and rapid denudation at Nanga Parbat (Pakistan Himalaya). Geology, 21(4), 347–350.

Zeitler, P. K., Koons, P. O., Bishop, M. P., Chamberlain, C. P., Craw, D., Edwards, M. A., Hamidullah, S., Jan, M. Q., Khan, M. A., & Khattak, M. U. K. (2001). Crustal reworking at Nanga Parbat, Pakistan: Metamorphic consequences of thermal-mechanical coupling facilitated by erosion. Tectonics, 20(5), 712–728.

Zeitler, P. K., Sutter, J. F., Williams, I. S., Zartman, R., & Tahirkheli, R. A. K. (1989). Geochronology and temperature history of the Nanga Parbat–Haramosh massif, Pakistan. In L. L. Malinconico & R. J. Lillie (Eds.), Tectonics of the western Himalayas (Vol. 232, pp. 1–22). Geological Society of America.

Zhang, Y. L., Li, X., Cheng, G. D., Jin, H. J., Yang, D. W., Flerchinger, G. N., Chang, X. L., Wang, X., & Liang, J. (2018). Influences of Topographic Shadows on the Thermal and Hydrological Processes in a Cold Region Mountainous Watershed in Northwest China. Journal of Advances in Modeling Earth Systems, 10(7), 1439–1457. https://doi.org/10.1029/2017MS001264

Zhao, J., Yuan, X., Liu, H., Kumar, P., Pei, S., Kind, R., Zhang, Z., Teng, J., Ding, L., Gao, X., Xu, Q., & Wang, W. (2010). The boundary between the Indian and Asian tectonic plates below Tibet. Proceedings of the National Academy of Sciences, 107(25), 11229–11233. https://doi.org/10.1073/pnas.1001921107

Appendix A – Chapter 3

Table A1: Details of remote sensing data used in chapter 3.

Sr No.	Scene ID	Acquisition Date (yy/mm/dd)	Resolution (m)
ASTER Daytime Near-Short Infrared Data			
1	AST_L1T_00309302001055842_20150420001123_106038	2001/09/30	30
2	AST_L1T_00306172006054618_20150514213249_93813	2006/06/17	30
3	AST_L1T_00306172006054627_20150514213252_3143	2006/06/17	30
4	AST_L1T_00309132004055826_20150506005301_111301	2004/09/13	30
5	AST_L1T_00309132004055817_20150506005307_100603	2004/09/13	30
6	AST_L1T_003062622001060058_20150418003532_1393	2001/06/26	30
7	AST_L1T_003102022005054558_20150511151822_107954	2005/10/20	30
8	AST_L1T_003090420000060155_20150411131129_5579	2000/09/04	30
ASTER Nighttime Thermal Infrared Data			
1	AST_L1T_003092262017165549_20170927144203_8404	2017/09/26	90
2	AST_L1T_003083122005170050_20150511000359_44010	2005/08/31	90
3	AST_L1T_003083122005170041_20170802151740_27366	2005/08/31	90
4	AST_L1T_003080622005170713_20150510154307_89580	2005/08/06	90
5	AST_L1T_003080622005170704_20170802180542_45907	2005/08/06	90
6	AST_L1T_003091822009170750_20170727041420_574	2009/09/18	90
7	AST_L1T_003091822009170759_20150529181959_77299	2009/09/18	90
8	AST_L1T_003101022017170831_20171011112714_28269	2017/10/10	90
9	AST_L1T_003062922011170130_20150606133104_46171	2011/06/29	90
10	AST_L1T_003062022011170735_20150606103547_50130	2011/06/20	90
11	AST_L1T_003092122019171358_20190922121154_1902	2019/09/21	90
Shuttle Radar Topographic Digital Elevation Model			
1	SRTM1N35E074V3	2000/02/11	1-ARC (30)
2	SRTM1N35E075V3	2000/02/11	1-ARC (30)
3	SRTM1N35E076V3	2000/02/11	1-ARC (30)
4	SRTM1N36E073V3	2000/02/11	1-ARC (30)
5	SRTM1N36E074V3	2000/02/11	1-ARC (30)

Appendix B – Additional Data to Chapter 4

Table B1: Radiogenic heat production (µWm^{-3}) calculated from in situ gamma spectrometry-based U (ppm), Th (ppm), and K (%) concentrations and the density of lithologies within Nanga Parbat Massif, Kohistan-Ladakh, and Karakoram batholiths.

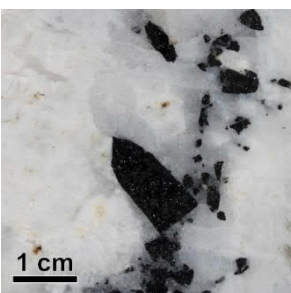| S. N.	Sample ID	Geographic Coordinates	Tectonic Domain	Lithology	U (ppm)	Th (ppm)	K (%)	Density (g/cm^3)	A (µW/m^3)
1	TTP-1	74.591125 35.415808	NPM	Granitic Gneiss	8.77	23.40	3.65	2.61	4.08
2	TTP-2	74.593992 35.430583	NPM	Pegmatite	4.91	18.59	3.58	2.66	2.84
3	TTP-3	74.593992 35.430583	NPM	Gneiss	5.44	27.87	3.67	2.70	3.67
4	TTP-4	74.594572 35.458372	NPM	Pegmatite	5.98	7.73	7.40	2.59	2.66
5	TTP-5	74.594472 35.482586	NPM	Augen Gneiss	9.95	45.13	3.53	2.67	5.94
6	Ast10	74.73430107 35.53131097	NPM	Leucogranite	9.39	17.66	4.96	2.58	3.92
7	Ast11	74.72649645 35.53941357	NPM	Biotite Gneiss	5.88	23.14	4.93	2.58	3.42
8	Ast12	74.70245833 35.54644833	NPM	Migmatitic Gneiss	3.48	19.67	3.35	2.60	2.48
9	Ast13	74.69908474 35.54701846	NPM	Granite	7.97	22.62	3.68	2.59	3.80
10	Ast14	74.69832333 35.54725167	NPM	Migmatitic Gneiss	15.64	57.82	3.82	2.59	8.03
11	Ast15	74.68168833 35.55775333	NPM	Augen gneiss	6.13	33.75	3.73	2.60	4.10
12	Ast16	74.6799145 35.56495076	NPM	Biotite granite	5.31	33.91	3.39	2.58	3.85
13	Ast4	74.82472297 35.41826372	NPM	Paragneiss	19.61	55.40	3.59	2.61	8.90
14	Ast5	74.81104838 35.4462679	NPM	Garnet schist	4.09	15.14	3.14	2.63	2.33
15	Ast6	74.796575 35.44758333	NPM	Gneiss	16.01	22.32	4.98	2.59	5.88
16	Ast7	74.76593963 35.50308758	NPM	Biotite gneiss	2.19	7.37	1.91	2.67	1.24
17	Ast8	74.74216 35.51352833	NPM	Gneiss	14.11	14.62	4.16	2.58	4.81
18	Ast9	74.7357309 35.52290573	NPM	Migmatitic Gneiss	13.06	58.09	3.51	2.60	7.42
19	Fm1	74.57458693 35.37820289	NPM	Gneiss	5.38	34.80	4.20	2.61	4.04
20	Fm2	74.573785 35.37840833	NPM	Gneiss	13.92	42.90	6.00	2.58	6.79
21	Fm3	74.57347 35.37759667	NPM	Gneiss	9.01	34.20	5.20	2.59	4.95
22	Fm4	74.570386 35.373135	NPM	Granite	22.57	25.88	4.03	2.59	7.66
23	Fm5	74.57273667 35.382259	NPM	Gneiss	6.02	32.90	4.60	2.60	4.10
24	NP1	74.72345095 35.84844241	NPM	Granitic gneiss	4.52	4.37	3.33	2.61	1.71
25	NP10	74.85705421 35.70978641	NPM	Granite	20.27	13.61	4.94	2.59	6.34
26	NP11	74.90218833 35.69817	NPM	Gneiss	6.80	21.71	4.32	2.59	3.51
27	NP12	74.91711137 35.6785222	NPM	Paragneiss	2.50	14.75	2.67	2.66	1.88
28	NP13	74.92889167 35.65432333	NPM	gneiss	2.01	17.39	2.27	2.68	1.92
29	NP14	74.94587042 35.64180843	NPM	Granitic gneiss	2.74	15.85	3.15	2.63	2.04
30	NP15	75.00745408 35.62699884	NPM	banded gneiss	0.31	0.66	0.76	2.78	0.20
31	NP16	75.02350667 35.634105	NPM	Psammite	0.30	1.60	0.50	2.81	0.24
32	NP17	75.02368193 35.63115483	NPM	Granitic gneiss	2.99	16.10	2.36	2.67	2.09

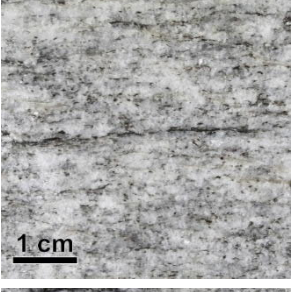| S. N.	Sample ID	Geographic Coordinates	Tectonic Domain	Lithology	U (ppm)	Th (ppm)	K (%)	Density (g/cm³)	A (µW/m³)
33	NP2	74.742255 35.84740167	NPM	Mica schist	1.97	6.37	1.47	2.73	1.10
34	NP3	74.7424179 35.8472583	NPM	Gneiss	2.27	9.08	2.29	2.68	1.41
35	NP4	74.74223742 35.81868065	NPM	Mica schist	2.99	12.89	2.04	2.69	1.85
36	NP5	74.73289618 35.78839445	NPM	Calc silicate schist	0.67	1.44	1.01	2.76	0.37
37	NP6	74.75916176 35.77013331	NPM	Gneiss	6.94	39.37	4.15	2.59	4.70
38	NP7	74.74161829 35.72651357	NPM	Biotite Gneiss	11.64	35.40	4.94	2.58	5.65
39	NP8	74.80936333 35.71175333	NPM	Migmatitic gneiss	18.78	86.17	3.69	2.59	10.69
40	NP9	74.83748833 35.71520167	NPM	Pegmatite	15.79	11.63	3.38	2.61	5.01
41	Rk1	74.59155979 35.48198165	NPM	Gneiss	13.14	40.20	3.87	2.62	6.33
42	Rk10	74.59475 35.461435	NPM	Gneiss	0.92	2.22	1.51	2.73	0.54
43	Rk15	74.59448 35.43053933	NPM	Biotite gneiss	12.31	29.24	4.44	2.60	5.40
44	Rk16	74.59154333 35.40420167	NPM	Gneiss	13.25	9.05	3.89	2.60	4.23
45	Rk18	74.59092 35.39583667	NPM	Biotite gneiss	2.59	16.00	3.08	2.61	2.00
46	Rk3	74.59477733 35.48170833	NPM	Gneiss	11.49	34.33	3.87	2.62	5.52
47	Rk5	74.59238 35.47724	NPM	Leucogranite	15.50	21.39	4.04	2.61	5.66
48	Rk7	74.59177116 35.47408647	NPM	Gneiss	10.34	22.56	3.27	2.64	4.42
49	St1	75.03308102 35.63403653	NPM	leucogranite	1.94	3.87	3.24	2.63	1.04
50	St2	75.03604167 35.63431	NPM	leucogranite	6.23	5.58	3.33	2.62	2.24
51	Tar1	74.73602167 35.23892333	NPM	Biotite Gneiss	16.10	76.50	3.30	2.64	9.52
52	Tar2	74.73472333 35.23948167	NPM	Muscovite gneiss	6.08	15.90	3.50	2.63	2.92
53	Tar3	74.79284667 35.22616667	NPM	Garnet mica schist	2.18	9.41	1.24	2.75	1.35
54	CG-1	74.621533 35.7373	KLB	Pegmatite	1.21	6.00	2.92	2.62	0.97
55	CG-2	74.621533 35.7373	KLB	Granite	2.08	16.80	3.27	2.62	1.94
56	JT-1	74.326619 35.989475	KLB	Diorite	1.12	7.31	2.57	2.72	1.04
57	JT-2	74.326619 35.989475	KLB	Granodiorite	1.09	14.16	3.03	2.66	1.52
58	GRT-1	74.295214 36.061872	KLB	Tonalite	0.14	3.60	0.60	2.69	0.34
59	GRT-2	74.295214 36.061872	KLB	Tonalite	0.36	2.30	0.70	2.68	0.32
60	BST-1	74.298311 36.139691	KLB	Basaltic andesite	0.12	1.01	0.08	2.99	0.12
61	DR-1	74.312319 36.208284	KLB	Andesite, Diorite	0.15	0.89	0.80	2.77	0.18
62	GB-1	74.223958 35.93615	KLB	Granodiorite	1.34	11.71	2.33	2.67	1.36
63	HZ-1	74.199809 35.980088	KLB	Leucogranite	2.02	15.48	4.12	2.60	1.90
64	HZ-2	74.187491 36.005323	KLB	Leucogranite	3.00	10.03	3.50	2.60	1.73
65	GZ-1	74.160556 36.041389	KLB	Granodiorite	1.50	7.38	2.76	2.60	1.11
66	GZ-2	74.160556 36.041389	KLB	Diorite	1.37	6.31	2.58	2.67	1.02
67	DL-1	73.965556 36.099722	KLB	Gabbro/Diorite	1.46	7.64	3.82	2.62	1.23
68	GW-1	73.82136 36.170781	KLB	Gabbro	0.60	5.08	1.51	2.84	0.68
69	GW-2	73.721111	KLB	Diorite	1.30	11.60	2.67	2.68	1.38
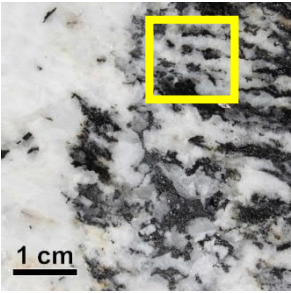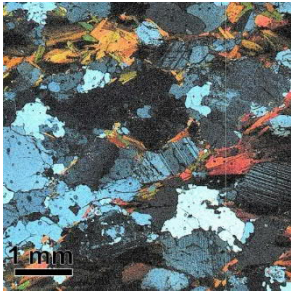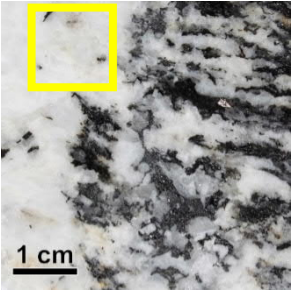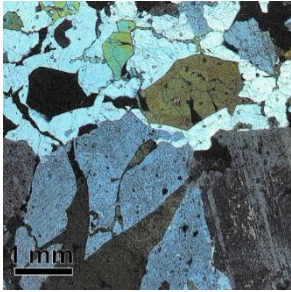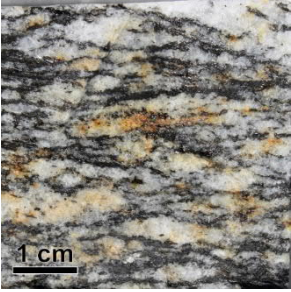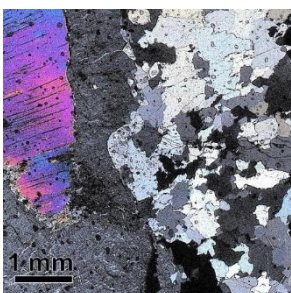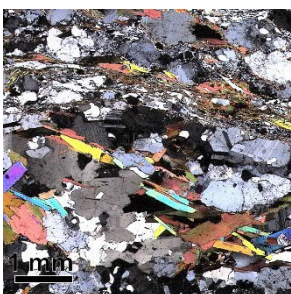
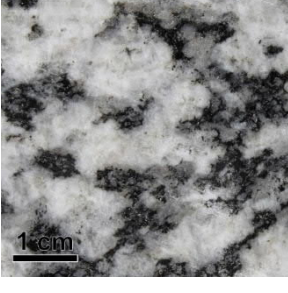| S. N.	Sample ID	Geographic Coordinates	Tectonic Domain	Lithology	U (ppm)	Th (ppm)	K (%)	Density (g/cm³)	A (µW/m³)
70	GP-1	36.214444 73.580208	KLB	Granodiorite	1.35	15.73	3.47	2.63	1.72
71	GP-2	36.250273 73.549167	KLB	Diorite	1.35	9.20	2.53	2.67	1.21
72	YK-1	36.237778 73.425368	KLB	Granodiorite	3.01	17.33	3.13	2.65	2.22
73	YK-2	36.24212 73.425368	KLB	Diorite	1.42	8.01	2.33	2.77	1.17
74	YK-3	36.24212 73.418775	KLB	Granite	4.27	21.47	4.33	2.61	2.89
75	YK-4	36.244894 73.377222	KLB	Granodiorite	2.05	18.13	3.47	2.63	2.05
76	KL-1	36.32 73.359444	KLB	Andesite	1.33	4.74	2.02	2.70	0.86
77	KL-2	36.247222 73.333333	KLB	Granodiorite	1.33	8.23	2.54	2.66	1.13
78	KL-3	36.241111 73.331667	KLB	Diorite	1.57	5.60	2.10	2.68	0.98
79	KL-4	36.240833 73.289444	KLB	Granodiorite	1.33	8.80	2.60	2.67	1.18
80	TH-1	36.216389 73.17223	KLB	Granodiorite	1.77	9.02	2.96	2.64	1.32
81	TH-2	36.169749 73.133582	KLB	Granite	2.64	9.76	2.67	2.62	1.56
82	Ast1	36.15793 74.86873219	KLB	Diorite	0.19	2.91	1.10	2.74	0.36
83	Ast2	35.26112753 74.85298082	KLB	Diorite	0.43	6.99	0.86	2.76	0.69
84	Ast3	35.26391837 74.85201	KLB	Amphibolite	0.19	1.54	0.69	2.77	0.23
85	KLB1	35.377825 75.05147458	KLB	Amphibolite	0.54	3.58	1.35	2.73	0.52
86	KLB2	35.63483706 75.06908573	KLB	Granodiorite	0.84	5.90	1.70	2.72	0.79
87	KLB21	35.60937361 75.72868167	KLB	Granite	1.09	12.13	2.41	2.68	1.34
88	KLB22	35.29723167 75.74274833	KLB	Diorite	1.95	9.70	2.70	2.67	1.41
89	KLB3	35.41108667 75.11580195	KLB	Granodiorite	0.45	1.57	1.07	2.76	0.33
90	KLB4	35.60311355 75.15883841	KLB	Diorite	0.30	1.34	1.34	2.74	0.30
91	KLB5	35.59688592 75.22848719	KLB	Granite	2.54	9.20	3.90	2.62	1.61
92	KLB6	35.59255979 75.27978833	KLB	Granodiorite	0.38	2.49	1.16	2.75	0.39
93	KLB7	35.58241667 75.3182237	KLB	Diorite	0.45	3.15	1.20	2.74	0.45
94	KLB8	35.59146378 75.4008	KLB	Gneiss	2.71	14.17	2.93	2.65	1.92
95	KLB9	35.480035 75.481345	KLB	Gneiss	2.24	14.31	2.18	2.69	1.77
96	koh1	35.40554833 74.609935	KLB	Diorite	2.59	9.10	2.45	2.68	1.51
97	koh2	35.75326167 74.6348093	KLB	Pegmatite	2.72	8.94	3.50	2.63	1.60
98	koh3	35.77605486 74.62160436	KLB	Diorite	1.28	6.69	2.26	2.69	1.00
99	Kp1	35.79003185 75.85693	KLB	Granite	2.12	7.43	2.93	2.65	1.31
100	Kp2	35.27806 75.95206833	KLB	Granite	2.91	17.16	4.00	2.61	2.24
101	Kp3	35.20479 76.128325	KLB	Granite	2.15	13.10	3.70	2.62	1.76
102	Kp4	35.20186667 76.17050833	KLB	Granodiorite	0.89	5.60	1.71	2.72	0.78
103	Kp5	35.1841 76.308435	KLB	Granodiorite	2.78	10.40	3.91	2.62	1.75
104	Kp6	35.17907833 76.36071167	KLB	Granodiorite	2.08	8.87	3.19	2.64	1.42
105	Kp7	35.172755 76.36754716 35.17543676	KLB	Granite	3.95	7.11	2.76	2.66	1.74
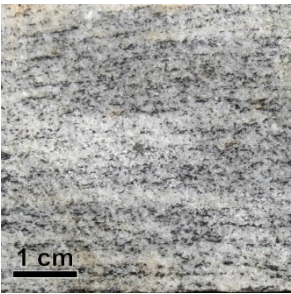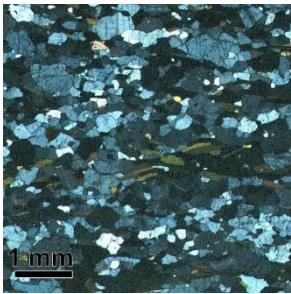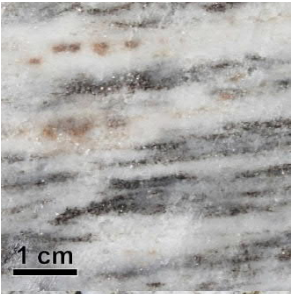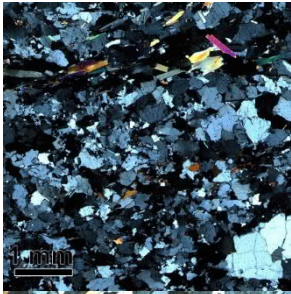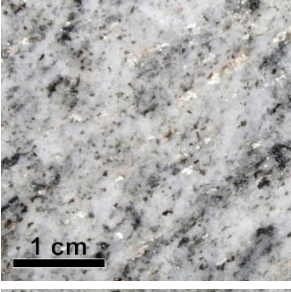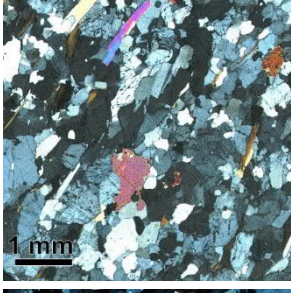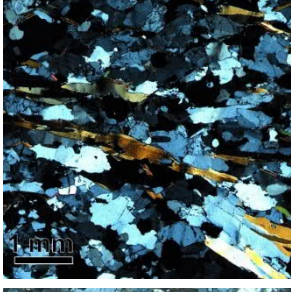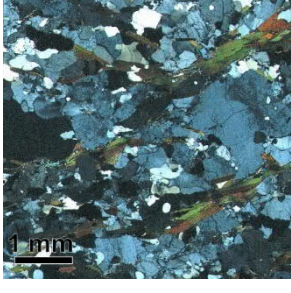
IV

S. N.	Sample ID	Geographic Coordinates	Tectonic Domain	Lithology	U (ppm)	Th (ppm)	K (%)	Density (g/cm^3)	A (µW/m^3)
106	Kp8	76.3871 35.17629	KLB	Granite	4.00	13.22	4.43	2.60	2.27
107	Kpl1	76.46802333 35.127045	KLB	Granite	2.95	16.27	4.27	2.61	2.20
108	Kpl2	76.43187 35.15723833	KLB	Granite	4.53	23.88	4.51	2.60	3.12
109	Kth1	75.44567167 35.41007833	KLB	Gneiss	3.23	12.15	2.43	2.68	1.88
110	Sgh11	75.47872833 35.633045	KLB	Greenstone/metabasalt	0.91	3.50	1.80	2.72	0.65
111	Sgh12	75.68896855 35.4527986	KLB	Diorite	0.94	5.60	1.40	2.74	0.77
112	Sgh13	75.68902167 35.45268	KLB	Granodiorite	1.00	7.11	2.31	2.69	0.96
113	Sgh14	75.71798241 35.41309095	KLB	Granodiorite	1.30	7.23	2.33	2.69	1.05
114	Sk1	74.26980193 35.92999012	KLB	Granodiorite	1.72	7.07	2.40	2.68	1.15
115	Sk2	74.26945167 35.93009167	KLB	Granodiorite	2.82	12.29	3.19	2.64	1.84
116	Sk3	74.27626833 35.93094333	KLB	Granodiorite	2.31	7.93	3.11	2.65	1.41
117	Sk4	74.28782333 35.92967	KLB	Granodiorite	1.42	8.56	2.33	2.69	1.17
118	At2	74.76244167 36.30295	KB	Pegmatite	6.16	3.66	4.51	2.60	2.18
119	KB-1	74.762489 36.302622	KB	Granite	1.78	10.53	4.13	2.62	1.52
120	KB-2	74.762489 36.302622	KB	Diorite	0.93	9.00	2.87	2.76	1.15
121	KB-3	74.767284 36.29868	KB	Pegmatite	8.54	8.00	3.00	2.58	2.90
122	KB-8	74.840833 36.301389	KB	Diorite Gneiss	5.29	20.44	3.47	2.63	3.02
123	KB-4i	74.85778 36.368964	KB	Pegmatite	9.95	16.41	3.50	2.59	3.86
124	KB-4ii	74.85778 36.368964	KB	Diorite	1.39	5.44	2.10	2.68	0.92
125	KB-5	74.872119 36.349715	KB	Granodiorite	2.78	21.33	2.49	2.70	2.43
126	KB-6	74.872119 36.349715	KB	Leucogranite	14.13	11.51	3.27	2.62	4.59
127	KB-7	74.872119 36.349715	KB	Pegmatite	5.48	5.13	2.88	2.66	2.00
128	Bk1	74.28372903 36.37631897	KB	Diorite	3.85	12.27	2.81	2.65	2.07
129	Bk2	74.28298 36.39059667	KB	Dioritic gneiss	1.94	7.77	1.55	2.73	1.20
130	Bk3	74.28092533 36.363006	KB	Granodiorite	7.56	16.40	3.90	2.62	3.34
131	Gl1	74.85780875 36.36888993	KB	Diorite	2.03	14.10	1.90	2.71	1.68
132	Gn1	74.673766 36.31180467	KB	Pegmatite	17.95	11.40	8.20	2.60	5.95
133	Gn2	74.67394167 36.31183333	KB	Gneiss	3.08	14.16	2.26	2.69	1.97
134	Hsh1	76.39439167 35.28332667	KB	Gneiss	5.11	18.53	3.72	2.62	2.86
135	Hsh2	76.43425334 35.23542759	KB	Granite	15.45	65.44	3.08	2.64	8.59
136	Hsh3	76.49577739 35.20639404	KB	Granodiorite	2.58	5.51	4.98	2.59	1.45
137	Hsh4	76.51443833 35.20374	KB	Hbl Granite	44.51	120.00	5.50	2.58	19.38
138	Hsh5	76.5600425 35.20269185	KB	Hbl Granite	37.93	154.00	4.50	2.60	20.06
139	Hsh6	76.58161242 35.20522186	KB	Granodiorite	0.34	4.80	0.90	2.78	0.52
140	Hsu1	76.375125 35.32054167	KB	Gneiss	6.14	23.80	5.50	2.58	3.58
141	Hsu2	76.36330667 35.36559	KB	Gneiss	2.58	11.20	3.90	2.62	1.75
142	Kds1	76.75423361	KB	Granite	6.68	40.10	3.10	2.61	4.63
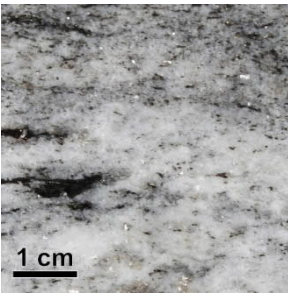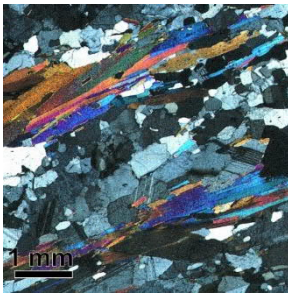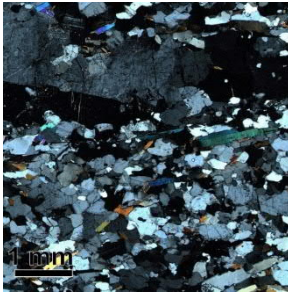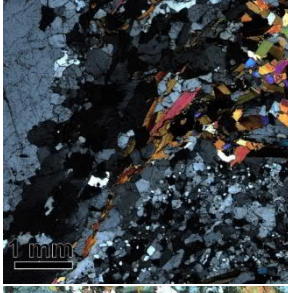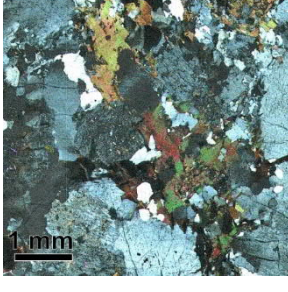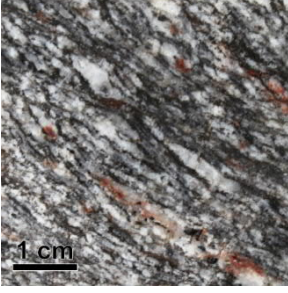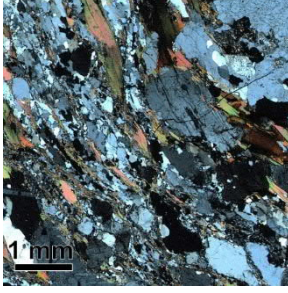
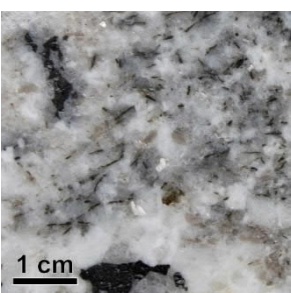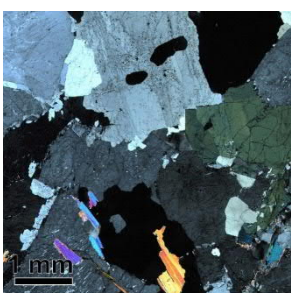| S. N.	Sample ID	Geographic Coordinates	Tectonic Domain	Lithology	U (ppm)	Th (ppm)	K (%)	Density (g/cm^3)	A (µW/m^3)
143	Kds2	35.30918537 76.72632325	KB	Porphyritic granite	1.94	19.82	2.40	2.68	2.08
144	Kds3	35.29721501 76.70846333	KB	Porphyritic granite	2.40	19.33	3.55	2.63	2.23
145	Kds4	35.29099 76.61308	KB	Gneiss	0.66	1.96	1.60	2.73	0.46
146	Ng1	35.21991 74.71001833	KB	Leucogranite	3.30	7.00	2.98	2.61	1.56
147	Sh2	36.28311167 74.87215273	KB	Leucogranite	18.90	11.60	3.90	2.62	5.84
148	Sh3	36.3494449 74.87167833	KB	Granodiorite	5.80	18.22	2.40	2.68	2.96
149	Shg1	36.35028167 75.57503409	KB	Pegmatite	3.31	14.98	2.69	2.67	2.11
150	Shg10	35.60352163 75.40329	KB	Garnet mica schist	1.27	5.78	1.24	2.75	0.86
151	Shg2	35.79442 75.57246667	KB	Gneiss	4.95	22.66	4.53	2.60	3.14
152	Shg3	35.602425 75.49207667	KB	Gneiss	5.52	7.13	3.80	2.62	2.20
153	Shg4	35.666805 75.49102667	KB	Gneiss	10.28	29.87	3.40	2.64	4.91
154	Shg5	35.66860167 75.48864667	KB	Gneiss	6.14	23.67	3.00	2.65	3.44
155	Shg6	35.67346333 75.4862	KB	Granodiorite	11.52	48.61	4.51	2.60	6.50
156	Shg7	35.68201833 75.40139423	KB	Syenite	3.88	13.84	7.70	2.59	2.57
157	Shg8	35.72541053 75.40123752	KB	Syenite	3.60	12.76	6.53	2.58	2.31
158	Shg9	35.72613523 75.401305 35.72578667	KB	Syenite	3.64	9.02	6.53	2.58	2.08
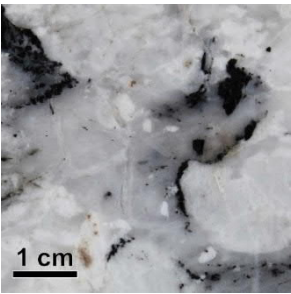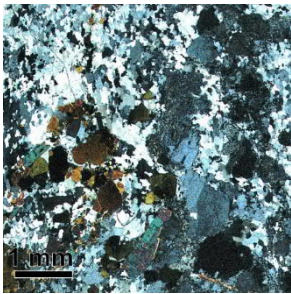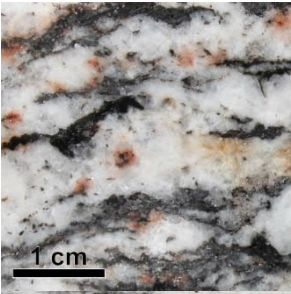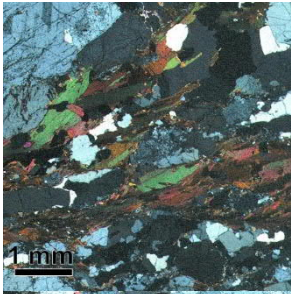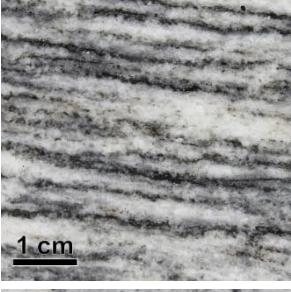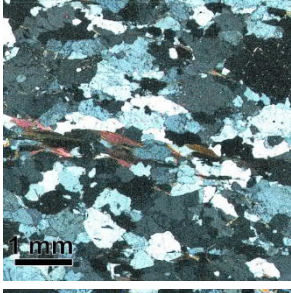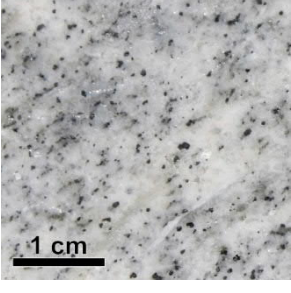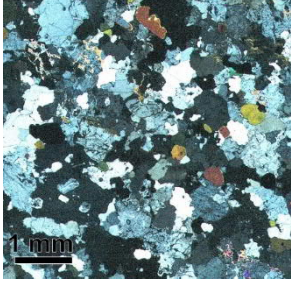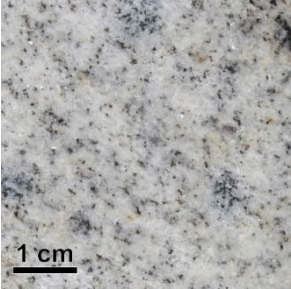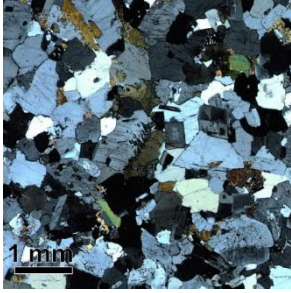
Appendix C – Additional Data to Chapter 5
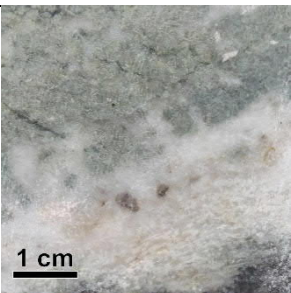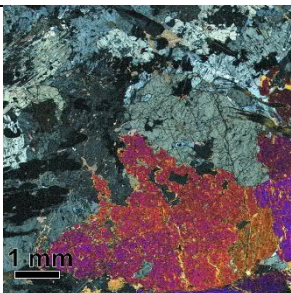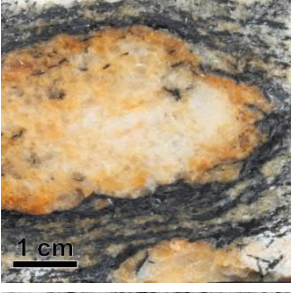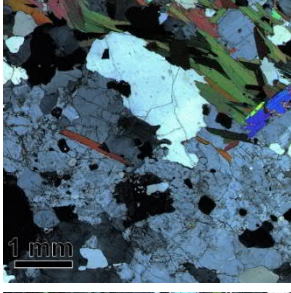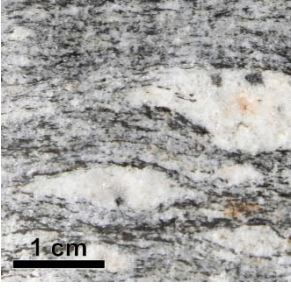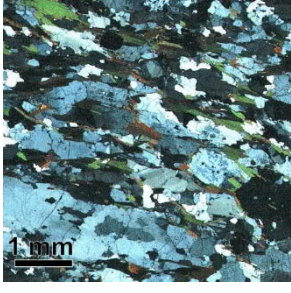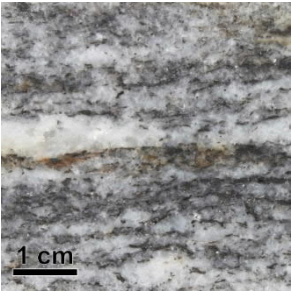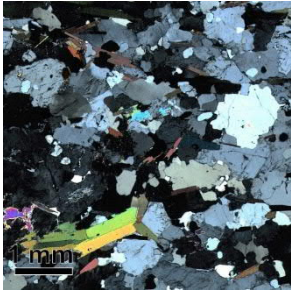
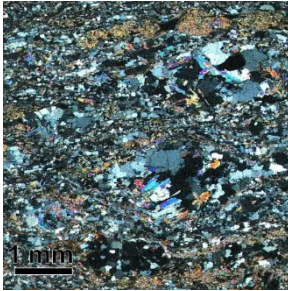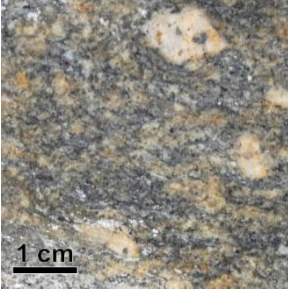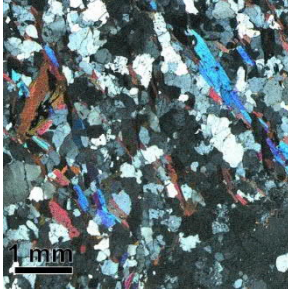Table C1: Petrographic observations and photomicographs of samples from study area.
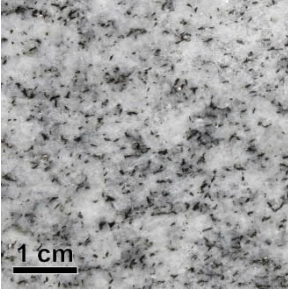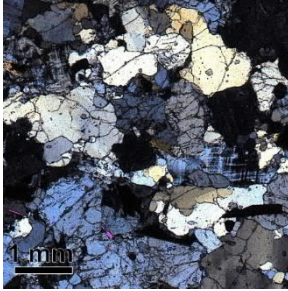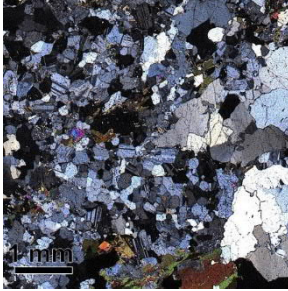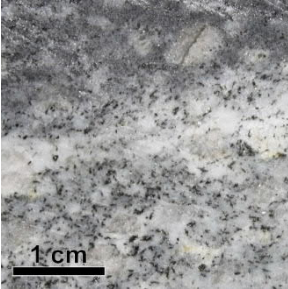
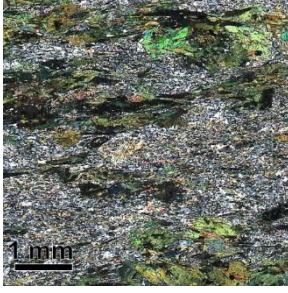| S. N	Sample ID Lithology (Tectonic domain)	Mineralogy	Textural Characteristics	Hand Specimen	Thin Section (XPL)
1	TTP-2i Biotite gneiss (NPM)	Major (> 5 %): Plagioclase, Quartz, Alkali-Feldspar, Biotite Accessory (< 5 %): Apatite, Zircon, Opaques	Grain size: 80 % < 3 mm 20 % > 3 mm Qz+F intergrowth Alteration: moderate alteration Chlorite Sericite		
2	TTP-2ii Pegmatitic granite (NPM)	Major (> 5 %): Plagioclase, Quartz, Alkali-Feldspar, Tourmaline, Biotite Accessory (< 5 %): Muscovite, Opaques, Apatite, Zircon	Grain size: 60 % < 3 mm 40 % > 3 mm Perthite Alteration: Weak alteration Sericite		
3	TTP-3 Biotite gneiss (NPM)	Major (> 5 %): Quartz, Alkali-Feldspar, Plagioclase, Biotite Accessory (< 5 %): Opaques, Apatite, Zircon, Monazite, Epidote	Grain size: 80 % < 3 mm 20 % > 3 mm Myrmekite, Qz-F intergrowth Orientation of micas due to stress Alteration: Weak alteration Sericite, Chlorite		
4	TTP-4 Pegmatite (NPM)	Major (> 5 %): Quartz, Alkali-Feldspar, Plagioclase, Tourmaline, Muscovite	Grain size: 40 % < 3 mm 60 % > 3 mm Perthite, Myrmekite Alteration: Moderate alteration Sericite		
5	TTP-5 Biotite gneiss (NPM)	Major (> 5 %): Alkali-Feldspar, Quartz, Plagioclase, Biotite Accessory (< 5 %): Muscovite, Apatite, Zircon, Monazite, Epidote, Opaques	Grain size: 70 % < 3 mm 30 % > 3 mm Myrmekite, mica fish, Qz+F intergrowth; HT deformation Qz and Bt; Grain boundary buldging and recrytallization in Qz Alteration: Moderate to strong alteration, Limonite, Sericite, Chlorite		

S. N	Sample ID Lithology (Tectonic domain)	Mineralogy	Textural Characteristics	Hand Specimen	Thin Section (XPL)
6	AST-4 Biotite gneiss (NPM)	Major (> 5 %): Quartz, Alkali-Feldspar, Plagioclase, Biotite Accessory (< 5 %): Garnet, Apatite, Zircon, Epidote, Allanite?	Grain size: 100 % < 3 mm Fine grained Alteration: Negligible		
7	AST-6 Biotite muscovite gneiss (NPM)	Major (> 5 %): Quartz, Alkali-Feldspar, Plagioclase Accessory (< 5 %): Garnet, Muscovite, Biotite, Sillimanite, Kynaite, Apatite, Zircon, Rutile	Grain size: 90 % < 3 mm 10 % > 3 mm Recrystallization in Qtz, Grain boundary interlocking Alteration: Negligible		
8	AST-8i Biotite muscovite gneiss (NPM)	Major (> 5 %): Quartz, Alkali-Feldspar, Plagioclase Accessory (< 5 %): Tourmaline, Muscovite, Biotite, Apatite	Grain size: 90 % < 3 mm 10 % > 3 mm Alteration: Weak alteration Chlorite, Sericite		
9	AST-8ii Biotite muscovite gneiss (NPM)	Major (> 5 %): Alkali-Feldspar, Quartz, Plagioclase, Muscovite, Biotite Accessory (< 5 %): Apatite, Zircon	Grain size: 90 % < 3 mm 10 % > 3 mm Alteration: Weak alteration Chlorite, Sericite		
10	AST-9 Biotite gneiss (NPM)	Major (> 5 %): Alkali-Feldspar, Quartz, Plagioclase, Biotite Accessory (< 5 %): Apatite, Zircon, Monazite	Grain size: 90 % < 3 mm 10 % > 3 mm Alteration: Weak alteration Chlorite, Sericite		
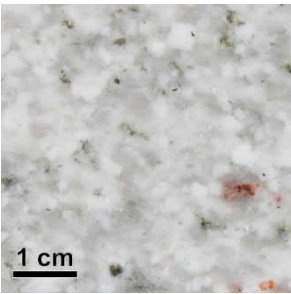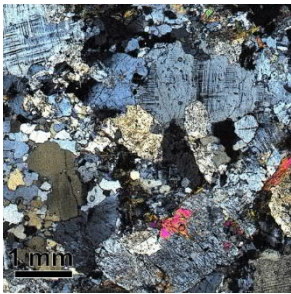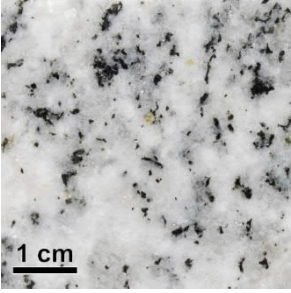
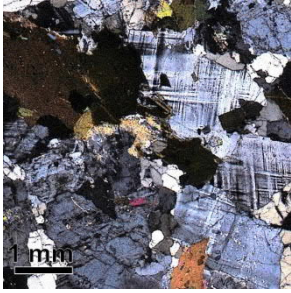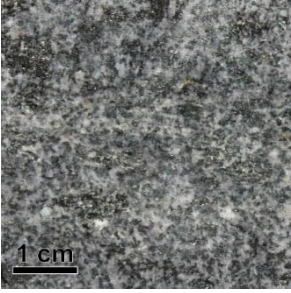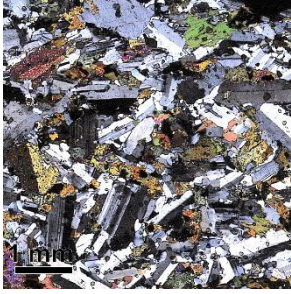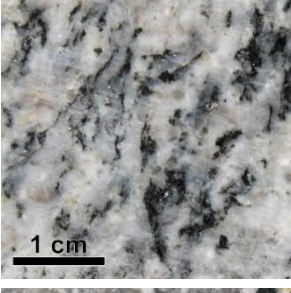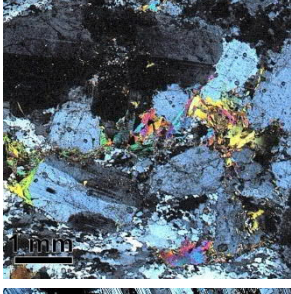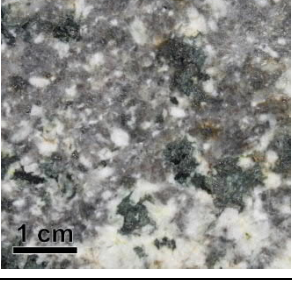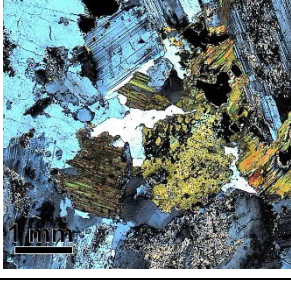| S. N	Sample ID Lithology (Tectonic domain)	Mineralogy	Textural Characteristics	Hand Specimen	Thin Section (XPL)
11	AST-13 Muscovite biotite gneiss (NPM)	Major (> 5 %): Quartz, Alkali-Feldspar, Plagioclase, Biotite, Muscovite Accessory (< 5 %): Apatite, Zircon	Grain size: 90 % < 3 mm 10 % > 3 mm Alteration: Weak alteration Chlorite, Sericite		
12	AST-14 Muscovite biotite gneiss (NPM)	Major (> 5 %): Alkali-Feldspar, Quartz, Plagioclase, Biotite, Muscovite Accessory (< 5 %): Apatite, Zircon, Monazite, Epidote	Grain size: 90 % < 3 mm 10 % > 3 mm Alteration: Moderate alteration Chlorite, Sericite		
13	AST-15 Muscovite biotite gneiss	Major (> 5 %): Alkali-Feldspar, Quartz, Plagioclase, Biotite, Muscovite Accessory (< 5 %): Opaques, Tourmaline, Apatite, Zircon, Monazite, Epidote	Grain size: 80 % < 3 mm 20 % > 3 mm Myrmekites along augen boundaries Micas forming augen type clusters Alteration: Moderate alteration Chlorite, Sericite, Limonite		
14	AST-16 Biotite gneiss	Major (> 5 %): Alkali-Feldspar, Quartz, Plagioclase, Biotite Accessory (< 5 %): Epidote, Apatite, Zircon, Monazite, Opaques	Grain size: 30 % < 3 mm 70 % > 3 mm Alteration: Moderate alteration Chlorite, Sericite		
15	RK-4i Biotite gneiss (NPM)	Major (> 5 %): Alkali-Feldspar, Quartz, Plagioclase, Biotite Accessory (< 5 %): Apatite, Zircon, Monazite, Tourmaline, Opaques	Grain size: 70 % < 3 mm 30 % > 3 mm Alkali-feldspar augens in deformed fabric; Grain boundary buldging and recrytallization in Qz Alteration: Moderate to strong, Limonite, Sericite, Chlorite		
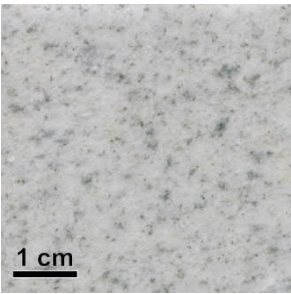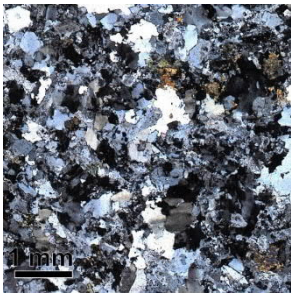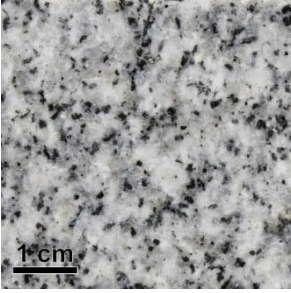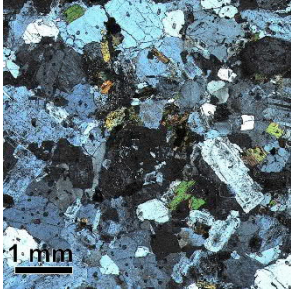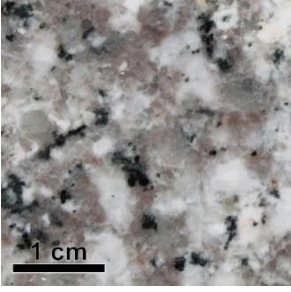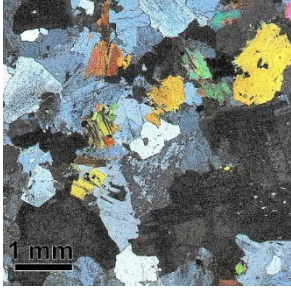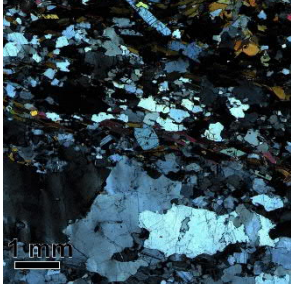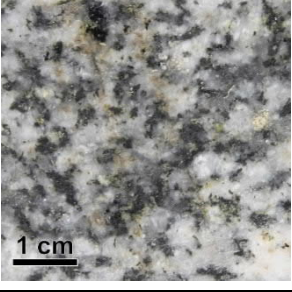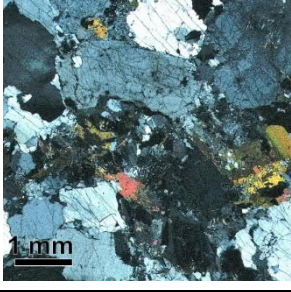
IX

S. N	Sample ID Lithology (Tectonic domain)	Mineralogy	Textural Characteristics	Hand Specimen	Thin Section (XPL)
16	RK-4ii Pegmatite (NPM)	Major (> 5 %): Alkali-Feldspar, Quartz, Plagioclase, Tourmaline Accessory (< 5 %): Muscovite, Biotite, Garnet, Apatite, Opaques Zircon, Monazite	Grain size: 80 % < 3 mm 20 % > 3 mm Alteration: moderate alteration, Sericite, Chlorite		
17	RK-9 Biotite gneiss (NPM)	Major (> 5 %): Alkali-Feldspar, Quartz, Plagioclase, Biotite Accessory (< 5 %): Muscovite, Apatite, Garnet, Opaques, Zircon, Monazite	Grain size: 60 % < 3 mm 40 % > 3 mm Grain size reduction in Bt; Grain boundary buldging and recrytallization in Qz Alteration: moderate alteration, Sericite, Chlorite		
18	RK-10 Biotite gneiss (NPM)	Major (> 5 %): Quartz, Alkali-Feldspar, Plagioclase, Biotite Accessory (< 5 %): Apatite, Zircon	Grain size: 90 % < 3 mm 10 % > 3 mm Gneissose banding Alteration: weak alteration Sericite, Chlorite		
19	RK-13 Granite (NPM)	Major (> 5 %): Alkali-Feldspar, Plagioclase, Quartz, Tourmaline Accessory (< 5 %): Biotite, Muscovite, Opaques, Garnet	Grain size: 95 % < 3 mm 5 % > 3 mm Alteration: weak alteration, Sericite, Chlorite		
20	FM-4 Granite (NPM)	Major (> 5 %): Alkali-Feldspar, Plagioclase, Quartz, Biotite, Tourmaline Accessory (< 5 %): Flourite, Muscovite, Apatite, Garnet, Zircon	Grain size: 95 % < 3 mm 5 % > 3 mm Alteration: Weak alteration Chlorite, Sericite		
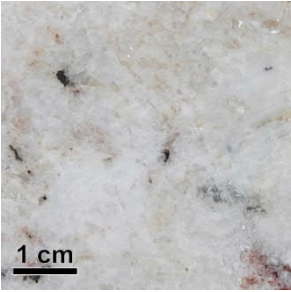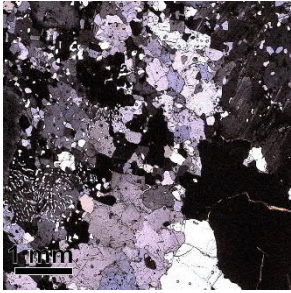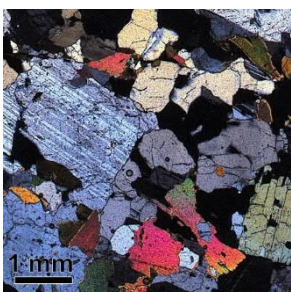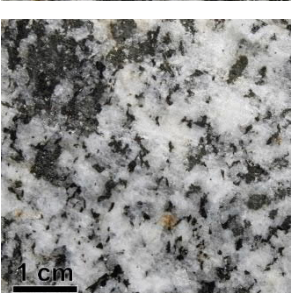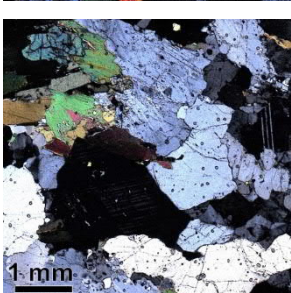
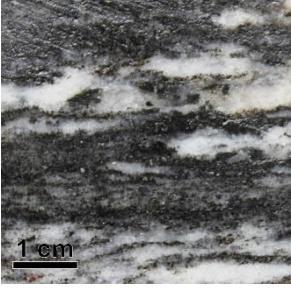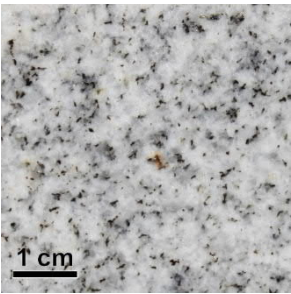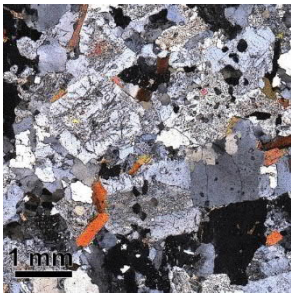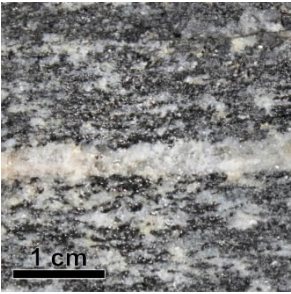| S. N	Sample ID Lithology (Tectonic domain)	Mineralogy	Textural Characteristics	Hand Specimen	Thin Section (XPL)
21	NP-2 Calc-silicate (NPM)	Major (> 5 %): Plagioclase, Pyroxene, Amphibole, Calcite, Quartz Accessory (< 5 %): Epidote, Titanite, Apatite	Grain size: 60 % < 3 mm 40 % > 3 mm Metasomatic late quartz and calcite filling veinlets and fractures Alteration: moderate alteration Sericite		
22	NP-6 Muscovite biotite gneiss (NPM)	Major (> 5 %): Quartz, Alkali-Feldspar, Plagioclase, Biotite Accessory (< 5 %): Muscovite, Apatite, Zircon, Garnet, Monazite, Opaques	Grain size: 60 % < 3 mm 40 % > 3 mm Qtz recrystallization in the strain zones; Myrmekites Alteration: Moderate alteration Chlorite, Sericite, Limonite		
23	NP-7 Biotite gneiss (NPM)	Major (> 5 %): Quartz, Alkali-Feldspar, Plagioclase, Biotite Accessory (< 5 %): Apatite, Zircon, Opaques	Grain size: 80 % < 3 mm 20 % > 3 mm Myrmekites Alteration: Weak alteration Chlorite, Sericite		
24	NP-8 Muscovite biotite gneiss (NPM)	Major (> 5 %): Alkali-Feldspar, Quartz, Plagioclase, Biotite Accessory (< 5 %): Muscovite, Apatite, Zircon, Epidote, Monazite, Opaques	Grain size: 90 % < 3 mm 10 % > 3 mm Myrmekite, Perthite Alteration: Weak alteration Chlorite, Sericite		
25	NP-10 Pegmatitic granite (NPM)	Major (> 5 %): Alkali-Feldspar, Quartz, Plagioclase, Muscoite, Tourmaline Accessory (< 5 %): Biotite, Apatite	Grain size: 30 % < 3 mm 70 % > 3 mm Myrmekite, Perthite Alteration: Weak alteration Chlorite, Sericite		
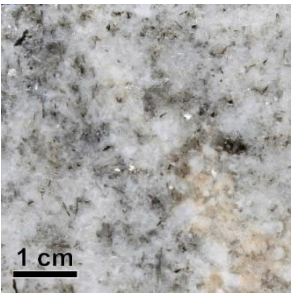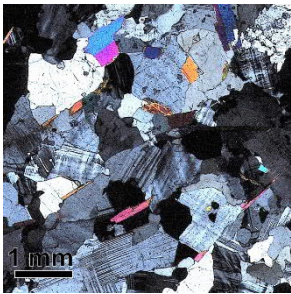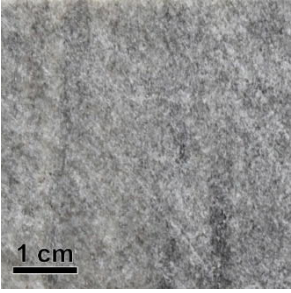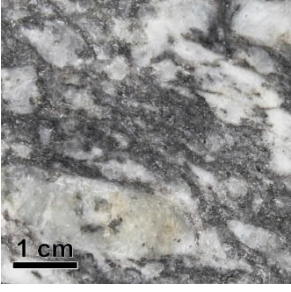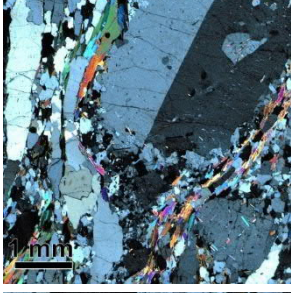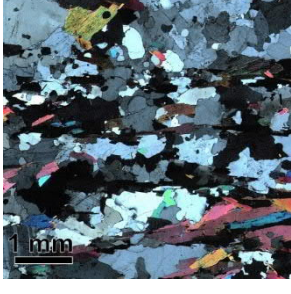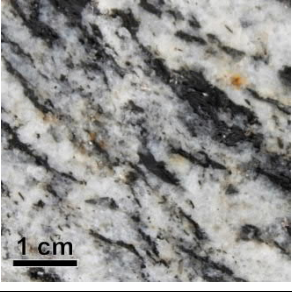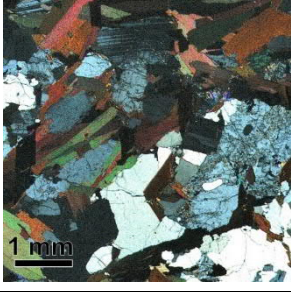
S. N	Sample ID Lithology (Tectonic domain)	Mineralogy	Textural Characteristics	Hand Specimen	Thin Section (XPL)
26	NP-12 Biotite muscovite gneiss (NPM)	Major (> 5 %): Quartz, Alkali-Feldspar, Plagioclase, Muscovite, Biotite Accessory (< 5 %): Opaques, Garnet, Apatite, Zircon	Grain size: 90 % < 3 mm 10 % > 3 mm Fine grained gneiss Alteration: Moderate alteration Chlorite, Sericite		
27	TAR-1 Biotite muscovite gneiss (NPM)	Major (> 5 %): Quartz, Alkali-Feldspar, Plagioclase, Muscovite, Biotite Accessory (< 5 %): Opaques, Apatite, Zircon, Sillimanite	Grain size: 90 % < 3 mm 10 % > 3 mm Alteration: Weak alteration Chlorite, Sericite		
28	CG-2 Granite (KLB)	Major (> 5 %): Quartz, Alkali-Feldspar, Plagioclase, Biotite Accessory (< 5 %): Muscovite, Apatite, Epidote, Zircon	Grain size: 95 % < 3 mm 5 % > 3 mm Myrmekite Alteration: Negligible		
29	GRT-1 Tonalite (KLB)	Major (> 5 %): Quartz, Plagioclase, Alkali-Feldspar, Biotite Accessory (< 5 %): Pyroxene, Apatite, Epidote	Grain size: 95 % < 3 mm 5 % > 3 mm Myrmekite Alteration: weak alteration Sericite		
30	GRT-2 Tonalite (KLB)	Plagioclase: 30 Alkali-Feldspar: 5 Quartz: 60 Amphibole: 1 Biotite: 4	Grain size: 100 % < 3 mm Alteration: Negligible		
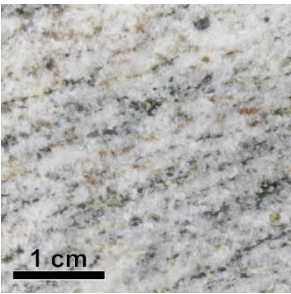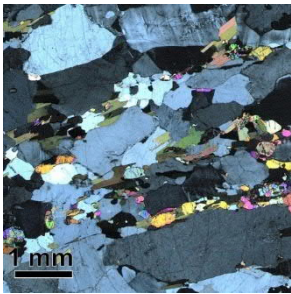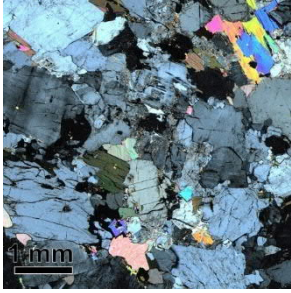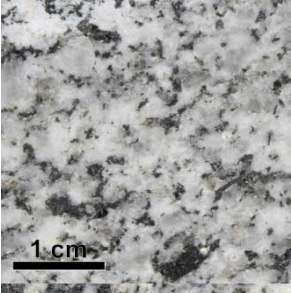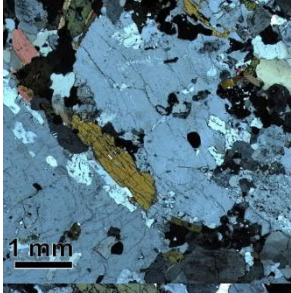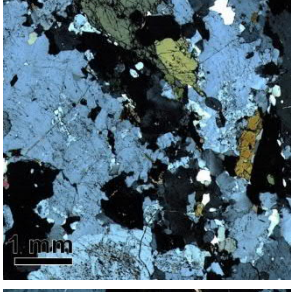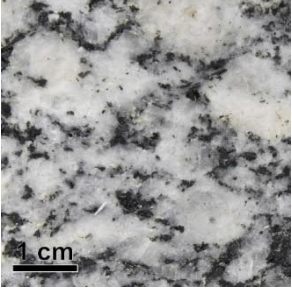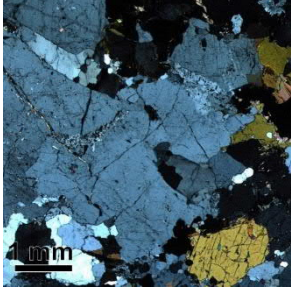
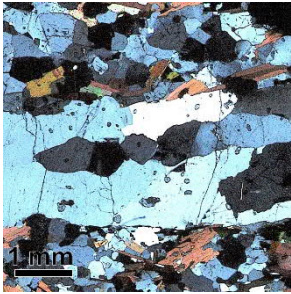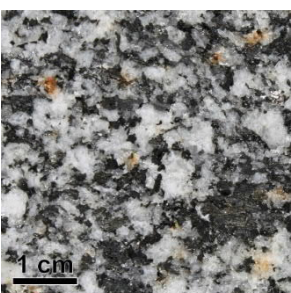| S. N	Sample ID Lithology (Tectonic domain)	Mineralogy	Textural Characteristics	Hand Specimen	Thin Section (XPL)
31	JT-1 Quartz monzonite (KLB)	Major (> 5 %): Plagioclase, Quartz, Biotite, Alkali-Feldspar, Amphibole Accessory (< 5 %): Titanite, Apatite, Epidote, Pyroxene	Grain size: 98 % < 3 mm 2 % > 3 mm Alteration: Negligible		
32	JT-2 Granodiorite (KLB)	Major (> 5 %): Quartz, Plagioclase, Biotite, Alkali-Feldspar Accessory (< 5 %): Titanite, Epidote, Pyroxene, Apatite, Zircon	Grain size: 80 % < 3 mm 20 % > 3 mm Deforamtion in Qz, Bt, Ap Alteration moderate alteration Chlorite, Sericite		
33	BST-1 Basalt (KLB)	Major (> 5 %): Amphibole, Quartz, Epidote Accessory (< 5 %): Opaques, Titanite	Grain size: 90 % < 3 mm 10 % > 3 mm Minor foliation Alteration: Negligible		
34	DR-1 Dacite (KLB)	Major (> 5 %): Quartz, Amphibole, Biotite, Plagioclase, Alkali-Feldspar Accessory (< 5 %): Opaques, Titanite	Grain size: 95 % < 3 mm 5 % > 3 mm Alteration: Negligible		
35	GB-1 Granite (KLB)	Major (> 5 %): Plagioclase, Quartz, Alkali-Feldspar, Biotite Accessory (< 5 %): Muscovite, Amphibole, Pyroxene? Epidote, Apatite, Zircon	Grain size: 70 % < 3 mm 30 % > 3 mm Alteration: moderate alteration Chlorite Sericite (>30% in Plagioclase)		

S. N	Sample ID Lithology (Tectonic domain)	Mineralogy	Textural Characteristics	Hand Specimen	Thin Section (XPL)
36	HZ-1 Granite (KLB)	<u>Major (> 5 %):</u> Alkali-Feldspar, Quartz, Plagioclase, <u>Accessory (< 5 %):</u> Muscovite, Garnet, Epidote	<u>Grain size:</u> 80 % < 3 mm 20 % > 3 mm Perthite <u>Alteration:</u> moderate alteration; Sericite		
37	GZ-1 Granite (KLB)	<u>Major (> 5 %):</u> Quartz, Alkali-Feldspar, Plagioclase, Biotite <u>Accessory (< 5 %):</u> Muscovite, Titanite, Epidote, Apatite, Zircon	<u>Grain size:</u> 80 % < 3 mm 20 % > 3 mm Perthite, Myrmekite <u>Alteration:</u> moderate alteration; Chlorite, Sericite		
38	GW-1 Monzodiorite /Gabbro (KLB)	<u>Major (> 5 %):</u> Plagioclase, Amphibole, Biotite <u>Accessory (< 5 %):</u> Opaques, Epidote, Titanite, Apatite	<u>Grain size:</u> 5 % < 3 mm 95 % > 3 mm <u>Alteration:</u> Moderate alteration; Chlorite, Sericite		
39	GP-1 Granite (KLB)	<u>Major (> 5 %):</u> Plagioclase, Alkali-Feldspar, Quartz, Biotite <u>Accessory (< 5 %):</u> Titanite, Epidote, Apatite, Zircon	<u>Grain size:</u> 60 % < 3 mm 40 % > 3 mm Perthite, Quartz Ribbon, Recrystallization <u>Alteration:</u> Weak alteration Chlorite, Sericite		
40	YK-2 Diorite (KLB)	<u>Major (> 5 %):</u> Plagioclase, Amphibole <u>Accessory (< 5 %):</u> Opaques, Biotite, Epidote, Apatite, Zircon	<u>Grain size:</u> 70 % < 3 mm 30 % > 3 mm Plg zoning, Op with Ca rims <u>Alteration:</u> Strong alteration; Chlorite, Sericite, Calcite, Epidote		

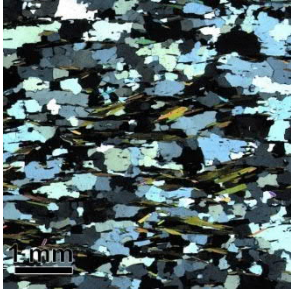| S. N	Sample ID Lithology (Tectonic domain)	Mineralogy	Textural Characteristics	Hand Specimen	Thin Section (XPL)
41	YK-3 Granite (KLB)	Major (> 5 %): Alkali-Feldspar, Plagioclase, Quartz Accessory (< 5 %): Titanite, Epidote, Apatite	Grain size: 100 % < 3 mm Perthite, Myrmekite Alteration: moderate alteration; Sericite	1 cm	1 mm
42	TH-1 Granodiorite (KLB)	Major (> 5 %): Plagioclase, Alkali-Feldspar, Biotite, Amphibole Accessory (< 5 %): Opaques, Quartz, Epidote, ZIrcon	Grain size: 90 % < 3 mm 10 % > 3 mm Perthite, Myrmekite, Plg zoning Alteration: moderate alteration; Chlorite (>50% in Biotite), Sericite	1 cm	1 mm
43	TH-2 Granite (KLB)	Major (> 5 %): Plagioclase, Alkali-Feldspar, Quartz Accessory (< 5 %): Biotite, Opaques, Epidote	Grain size: 60 % < 3 mm 40 % > 3 mm Perthite, Alteration: moderate alteration; Chlorite, Sericite	1 cm	1 mm
44	KOH-4 Meta-diorite (KLB)	Major (> 5 %): Plagioclase, Quartz, Biotite Accessory (< 5 %): Opaques, Amphibole, Zoisite, Garnet, ZIrcon	Grain size: 90 % < 3 mm 10 % > 3 mm Alteration: Neglegible	1 cm	1 mm
45	SK-2 Granite (KLB)	Major (> 5 %): Plagioclase, Quartz, Alkali-Feldspar, Biotite Accessory (< 5 %): Amphibole, Pyxroxene, Opaques, Titanite, Epidote, Apatite	Grain size: 80 % < 3 mm 20 % > 3 mm Myrmekite Alteration: moderate alteration; Chlorite, Sericite (>30% in Plagioclase)	1 cm	1 mm

S. N	Sample ID Lithology (Tectonic domain)	Mineralogy	Textural Characteristics	Hand Specimen	Thin Section (XPL)
46	KB-1 Granite (KB)	Major (> 5 %): Alkali-Feldspar, Quartz, Plagioclase, Biotite Accessory (< 5 %): Muscovite, Opaques, Apatite, Zircon	Grain size: 90 % < 3 mm 10 % > 3 mm Perthite, Myrmekite Alteration: moderate alteration; Sericite, Chlorite		
47	KB-2 Quartz monzonite (KB)	Major (> 5 %): Quartz, Alkali-Feldspar, Plagioclase, Biotite Accessory (< 5 %): Calcite, Muscovite, Apatite, Epidote, Tourmaline, Zircon	Grain size: 80 % < 3 mm 20 % > 3 mm Alteration: weak alteration; Sericite		
48	KB-4i Pegmatitic granite (KB)	Major (> 5 %): Plagioclase, Quartz, Alkali-Feldspar, Accessory (< 5 %): Garnet, Muscovite	Grain size: 20 % < 3 mm 80 % > 3 mm Intense myrmekite, Qz+F intergrowth Alteration: moderate alteration; Sericite		
49	KB-4ii Diorite (KB)	Major (> 5 %): Plagioclase, Quartz, Biotite, Alkali-Feldspar, Amphibole Accessory (< 5 %): Epidote, Titanite, Opaques, Apatite, Zircon	Grain size: 80 % < 3 mm 20 % > 3 mm Alteration: Negligible		
50	KB-5 Granodiorite (KB)	Major (> 5 %): Plagioclase, Quartz, Alkali-Feldspar, Biotite, Amphibole, Pyroxene Accessory (< 5 %): Epidote, Titanite, Opaques, Apatite, Zircon	Grain size: 80 % < 3 mm 20 % > 3 mm Myrmekite Alteration: Weak alteration; Focused in amphiboles		

S. N	Sample ID Lithology (Tectonic domain)	Mineralogy	Textural Characteristics	Hand Specimen	Thin Section (XPL)
51	KB-6 Granite (KB)	Major (> 5 %): Alkali-Feldspar, Plagioclase, Quartz, Muscovite Accessory (< 5 %): Biotite, Garnet, Apatite	Grain size: 70 % < 3 mm 30 % > 3 mm Myrmekite Alteration: Weak alteration; Chlorite (>50% in Biotite)	1 cm	1 mm
52	SGH-1 Garnet mica schist (KB)	Major (> 5 %): Quartz, Alkali-Feldspar, Mica Accessory (< 5 %): Garnet, Titanite, Epidote, Zircon, Opaques	Grain size: 998 % < 3 mm 1 % > 3 mm Alteration: Negligible	1 cm	1 mm
53	SGH-2 Muscovite biotite gneiss (KB)	Major (> 5 %): Plagioclase, Quartz, Alkali-Feldspar, Biotite, Muscovite Accessory (< 5 %): Apatite, Zircon, Garnet	Grain size: 40 % < 3 mm 60 % > 3 mm Alteration: Weak alteration; Sericite, Chlorite	1 cm	1 mm
54	SGH-4 Muscovite biotite gneiss (KB)	Major (> 5 %): Plagioclase, Quartz, Alkali-Feldspar, Biotite, Muscovite Accessory (< 5 %): Apatite, Epidote, Zircon, Garnet, Opaques	Grain size: 90 % < 3 mm 10 % > 3 mm Alteration: moderate alteration; Chlorite, Sericite	1 cm	1 mm
55	SGH-6 Biotite gneiss (KB)	Major (> 5 %): Quartz, Plagioclase, Alkali-Feldspar, Biotite, Accessory (< 5 %): Muscovite, Apatite, Epidote, Zircon, Garnet, Opaques	Grain size: 80 % < 3 mm 20 % > 3 mm Alteration: moderate alteration; Chlorite, Sericite	1 cm	1 mm

S. N	Sample ID Lithology (Tectonic domain)	Mineralogy	Textural Characteristics	Hand Specimen	Thin Section (XPL)
56	SGH-7 Syenite (KB)	Major (> 5 %): Alkali-Feldspar, Plagioclase, Quartz, Biotite, Epidote Accessory (< 5 %): Apatite, Garnet, Titanite, Opaques	Grain size: 90 % < 3 mm 10 % > 3 mm Alteration: Weak alteration; Albitization in Plagioclase		
57	SGH-9 Syenite (KB)	Major (> 5 %): Alkali-Feldspar, Plagioclase, Muscovite, Biotite Accessory (< 5 %): Quartz, Calcite, Opaques, Apatite, Epidote, Zircon	Grain size: 90 % < 3 mm 10 % > 3 mm Alteration: Moderate alteration; Calcite, Sericite, Chlorite		
58	HSH-2 Quartz monzonite (KB)	Major (> 5 %): Alkali-Feldspar, Plagioclase, Quartz, Amphibole, Biotite Accessory (< 5 %): Opaques, Titanite, Epidote, Clinozoisite, Apatite, Zircon, Allanite	Grain size: 60 % < 3 mm 40 % > 3 mm Myrmekite, Perthite Alteration: Weak alteration; Caclite, Sericite, Chlorite		
59	HSH-4 Syenite (KB)	Major (> 5 %): Alkali-Feldspar, Quartz, Plagioclase, Amphibole Accessory (< 5 %): Biotite, Opaques, Titanite, Epidote, Apatite, Zircon, Allanite	Grain size: 70 % < 3 mm 30 % > 3 mm Myrmekite, Perthite Alteration: Moderate aleration; Calcite, Sericite		
60	HSH-5 Syenite (KB)	Major (> 5 %): Alkali-Feldspar, Plagioclase, Quartz, Amphibole, Biotite Accessory (< 5 %): Titanite, Epidote, Apatite, Zircon, Allanite, Opaques	Grain size: 30 % < 3 mm 70 % > 3 mm Alteration : Moderate alteration; Chlorite, Calcite		
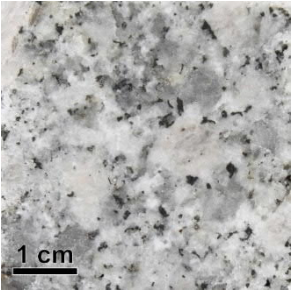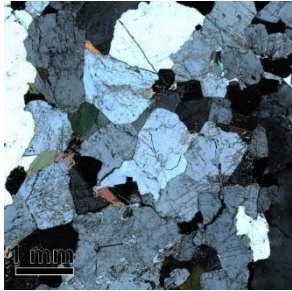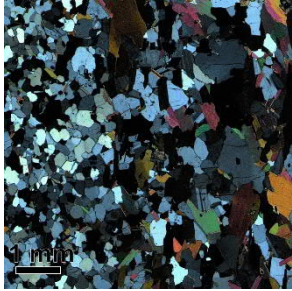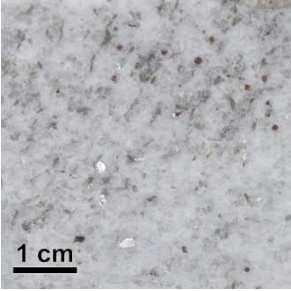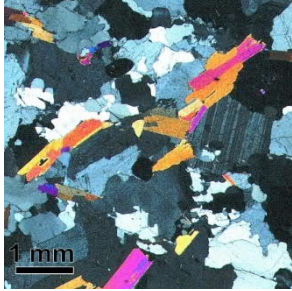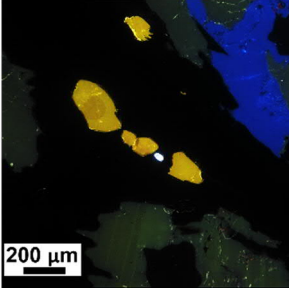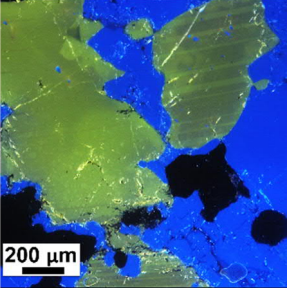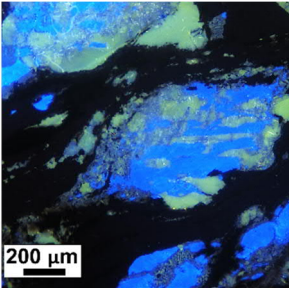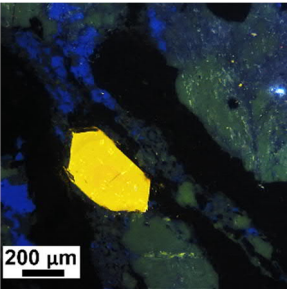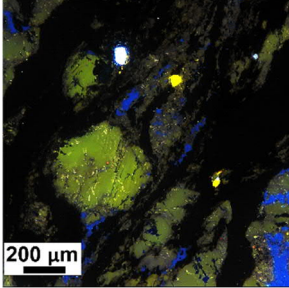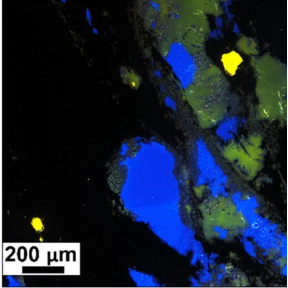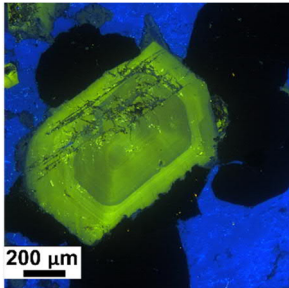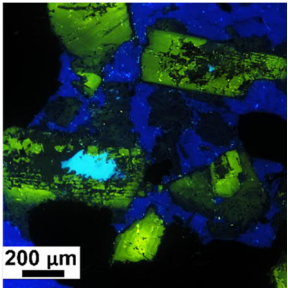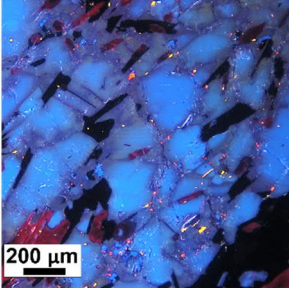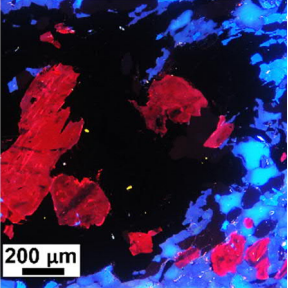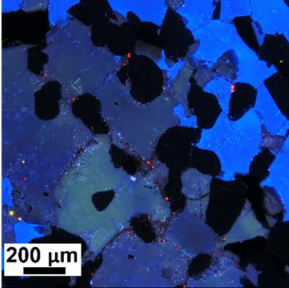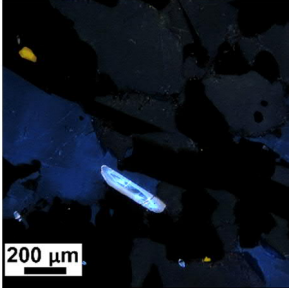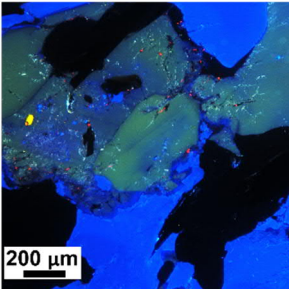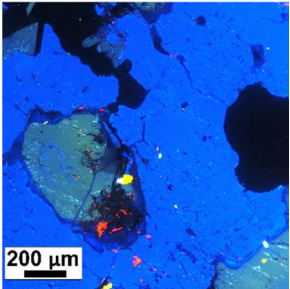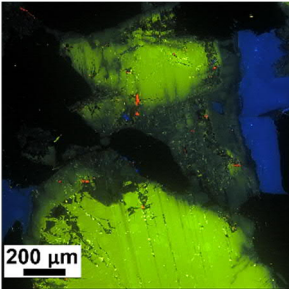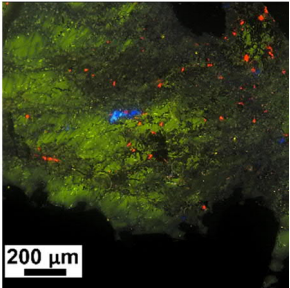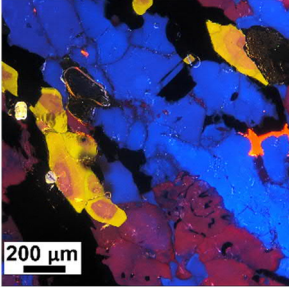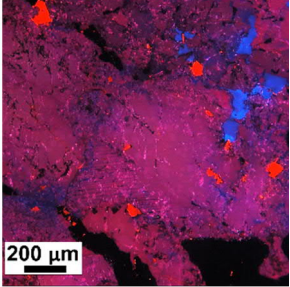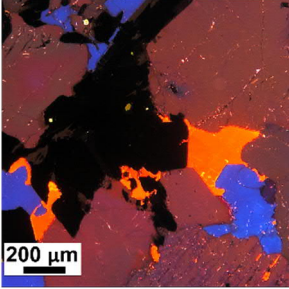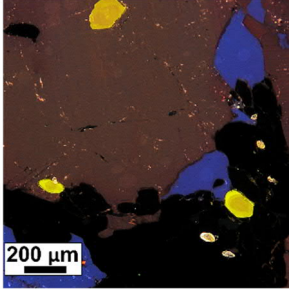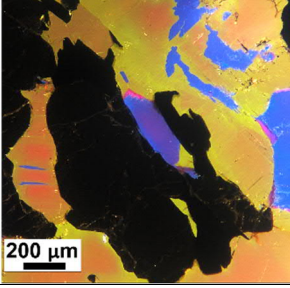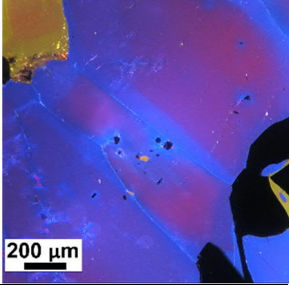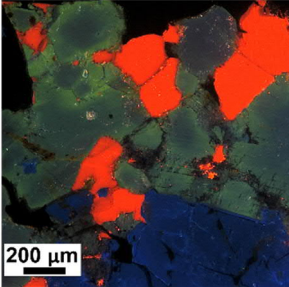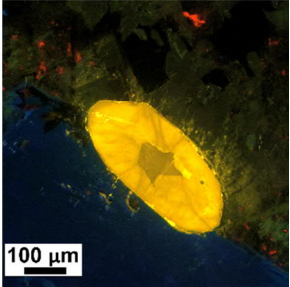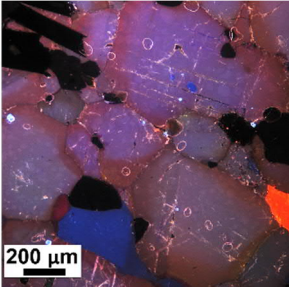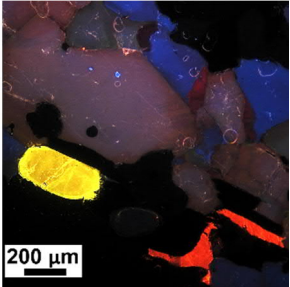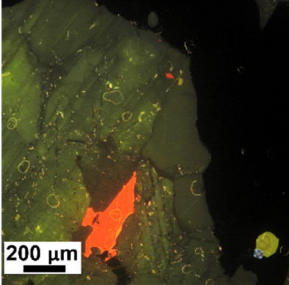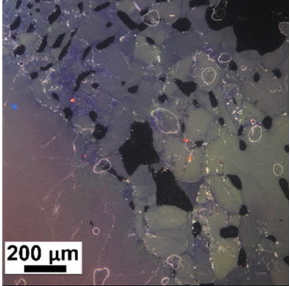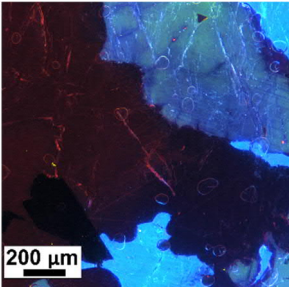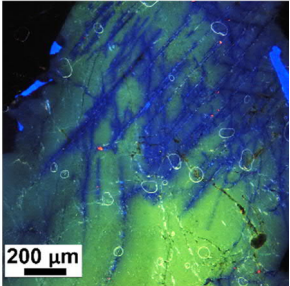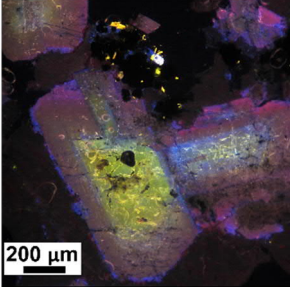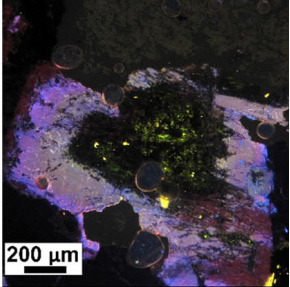
S. N	Sample ID Lithology (Tectonic domain)	Mineralogy	Textural Characteristics	Hand Specimen	Thin Section (XPL)
61	KDS-1 Granite (KB)	Major (> 5 %): Plagioclase, Alkali-Feldspar, Quartz, Biotite Accessory (< 5 %): Opaques, Apatite, Zircon, Titanite	Grain size: 40 % < 3 mm 60 % > 3 mm Alkali feldspar phenocrysts Alteration: Moderate alteration; Sericite, Chlorite (Strong)		
62	GL-3 Granodiorite (KB)	Major (> 5 %): Quartz, Plagioclase, Biotite Accessory (< 5 %): Epidote, Titanite, Zircon, Opaques	Grain size: 99 % < 3 mm 1 % > 3 mm Alteration: Neglegible		
63	NG-1 Granite (KB)	Major (> 5 %): Alkali-Feldspar, Plagioclase, Quartz, Muscovite Accessory (< 5 %): Garnet, Apatite, Zircon	Grain size: 90 % < 3 mm 10 % > 3 mm Alteration: Negligible		

Table C2: Cathodoluminescence observations and photomicrographs of samples from study area.

S. N	Sample ID Lithology (Tectonic domain)	Observations	CL Photomicrographs
1	TTP-3 Biotite gneiss (NPM)	Plagioclase: Light to dark yellowish green (Mn), slight alteration K-Feldspar: Deep blue, unaltered Apatite: Zoned and unzoned, brownish yellow core with yellow margin Zircon: Complex zoning, with alternating dark and light blue bands, Associated with biotite Others: Minor secondary calcite in intragranular cleavage space	
2	TTP-5 Biotite gneiss (NPM)	Plagioclase: Light to dark yellowish green (Mn) with Intense albitization in grains along the strain zones K-Feldspar: Deep blue, unaltered Apatite: Simple, without clear zoning Zircon: Zoned, with alternating dark and light blue bands	
3	RK-4i Biotite gneiss (NPM)	Plagioclase: Yellowish green (Mn) cores with reddish green margins with some alteration and secondary calcite. Albitization along the strain zones. Microfractures showing evidence of alteration due to fluid flow K-Feldspar: Deep blue, Mostly unaltered Quartz: Homogenous purplish tint Apatite: Simple, unzoned Zircon: Zoned, with alternating dark and light blue bands	
4	FM-4 Granite (NPM)	Plagioclase: Euhedral, zoned, Dark green cores (Mn) with reddish blue margins, some replacement within core by alkali feldspars or sometime by fluorite K-Feldspar: Deep blue, unaltered Others: Light blue Fluorite	
5	AST-6 Biotite muscovite gneiss (NPM)	Plagioclase: Two different varieties, Blue unaltered ones and reddish green with calcic altered cores K-Feldspar: Blue cores with reddish green margins Quartz: Purplish tint Apatite: Unzoned, dark yellow Others: Dark red Sillimanite and Kyanite	

6	AST-14 Muscovite biotite gneiss (NPM)	<u>Plagioclase:</u> Reddish green (Mn, Fe) with slightly altered margins <u>K-Feldspar:</u> Deep blue, unaltered <u>Quartz:</u> Weakly reddish luminescent <u>Apatite:</u> Simple, unzoned <u>Zircon:</u> Zoned, dark blue cores with light blue margins		
7	NP-8 Muscovite biotite gneiss (NPM)	<u>Plagioclase:</u> Yellowish green (Mn) cores with reddish blue margins with some alteration and secondary calcite. Albitization at few places <u>K-Feldspar:</u> Deep blue, Mostly unaltered <u>Quartz:</u> Short-lived bottle green luminesces <u>Apatite:</u> Unzoned, dark yellow <u>Zircon:</u> Zoned, light blue core with light brown margins		
8	NP-10 Pegmatitic granite (NPM)	<u>Plagioclase:</u> Bright green (Mn) with medium alteration along margins. Calcitization, Albitization <u>K-Feldspar:</u> Deep blue, Mostly unaltered <u>Quartz:</u> Homogenous purplish tint <u>Apatite:</u> Unzoned, dark yellow		
9	HSH-4 Syenite (KB)	<u>Plagioclase:</u> Bluish red core with pinkish red margin (Fe,Ti), slight calcic alteration and albitization at few places <u>K-Feldspar:</u> Deep blue, with reddish slightly altered margins at few places <u>Apatite:</u> Zoned, orange core and yellow margin <u>Zircon:</u> Zoned, bright orange <u>Others:</u> Secondary calcite		
10	HSH-5 Syenite (KB)	<u>Plagioclase:</u> Bluish red core with pinkish red margin, slight calcic alteration and albitization along cleavage <u>K-Feldspar:</u> Deep blue, with reddish slightly altered patches of reddish plagioclase <u>Apatite:</u> Zoned, brownish orange core and yellow margin <u>Zircon:</u> Zoned, brown core with bright orange margin <u>Others:</u> Secondary calcite		
11	SGH-7 Syenite (KB)	<u>Plagioclase:</u> Reddish green core (Fe) with yellowish green (Mn) margin, slight alteration along margins, patches of albite at few places <u>K-Feldspar:</u> Pinkish blue core with deep blue margin, mostly unaltered <u>Apatite:</u> Zoned, brownish orange core and bright yellow margin		

12	SGH-9 Syenite (KB)	Plagioclase: Reddish green core with bright green margin, medium calcic alteration along margins, albitization along cleavage K-Feldspar: Deep blue, Mostly unaltered Apatite: Zoned, brownish orange core and bright yellow margin Others: Secondary calcite	
13	KB-2 Quartz monzonite (KB)	Plagioclase: Pinkish red core (Fe) with brownish red margins due to oxidation. K-Feldspar: Deep blue, Mostly unaltered Quartz: Reddish, weakly luminescent Apatite: Zoned, brownish yellow core with bright yellow margin Zircon: light blue core with bluish white margins Others: Secondary calcite in intergranular spaces and fractures veinlets	
14	KB-4i/4ii Pegmatite- Diorite (contact) (KB)	Plagioclase: Yellowish to reddish green (Mn), minor calcitization Apatite: Zoned, brownish yellow core with bright yellow margin Zircon: light blue core with bluish white margins Others: Secondary calcite filling intragranular veinlets and alteration voids	
15	KB-6 Granite (KB)	Plagioclase: Yellowish to reddish green (Mn), albitization and minor calcite along cleavage. Reddish margins due to Fe+3 K-Feldspar: Deep blue, Mostly unaltered Quartz: Reddish, weakly luminescent	
16	TH-1 Granodiorite (KLB)	Plagioclase: Euhedral, zoned, yellowish green cores with greenish to pinkish red margins. Bluish thin margins K-Feldspar: Bright blue, With reddish Fe+3 alteration	
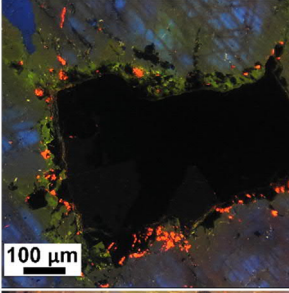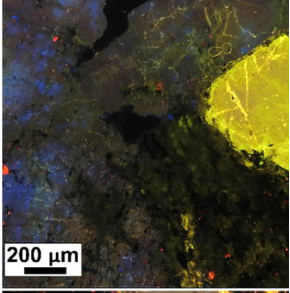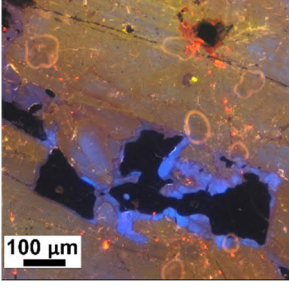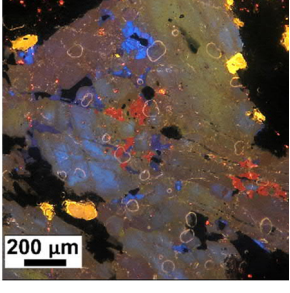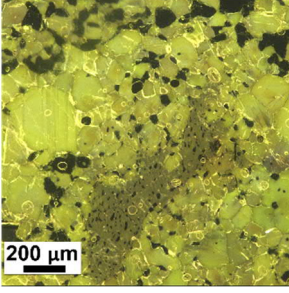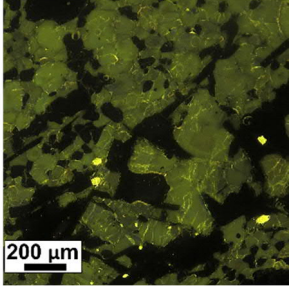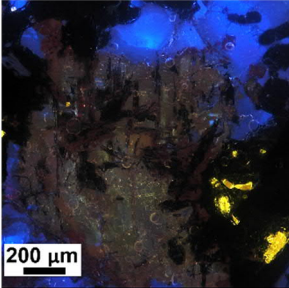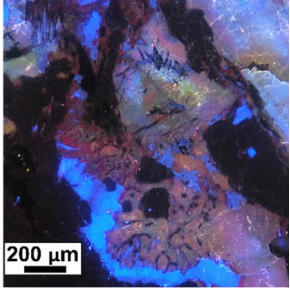
17	YK-2 Diorite (KLB)	Plagioclase: Yellowish green to greenish red. Medium to high alteration: Sericitization, Calcitization, Albitization K-Feldspar: Bright blue, Dark blue patches with secondary minerals and calcite Apatite: Brownish orange core and thin bright yellow margin Others: Secondary calcite		
18	GW-1 Monzodiorite / Gabbro (KLB)	Plagioclase: Two different varieties One with bluish core and other with yellowish green to red core. Margin in both are greenish red. medium calcic alteration and albitization in cores Quartz: Weakly luminescent, forming albite rim along contact with Plagioclase Apatite: Zoned, brownish orange core and thin bright yellow margin Others: Secondary calcite		
19	GRT-2 Tonalite (KLB)	Plagioclase: Dark green to yellowish green variations, mostly unaltered		
20	JT-2 Granodiorite (KLB)	Plagioclase: Yellowish green core with greenish red margin, slight alteration along margins, high alteration in patches, mostly albitization with bluish tint in core and solid rims at margins K-Feldspar: Bright blue, Mostly unaltered Apatite: Zoned, greenish yellow core and thin bright yellow margin		

Table C3: Results of major and minor (trace and rare earth) elements.

Sample_ID	TTP-1	TTP-2	TTP-3	TTP-4	TTP-5	AST-4	AST-6	AST-8i	AST-8ii	AST-9
Major elements										
SiO_2	72.75	71.57	65.93	74.31	69.38	66.52	72.87	73.72	72.81	70.09
TiO_2	0.27	0.47	0.87	0.06	0.68	0.48	0.23	0.13	0.19	0.48
Al_2O_3	13.92	13.26	13.83	13.85	13.82	16.03	15.06	14.78	14.67	14.33
MnO	0.02	0.04	0.07	0.01	0.05	0.09	0.03	0.01	0.01	0.03
MgO	0.91	0.77	1.46	0.13	0.81	0.72	0.29	0.28	0.40	0.65
CaO	1.35	1.18	2.34	0.65	1.66	1.67	0.93	0.74	0.60	1.13
Na_2O	2.89	2.62	2.49	3.02	2.39	4.69	2.81	3.30	2.74	2.59
K_2O	4.12	5.22	4.14	5.51	5.19	4.95	5.66	5.06	5.90	6.42
P_2O_5	0.12	0.14	0.19	0.02	0.18	0.17	0.25	0.15	0.16	0.23
Fe_2O_3	2.34	3.40	6.08	0.82	4.46	3.99	1.41	1.12	1.47	3.37
LOI	0.92	0.58	0.93	0.50	0.82	0.44	0.37	0.63	0.85	0.51
Sum	99.61	99.25	98.33	98.88	99.43	99.76	99.91	99.92	99.80	99.83
Trace elements										
Sc	6.46	8.71	16.36	1.38	10.06	5.86	6.28	1.76	1.80	5.49
Cr	53.41	31.98	67.99	0.43	35.40	13.63	6.91	1.94	4.91	17.53
Co	8.48	9.39	17.51	1.02	10.87	7.00	2.56	1.60	3.33	8.09
Ni	21.32	12.55	25.74	1.72	16.83	9.83	2.93	0.78	3.44	9.03
Zn	43.47	52.65	93.30	21.16	89.62	77.32	42.51	39.53	48.68	73.03
Rb	189.40	323.92	236.61	353.37	396.29	198.23	313.29	306.27	314.62	370.64
Sr	178.91	79.75	174.12	33.67	99.91	326.62	58.28	47.18	72.44	74.46
Y	18.01	19.27	38.81	23.67	34.02	36.79	13.07	3.87	5.83	32.66
Zr	33.78	16.68	25.83	4.43	63.19	56.69	28.04	65.40	95.90	57.99
Nb	8.51	10.73	16.02	17.17	22.64	91.57	17.42	11.93	13.93	20.53
Cs	5.41	22.98	7.25	12.74	14.13	10.79	10.89	6.21	6.25	8.17
Ba	575.35	326.19	678.70	117.06	481.39	636.25	208.54	112.69	244.55	430.50
Hf	0.92	0.49	0.69	0.29	1.65	1.35	0.85	2.04	2.79	1.51
Ta	0.78	1.33	1.36	0.49	1.62	5.11	0.90	0.70	0.87	1.97
Pb	34.09	26.24	32.83	64.72	42.14	35.47	43.65	29.78	38.64	47.40
Th	28.24	15.58	26.29	9.00	74.45	41.58	16.73	15.39	31.98	82.60
U	6.65	30.46	4.75	10.41	8.82	6.85	15.55	21.01	7.60	9.07
Rare earth elements										
La	48.23	26.86	57.09	7.83	81.50	131.24	26.38	23.09	49.13	85.82
Ce	95.79	55.24	115.25	16.89	177.65	235.73	59.37	51.13	103.27	193.39
Pr	11.68	6.36	13.61	2.01	22.07	26.11	6.83	5.98	12.59	24.41
Nd	43.01	23.08	49.78	7.47	80.30	88.57	25.12	21.29	45.36	90.10
Sm	7.99	4.65	9.52	2.38	14.68	14.15	6.12	4.79	8.68	16.31
Eu	1.06	0.60	1.30	0.19	0.91	1.99	0.55	0.43	0.76	0.59
Gd	5.86	4.00	8.19	2.40	9.64	10.93	4.90	2.82	4.66	10.84
Tb	0.76	0.62	1.21	0.51	1.25	1.45	0.64	0.28	0.43	1.35
Dy	3.73	3.52	6.82	3.32	6.34	7.35	2.74	0.97	1.51	6.35
Ho	0.62	0.63	1.30	0.63	1.13	1.29	0.41	0.12	0.20	1.09
Er	1.43	1.65	3.43	1.98	2.82	3.27	1.00	0.27	0.44	2.71
Tm	0.17	0.24	0.47	0.37	0.40	0.45	0.14	0.03	0.06	0.35
Yb	0.92	1.59	2.93	2.87	2.55	2.73	0.84	0.21	0.34	2.02
Lu	0.12	0.23	0.43	0.44	0.36	0.39	0.11	0.03	0.05	0.27
ΣREE	221.37	129.27	271.33	49.29	401.60	525.65	135.15	111.44	227.48	435.60

Sample_ID	AST-13	AST-14	AST-15	AST-16	RK-1	RK-4i	RK-4ii	RK-9	RK-10	RK-13
Major elements										
SiO_2	74.06	71.72	68.16	69.13	69.11	68.96	73.82	68.88	71.56	74.78
TiO_2	0.18	0.40	0.91	0.71	0.64	0.73	0.14	0.70	0.26	0.07
Al_2O_3	13.05	14.50	14.83	14.04	14.42	14.37	13.82	14.61	15.56	14.36
MnO	0.03	0.02	0.04	0.05	0.05	0.06	0.02	0.05	0.03	0.04
MgO	0.98	0.73	0.90	0.44	0.70	0.89	0.27	0.79	0.67	0.17
CaO	0.62	0.87	1.68	1.72	2.05	1.42	1.10	1.73	2.60	0.66
Na_2O	3.13	3.13	2.35	2.37	2.47	2.10	2.19	2.75	5.39	3.56
K_2O	4.80	5.15	5.65	6.27	5.30	5.16	6.12	5.15	1.06	4.49
P_2O_5	0.12	0.15	0.24	0.24	0.18	0.17	0.11	0.25	0.07	0.25
Fe_2O_3	2.33	2.55	4.33	4.32	4.23	4.97	1.35	4.44	2.30	1.26
LOI	0.59	0.62	0.66	0.42	0.64	0.97	0.95	0.45	0.38	0.29
Sum	99.89	99.84	99.75	99.71	99.79	99.80	99.89	99.80	99.87	99.94
Trace elements										
Sc	6.63	4.75	6.77	7.03	9.21	10.79	3.74	9.26	4.25	3.41
Cr	3.69	30.11	30.82	7.45	31.20	37.36	3.50	28.64	29.67	2.22
Co	3.42	5.77	9.65	6.34	9.51	12.07	2.70	10.10	7.50	1.49
Ni	0.84	12.72	11.41	2.45	15.85	17.18	3.56	10.92	14.12	1.20
Zn	16.45	39.14	84.57	97.61	67.18	77.78	23.56	73.59	35.96	27.03
Rb	263.92	304.84	288.65	324.55	354.30	368.27	388.20	336.18	17.92	340.58
Sr	69.12	99.70	124.66	92.78	134.20	99.67	57.64	114.12	498.85	34.00
Y	29.13	30.43	34.82	51.81	41.28	51.32	16.16	35.92	3.69	10.50
Zr	43.49	92.00	70.82	102.87	43.37	28.75	32.61	64.18	18.93	28.22
Nb	12.87	18.74	19.58	29.09	18.63	19.59	6.45	19.83	3.73	6.43
Cs	4.01	1.77	3.78	3.04	14.56	19.35	8.01	5.73	1.58	3.85
Ba	174.96	384.12	713.38	772.97	721.09	549.80	284.96	536.72	413.24	87.30
Hf	1.25	2.51	1.86	2.73	1.15	0.76	0.99	1.65	0.52	0.94
Ta	0.81	1.19	1.24	1.69	1.82	1.69	0.69	1.13	0.37	0.57
Pb	21.77	34.73	53.19	65.97	41.92	37.83	54.89	40.33	7.12	20.02
Th	25.28	98.97	49.35	63.77	42.80	53.41	37.15	84.03	2.37	4.77
U	5.39	11.31	6.60	3.08	6.51	10.15	23.62	5.51	0.90	15.89
Rare earth elements										
La	27.18	86.67	102.75	206.46	72.51	76.00	25.99	83.31	14.29	7.43
Ce	58.69	198.22	220.43	413.81	147.63	172.51	56.04	187.02	25.98	15.40
Pr	7.07	23.51	25.19	46.47	17.71	19.79	7.02	23.17	2.74	1.75
Nd	25.35	84.00	92.18	166.48	64.28	71.31	25.96	86.56	9.60	6.02
Sm	4.72	14.81	16.07	26.59	11.90	13.28	5.42	16.19	1.55	1.52
Eu	0.27	0.55	0.80	1.10	1.16	0.92	0.33	0.90	0.47	0.19
Gd	3.58	9.26	10.71	18.48	9.52	10.37	4.09	10.98	1.10	1.47
Tb	0.65	1.15	1.33	2.17	1.35	1.51	0.57	1.38	0.14	0.28
Dy	4.37	5.73	6.64	10.81	7.32	8.54	2.95	6.89	0.68	1.73
Ho	0.88	1.01	1.18	1.92	1.36	1.64	0.50	1.22	0.12	0.30
Er	2.56	2.63	3.00	5.00	3.68	4.49	1.27	3.01	0.32	0.82
Tm	0.39	0.35	0.40	0.69	0.53	0.63	0.17	0.38	0.05	0.12
Yb	2.42	2.11	2.41	4.23	3.33	3.78	0.97	2.14	0.37	0.82
Lu	0.32	0.29	0.34	0.63	0.48	0.55	0.13	0.29	0.06	0.12
ΣREE	138.45	430.29	483.43	904.84	342.76	385.32	131.41	423.44	57.47	37.97

Sample_ID	FM-4	NP-2	NP-6	NP-7	NP-8	NP-10	NP-12	TAR-1	CG-1	CG-2
Major elements										
SiO_2	74.21	53.10	64.77	66.91	70.56	73.80	68.22	67.72	76.07	73.31
TiO_2	0.07	0.37	0.68	1.07	0.50	0.06	0.68	0.91	0.03	0.14
Al_2O_3	14.36	14.17	16.22	14.72	14.60	15.25	16.10	15.17	13.16	14.26
MnO	0.03	0.08	0.04	0.06	0.02	0.03	0.07	0.03	0.03	0.03
MgO	0.01	5.39	1.72	1.13	0.63	0.12	1.12	1.24	0.05	0.26
CaO	1.34	19.12	1.26	2.22	0.91	0.94	0.86	1.12	1.74	1.70
Na_2O	3.42	0.21	2.64	2.57	2.12	3.53	2.73	2.53	4.56	3.65
K_2O	4.85	0.37	5.81	5.02	6.58	4.65	3.13	5.44	1.68	4.50
P_2O_5	0.05	0.11	0.18	0.21	0.15	0.09	0.06	0.24	0.01	0.05
Fe_2O_3	1.06	4.62	5.62	5.37	3.13	0.79	5.12	4.46	2.36	1.16
LOI	0.42	2.34	0.84	0.48	0.59	0.67	1.58	0.91	0.87	0.98
Sum	99.81	99.88	99.79	99.76	99.79	99.92	99.68	99.77	100.57	100.04
Trace elements										
Sc	3.55	10.12	9.94	10.79	6.62	4.83	15.43	8.49	4.83	2.16
Cr	1.53	57.27	62.04	39.87	12.59	0.13	80.61	36.18	0.96	2.70
Co	0.98	11.82	12.20	11.98	6.04	0.48	16.27	9.44	0.16	2.08
Ni	0.79	28.69	26.34	13.09	4.18	-0.03	37.56	11.72	0.89	2.15
Zn	25.96	59.36	64.35	81.22	52.79	14.21	83.47	52.93	18.77	27.03
Rb	462.03	35.82	375.29	245.75	384.50	301.64	113.78	298.59	58.38	97.93
Sr	61.59	150.14	109.10	139.98	69.77	37.68	151.64	99.29	124.18	384.98
Y	41.46	40.17	24.16	31.36	25.30	26.06	30.98	38.40	1.76	2.62
Zr	58.68	13.07	31.72	48.45	53.79	8.87	64.74	48.56	19.59	58.68
Nb	11.00	14.22	20.70	21.33	17.35	13.16	15.71	23.96	4.77	3.31
Cs	50.11	1.82	9.65	3.82	3.12	24.51	18.67	1.91	1.18	1.31
Ba	161.38	176.18	548.98	679.16	470.33	35.06	777.82	603.69	21.85	1144.00
Hf	2.29	0.49	0.85	1.22	1.39	0.40	1.79	1.29	0.71	1.58
Ta	2.28	1.94	1.30	1.37	0.81	2.81	1.01	1.34	0.36	0.15
Pb	81.08	27.67	35.18	36.04	51.01	45.04	24.99	27.22	28.07	32.47
Th	15.37	16.06	58.27	39.26	68.16	5.77	16.83	129.63	1.61	10.70
U	27.71	6.71	6.04	4.90	3.38	14.82	1.72	5.28	0.91	1.30
Rare earth elements										
La	13.81	37.92	79.79	99.42	89.08	6.29	49.90	133.08	1.92	17.17
Ce	29.21	73.48	178.02	208.15	192.31	12.44	106.34	301.08	3.28	27.02
Pr	3.42	8.43	20.38	24.25	23.23	1.60	12.11	35.84	0.43	2.71
Nd	12.60	30.22	73.55	87.44	82.83	5.70	45.11	132.91	1.68	8.64
Sm	3.29	6.26	12.75	14.88	14.68	1.89	8.98	22.83	0.41	1.28
Eu	0.26	1.10	0.68	1.04	0.62	0.19	1.30	0.87	0.23	0.45
Gd	3.64	5.98	8.40	10.17	9.67	2.23	7.79	13.90	0.37	0.93
Tb	0.73	1.04	1.04	1.23	1.13	0.50	1.10	1.61	0.05	0.11
Dy	5.01	6.41	4.97	5.97	5.33	3.57	5.80	7.48	0.28	0.51
Ho	1.08	1.32	0.84	1.06	0.89	0.74	1.07	1.29	0.06	0.09
Er	3.43	3.71	2.01	2.77	2.10	2.22	2.94	3.31	0.19	0.23
Tm	0.57	0.56	0.25	0.39	0.26	0.36	0.44	0.45	0.04	0.03
Yb	3.93	3.41	1.43	2.39	1.37	2.37	2.91	2.65	0.26	0.20
Lu	0.62	0.48	0.19	0.36	0.18	0.34	0.45	0.37	0.05	0.03
ΣREE	81.60	180.32	384.30	459.52	423.68	40.44	246.24	657.67	9.25	59.40

Sample_ID	GRT-1	GRT-2	JT-1	JT-2	BST-1	DR-1	GB-1	HZ-1	HZ-2	GZ-1
Major elements										
SiO_2	74.96	73.82	55.61	68.83	50.13	65.60	72.26	75.80	75.68	73.49
TiO_2	0.23	0.26	1.39	0.39	0.39	0.53	0.25	0.03	0.05	0.22
Al_2O_3	12.45	13.47	16.50	15.15	16.73	14.60	14.22	13.35	13.05	13.48
MnO	0.06	0.08	0.11	0.04	0.13	0.06	0.05	0.04	0.01	0.03
MgO	0.71	0.61	3.93	0.91	6.82	2.39	0.61	0.03	0.04	0.49
CaO	3.30	3.54	5.79	3.01	12.67	4.12	3.53	0.72	1.02	1.86
Na_2O	3.28	3.98	4.12	3.87	1.66	4.52	3.01	4.01	3.51	3.29
K_2O	0.80	0.62	2.99	3.16	0.06	0.63	2.28	4.40	4.72	4.21
P_2O_5	0.04	0.05	0.71	0.15	0.03	0.09	0.05	0.01	0.01	0.07
Fe_2O_3	2.75	2.60	7.15	2.64	9.78	6.37	2.30	0.40	0.67	1.57
LOI	0.78	0.73	1.03	0.86	1.66	0.99	1.40	0.98	1.00	0.83
Sum	99.36	99.75	99.33	99.02	100.06	99.90	99.97	99.77	99.76	99.53
Trace elements										
Sc	11.96	10.54	12.44	4.06	51.06	25.85	7.61	3.02	0.71	2.88
Cr	1.47	1.24	65.80	13.47	108.86	9.86	7.80	bdl	0.66	6.69
Co	6.77	5.37	20.26	7.80	34.35	12.45	4.98	0.08	0.48	4.03
Ni	1.22	1.10	52.22	10.29	33.57	6.29	5.48	0.09	0.23	4.73
Zn	26.80	43.14	100.67	46.86	28.49	61.94	35.88	15.16	4.19	24.72
Rb	13.42	8.93	90.72	90.08	0.68	9.13	83.43	228.19	149.40	96.83
Sr	122.66	159.52	984.46	576.69	169.94	123.27	272.52	6.64	89.31	290.01
Y	16.33	18.06	17.04	8.04	7.10	17.51	16.67	6.85	2.98	4.06
Zr	23.61	57.90	52.55	47.36	4.50	49.91	34.68	35.62	74.16	26.04
Nb	1.49	0.91	30.03	12.87	0.08	1.11	6.77	14.05	3.44	5.90
Cs	0.34	0.17	2.98	1.15	0.06	0.37	3.28	4.83	2.24	1.29
Ba	125.04	83.32	632.46	709.53	6.79	50.15	403.67	0.74	109.09	578.37
Hf	0.80	1.62	1.64	1.11	0.18	1.51	1.04	2.05	2.56	0.89
Ta	0.12	0.07	1.62	0.90	0.01	0.08	0.41	1.08	0.40	0.39
Pb	1.79	2.33	12.52	12.82	0.59	3.92	18.26	23.15	20.01	15.21
Th	0.52	0.75	7.54	11.77	0.04	0.61	13.69	12.52	11.37	4.24
U	0.28	0.30	1.57	0.90	0.05	0.31	0.95	2.08	3.89	0.79
Rare earth elements										
La	2.77	4.35	55.81	39.95	0.55	2.90	26.89	8.41	7.12	14.63
Ce	6.56	9.94	117.56	67.65	1.37	7.36	55.20	15.98	12.05	25.84
Pr	0.96	1.44	13.86	7.23	0.24	1.11	6.35	1.99	1.46	2.74
Nd	4.57	6.60	51.12	24.00	1.43	5.54	24.12	7.50	5.28	9.41
Sm	1.39	1.79	8.47	3.55	0.58	1.78	4.77	1.92	1.01	1.56
Eu	0.45	0.57	2.20	0.92	0.33	0.61	1.14	0.14	0.25	0.43
Gd	1.81	2.15	6.13	2.57	0.92	2.35	4.10	1.69	0.75	1.21
Tb	0.33	0.39	0.76	0.32	0.18	0.45	0.57	0.24	0.10	0.15
Dy	2.33	2.62	3.58	1.59	1.21	2.91	3.07	1.24	0.51	0.76
Ho	0.53	0.59	0.61	0.28	0.27	0.65	0.58	0.21	0.10	0.14
Er	1.62	1.83	1.49	0.70	0.79	1.95	1.57	0.56	0.30	0.34
Tm	0.26	0.29	0.20	0.09	0.12	0.31	0.22	0.07	0.05	0.05
Yb	1.79	2.07	1.15	0.56	0.80	2.04	1.43	0.50	0.33	0.29
Lu	0.30	0.35	0.17	0.07	0.13	0.33	0.22	0.07	0.05	0.04
ΣREE	25.67	34.98	263.11	149.48	8.92	30.29	130.23	40.52	29.36	57.59

Sample_ID	GW-1	GP-1	YK-2	YK-3	TH-1	TH-2	KOH-4	SK-2	KPL-2	KB-1
Major elements										
SiO_2	51.96	73.72	56.03	74.41	71.06	75.35	73.79	70.61	77.30	73.46
TiO_2	1.12	0.24	0.73	0.23	0.37	0.18	0.51	0.37	0.12	0.20
Al_2O_3	17.08	13.16	20.12	13.10	14.11	12.76	12.48	14.84	12.05	15.16
MnO	0.15	0.05	0.08	0.02	0.08	0.06	0.09	0.05	0.02	0.02
MgO	4.67	0.56	1.51	0.30	0.71	0.31	1.53	0.81	0.14	0.35
CaO	8.19	1.95	7.55	1.83	2.37	1.46	5.02	2.55	0.79	1.99
Na_2O	3.76	3.11	3.84	3.09	4.03	3.97	1.26	3.80	2.74	4.22
K_2O	1.68	4.15	1.92	5.55	3.05	3.11	1.06	3.72	5.46	3.69
P_2O_5	0.49	0.07	0.26	0.04	0.10	0.03	0.11	0.15	0.00	0.04
Fe_2O_3	8.62	1.97	5.40	0.62	2.51	1.59	3.58	2.37	0.84	1.10
LOI	1.85	0.65	1.90	0.56	0.67	0.80	0.43	0.54	0.37	1.12
Sum	99.57	99.63	99.34	99.75	99.06	99.62	99.85	99.80	99.83	101.34
Trace elements										
Sc	20.19	3.84	13.11	3.06	6.01	2.99	7.75	3.92	0.85	1.41
Cr	22.12	2.93	0.99	3.54	3.19	1.54	85.38	12.21	0.28	1.75
Co	27.22	4.66	11.08	1.44	5.61	2.22	10.00	6.82	1.36	1.78
Ni	31.78	2.37	4.01	2.60	2.50	1.06	32.48	8.78	0.98	1.42
Zn	89.63	21.20	42.92	10.27	35.75	15.84	43.55	45.56	8.82	37.56
Rb	30.29	112.60	41.73	191.34	89.95	92.36	50.28	131.17	116.39	133.51
Sr	928.80	244.55	514.85	145.96	211.54	115.19	207.92	457.69	152.00	586.66
Y	23.43	14.01	21.66	22.97	17.19	10.62	20.06	9.17	3.03	4.45
Zr	34.93	43.38	40.17	145.33	74.10	46.63	34.13	45.00	18.91	46.24
Nb	6.75	4.70	4.82	8.35	5.55	4.33	8.90	16.37	4.09	3.97
Cs	0.98	2.54	3.17	6.71	3.66	2.57	1.73	8.94	0.73	10.97
Ba	379.87	516.96	234.87	297.87	390.87	401.17	193.96	653.03	468.58	1079.10
Hf	1.21	1.31	1.34	4.35	2.15	1.38	0.92	1.30	0.63	1.32
Ta	0.38	0.56	0.32	1.01	0.49	0.43	0.55	1.66	0.23	0.37
Pb	8.25	9.86	6.70	8.76	9.01	11.40	7.51	21.69	14.65	33.62
Th	3.85	10.69	7.04	30.63	8.30	9.96	11.61	11.14	36.06	6.75
U	0.81	1.83	1.80	4.58	1.94	1.44	0.51	3.61	1.26	1.56
Rare earth elements										
La	33.44	32.98	17.07	19.82	17.04	22.04	33.14	32.02	22.91	19.66
Ce	70.99	54.62	35.87	49.89	33.07	37.97	66.06	58.27	40.94	34.95
Pr	9.27	5.23	4.52	6.23	3.79	3.82	7.48	6.11	4.00	3.77
Nd	38.04	16.60	18.36	21.80	13.98	12.62	26.98	20.38	12.22	12.25
Sm	7.17	2.55	4.17	4.10	2.79	2.09	4.79	3.21	1.55	1.89
Eu	1.93	0.64	1.42	0.56	0.83	0.48	1.05	0.80	0.49	0.53
Gd	5.84	2.19	4.09	3.59	2.70	1.84	4.06	2.38	1.01	1.26
Tb	0.80	0.33	0.64	0.57	0.43	0.27	0.60	0.32	0.12	0.16
Dy	4.29	2.08	3.73	3.44	2.64	1.60	3.40	1.64	0.57	0.79
Ho	0.83	0.44	0.76	0.72	0.56	0.34	0.68	0.30	0.10	0.14
Er	2.24	1.36	2.12	2.17	1.67	1.03	1.92	0.81	0.28	0.38
Tm	0.33	0.22	0.31	0.36	0.26	0.17	0.29	0.12	0.04	0.06
Yb	2.06	1.55	1.97	2.35	1.79	1.19	1.83	0.76	0.31	0.37
Lu	0.31	0.25	0.30	0.37	0.29	0.20	0.27	0.11	0.05	0.05
ΣREE	177.54	121.04	95.33	115.97	81.84	85.66	152.55	127.23	84.59	76.26

Sample_ID	KB-2	KB-3	KB-4i	KB-4ii	KB-5	KB-6	SGH-2	SGH-4	SGH-6	SGH-7
Major elements										
SiO_2	61.08	74.58	77.88	60.62	66.76	74.34	70.62	70.74	68.17	59.32
TiO_2	0.94	0.01	0.01	0.85	0.53	0.02	0.42	0.44	0.82	0.54
Al_2O_3	12.78	13.10	12.23	17.26	14.81	14.85	14.96	13.84	14.19	20.51
MnO	0.32	0.01	0.14	0.08	0.07	0.01	0.04	0.04	0.06	0.35
MgO	0.58	0.01	0.01	3.18	1.86	0.07	0.76	1.32	1.10	0.56
CaO	1.67	0.83	0.96	5.32	3.85	0.92	1.68	1.29	1.62	3.32
Na_2O	2.43	1.79	3.31	3.06	2.39	4.44	3.16	2.34	2.33	4.18
K_2O	5.59	8.08	4.25	2.36	3.78	2.95	4.31	4.50	5.30	7.57
P_2O_5	0.04	0.07	0.01	0.21	0.13	0.09	0.24	0.08	0.21	0.07
Fe_2O_3	11.71	0.25	0.63	5.39	4.41	0.59	3.09	3.91	5.43	2.90
LOI	1.58	0.68	0.34	1.04	0.86	0.94	0.59	1.23	0.53	0.44
Sum	98.72	99.39	99.76	99.37	99.45	99.22	99.87	99.72	99.76	99.76
Trace elements										
Sc	1.02	0.34	4.09	11.03	9.85	1.03	6.14	7.50	10.93	2.28
Cr	bdl	0.32	bdl	75.83	27.20	bdl	27.29	102.05	22.74	0.61
Co	1.05	0.70	0.13	25.13	8.83	0.14	7.85	9.62	8.18	4.55
Ni	2.22	3.75	0.29	26.64	6.00	0.09	9.41	20.11	8.72	0.74
Zn	171.14	3.50	4.33	60.66	56.30	14.66	70.58	74.26	90.02	99.87
Rb	137.34	327.36	219.95	224.74	128.42	127.83	240.02	215.63	291.97	171.91
Sr	54.86	72.10	11.49	381.95	382.92	40.20	146.61	184.78	130.39	899.44
Y	56.88	7.35	97.55	13.86	12.14	19.73	16.51	15.97	29.43	27.52
Zr	95.07	2.72	26.55	16.98	24.42	34.63	39.88	25.16	24.75	58.94
Nb	82.22	7.32	31.59	9.92	13.68	19.98	20.37	10.88	20.49	11.08
Cs	5.79	27.18	3.40	11.31	6.67	1.93	10.63	5.67	7.08	2.36
Ba	491.81	392.07	13.13	423.26	1830.59	15.37	429.79	695.80	727.62	275.73
Hf	1.94	0.16	1.43	0.48	0.76	1.33	1.08	0.71	0.74	1.57
Ta	3.11	2.53	0.28	0.80	0.79	2.84	1.56	0.55	1.50	0.61
Pb	10.84	83.22	68.50	20.72	23.78	39.39	37.34	34.99	39.55	31.33
Th	6.33	2.55	9.25	6.47	22.89	3.28	18.89	21.90	60.04	8.76
U	0.27	6.04	21.82	1.77	3.05	22.45	3.51	5.34	5.72	3.53
Rare earth elements										
La	90.70	3.74	3.72	21.44	63.46	4.89	38.95	44.54	68.86	31.82
Ce	182.79	6.86	7.99	40.74	118.85	9.26	82.42	94.38	154.66	58.55
Pr	21.36	0.74	1.19	4.40	12.14	1.09	8.99	10.40	18.81	7.37
Nd	79.59	2.48	5.60	16.18	39.52	3.53	32.33	37.25	70.54	26.21
Sm	15.00	0.69	3.52	3.09	5.48	1.27	6.59	6.82	13.32	4.83
Eu	4.37	0.25	0.05	1.15	1.31	0.13	0.86	0.79	0.97	0.97
Gd	12.64	0.76	6.20	2.81	3.76	1.68	5.34	5.02	9.18	4.19
Tb	1.89	0.16	1.50	0.41	0.47	0.42	0.73	0.63	1.17	0.64
Dy	10.90	1.05	11.23	2.35	2.29	2.80	3.38	3.13	5.84	4.07
Ho	2.18	0.21	2.53	0.47	0.42	0.52	0.52	0.54	1.06	0.87
Er	6.06	0.57	8.33	1.29	1.14	1.45	1.23	1.35	2.72	2.64
Tm	0.89	0.08	1.50	0.18	0.17	0.22	0.16	0.18	0.38	0.41
Yb	5.76	0.53	11.15	1.17	1.18	1.34	0.94	1.03	2.34	2.73
Lu	0.91	0.07	1.79	0.17	0.19	0.19	0.12	0.15	0.34	0.42
ΣREE	435.04	18.19	66.30	95.85	250.38	28.79	182.56	206.21	350.19	145.72

Sample_ID	SGH-9	HSH-2	HSH-4	HSH-5	KDS-1	GL-3	GL-2	NG-1
Major elements								
SiO_2	59.07	65.19	61.52	60.28	71.29	62.95	74.92	74.47
TiO_2	0.46	0.43	0.72	0.53	0.35	1.22	0.00	0.03
Al_2O_3	20.58	16.73	15.48	19.51	15.10	14.40	14.95	15.18
MnO	0.37	0.06	0.10	0.05	0.02	0.07	0.03	0.10
MgO	0.23	1.13	2.52	0.88	0.44	3.41	0.01	0.01
CaO	2.52	2.92	3.76	3.34	2.12	3.21	0.81	1.46
Na_2O	5.32	4.68	3.90	4.67	4.34	2.09	4.77	4.36
K_2O	6.65	4.39	5.65	6.02	3.46	3.29	3.00	2.81
P_2O_5	0.05	0.21	0.53	0.20	0.10	0.10	0.11	0.03
Fe_2O_3	2.50	3.20	4.41	2.70	1.81	7.76	0.60	0.89
LOI	2.07	0.37	0.52	0.43	0.57	1.09	0.67	0.54
Sum	99.81	99.31	99.12	98.61	99.61	99.59	99.86	99.87
Trace elements								
Sc	1.67	4.76	8.33	3.62	1.31	20.93	0.54	3.45
Cr	0.73	17.33	52.96	7.32	3.16	103.23	0.79	0.88
Co	3.07	8.55	11.25	7.03	3.42	15.32	0.41	0.28
Ni	0.31	19.58	42.08	8.00	2.27	25.94	0.19	0.20
Zn	207.14	51.12	70.87	43.35	36.89	84.45	12.04	18.54
Rb	151.57	151.19	232.94	113.58	82.84	135.30	136.81	100.53
Sr	467.57	1716.80	1877.27	2346.26	766.31	334.99	17.72	105.22
Y	21.73	16.07	23.47	12.06	3.12	5.38	10.25	15.63
Zr	49.31	51.62	74.06	57.34	40.91	56.49	42.65	9.02
Nb	10.27	20.96	30.92	16.97	8.47	23.35	18.94	22.37
Cs	3.51	7.33	14.59	0.89	4.48	6.74	3.57	1.34
Ba	84.76	3412.65	4469.81	9138.05	1759.11	902.04	6.34	68.67
Hf	1.13	1.38	2.43	1.44	1.02	1.53	1.67	0.46
Ta	0.56	1.36	1.71	0.96	0.48	1.07	5.25	1.20
Pb	59.15	75.61	83.41	55.64	50.88	12.84	38.29	26.38
Th	11.22	75.27	127.45	84.47	95.47	63.58	1.75	6.16
U	2.23	6.04	15.09	2.75	3.80	0.83	14.80	13.40
Rare earth elements								
La	34.29	125.73	144.11	91.64	72.26	126.39	2.75	10.41
Ce	62.02	221.93	283.17	168.20	124.56	225.06	4.89	19.93
Pr	6.96	23.51	33.01	18.66	12.03	22.43	0.57	2.29
Nd	23.05	78.89	121.79	64.41	36.88	72.47	1.72	8.55
Sm	3.83	11.34	19.80	9.62	4.34	8.92	0.59	2.21
Eu	0.72	2.36	3.76	2.29	0.95	1.16	0.06	0.22
Gd	3.26	6.72	11.63	5.55	2.34	5.23	0.65	2.38
Tb	0.49	0.72	1.21	0.59	0.24	0.46	0.18	0.42
Dy	3.17	3.18	4.94	2.50	0.89	1.55	1.27	2.53
Ho	0.70	0.52	0.78	0.40	0.12	0.22	0.26	0.45
Er	2.21	1.31	1.86	0.98	0.19	0.44	0.82	1.07
Tm	0.36	0.18	0.25	0.13	0.02	0.05	0.16	0.15
Yb	2.48	1.11	1.51	0.78	0.15	0.34	1.27	0.85
Lu	0.39	0.16	0.22	0.11	0.03	0.06	0.20	0.11
ΣREE	143.93	477.66	628.04	365.86	255.00	464.78	15.39	51.57

Table C4: Petrophysical properties samples at laboratory conditions

Sample_ID	WA (%)	Φ (%)	ρ_m (g cm^{-3})	ρ_b (g cm^{-3})	λ (W m^{-1} K^{-1})	α (10^{-6} m^2 s^{-1})	C_p (J kg^{-1} K^{-1})	C_{vol} (KJ m^{-3} K^{-1})
TTP-3	0.62	1.67	2.75	2.7	2.65	1.14	749.6	2023.92
TTP-5	0.38	1.01	2.7	2.67	2.78	1.07	752.7	2009.71
AST-4	0.5	1.32	2.69	2.66	1.78	0.77	755.2	2008.83
AST-6	0.39	1.03	2.67	2.64	1.98	1.08	750.3	1980.79
AST-8ii	0.47	1.23	2.65	2.62	2.72	1.38	748.7	1961.59
AST-16	0.52	1.39	2.69	2.65	2.03	1.18	750.9	1989.89
RK-4ii	0.6	1.55	2.64	2.59	3.37	1.95	754.5	1954.16
RK-9	0.53	1.42	2.7	2.66	1.99	0.89	746.9	1986.75
FM-4	0.87	2.24	2.64	2.58	1.86	1.09	749.3	1933.19
NP-2	0.34	1.03	3.03	3	2.73	1.19	751.3	2253.9
NP-6	0.47	1.26	2.71	2.67	2.17	0.95	748	1997.16
NP-8	0.36	0.95	2.64	2.62	2.2	1.12	752.3	1971.03
NP-12	0.55	1.43	2.65	2.62	2.12	1.16	758.5	2070.71
TAR-1	0.51	1.38	2.72	2.68	1.93	0.87	755.6	2025.01
CG-1	0.56	1.46	2.66	2.62	2.3	1.08	752.8	1972.34
CG-2	0.46	1.2	2.65	2.62	2	1	748.3	1960.55
GRT-1	0.33	0.9	2.72	2.69	2.39	1.14	755.2	2054.14
JT-2	0.61	1.61	2.71	2.66	2.03	0.79	758.5	2032.78
DR-1	0.23	0.64	2.79	2.77	2.13	1	760.4	2106.31
GB-1	0.56	1.49	2.71	2.67	2.17	0.88	755.7	2016.2
KOH-4	0.26	0.72	2.76	2.74	2.91	1.18	753.3	2064.04
KPL-2	0.57	1.51	2.69	2.65	2.42	1.43	744.3	1972.4
KB-1	0.33	0.87	2.64	2.62	2.31	1.31	743.3	1945.69
KB-4ii	1.31	3.52	2.78	2.68	1.52	0.77	767.1	2055.83
KB-6	0.58	1.51	2.66	2.62	2.44	1.13	764.7	2000.41
SGH-2	0.39	1.05	2.69	2.66	2.14	0.79	746.4	1985.42
SGH-4	0.46	1.22	2.7	2.66	2.39	1.23	758.4	2017.34
SGH-6	0.47	1.27	2.71	2.68	1.97	1.01	748.1	2004.91
SGH-9	0.54	1.41	2.66	2.62	1.66	0.75	764.3	2002.47
HSH-2	0.81	2.14	2.69	2.64	1.71	0.76	751.3	1983.43
HSH-5	0.77	2.04	2.69	2.64	1.48	0.68	747.8	1974.19
KDS-1	0.52	1.35	2.66	2.63	2.11	1.05	755.7	1987.49

Abbreviations: WA = water absorption, ρm = matrix density, ρb = bulk density, ϕ = porosity, λ = thermal conductivity, α = thermal diffusivity, cp = specific heat capacity, cvol = volumetric heat capacity

Table C5: EPMA point analysis of accessory minerals in syenite (HSH-5) from Kande pluton of Karakoram batholith

Sr. No	Mineral	Na_2O	SiO_2	Al_2O_3	MgO	SrO	UO_2	ThO_2	ZrO_2	Fe_2O_3	La_2O_3	Ce_2O_3	Nd_2O_3	CaO	TiO_2	MnO	Pr_2O_3	Sm_2O_3	Total
1	Allanite	0.06	35.26	20.25	0.41	0.24	0.15	2.11	bdl	14.45	2.05	3.88	1.47	17.92	0.25	0.24	0.37	0.16	98.94
2	Allanite	0.07	33.35	17.51	0.67	0.09	0.19	3.01	bdl	15.35	3.58	6.98	2.47	14.38	0.48	0.42	0.73	0.24	98.86
3	Allanite	0.04	33.27	17.63	0.64	0.09	0.18	3.01	bdl	15.87	3.53	6.99	2.51	14.29	0.48	0.43	0.72	0.21	99.27
4	Allanite	0.07	33.02	17.06	0.72	0.08	0.18	3.85	bdl	15.69	4.53	7.22	1.85	13.76	0.52	0.40	0.55	0.15	98.99
5	Allanite	0.04	36.47	21.55	0.13	0.38	0.12	1.02	bdl	14.53	1.32	2.40	0.88	19.85	0.07	0.20	0.22	0.09	98.99
6	Allanite	bdl	33.64	17.60	0.67	0.16	0.14	2.65	bdl	15.82	4.25	6.89	1.86	14.75	0.47	0.33	0.66	0.12	99.45
7	Allanite	0.04	35.26	20.46	0.44	0.27	0.12	1.84	bdl	14.06	2.13	4.00	1.63	17.77	0.26	0.21	0.40	0.19	94.78
8	Allanite	bdl	36.81	21.96	0.08	0.41	0.10	0.59	bdl	14.42	0.77	1.60	0.63	20.81	0.06	0.23	0.19	0.12	98.66
9	Allanite	0.07	33.00	16.77	0.88	0.07	0.19	3.86	bdl	15.80	4.07	7.20	2.03	13.96	0.56	0.44	0.64	0.12	66.07
10	Allanite	0.04	34.78	19.98	0.43	0.23	0.10	2.21	bdl	14.45	2.53	4.55	1.42	17.14	0.25	0.22	0.45	0.09	98.5
11	Allanite	0.06	33.40	17.69	0.61	0.09	0.14	2.97	bdl	15.57	3.53	7.01	2.57	14.37	0.45	0.39	0.73	0.24	99.32
12	Allanite	0.08	32.83	16.99	0.71	0.11	0.18	3.78	bdl	15.64	3.24	7.38	2.71	13.72	0.52	0.41	0.75	0.21	98.65
13	Titanite	0.04	29.90	1.45	bdl	bdl	bdl	0.02	bdl	1.13	bdl	0.07	0.13	27.97	36.16	0.03	bdl	0.05	97.36
14	Zircon	bdl	32.34	bdl	bdl	0.03	0.21	0.07	65.31	0.18	bdl	bdl	bdl	0.03	0.07	bdl	bdl	bdl	98.28
15	Apatite	0.07	0.18	0.02	bdl	0.15	bdl	bdl	bdl	0.04	bdl	0.03	0.03	54.28	0.02	bdl	bdl	0.04	56.75
16	Allanite	0.04	32.90	16.72	0.79	0.08	0.17	3.96	bdl	16.08	4.76	7.12	1.82	13.53	0.61	0.45	0.62	0.13	99.16
17	Allanite	0.04	34.96	20.44	0.38	0.26	0.10	2.17	bdl	14.29	2.14	4.22	1.65	17.40	0.24	0.21	0.44	0.19	98.79
18	Allanite	0.05	32.91	16.58	0.88	0.11	0.16	3.90	bdl	16.11	4.54	7.26	1.92	13.68	0.53	0.51	0.63	0.12	99.23
19	Allanite	0.05	34.50	19.32	0.41	0.20	0.11	2.20	bdl	14.72	2.86	5.07	1.72	16.67	0.25	0.28	0.51	0.17	98.68
20	Zircon	bdl	32.68	0.03	bdl	0.05	0.17	0.03	65.12	0.43	bdl	0.05	0.03	0.12	bdl	bdl	bdl	bdl	98.77
21	Allanite	0.06	32.71	16.80	0.72	0.07	0.15	3.39	0.03	15.97	4.09	7.97	2.73	13.29	0.52	0.38	0.78	0.25	99.3
22	Allanite	0.03	34.63	19.66	0.47	0.19	0.15	2.32	bdl	14.60	2.71	4.99	1.68	16.80	0.28	0.29	0.46	0.16	99.01
23	Allanite	0.04	33.02	16.98	0.89	0.07	0.15	3.88	bdl	15.71	4.41	7.25	1.95	13.65	0.50	0.46	0.59	0.15	99.07
24	Allanite	0.05	34.92	19.85	0.45	0.22	0.11	2.13	bdl	14.72	2.82	4.91	1.55	16.85	0.26	0.24	0.46	0.12	99.26
25	Allanite	0.06	32.00	15.15	0.92	0.04	0.10	1.44	bdl	16.74	8.47	10.72	1.72	11.24	0.89	0.41	0.74	0.06	68.05
26	Allanite	0.04	34.84	19.70	0.52	0.19	0.12	2.50	0.02	14.55	2.86	5.07	1.77	16.47	0.28	0.25	0.54	0.16	99.45
27	Allanite	0.03	33.29	17.91	0.53	0.18	0.12	3.23	0.03	15.40	3.45	6.09	1.75	15.24	0.37	0.31	0.59	0.15	98.22
28	Allanite	0.07	32.74	16.58	0.90	0.09	0.17	3.67	bdl	15.95	3.31	7.43	3.23	13.37	0.51	0.53	0.88	0.32	99.13
29	Allanite	0.06	32.63	16.50	0.91	0.08	0.16	3.45	bdl	15.71	3.66	7.71	2.88	13.23	0.48	0.50	0.82	0.27	98.48
30	Allanite	0.03	34.21	18.14	0.66	0.14	0.16	2.67	bdl	15.21	3.06	6.03	2.34	15.24	0.37	0.45	0.67	0.24	99.1
31	Allanite	< 0.03	35.08	20.56	0.40	0.28	0.11	1.92	bdl	14.02	2.23	4.08	1.45	17.77	0.24	0.20	0.42	0.17	98.68

| Sr. No	Mineral	Na_2O	SiO_2	Al_2O_3	MgO	SrO	UO_2	ThO_2	ZrO_2	Fe_2O_3	La_2O_3	Ce_2O_3	Nd_2O_3	CaO	TiO_2	MnO	Pr_2O_3	Sm_2O_3	Total
32	Allanite	0.08	33.77	19.30	0.41	0.21	0.1062	2.26	bdl	14.63	2.81	4.97	1.65	16.80	0.26	0.22	0.48	0.14	97.71
33	Allanite	0.02	34.02	19.09	0.44	0.17	0.12	2.52	bdl	15.09	2.87	5.17	1.68	16.47	0.26	0.31	0.51	0.15	98.43
34	Allanite	0.06	33.37	18.46	0.53	0.17	0.10	3.04	bdl	15.04	3.61	5.76	1.57	15.87	0.34	0.29	0.54	0.14	98.49
35	Allanite	0.05	34.14	18.60	0.54	0.14	0.11	2.51	bdl	15.63	4.09	6.69	1.72	15.45	0.40	0.37	0.50	0.16	100.52
36	Allanite	0.04	32.44	16.45	0.86	0.05	0.11	2.63	bdl	15.91	5.69	8.35	1.68	13.49	0.55	0.51	0.64	0.07	98.92
37	Allanite	0.04	31.24	16.16	0.88	0.07	0.14	4.13	bdl	16.00	4.51	7.00	1.72	13.85	0.52	0.52	0.65	0.12	73.98
38	Allanite	0.07	32.61	16.62	0.88	0.10	0.14	3.96	bdl	15.92	4.17	6.80	1.88	14.04	0.53	0.52	0.68	0.15	98.54
39	Allanite	0.08	32.35	16.38	1.00	0.07	0.17	4.02	bdl	15.91	3.22	7.76	3.00	13.33	0.55	0.51	0.84	0.27	95.74
40	Allanite	0.09	32.56	16.64	0.87	0.06	0.14	3.51	bdl	15.83	3.41	7.69	3.13	13.19	0.55	0.44	0.92	0.30	98.78
41	Allanite	0.07	34.46	20.11	0.44	0.28	0.08	2.54	bdl	14.55	2.52	4.37	1.24	17.49	0.26	0.21	0.39	0.10	98.86
42	Allanite	0.04	34.13	19.84	0.44	0.20	0.09	1.83	bdl	14.21	2.35	4.43	1.83	17.30	0.27	0.20	0.47	0.22	97.54
43	Allanite	0.06	34.51	20.13	0.42	0.26	0.09	2.09	bdl	14.30	2.36	4.42	1.72	17.43	0.24	0.22	0.47	0.19	98.68
44	Allanite	0.05	34.01	19.36	0.45	0.15	0.11	2.28	bdl	14.48	2.80	4.97	1.69	16.55	0.26	0.30	0.53	0.16	97.72
45	Allanite	0.04	33.57	19.30	0.41	0.25	0.14	1.96	bdl	14.89	2.49	4.80	1.74	17.08	0.25	0.26	0.50	0.16	97.46
46	Allanite	bdl	34.38	19.20	0.39	0.24	0.15	2.14	bdl	15.07	2.49	4.69	1.75	17.08	0.27	0.27	0.48	0.18	98.42
47	Allanite	0.05	33.82	20.24	0.44	0.26	0.10	2.38	bdl	14.01	2.14	3.80	1.26	18.00	0.23	0.18	0.35	0.12	79.06
48	Allanite	0.04	34.09	19.22	0.48	0.18	0.09	2.15	0.02	14.68	2.85	5.16	1.82	16.66	0.34	0.26	0.51	0.17	98.42
49	Allanite	0.07	32.25	17.02	0.75	0.11	0.13	3.79	bdl	15.46	4.41	7.03	1.90	13.96	0.51	0.43	0.65	0.17	98.09
50	Allanite	bdl	33.90	18.73	0.42	0.22	0.11	2.36	bdl	15.23	3.15	5.61	1.80	16.30	0.24	0.26	0.55	0.15	98.6
51	Allanite	0.03	32.40	16.85	0.93	0.10	0.17	4.10	bdl	15.67	4.02	7.06	2.04	13.99	0.53	0.44	0.65	0.15	98.49
52	Allanite	0.08	32.19	16.53	0.79	0.04	0.15	3.55	bdl	15.90	3.59	7.58	3.15	13.24	0.57	0.46	0.86	0.32	98.39
53	Allanite	0.07	33.16	17.40	0.76	0.09	0.11	3.34	bdl	15.36	3.75	7.09	2.53	13.98	0.46	0.44	0.75	0.22	98.97
54	Allanite	0.06	33.25	18.00	0.58	0.11	0.14	3.41	0.03	15.39	3.08	6.26	2.55	14.76	0.35	0.35	0.73	0.29	80.91
55	Allanite	0.03	33.23	18.32	0.59	0.12	0.12	3.00	bdl	15.10	2.99	6.18	2.52	15.10	0.35	0.35	0.63	0.27	95.47
56	Allanite	0.06	33.47	19.20	0.49	0.20	0.12	2.21	bdl	14.54	2.75	5.08	1.78	16.80	0.26	0.25	0.51	0.17	97.48
57	Zircon	bdl	31.98	bdl	bdl	bdl	0.17	bdl	65.98	0.33	bdl	0.06	0.03	0.10	bdl	bdl	bdl	bdl	98.65
58	Zircon	bdl	31.91	bdl	bdl	0.04	0.28	0.11	65.43	0.21	bdl	bdl	bdl	0.03	bdl	bdl	bdl	bdl	98.11
59	Zircon	bdl	32.16	bdl	bdl	0.06	0.24	0.08	65.73	0.35	0.04	0.07	0.04	0.12	bdl	bdl	bdl	0.03	99.02
60	Zircon	bdl	32.22	bdl	bdl	0.04	0.20	0.05	65.61	0.55	bdl	bdl	bdl	0.13	bdl	bdl	bdl	bdl	98.83
61	Zircon	bdl	32.46	0.02	bdl	bdl	0.10	bdl	65.39	0.28	0.05	bdl	bdl	0.06	bdl	bdl	bdl	bdl	98.36
62	Zircon	bdl	32.49	7.41	0.13	0.11	0.16	0.84	45.58	6.16	1.07	1.71	0.54	8.01	0.09	bdl	0.19	0.06	104.56
63	Zircon	bdl	32.27	0.02	bdl	0.04	0.55	0.04	63.79	0.40	bdl	0.07	0.04	0.12	bdl	bdl	bdl	bdl	97.38
64	Zircon	bdl	30.33	1.57	bdl	bdl	0.01	0.09	10.12	1.50	0.12	0.22	0.17	23.77	30.05	0.04	bdl	0.03	98.31
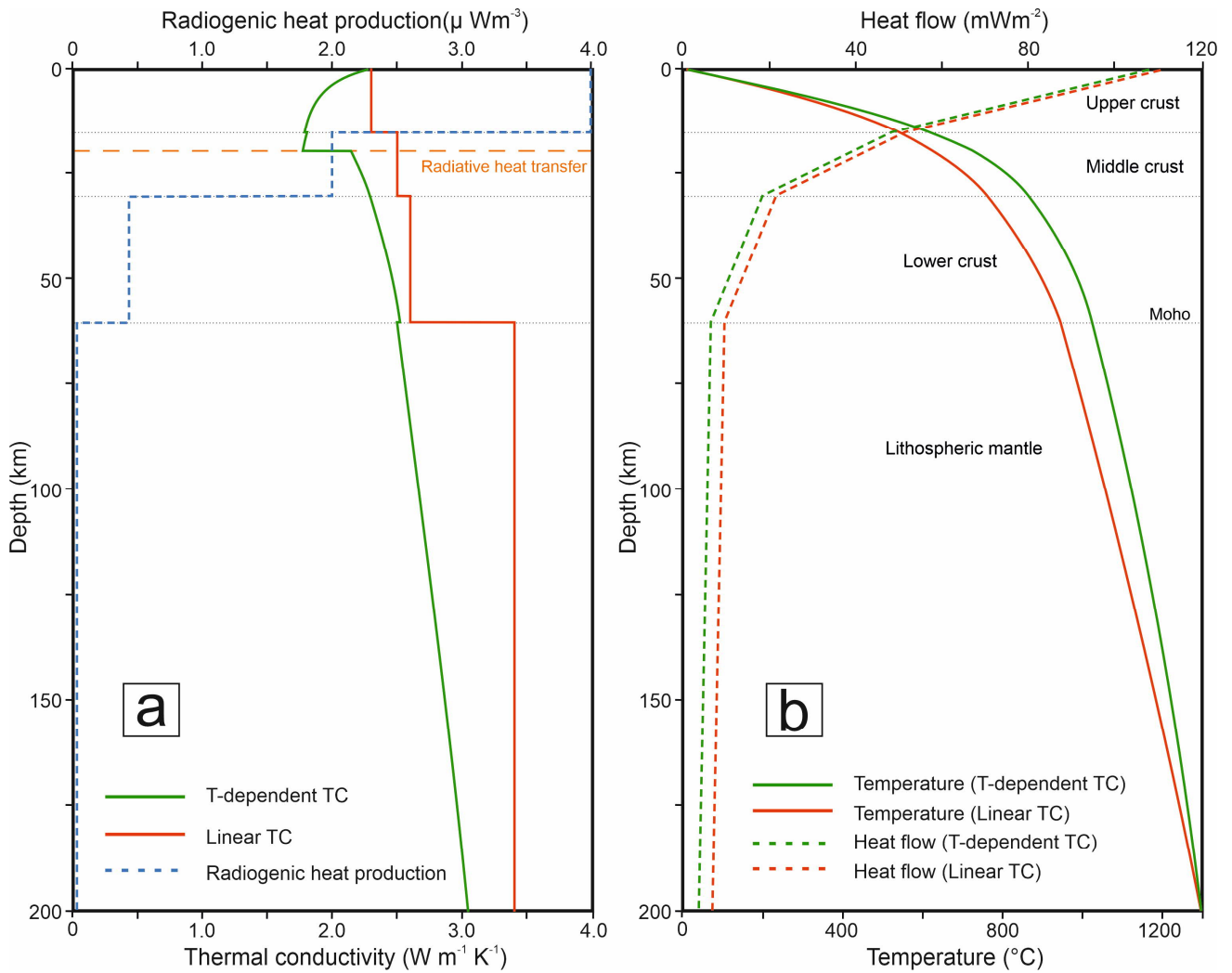
Figure D1: Effect of temperature-dependent thermal conductivity (TC). (a) Conversion of input linear TC into temperature-dependent TC using Jaupart et al. (2016) equation. Dashed golden line shows additional effect of radiative heat transfer on TC for temperatures above 1000 K. Blue dashed line shows the input values of radiogenic heat production. (b) Comparison of geotherms (solid lines) and heat flow (dashed lines) based on Temperature-dependent TC and linear TC.
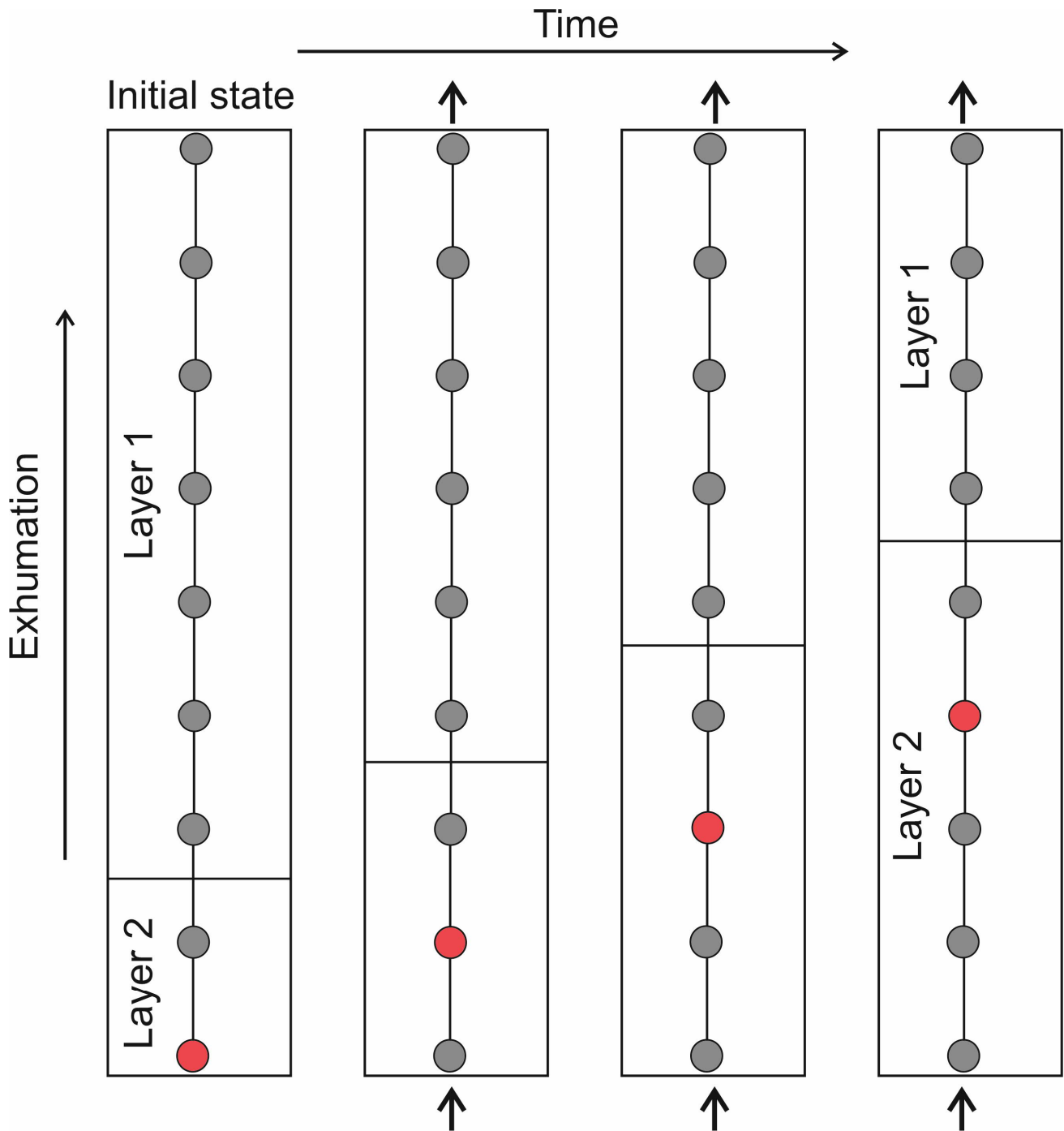
Figure D2: Simplified sketch showing the workflow of 1D transient model, in which the nodes below are added while the top ones are removed to depict exhumation and erosion.

List of publications

Journal articles

Anees, M., Kley, J., Leiss, B., Hindle, D., Wajid, AA., Wagner, B., Shah, MM., and Luijendijk, E.: Application of in-situ gamma spectrometry for radiogenic heat production estimation in the Western Himalaya, Kohistan, and Karakoram in northern Pakistan. Geotherm Energy 11, 29 (2023). https://doi.org/10.1186/s40517-023-00273-3

Anees, M., Sosa, G., van den Kerkhof, A., Leiss, B., Kley, J., Shah, MM., and Weydt, L.: Granitoids of the western Himalaya and Karakoram as potential geothermal reservoirs – A petrological, geochemical and petrophysical study. Geothermics (in review).

Conference proceedings

Anees, M., Kley, J., Leiss, B., Luijendijk, E., Wagner, B., and Shah, MM.: Exploration of Potential Geothermal Resources in the Himalaya-Karakoram Orogenic Belt, Northern Pakistan. Stanford Geothermal Workshop, California, USA, 12 – 14 February 2024.

Anees, M., Kley, J., Leiss, B., Luijendijk, E., Wagner, B., and Shah, MM.: Heat-producing granitoids of North Pakistan as potential geothermal prospects. Proceedings European Geothermal Congress 2022, Berlin, Germany, 17 – 21 October 2022, 8 pp., 2022.

Oral and poster presentations

Anees, M., Kley, J., Leiss, B., Wagner, B., and Shah, MM.: Heat-producing granitoids of North Pakistan as potential geothermal prospects. Proceedings European Geothermal Congress 2022, Berlin, Germany, 17 – 21 October 2022.

Anees, M., Kley, J., Leiss, B., Wagner, B., and Shah, MM.: Spatial variation of radiogenic heat production related to the crystalline rock types in the western Himalaya-Karakoram region of Pakistan. EGU General Assembly 2022, Vienna, Austria, 23 – 27 May 2022.